

---

# **Realization of Floquet topological systems with ultracold atoms in optical honeycomb lattices**

**Karen Maria Margarete Wintersperger**

---



München 2020



---

# **Realization of Floquet topological systems with ultracold atoms in optical honeycomb lattices**

**Karen Maria Margarete Wintersperger**

---

Dissertation  
an der Fakultät für Physik  
der Ludwig-Maximilians-Universität  
München

vorgelegt von  
Karen Maria Margarete Wintersperger  
aus Kassel

München, den 06.08.2020

Tag der mündlichen Prüfung: 23.09.2020  
Erstgutachter: Prof. Dr. Immanuel Bloch  
Zweitgutachter: Prof. Dr. Frank Pollmann  
Vorsitz: Prof. Dr. Jan Lipfert  
Weiteres Mitglied: Prof. Dr. Alexander Högele

## Zusammenfassung

Diese Doktorarbeit beschreibt die Realisierung von topologischen Floquet-Systemen mit ultrakalten Atomen in einem optischen, zweidimensionalen hexagonalen Gitter. Topologische Phasen können mittels periodisch getriebener Quantensysteme simuliert werden. Dabei wird ein statisches System als Zeit-Mittel über eine Modulationsperiode dargestellt, was unter dem Begriff Floquet-Engineering bekannt ist. Periodische Modulation kann jedoch auch dazu verwendet werden, intrinsisch zeit-abhängige Konfigurationen zu erzeugen, die in keinem statischen System auftreten können. Ein Beispiel dafür sind zweidimensionale, anomale Floquet-Phasen, in denen die Chern-Zahlen aller Energiebänder gleich null sind, aber trotzdem robuste Randzustände existieren. Ein statisches System hingegen, in dem alle Chern-Zahlen verschwinden, ist topologisch trivial.

Im optischen, hexagonalen Gitter können anomale Floquet-Systeme durch kontinuierliche, periodische Modulation der Laser-Intensitäten erzeugt werden. Das resultierende topologische Phasen-Diagramm beinhaltet unterschiedliche Bereiche, von denen drei genauer untersucht werden, unter anderem die anomale Floquet-Phase und eine Haldane-ähnliche Phase. Zeit-periodische Systeme besitzen periodische Quasi-Energien und können durch Windungszahlen beschrieben werden, welche die Anzahl der Randzustände in den Quasi-Energie-Lücken angeben. Das Schließen der Bandlücken definiert topologische Phasen-Übergänge, die mit Hilfe von interferometrischen Messungen nachgewiesen werden. Die entsprechende Änderung der Windungszahlen ist mit einem Vorzeichenwechsel der Berry-Krümmung an den Berührpunkten der Bänder verknüpft. Die Berry-Krümmung im Impulsraum wird anhand einer transversalen Ablenkung im Realraum gemessen, was die Bestimmung der Windungszahlen ermöglicht. Dies gibt direkt Aufschluss über die Existenz von Randzuständen, auch in einem System mit flachen Rändern, wie es im Experiment verwendet wird. Die gemessenen Bandlücken und transversalen Ablenkungen stimmen quantitativ sehr gut mit theoretischen Werten überein, die auf einer numerischen Berechnung der Floquet-Bandstruktur basieren. Um ein System mit Rändern zu beschreiben, wird außerdem ein Tight-Binding-Modell für das modulierte Gitter eingeführt.

Anomale Floquet-Phasen können ebenfalls in frequenz-modulierten, zweidimensionalen hexagonalen Gittern auftreten, falls die Inversions-Symmetrie des Gitters gebrochen wird. Die beiden Modulations-Schemata werden hinsichtlich ihrer Phasen-Diagramme und der experimentellen Umsetzbarkeit verglichen.

Die Zustände im Inneren eines anomalen Floquet-Systems können durch ein ungeordnetes Potential vollständig lokalisiert werden, was dazu verwendet werden könnte, wechselwirkende, periodisch getriebene Systeme gegen Heizeffekte zu stabilisieren. Die experimentelle Realisierung eines ungeordneten Potentials und starker Wechselwirkung wird diskutiert, ebenso wie eine direkte Messung der Randzustände.

Darüber hinaus werden die Eigenwerte von Wilson-Linien im zweidimensionalen hexagonalen Gitter betrachtet, welche die geometrischen Eigenschaften von entarteten Bloch-Bändern beschreiben, sowie Heizeffekte in schwach-wechselwirkenden, getriebenen Systemen am Beispiel eines eindimensionalen Gitters untersucht.

## Abstract

This thesis reports on the realization of Floquet topological systems with ultracold atoms in an optical honeycomb lattice. Using periodically driven quantum systems, topological phases of matter can be simulated by an effective, static Hamiltonian related to the time-evolution at integer multiples of the driving period, which is known as Floquet engineering. However, periodic driving can also give rise to genuinely time-dependent settings without static counterparts. One example is the anomalous Floquet phase in two dimensions, in which all bulk bands have a Chern number of zero but nevertheless robust chiral edge modes appear, which would be precluded by the bulk-edge correspondence in a static system.

In an optical honeycomb lattice, anomalous Floquet systems can be created by continuous, periodic modulation of the laser intensities. This driving scheme results in different topological regimes, three of which are investigated, including the anomalous Floquet phase and a Haldane-like phase. Periodically driven systems feature periodic quasienergies and can be characterized in terms of winding numbers, which count the number of chiral edge modes in each quasienergy gap. By interferometric measurements of the quasienergy gaps between the first two Floquet bands, the topological phase transitions, emerging as gap closings, are located. For periodically driven systems, a modified bulk-edge correspondence can be formulated. In particular, the change of the winding number at a phase transition is related to the sign change of the local Berry curvature. The Berry curvature at the gap closing points is probed by Hall deflection measurements to obtain the winding numbers in each of the topological regimes, revealing the existence of chiral edge modes also in a setting with smooth boundaries as used in the experiments. The measured quasienergy gaps and transverse deflections are quantitatively well described by a numerical calculation of the Floquet bandstructure that includes coupling to higher bands during the driving period. To derive the spectrum of the modulated lattice in a geometry with edges, a tight-binding description of the system is discussed.

Circular phase modulation of the honeycomb lattice can also give rise to an anomalous Floquet system when inversion symmetry is broken. The topological phase diagrams and the experimental feasibility are compared for both modulation schemes.

Due to the vanishing Chern numbers, the bulk states in the anomalous Floquet regime can be fully localized by a disorder potential. This could prevent heating in interacting, periodically driven systems, resulting in a many-body localized bulk coexisting with thermalizing edge states. The experimental realization of disorder and strong interactions, as well as independent probes of the edge states are investigated.

Bloch band geometry can be extended to multiband systems, using Wilson lines. The possible symmetry protection of their eigenvalues is discussed, along with measurements in the optical honeycomb lattice. Moreover, the onset of heating in weakly-interacting, periodically driven systems, triggered by parametric instabilities, is studied experimentally in a one-dimensional lattice.

# Contents

<b>1</b>	<b>Introduction</b>	<b>1</b>
<b>2</b>	<b>Floquet topological phases</b>	<b>7</b>
2.1	Topological characterization of static systems . . . . .	7
2.1.1	Geometric properties of Bloch bands . . . . .	8
2.1.2	Chern number and bulk-edge correspondence . . . . .	9
2.1.3	The topological Haldane model . . . . .	10
2.2	Floquet engineering . . . . .	14
2.2.1	Simulation of an effective Hamiltonian via periodic driving . . . . .	15
2.2.2	High-frequency limit . . . . .	17
2.3	Anomalous Floquet phases . . . . .	18
2.3.1	Topological characterization of periodically driven systems . . . . .	18
2.3.2	Change of the winding numbers at band touching points . . . . .	22
2.3.3	Anomalous Floquet phases in the presence of disorder and interactions	25
<b>3</b>	<b>Anomalous Floquet phases in a honeycomb lattice</b>	<b>27</b>
3.1	The optical honeycomb lattice . . . . .	27
3.1.1	Creation of the honeycomb lattice . . . . .	28
3.1.2	Calculation of the energy bands and Berry curvature . . . . .	29
3.1.3	Breaking of inversion or rotational symmetry . . . . .	33
3.2	Periodic intensity modulation . . . . .	35
3.2.1	Lattice modulation scheme . . . . .	35
3.2.2	Floquet band structure calculation . . . . .	36
3.2.3	Phase diagram . . . . .	40
3.2.4	Topological phases with a sublattice offset . . . . .	45
3.3	Tight-binding description of the modulated honeycomb lattice . . . . .	49
3.3.1	Two-band tight-binding model . . . . .	50
3.3.2	Eight-band tight-binding model . . . . .	57
3.3.3	Fitting the effective bands in the Haldane phase . . . . .	61
3.3.4	Derivation of the Haldane model in the high-frequency limit . . . . .	62
3.4	Calculation of the edge mode dispersion . . . . .	64
3.4.1	Tight-binding model in the stripe-geometry . . . . .	65
3.4.2	Quasienergy dispersion . . . . .	67

<b>4 Overview of the experimental setup and techniques</b>	<b>71</b>
4.1 Experimental setup . . . . .	71
4.1.1 Creation of the BEC . . . . .	72
4.1.2 Imaging techniques . . . . .	75
4.1.3 Honeycomb lattice setup . . . . .	77
4.1.4 Dipole trapping frequencies . . . . .	79
4.1.5 Vertical lattice . . . . .	80
4.2 Measurement techniques . . . . .	87
4.2.1 Lattice acceleration: Creating a gradient . . . . .	87
4.2.2 Stückelberg interferometry . . . . .	89
4.2.3 Momentum space width . . . . .	91
4.2.4 Deflection measurements and simulations . . . . .	93
<b>5 Characterization of the Floquet topological regimes</b>	<b>99</b>
5.1 Determination of the winding numbers . . . . .	99
5.1.1 Stückelberg interferometry in the modulated lattice . . . . .	101
5.1.2 Measurement of the phase transition points . . . . .	104
5.1.3 Deflection measurements in the lowest band . . . . .	107
5.1.4 Derivation of the winding numbers . . . . .	114
5.2 Probing the phase diagram . . . . .	119
5.2.1 Quasienergy gaps . . . . .	119
5.2.2 Berry curvature . . . . .	124
5.3 Deflection measurements in the second band . . . . .	126
5.3.1 Loading into the second band . . . . .	126
5.3.2 Probing the different topological regimes . . . . .	130
5.4 Lifetimes . . . . .	132
5.4.1 Measurement of the lifetimes . . . . .	132
5.4.2 Lifetimes in the different topological regimes . . . . .	134
<b>6 Anomalous Floquet phases in a shaken honeycomb lattice</b>	<b>139</b>
6.1 Modulation scheme and topological phase diagram . . . . .	139
6.1.1 Circular shaking of the honeycomb lattice . . . . .	140
6.1.2 Overview of the topological phases . . . . .	141
6.2 Tight-binding-description . . . . .	147
6.2.1 Two-band tight-binding model . . . . .	148
6.2.2 Haldane model for large shaking frequencies . . . . .	151
6.2.3 Edge mode dispersion . . . . .	154
6.3 Measured energy gaps and lifetimes . . . . .	156
6.3.1 Probing the energy gaps in the shaken honeycomb lattice . . . . .	156
6.3.2 Lifetimes . . . . .	157

---

<b>7 Novel phenomena in anomalous Floquet systems</b>	<b>161</b>
7.1 Probing disordered anomalous Floquet systems . . . . .	161
7.1.1 Direct imaging of the edge modes . . . . .	162
7.1.2 Adding disorder and probing the bulk . . . . .	163
7.1.3 Interplay with interactions . . . . .	165
7.2 Fermionization in the anomalous Floquet regime . . . . .	168
7.2.1 Statistical transmutation in a degenerate band minimum . . . . .	168
7.2.2 Probing the fermionization . . . . .	169
<b>8 Measuring symmetry protected Wilson lines</b>	<b>173</b>
8.1 Wilson lines . . . . .	174
8.1.1 Transport in degenerate band subspaces . . . . .	174
8.1.2 Real space picture . . . . .	177
8.1.3 Symmetry protection of the eigenvalue phase difference . . . . .	178
8.1.4 Correction terms . . . . .	180
8.2 Measurement of the eigenvalue phases . . . . .	181
8.2.1 Experimental sequence to obtain the eigenvalue phase . . . . .	181
8.2.2 Strong gradient regime . . . . .	184
8.2.3 Investigating the symmetry protection . . . . .	185
<b>9 Parametric instabilities in a shaken 1D optical lattice</b>	<b>189</b>
9.1 Heating effects in 1D shaken lattices . . . . .	189
9.1.1 Parametric instabilities . . . . .	190
9.1.2 Most unstable mode . . . . .	191
9.2 Measurement of parametric instabilities . . . . .	192
9.2.1 Modulated lattice potential . . . . .	192
9.2.2 Determination of the most unstable mode . . . . .	193
<b>10 Conclusions and Outlook</b>	<b>199</b>
<b>A Shape of the calculated Berry curvature distribution</b>	<b>203</b>
<b>B Details on the eight-band tight-binding model</b>	<b>207</b>
<b>C Edge modes in the zigzag-geometry</b>	<b>211</b>
<b>D Changing between ramp-up schemes in the anomalous regime</b>	<b>215</b>



# Chapter 1

## Introduction

The properties of a material emerge not only from the properties of its constituents, but also from their arrangement. According to Landau's approach [1], phases of matter can be characterized by underlying symmetries, related to different kinds of order in the organization of particles. A transition between two distinct phases corresponds to the spontaneous breaking of a symmetry. One example is the transition from a liquid to a solid: In the liquid phase, particles can be displaced arbitrarily without changing the properties of the system. In contrast, in a crystal, the energy is minimized when the particles are arranged in a periodic pattern, which only exhibits discrete translational symmetry. Thus, at the phase transition from a liquid to a solid, continuous translational symmetry is broken.

Triggered by the discovery of the integer quantum Hall effect (QHE) in 1980 [2], the symmetry-based classification of phases has been extended by the concept of topological order [3, 4]. In the QHE, the transverse conductivity of a two-dimensional (2D) sample takes quantized values  $\nu e^2/(2\pi\hbar)$ ,  $\nu \in \mathbb{N}$ , at low temperatures and high magnetic fields. The plateaus of the conductivity, described by different values of the integer  $\nu$ , correspond to states with the same symmetries but different properties, which define distinct topological phases [5, 6]. The value of  $\nu$  is insensitive to continuous deformations or smooth variations of the material properties [7]. Due to its robustness, the quantization of the Hall conductivity has been measured with a great degree of accuracy and is currently used to define the standard of resistance [8].

Topological order of a physical system manifests in complex properties of the quantum mechanical ground state wave function. In many cases, it is rooted in the dependence of the Bloch eigenstates on the electrons' quasimomentum in the crystal. The notion of topology originally stems from the field of differential geometry, describing the global properties of curved manifolds [9]. A closed surface can be classified by its genus  $g$ , which basically counts the number of holes in it. Hence, a sphere has a genus of  $g = 0$  and is topologically different from a torus with  $g = 1$ . Two surfaces are characterized by the same value of  $g$ , if they can continuously be deformed into each other. In QHE systems, the genus corresponds to the integer  $\nu$  counting the plateaus in the conductivity. It is identical to the sum over the Chern numbers of all occupied energy bands. These invari-

ants characterize the topological properties of non-interacting, static systems. Similarly as the genus is defined as the integral over the local curvature of the manifold, the Chern number is given by the integral over the Berry curvature, which quantifies the curvature of the Bloch states in quasimomentum space.

Although the general concept of topological phase transitions is not rooted in symmetry breaking, there are topological phases which require a certain symmetry of the Hamiltonian. The topological phases of static, free particle systems are grouped according to their symmetries and dimensionality by the Altland-Zirnbauer (AZ) classification [10, 11]. Depending on the presence of time-reversal, particle-hole or chiral symmetry and the dimension of the system, it specifies the number of equivalence classes of gapped Hamiltonians. If two Hamiltonians are in the same equivalence class, they can be continuously deformed into each other without breaking the protecting symmetry or closing an energy gap [12]. For the QHE states, in which all of the three mentioned symmetries are absent, the set of equivalence classes is given by  $\mathbb{Z}$ . Thus, each class is characterized by a single, integer number, which corresponds to  $\nu$ . A prominent example of a topological phase respecting time-reversal symmetry are topological insulators [13–17] characterized by a  $\mathbb{Z}_2$  invariant, which have been predicted theoretically [18, 19] and observed experimentally in different kinds of solid state materials [20–23].

Topological order can give rise to new, interesting phenomena such as long-range entanglement and quasi-particles with fractional statistics [24, 25], that can also be non-Abelian [26, 27], being of particular interest for topological quantum computation [28]. Moreover, topologically non-trivial Bloch bands involve the existence of robust boundary modes [29–31] at the edge of the system or at interfaces between systems being characterized by different topological indices. These edge modes are topologically protected, which makes them insensitive to local defects and therefore interesting for technical applications like the realization of robust analog signal processing [32]. The appearance of gapless edge modes is described by the *bulk-edge correspondence*, which relates the topological invariants of the bulk bands directly to the states at the boundary. In the case of Chern insulators, such as the QHE states, the Chern number of each energy band is given by the difference between the number of chiral edge modes being present in the gaps above and below the band.

In analogy to topological insulators there exist also time-reversal invariant topological superconductors and superfluids [33–35], where the superconducting gap directly corresponds to the band gap of the insulator [36]. The counterpart of Chern insulators are chiral superconductors in 2D, exhibiting chiral Majorana modes at their boundaries, which can give rise to non-Abelian statistics [37–39].

**Topology in periodically driven systems** The description of phases in terms of symmetry breaking and topological order can be applied in a modified form also to stationary states of non-equilibrium systems [12]. In periodically driven lattices, the role of the Bloch waves, defining the topological properties at the single particle level, is taken by the eigenstates of an effective Floquet Hamiltonian that is derived from the time-evolution operator over one period of the driving. In many cases, the concepts developed

---

to describe the topology in equilibrium settings, such as Chern numbers, can directly be applied to the effective Hamiltonian. By optimizing the properties of the periodic drive, systems with specific properties can be tailored using periodic driving. This stroboscopic simulation of a static system is called Floquet engineering [40].

Periodically driven systems can, however, also realize genuinely time-dependent settings which have no static counterpart. These systems can not be described by standard topological invariants being derived from the stroboscopic evolution, since their properties are related to the micromotion that occurs within the driving period. In 2D, an anomalous Floquet phase exists [41], in which the Chern numbers of all bulk bands are equal to zero, but nevertheless robust chiral edge modes appear at the boundary of the system. The existence of such edge modes would be ruled out by the bulk-edge correspondence in a time-independent setting. Due to the time-periodicity of the Hamiltonian, its spectrum also becomes periodic and the energies are only defined up to integer multiples of the driving frequency. Similar to the quasimomentum in a space-periodic potential, they are called quasienergies. Thus, there is no notion of a lowest band anymore and edge states can exist in the quasienergy gap below the first band. While in a static system the knowledge of all Chern numbers is sufficient to derive the number of chiral edge modes in all energy gaps, in the periodic quasienergy spectrum there is no reference point to start counting.

Periodically driven systems can be characterized in terms of winding numbers which count the number of edge modes in each quasienergy gap. The topological properties of  $N$  quasienergy bands are encoded either in the  $N$  winding numbers or, alternatively, in the  $N - 1$  independent Chern numbers and one winding number. The symmetry classification of topological phases provided by the AZ scheme can also be extended to Floquet topological systems. Instead of considering the Hamiltonians, it gives the number of equivalence classes of unitary evolution operators with a gapped spectrum at the end point [12]. Based on the description by winding numbers, a modified bulk-edge correspondence can be formulated for periodically driven systems. The change of the winding numbers at a topological phase transition can be directly related to the sign change of the local Berry curvature at the gap closing point. Thus, the number of chiral edge modes can be determined by probing the properties of the bulk eigenstates, which will be used in the experiments presented in this work.

Anomalous Floquet phases exhibit remarkable properties, especially in the presence of disorder. Since the Chern numbers of all bands are equal to zero, the bulk states can be fully localized by the disorder [42], which is not possible in conventional topological insulators characterized by non-zero Chern numbers. At the same time, the chiral egde modes remain mobile, as they can be viewed as a single mode winding around the entire quasienergy spectrum [43]. The complete localization of bulk states could help to stabilize interacting Floquet systems. Due to the relaxation of energy conservation, periodically driven many-body systems are expected to heat up to a featureless, infinite temperature state in the thermodynamic limit [44, 45]. This heating problem could be overcome by either investigating prethermalization regimes [46–54] at intermediate timescales or

by many-body localization [12, 55–58]. In anomalous Floquet systems with an additional disorder potential, a many-body localized bulk could exist in the presence of thermalizing edge states [59], serving as a starting point for the exploration of interacting, topological systems.

**Realization with ultracold atoms** Ultracold atoms in optical lattices have emerged as a powerful tool to study exotic phases of matter, which are otherwise difficult to observe in conventional solid state experiments [60, 61]. The relatively large lattice spacings and low densities have allowed for the verification of many theoretical concepts, such as the observation of Bloch oscillations in real- and momentum space [62–64]. Moreover, by controlling the kinetic energy via the lattice depth and the interaction energy by the use of Feshbach resonances, strongly correlated many-body phases have been realized [65, 66]. Topological phases of matter can be simulated via Floquet engineering with ultracold atoms loaded into periodically driven optical lattice potentials [67–70].

In this work, the experimental realization of an anomalous Floquet system using a Bose-Einstein condensate (BEC) subjected to a periodically driven optical honeycomb lattice [71] is described. The modulated lattice gives rise to a variety of different topological regimes, which are fully characterized in terms of their winding numbers. By probing the quasienergy gaps in the Floquet spectrum, the transitions between the different regimes are identified. Combining these results with Hall deflection measurements of the local Berry curvature allows to derive the winding numbers. Due to the modified bulk-edge correspondence, probing the properties of the bulk states directly reveals the number of chiral edge modes in each quasienergy gap, even in a system with smooth boundaries defined by a harmonic trap, as it is used in this work.

## Thesis contents

This thesis is structured as follows. The basic theoretical concepts describing the topology of static and periodically driven 2D systems are introduced in **chapter 2** along with a short introduction into Floquet engineering. The properties of the anomalous Floquet phase are discussed and the relation of the winding numbers to the bulk states is derived, constituting the basis for their measurement using an ultracold bosonic quantum gas.

In **chapter 3**, the realization of an anomalous Floquet system via chiral modulation of the tunnelings in an optical honeycomb lattice is presented. This is achieved by periodically varying the intensities of the laser beams. The Floquet band structure is calculated numerically, providing a theoretical model which can be quantitatively compared to the experimental results. In order to derive the dispersion of the edge modes in a semi-finite geometry, a tight-binding description is introduced.

**Chapter 4** is dedicated to the experimental setup. The creation of the BEC and the characterization of the optical lattice is described, as well as the techniques used to determine the quasienergy gaps and Berry curvature. Moreover, the combination of the 2D honeycomb lattice with an additional lattice along the vertical direction is discussed, which will be important for future experiments involving strong interactions.

---

The characterization of the different Floquet topological regimes by energy gap and deflection measurements is presented in **chapter 5**, which is based on the results presented in [71]. Starting from the limit of high modulation frequencies, the winding numbers are derived in each regime, directly revealing the existence of an anomalous Floquet setting. By systematically scanning the modulation parameters, the full 2D phase diagram is obtained. Different loading schemes are explained, which are needed to probe the system in each topological regime, enabling also an investigation of the second band.

Anomalous Floquet regimes can also be realized by a periodic modulation of the lattice phases, leading to a chiral motion of the complete potential in real space, as described in **chapter 6**. The theoretical phase diagram of the model is discussed, being supported by the edge mode dispersion derived from a tight-binding description of the semi-finite setting. The phase shaking is compared to the intensity modulation regarding their experimental feasibility to probe the anomalous Floquet regime.

Based on the previous results, **chapter 7** provides an outlook on future experiments utilizing the special properties of anomalous Floquet systems. Amongst others, modifications to the setup allowing for direct imaging of the chiral edge modes and the creation of a sharp boundary are discussed, as well as the realization of a disorder potential.

The topological properties of degenerate multiband systems can be described by Wilson lines. In **chapter 8**, the symmetry protection of the eigenvalue phases of certain Wilson lines is discussed along with attempts to probe these in the optical honeycomb lattice, based on the measurements reported in [72, 73].

As mentioned above, periodic driving of interacting systems in general leads to heating. To gain insight into the physical processes involved, a periodically driven one-dimensional optical lattice is studied. While the dynamics at long time-scales can be understood by a Floquet Fermi's golden rule [74], the onset of heating at short timescales is expected to be triggered by coherent excitations. The experimental investigation of these parametric instabilities is briefly described in **chapter 9**, while a more detailed discussion can be found in [75, 76].

The thesis concludes with a summary of the results and a short outlook in **chapter 10**.

## Publications

K. Wintersperger, C. Braun, F. N. Ünal, A. Eckardt, M. Di Liberto, N. Goldman, I. Bloch, and M. Aidelsburger, *Realization of an anomalous Floquet topological system with ultracold atoms*, Nat. Phys. 16, 1058–1063 (2020).

K. Wintersperger, M. Bükov, J. Näger, S. Lellouch, E. Demler, U. Schneider, I. Bloch, N. Goldman, and M. Aidelsburger, *Parametric Instabilities of Interacting Bosons in Periodically Driven 1D Optical Lattices*, Phys. Rev. X 10, 011030 (2020).

M. Reitter, J. Näger, K. Wintersperger, C. Sträter, I. Bloch, A. Eckardt, and U. Schneider, *Interaction Dependent Heating and Atom Loss in a Periodically Driven Optical Lattice*, Phys. Rev. Lett. 119, 200402 (2017)



# Chapter 2

## Floquet topological phases

The motion of electrons in a periodic potential is described in terms of quantized energy bands which can be classified according to their topological properties. The chapter starts with a brief introduction into the notion of Bloch band topology for two-dimensional (2D) systems, which is exemplified by the characterization of electrons in a magnetic field [2.1]. Here, the connection between the topological properties of the bulk eigenstates and the existence of chiral edge modes is illustrated. The generation of artificial magnetic fields for ultracold atoms using periodic modulation, called Floquet engineering, is discussed in Sec. 2.2. Periodically driven lattices can also be used to simulate systems with novel properties that exceed those of conventional static systems, one example being the anomalous Floquet phase. The topological characterization of periodically driven systems and the properties of the anomalous Floquet phase are presented in the last section [2.3].

### 2.1 Topological characterization of static systems

The concept of topology, originally defined in differential geometry for the description of curved manifolds, can be generalized to the Hilbert space of quantum mechanical systems. The topological properties of non-degenerate Bloch bands in two dimensions are usually described in terms of an integer-valued invariant, called the Chern number, which can be viewed as the counterpart of the genus in mathematics, counting the number of handles on a connected, orientable surface. The Chern number can be derived from the geometric properties of the Bloch bands, which will be introduced in the first section. The connection between the Chern number of a bulk energy band and the number of chiral modes at the boundary of a system with edges is discussed, being apparent in the description of the integer Quantum Hall effect. A paradigmatic example for topological Bloch bands in a honeycomb lattice is the Haldane model, which is introduced in the last part.

### 2.1.1 Geometric properties of Bloch bands

The Schrödinger equation for a single particle in a periodic potential  $V(\mathbf{r}) = V(\mathbf{r} + \mathbf{R})$  in the  $n$ th energy band with quasimomentum  $\mathbf{q}$  reads:

$$\hat{H}(\mathbf{r}) \psi_{\mathbf{q}}^n(\mathbf{r}) = \left( \frac{\hat{\mathbf{p}}^2}{2m} + V(\hat{\mathbf{r}}) \right) \psi_{\mathbf{q}}^n(\mathbf{r}) = E_{\mathbf{q}}^n \psi_{\mathbf{q}}^n(\mathbf{r}) \quad (2.1)$$

According to Bloch's theorem [77], the eigenstates  $\psi_{\mathbf{q}}^n(\mathbf{r})$  are Bloch-waves, which can be written as the product of a plane wave and a periodic function  $u_{\mathbf{q}}^n(\mathbf{r}) = u_{\mathbf{q}}^n(\mathbf{r} + \mathbf{R})$  with the same periodicity as the lattice:

$$\psi_{\mathbf{q}}^n(\mathbf{r}) = e^{i\mathbf{qr}} u_{\mathbf{q}}^n(\mathbf{r}). \quad (2.2)$$

This leads to the Schrödinger equation of the periodic functions:

$$\left( \frac{(\hat{\mathbf{p}} + \hbar\mathbf{q})^2}{2m} + V(\mathbf{r}) \right) u_{\mathbf{q}}^n(\mathbf{r}) = E_{\mathbf{q}}^n u_{\mathbf{q}}^n(\mathbf{r}), \quad (2.3)$$

which depends explicitly on the quasimomentum, yielding an eigenvalue equation for each value of  $\mathbf{q}$ . In contrast, the Bloch-waves  $\psi_{\mathbf{q}}^n(\mathbf{r})$  are just labeled by the quasimomentum and  $\langle \psi_{\mathbf{q}}^n(\mathbf{r}) | \psi_{\mathbf{q}'}^n(\mathbf{r}) \rangle = \delta_{\mathbf{q},\mathbf{q}'}$  per definition, which is not necessarily the case for the cell-periodic functions  $u_{\mathbf{q}}^n(\mathbf{r})$ . The geometric properties of Bloch bands become apparent when considering the adiabatic transport of an eigenstate in quasimomentum space. The system is initialized at  $t = 0$  in the eigenstate  $u_{\mathbf{q}(0)}^n$  and its quasimomentum is changed slowly enough such that it remains in the instantaneous eigenstate  $u_{\mathbf{q}}^n$  during the evolution, according to the adiabatic theorem [78]. After a time  $t$ , the state has acquired a phase factor

$$u_{\mathbf{q}(0)}^n \rightarrow e^{i\phi(t)} u_{\mathbf{q}(t)}^n, \quad (2.4)$$

which is the sum of the dynamical phase  $\phi_d$ , arising from the energy dispersion, and a geometric phase  $\phi_g$ :

$$\phi(t) = \phi_d + \phi_g = -\frac{1}{\hbar} \int_0^t E_{\mathbf{q}(t')}^n dt' + i \int_{\mathbf{q}(0)}^{\mathbf{q}(t)} \langle u_{\mathbf{q}'}^n | \nabla_{\mathbf{q}'} | u_{\mathbf{q}'}^n \rangle \cdot d\mathbf{q}' \quad (2.5)$$

The geometric phase can be written in terms of the Berry connection  $\mathbf{A}^n(\mathbf{q})$ , that describes the change of the eigenstates along the path in quasimomentum space

$$\mathbf{A}^n(\mathbf{q}) = i \langle u_{\mathbf{q}}^n | \nabla_{\mathbf{q}} | u_{\mathbf{q}}^n \rangle. \quad (2.6)$$

In general, the Berry connection and the geometric phase are gauge dependent, i.e. they change under a gauge transformation  $u_{\mathbf{q}}^n \rightarrow e^{i\chi(\mathbf{q})} u_{\mathbf{q}}^n$ , which leaves the physical properties of the system unchanged. However, when considering the evolution along a closed path

$\partial S$ , the geometric phase becomes gauge-independent and is called the *Berry phase* [79]. In this case, Stokes' theorem can be applied and the Berry phase  $\phi_B$  can be expressed as:

$$\phi_B = \oint_{\partial S} \mathbf{A}^n(\mathbf{q}) \cdot d\mathbf{q} = \int_S \Omega^n(\mathbf{q}) d^2q, \quad (2.7)$$

where  $\Omega^n(\mathbf{q})$  denotes the Berry curvature, which is gauge-independent and defined by

$$\Omega^n(\mathbf{q}) = \nabla_{\mathbf{q}} \times \mathbf{A}^n(\mathbf{q}) = i \langle \nabla_{\mathbf{q}} u_{\mathbf{q}}^n | \times | \nabla_{\mathbf{q}} u_{\mathbf{q}}^n \rangle. \quad (2.8)$$

The Berry curvature can be viewed as an effective magnetic field  $\mathbf{B} = \nabla \times \mathbf{A}$  in quasimomentum space, whereas the Berry connection corresponds to the vector potential. Using the Schrödinger equation, the Berry curvature can be rewritten as [79]:

$$\Omega^n(\mathbf{q}) = i \sum_{m \neq n} \frac{\langle u_{\mathbf{q}}^n | \nabla_{\mathbf{q}} \hat{H}(\mathbf{q}) | u_{\mathbf{q}}^m \rangle \times \langle u_{\mathbf{q}}^m | \nabla_{\mathbf{q}} \hat{H}(\mathbf{q}) | u_{\mathbf{q}}^n \rangle}{(E^n - E^m)^2}. \quad (2.9)$$

An example for a Berry phase being directly observable is the Aharonov-Bohm-effect [80], where the motion of two fractions of the same initial wavepacket around a magnetic solenoid is considered. Although the magnetic flux is confined to the interior of the solenoid, the two parts pick up a phase difference when passing the solenoid on the left and right, which directly corresponds to the Berry phase and can be measured interferometrically.

The concept of the Berry phase presented here is defined for a single Bloch band  $n$ , but can be generalized to multiband systems. If the transport of the Bloch state is non-adiabatic with respect to the gap between several energy bands, these bands are mixed and the time-evolution can be described by the matrix-valued Wilson line [81, 82], which is discussed in more detail in chapter 8.

### 2.1.2 Chern number and bulk-edge correspondence

The topological properties of non-interacting, static systems can be completely characterized in terms of the Chern numbers associated with their energy bands. For a finite system, these are defined in terms of the bulk bands, but also contain information about the states at the edge of the system. In the following, this is illustrated by means of the Quantum Hall effect (QHE) [2], describing the quantization of the Hall conductance at high magnetic fields and low temperatures. In these experiments, a constant current is sent through a 2D solid state sample in the presence of a large magnetic field normal to its surface. This leads to a potential drop across the sample perpendicular to the direction of the current, that is measured to derive the transverse conductivity  $\sigma_{xy}$ . As a function of the magnetic field, the conductivity exhibits plateaus at quantized values

$$\sigma_{xy} = \nu \frac{e^2}{2\pi\hbar}, \quad (2.10)$$

with  $e$  being the elementary charge. The existence of these plateaus is related to the population of chiral edge states propagating along the boundary of the system. The solid state sample can be described by a 2D electron gas moving in the periodic potential of the crystalline lattice and a random onsite potential modeling the disorder, which is always present in real materials due to defects. The resulting energy dispersion consists of broadened bands describing the bulk, which are separated by gaps. The centers of the bands in energy correspond to states being delocalized over the interior of the sample and their tails to localized states [83]. In addition, the gaps between the bulk bands are crossed by single energy levels, which belong to states at the edge of the sample, which are delocalized along the complete boundary.

If the Fermi energy lies within a bulk gap, the conductivity will exhibit a quantized value according to Eq. 2.10. Decreasing the magnetic field reduces the number of available states within each band, and additional levels are populated. As the lower lying levels of the next band belong to localized states, the conductivity is not changed when these are occupied. If the Fermi energy reaches the center region of the bulk bands, delocalized states start to contribute which leads to an increase of  $\sigma_{xy}$ . The next plateau is reached when the band is completely filled and another edge state in the following gap is occupied. Hence, the integer number  $\nu$  in Eq. 2.10 counts the number of populated chiral edge modes.

On the other hand, it has been shown, that the quantization of the Hall conductance can be directly related to the topological properties of the bulk bands when calculating the conductivity using *Kubo's formula* [3]. In fact, the integer  $\nu$  equals the sum over the Chern numbers of all occupied energy bands. The Chern number of the  $n$ th energy band can be expressed as the integral of the Berry curvature over the first Brillouin zone (BZ) [3]:

$$\mathcal{C}^n = \frac{1}{2\pi} \int_{BZ} \Omega^n(\mathbf{q}) d^2q. \quad (2.11)$$

The Chern number  $\mathcal{C}$  is defined for a non-degenerate energy band and is a topological invariant, which means that it is robust against deformations of the Hamiltonian that preserve the gaps to the neighboring bands.

The connection between the Chern number of the bulk bands and the number of populated edge modes is in general known as the *bulk-edge correspondence* [5, 84–86]:

$$\mathcal{C}^n = N_u - N_l, \quad (2.12)$$

where  $N_u$  and  $N_l$  denote the net number of chiral edge modes in the gaps above and below the band. The net number of edge modes inside a gap is obtained by counting the states according to their propagation direction, i.e. subtracting the right-moving from the left-moving contributions.

### 2.1.3 The topological Haldane model

In the quantum Hall effect, the presence of the magnetic field changes the eigenstates and -energies of the system such that there are regions in quasimomentum space with

finite Berry curvature which sum up to a non-zero Chern number. In general, a non-zero Chern number can also appear in the absence of an external magnetic field. One prominent example is the Haldane model [87], conceived in 1988, which considers a tight-binding model on a honeycomb lattice, describing systems similar to graphene.

The constant, external magnetic field in the QHE breaks time-reversal symmetry (TRS), which is already apparent in classical electrodynamics. Since the transverse conductivity  $\sigma_{xy} \sim j_x/E_y$  changes sign under time-reversal ( $j_x \rightarrow -j_x$ ,  $E_y \rightarrow E_y$ ), it can only acquire a non-zero value if TRS is broken. In the Haldane model, this is realized by an internal magnetic field with zero net flux per unit cell but a staggered flux pattern exhibiting the symmetry of the honeycomb lattice (see Fig. 2.1a). The honeycomb lattice is not a Bravais lattice, it consists of two interlaced triangular sublattices, denoted by A and B. The unit cell is spanned by the two direct lattice vectors  $\mathbf{a}_1$  and  $\mathbf{a}_2$  and contains a single A- and B-site.

$$\mathbf{a}_1 = \frac{a}{2} \begin{pmatrix} 3 \\ \sqrt{3} \end{pmatrix}, \quad \mathbf{a}_2 = \frac{a}{2} \begin{pmatrix} 3 \\ -\sqrt{3} \end{pmatrix}, \quad (2.13)$$

where the lattice spacing  $a$  is defined as the distance between two adjacent sites. The reciprocal lattice of the honeycomb lattice is again a honeycomb lattice, but rotated by  $90^\circ$  and is spanned by the vectors  $\mathbf{K}_1$  and  $\mathbf{K}_2$  which comprise the first Brillouin zone (BZ):

$$\mathbf{K}_1 = \frac{k_L}{2} \begin{pmatrix} \sqrt{3} \\ 3 \end{pmatrix}, \quad \mathbf{K}_2 = \frac{k_L}{2} \begin{pmatrix} \sqrt{3} \\ -3 \end{pmatrix}, \quad k_L = \frac{4\pi}{3\sqrt{3}a}. \quad (2.14)$$

In the Haldane model, tunneling between neighboring sites with amplitude  $J$  is considered, as well as tunneling between next-nearest neighbors with amplitude  $\tilde{J}$ . The A- and B-sites are connected by the vectors  $\boldsymbol{\delta}_j$  and the sites of the same types via  $\mathbf{a}_1$ ,  $\mathbf{a}_2$  and  $\mathbf{a}_3 = \mathbf{a}_1 - \mathbf{a}_2$ .

$$\boldsymbol{\delta}_1 = a \begin{pmatrix} -1 \\ 0 \end{pmatrix} \quad \boldsymbol{\delta}_2 = \frac{a}{2} \begin{pmatrix} 1 \\ -\sqrt{3} \end{pmatrix} \quad \boldsymbol{\delta}_3 = \frac{a}{2} \begin{pmatrix} 1 \\ \sqrt{3} \end{pmatrix}. \quad (2.15)$$

The directions corresponding to a positive sign of the tunneling coefficients are depicted in Fig. 2.1b, whereas hopping  $A \rightarrow A$  is defined along  $-\mathbf{a}_1$ ,  $\mathbf{a}_2$ ,  $\mathbf{a}_3$  (solid red arrows), which will be referred to as  $\mathbf{a}_j$ , and  $B \rightarrow B$  accordingly along  $-\mathbf{a}_j$  (dashed gray arrows). In this way, next-nearest neighbor hopping along a closed triangular path connecting three A- or B-sites encloses a net flux of  $3\Phi$ , which leads to a phase factor  $\phi = 2\pi(3\Phi/\Phi_0)$ , with  $\Phi_0 = h/e$  denoting the flux quantum. Considering nearest neighbor hopping around the plaquette, the total enclosed flux is zero (see Fig. 2.1a). Hence, the staggered flux configuration emerges as a complex-valued tunneling coefficient  $\tilde{J} = t e^{i\phi}$  and a real hopping amplitude  $J$ . A non-zero value of  $\text{Im}[\tilde{J}]$  directly reflects broken TRS, as the latter corresponds to complex conjugation, which reverts the sign of the phase  $\phi$ , describing hopping of particles along the other direction. In addition to the tunneling, an energy offset  $\Delta$  between the A- and B-sites is introduced, breaking inversion symmetry (IS).

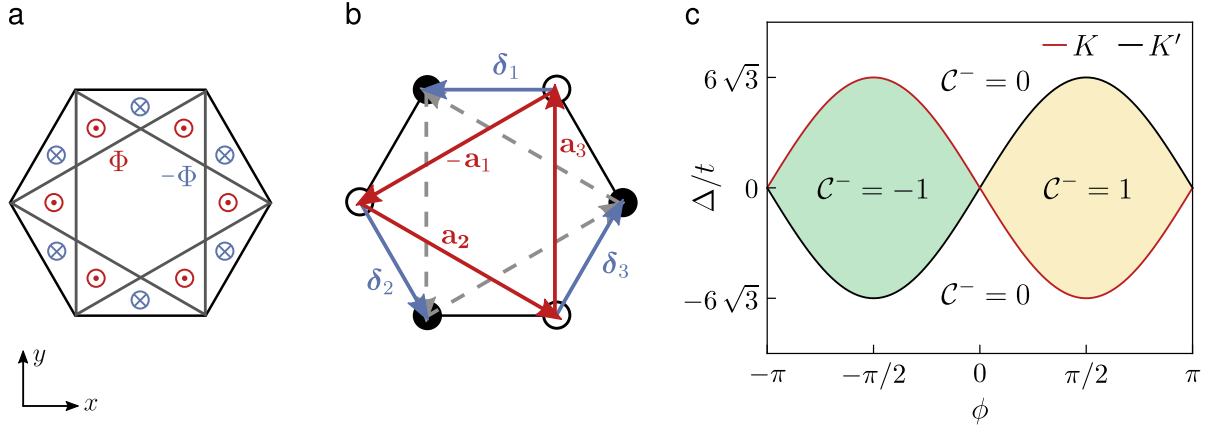


**Figure 2.1: Flux configuration, tunneling directions and phase diagram in the Haldane model.** **a.** Staggered flux pattern with zero net flux per plaquette. The positive flux  $\Phi$  points out of the plane. **b.** Vectors  $\delta_j$  and  $a_j$ ,  $j = \{1, 2, 3\}$ , connecting nearest neighbors and next-nearest neighbors. Positive tunneling coefficients are associated with the directions  $\delta_1$ ,  $\delta_2$ ,  $\delta_3$  and  $-a_1, a_2, a_3$  (blue and red arrows). In this way, next-nearest neighbor hopping on a closed loop connecting A- or B-sites encloses a flux of  $3\Phi$ . **c.** Phase diagram of the Haldane model as a function of the phase  $\phi$  of the complex next-nearest neighbor tunneling and the sublattice offset  $\Delta$ , given in terms of the absolute value  $t$  of the next-nearest neighbor tunneling. The phase boundaries are obtained by the closing of the energy gap at  $K'$  or  $K$  (black and red solid lines).

The tight-binding Hamiltonian of the Haldane model reads

$$\hat{H} = \sum_{\mathbf{r}_A} \left[ J \sum_{j=1}^3 (\hat{a}_{\mathbf{r}_A}^\dagger \hat{a}_{\mathbf{r}_A + \delta_j} + h.c.) + \frac{\Delta}{2} (\hat{a}_{\mathbf{r}_A}^\dagger \hat{a}_{\mathbf{r}_A} - \hat{a}_{\mathbf{r}_A + \delta_1}^\dagger \hat{a}_{\mathbf{r}_A + \delta_1}) \right. \\ \left. + \sum_{j=1}^3 (\tilde{J} \hat{a}_{\mathbf{r}_A}^\dagger \hat{a}_{\mathbf{r}_A + \mathbf{a}_j} + h.c.) + \sum_{j=1}^3 (\tilde{J} \hat{a}_{\mathbf{r}_A + \delta_1}^\dagger \hat{a}_{\mathbf{r}_A + \delta_1 - \mathbf{a}_j} + h.c.) \right]. \quad (2.16)$$

Here, the operator  $\hat{a}_\mathbf{r}^\dagger$  creates a particle on a lattice site located at  $\mathbf{r}$ . The sum is taken over all A-sites and the locations of the B-sites have been expressed in terms of  $\mathbf{r}_A$ . To derive the energy dispersion, the Hamiltonian is written in quasimomentum space by taking the Fourier transform of the creation and annihilation operators.

$$\hat{a}_{\mathbf{r}_A}^\dagger = \sum_{\mathbf{q}} e^{-i\mathbf{q}\cdot\mathbf{r}_A} \hat{a}_\mathbf{q}^\dagger \quad \hat{a}_{\mathbf{r}_A + \delta_j}^\dagger = \sum_{\mathbf{q}} e^{-i\mathbf{q}\cdot(\mathbf{r}_A + \delta_j)} \hat{b}_\mathbf{q}^\dagger. \quad (2.17)$$

Using  $\sum_{\mathbf{r}_A} e^{-i\mathbf{r}_A(\mathbf{q}-\mathbf{q}')} = \delta_{\mathbf{q},\mathbf{q}'}$ , the Hamiltonian reduces to

$$\hat{H} = \sum_{\mathbf{q}} \left[ J \sum_{j=1}^3 \left( e^{i\mathbf{q}\cdot\boldsymbol{\delta}_j} \hat{a}_{\mathbf{q}}^\dagger \hat{b}_{\mathbf{q}} + e^{-i\mathbf{q}\cdot\boldsymbol{\delta}_j} \hat{b}_{\mathbf{q}}^\dagger \hat{a}_{\mathbf{q}} \right) + \frac{\Delta}{2} \left( \hat{a}_{\mathbf{q}}^\dagger \hat{a}_{\mathbf{q}} - \hat{b}_{\mathbf{q}}^\dagger \hat{b}_{\mathbf{q}} \right) \right. \\ \left. + \sum_{j=1}^3 \left( \tilde{J} e^{i\mathbf{q}\cdot\mathbf{a}_j} + \tilde{J}^* e^{-i\mathbf{q}\cdot\mathbf{a}_j} \right) \hat{a}_{\mathbf{q}}^\dagger \hat{a}_{\mathbf{q}} + \sum_{j=1}^3 \left( \tilde{J} e^{-i\mathbf{q}\cdot\mathbf{a}_j} + \tilde{J}^* e^{i\mathbf{q}\cdot\mathbf{a}_j} \right) \hat{b}_{\mathbf{q}}^\dagger \hat{b}_{\mathbf{q}} \right]. \quad (2.18)$$

The Hamiltonian  $\hat{H}_{\mathbf{q}}$  for each quasimomentum, being a hermitian  $2 \times 2$ -matrix, can be written in terms of the Pauli matrices

$$\hat{\sigma}_0 = \begin{pmatrix} 1 & 0 \\ 0 & 1 \end{pmatrix} \quad \hat{\sigma}_x = \begin{pmatrix} 0 & 1 \\ 1 & 0 \end{pmatrix} \quad \hat{\sigma}_y = \begin{pmatrix} 0 & -i \\ i & 0 \end{pmatrix} \quad \hat{\sigma}_z = \begin{pmatrix} 1 & 0 \\ 0 & -1 \end{pmatrix} \quad (2.19)$$

as

$$\hat{H}_{\mathbf{q}} = \hat{\sigma}_0 h_0(\mathbf{q}) + \hat{\boldsymbol{\sigma}} \cdot \mathbf{h}(\mathbf{q}). \quad (2.20)$$

The respective components are given by

$$h_0(\mathbf{q}) = 2t \cos(\phi) \sum_{j=1}^3 \cos(\mathbf{q} \cdot \mathbf{a}_j) \\ h_x(\mathbf{q}) = J \sum_{j=1}^3 \cos(\mathbf{q} \cdot \boldsymbol{\delta}_j) \\ h_y(\mathbf{q}) = -J \sum_{j=1}^3 \sin(\mathbf{q} \cdot \boldsymbol{\delta}_j) \\ h_z(\mathbf{q}) = \frac{\Delta}{2} - 2t \sin(\phi) \sum_{j=1}^3 \sin(\mathbf{q} \cdot \mathbf{a}_j). \quad (2.21)$$

Calculating the eigenvalues as a function quasimomentum yields

$$E^\mp(\mathbf{q}) = h_0(\mathbf{q}) \mp |\mathbf{h}(\mathbf{q})|. \quad (2.22)$$

Applying time-reversal to Eq. 2.21, corresponds to taking  $\mathbf{q} \rightarrow -\mathbf{q}$  and complex conjugation, leading to  $h_z(\mathbf{q}) = h_z(-\mathbf{q})$  as  $\phi \rightarrow -\phi$ . On the other hand, invoking inversion symmetry yields  $h_z(\mathbf{q}) = -h_z(-\mathbf{q})$ , which means that  $h_z = 0$  if both symmetries are present [5]. In this case, the two energy bands defined in Eq. 2.22 touch at the two quasimomenta  $\mathbf{q} = (0, 1) := K$  and  $\mathbf{q} = (0, -1) := K'$ . In the case of broken IS or TRS, energy gaps open at these points with a size of

$$\Delta E(K) = 2|\Delta/2 + 3\sqrt{3}t \sin(\phi)|, \quad \Delta E(K') = 2|\Delta/2 - 3\sqrt{3}t \sin(\phi)|. \quad (2.23)$$

The case of unbroken TRS corresponds to  $t \sin(\phi) = 0$ , leading to gaps of equal size  $\Delta E = \Delta$  at both points. If inversion symmetry is present,  $\Delta = 0$  and  $\Delta E = 6\sqrt{3}t \sin(\phi)$ . In the first case the system is topologically trivial with Chern number zero, whereas in the latter case the Chern numbers of the two bands are  $\pm 1$ , constituting a Chern insulator. In the situation where both IS and TRS are broken, the trivial phase occurs for  $t \sin(\phi) < \Delta/(6\sqrt{3})$  and the topological phase for  $t \sin(\phi) > \Delta/(6\sqrt{3})$ . At the transition,  $t \sin(\phi) = \Delta/(6\sqrt{3})$ , and either the gap at  $K'$  or  $K$  closes, depending on the sign of the sublattice offset  $\Delta$ . The phase diagram as a function of  $\phi$  and  $\Delta/t$  is shown in Fig. 2.1c.

The Chern numbers in the different phases can be derived from the Berry curvature, which is concentrated around the points  $K$  and  $K'$ . The transition from the trivial to the topological regime is accompanied by a sign change of the Berry curvature at  $K$  or  $K'$ , which can be directly seen when considering the Hamiltonian in the vicinity of these points. Expanding Eq. 2.20 around the  $K$  and  $K'$  points up to first order results in a Hamiltonian which is linear in quasimomentum, where 1 and 2 denote  $K$  and  $K'$ :

$$\hat{H}'_{1/2}(\mathbf{q}) = -3t \cos(\phi) \hat{\sigma}_0 \mp \frac{3}{2} J a q_y \hat{\sigma}_x + \frac{3}{2} J a q_x \hat{\sigma}_y + (\Delta/2 \pm 3\sqrt{3}t \sin(\phi)) \hat{\sigma}_z. \quad (2.24)$$

Apart from the term proportional to  $\hat{\sigma}_0$ , which only leads to a constant energy offset, Eq. 2.24 takes the form of a Dirac Hamiltonian with mass  $m_{1/2} = \Delta/2 \pm 3\sqrt{3}t \sin(\phi)$ , which is the reason why  $K$  and  $K'$  are in general called Dirac points. Calculating the eigenstates and applying Eq. 2.9 yields for the Berry curvature  $\Omega^-$  of the lower band in the vicinity of the  $K$  ( $K'$ ) point:

$$\Omega_{1/2}^- = \pm \frac{9J^2a^2}{8} \frac{h'_z}{|\mathbf{h}'|^3} = \pm \frac{9J^2a^2}{8|\mathbf{h}'|^3} m_{1/2}. \quad (2.25)$$

Hence, the sign of the Berry curvature is given by  $+\text{sgn}(m_1)$  at  $K$  and  $-\text{sgn}(m_2)$  at  $K'$ , whereas its magnitude is similar at both points. For  $\Delta > 0$  and  $\sin(\phi) > 0$ , the mass term  $m_1$  at  $K$  is always positive which corresponds to positive Berry curvature. At  $K'$ , in the trivial phase,  $m_2 > 0$ , leading to negative Berry curvature which cancels the contribution of  $K$  when summing over the complete BZ and hence giving  $\mathcal{C}^\mp = 0$ , where  $\mp$  denotes the first (second) band. In the topological phase, the mass term at  $K'$  has opposite sign,  $m_2 < 0$ , and the Berry curvature is positive which yields  $\mathcal{C}^\mp = \pm 1$ . The Berry curvature in the upper band is given by  $\Omega_{1/2}^+ = -\Omega_{1/2}^-$ .

## 2.2 Floquet engineering

In the previous section, the influence of either a homogeneous external magnetic field or a staggered flux pattern on the topological properties of Bloch bands have been discussed. In experiments with charge-neutral, ultracold atoms, different methods exist to simulate the effect of a magnetic field. A homogeneous flux can be implemented using laser-assisted tunneling [88–90] or Raman-coupling between internal states of the atoms [91–93], resulting amongst other in the realization of the Harper-Hofstadter model [94, 95].

In general, as discussed in the context of the Haldane model, the presence of a magnetic field breaks time-reversal symmetry, which can be achieved by a time-periodic modulation of the system's Hamiltonian in a chiral manner. The periodically driven system is usually mapped to an effective Hamiltonian exhibiting tailored properties, such as topologically non-trivial band structures, which is called *Floquet-engineering* [67, 68, 70]. This has successfully been incorporated in many different experimental platforms including the irradiation of solid state samples with circularly polarized light [96–98] or coupled waveguide arrays [99–101], where time is represented by the propagation direction of the light. Topological band structures for ultracold atoms in optical lattices have been created using time-periodic modulation in the context of laser-assisted tunneling [102] or circular shaking of an optical honeycomb lattice [103–105], which effectively realizes the Haldane model. Other non-equilibrium phenomena such as frustrated magnetism [106] or the superfluid to Mott-insulator transition [107] have also been observed by employing periodic driving. In this section, the basic principles of Floquet-engineering are introduced and the calculation of the effective Hamiltonian is described.

### 2.2.1 Simulation of an effective Hamiltonian via periodic driving

According to Floquet's theorem [108–110], the evolution of a time-periodic system with  $\hat{H}(t+T) = \hat{H}(t)$  over one full period  $T$  can be described by an effective, time-independent Hamiltonian. In this way, systems with new properties governed by the effective Hamiltonian can be realized by a stroboscopic simulation. In analogy to Bloch's theorem for a Hamiltonian being periodic in real space, the eigenstates of  $\hat{H}(t)$ , defined by the time-dependent Schrödinger equation

$$i\hbar \frac{\partial}{\partial t} |\psi(t)\rangle = \hat{H}(t) |\psi(t)\rangle, \quad (2.26)$$

can be written as the product of an exponential and a wavefunction  $|\phi(t+T)\rangle = |\phi(t)\rangle$  exhibiting the same periodicity as  $\hat{H}(t)$ :

$$|\psi_n(t)\rangle = e^{-\frac{i}{\hbar}\varepsilon_n t} |\phi_n(t)\rangle. \quad (2.27)$$

The periodic functions  $|\phi_n(t)\rangle$  are called Floquet modes and  $\varepsilon_n$  is the quasienergy. Inserting this ansatz into Eq. 2.26 yields the eigenvalue equation of the Floquet modes:

$$\left( \hat{H}(t) - i\hbar \frac{\partial}{\partial t} \right) |\phi_n(t)\rangle = \varepsilon_n |\phi_n(t)\rangle. \quad (2.28)$$

Similar as the quasimomentum  $\mathbf{q}$  for space-periodic systems, the quasienergy  $\varepsilon_n$  is only defined up to multiples of  $\hbar\omega$ , where  $\omega = 2\pi/T$  denotes the driving frequency. This becomes apparent when multiplying the Floquet mode by a phase factor such that

$$|\phi_{n,m}(t)\rangle = e^{im\omega t} |\phi_n(t)\rangle \quad m \in \mathbb{Z}, \quad (2.29)$$

which leaves the eigenstate  $|\psi\rangle$  of the time-dependent Hamiltonian unchanged:

$$|\psi_{n,m}(t)\rangle = e^{-\frac{i}{\hbar}(\varepsilon_n+m\hbar\omega)t} |\phi_{n,m}(t)\rangle = |\psi_n(t)\rangle. \quad (2.30)$$

Hence, the quasienergy  $\varepsilon_n + m\hbar\omega$  describes the same physical state as  $\varepsilon_n$ . This means that the eigenvalue spectrum defined in Eq. 2.28 consists of infinitely many copies of each band, spaced in energy by  $\hbar\omega$ . The set of quasienergy bands  $\varepsilon_n$  can be chosen to lie within the interval  $[-\hbar\omega/2, \hbar\omega/2]$ , which is called the Floquet Brillouin zone (FBZ), analogously to the Brillouin zone in quasimomentum space.

**Effective Hamiltonian** The evolution of an eigenstate  $|\psi_n(t)\rangle$  within the time-interval  $[t_0, t]$  is described by the unitary time-evolution operator  $\hat{U}(t, t_0)$ :

$$|\psi_n(t)\rangle = \hat{U}(t, t_0) |\psi_n(t_0)\rangle, \quad (2.31)$$

which is defined as

$$\hat{U}(t, t_0) = \hat{\mathcal{T}} e^{-\frac{i}{\hbar} \int_{t_0}^t \hat{H}(t') dt'}, \quad (2.32)$$

where  $\hat{\mathcal{T}}$  denotes the time-ordering operator. For time-periodic systems, the evolution over  $n$  full periods of the drive is given by [111]:

$$\hat{U}(\tau + nT, \tau) = [\hat{U}(\tau + T, \tau)]^n. \quad (2.33)$$

Hence, the long-time behavior of the system after  $n$  driving periods is obtained by repeated application of the evolution operator over a single driving period, which defines an effective, time-independent Hamiltonian  $\hat{H}_{\text{eff}}$ :

$$\hat{U}(\tau + T, \tau) = e^{-\frac{i}{\hbar} \hat{H}_{\text{eff}} T}. \quad (2.34)$$

This means that the evolution of the system at stroboscopic times  $nT$  is governed by  $\hat{H}_{\text{eff}}$ . By adapting the specific shape of the driving protocol, the properties of  $\hat{H}_{\text{eff}}$  can be tailored to give rise to topological systems.

**Micromotion and initial driving phase** The effective Hamiltonian defined in Eq. 2.34 in general depends on the initial time  $\tau$  of the driving. Moreover, the stroboscopic description of the system neglects the evolution within the driving period which is often called the *micromotion*. In a more general form, the time-evolution operator can be written as [67, 112]:

$$\hat{U}(t_f, t_i) = e^{-\frac{i}{\hbar} \hat{K}(t_f)} e^{-\frac{i}{\hbar} \hat{H}_{\text{eff}}(t_f - t_i)} e^{\frac{i}{\hbar} \hat{K}(t_i)}, \quad (2.35)$$

where the time-periodic kick-operator  $\hat{K}(t + T) = \hat{K}(t)$  evaluated at the initial and final times  $t_i$  and  $t_f$  contains the information about the launch of the drive and the micromotion, respectively. In this way, the dependence on the initial phase of the driving

is moved from the effective Hamiltonian into the kick-operators. The information about the initial phase becomes irrelevant, if the driving is ramped up adiabatically, as in the experiments presented in this work. In this case,  $\tau = 0$  can be used and Eq. 2.34 simplifies to

$$\hat{U}(T, 0) \equiv \hat{U}(T) = e^{-\frac{i}{\hbar} \hat{H}_{\text{eff}} T} \quad \hat{H}_{\text{eff}} = \frac{i\hbar}{T} \ln(U(T)). \quad (2.36)$$

The decomposition of the time-evolution operator in Eq. 2.35 corresponds to splitting the evolution into a fast part, captured by  $\hat{K}$ , and its long-time behavior which is governed by  $\hat{H}_{\text{eff}}$ . The full time-dependent Hamiltonian  $\hat{H}(t)$  is connected to the time-independent effective Hamiltonian by a unitary transformation  $e^{-\frac{i}{\hbar} \hat{K}}$ , which means that they share the same quasienergy spectrum and the eigenstates  $|u\rangle$  of the effective Hamiltonian are connected to the Floquet modes as

$$|\phi(t)\rangle = e^{-\frac{i}{\hbar} \hat{K}} |u\rangle. \quad (2.37)$$

### 2.2.2 High-frequency limit

In most cases, the unitary transformations  $e^{-\frac{i}{\hbar} \hat{K}}$  and the effective Hamiltonian can not be computed analytically. To describe the modulated honeycomb lattice presented in chapter 3 for general parameters of the driving, the effective Hamiltonian is calculated numerically by replacing the time-integral in Eq. 2.32 with a discrete sum. In the limit of large driving frequencies, however, it is possible to derive an analytic expression for  $\hat{H}_{\text{eff}}$ . Applying the Magnus-expansion approach [113, 114], the effective Hamiltonian can be expressed as a series in  $1/(\hbar\omega)$ :

$$\hat{H}_{\text{eff}} = \hat{H}_{0\omega} + \hat{H}_{1\omega} + \mathcal{O}\left(\frac{1}{(\hbar\omega)^2}\right). \quad (2.38)$$

Using the  $\tau$ -independent definition of  $\hat{H}_{\text{eff}}$  in Eq. 2.35 and writing the time-dependent Hamiltonian  $\hat{H}(t)$  in terms of its Fourier components

$$\hat{H}(t) = \sum_{n=-\infty}^{\infty} \hat{H}_n e^{in\omega t}, \quad (2.39)$$

the first two terms in Eq. 2.38 can be derived as

$$\begin{aligned} \hat{H}_{0\omega} &= \hat{H}_0 \\ \hat{H}_{1\omega} &= \frac{1}{\hbar\omega} \sum_{n=1}^{\infty} \frac{1}{n} [\hat{H}_n, \hat{H}_{-n}]. \end{aligned} \quad (2.40)$$

This form of the effective Hamiltonian can be employed to explicitly show the equivalence of a periodically modulated honeycomb lattice to the Haldane model introduced in Sec. 2.1.3 for large driving frequencies  $\hbar\omega \gg 1$ .

## 2.3 Anomalous Floquet phases

Periodically driven systems can be used to simulate the behavior of other systems, which are governed by the effective Hamiltonian, corresponding to the integrated time-evolution of the original Hamiltonian over one full period of the driving. In this way, effective static systems can be represented with their topological properties being fully described by the Chern numbers of the bulk bands. However, periodic driving can also be applied to realize settings that have no static counterpart, exploiting the periodicity of the quasienergy spectrum. An intriguing example for such a system is the *anomalous Floquet phase*. The topological characterization in terms of the bulk Chern numbers is in general not sufficient for periodically driven systems. A new description using winding numbers of the quasienergy bands is presented in the first part of this section [2.3.1], leading to a modified bulk-edge correspondence. In the second part [2.3.2], the change of the winding numbers at topological phase transitions is derived and related to the Berry curvature of the bulk bands, being directly accessible in the experiments. In the presence of disorder and interactions, anomalous Floquet systems are expected to behave differently than conventional topological insulators, potentially paving the way for the realization of robust chiral edge modes in many-body systems, as discussed in [2.3.3].

Experimentally, anomalous Floquet regimes have been realized in photonic systems where coupled waveguides are arranged in a square lattice pattern [100, 101], implementing the model depicted in Fig. 2.3, as well as in arrays of coupled microwave resonators [115, 116] and liquid crystal devices [117]. These experiments are well suited to study the propagation of chiral edge modes along the boundary of the sample, whereas cold atomic systems offer more possibilities to investigate the bulk properties as well as the implementation of interacting systems.

### 2.3.1 Topological characterization of periodically driven systems

The anomalous Floquet phase describes a system where the Chern numbers of all bulk bands are equal to zero, but nevertheless chiral edge modes exist in the energy gaps [41, 118], which is depicted in Fig. 2.2b for the case of two bands. A situation like this, where edge modes enter the lowest band from below and leave the highest band at the top, is only possible in periodically driven systems with an unbounded spectrum of periodic quasienergies.

In static systems (Fig. 2.2a), the energies are bounded, meaning that there cannot be any state having an energy below the minimum of the lowest band. Hence, the anomalous Floquet phase constitutes a genuinely time-dependent setting, which can not occur in static systems.

A simple example of an anomalous Floquet phase is a finite-size bipartite square lattice with stepwise modulated hoppings, as introduced in [41], and indicated in Fig. 2.3. The driving period  $T$  is divided into four equal steps, during which the tunneling along a certain bond direction is enabled, while it vanishes along the other directions, such that

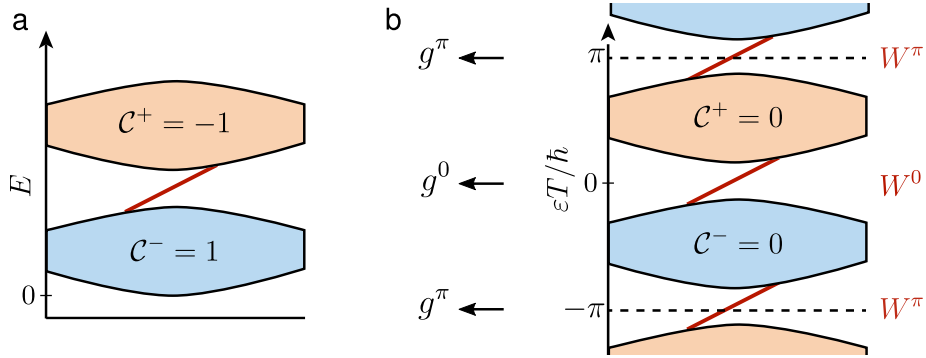


**Figure 2.2: Schematics of energy bands in static and periodically driven systems for a two-band model.** **a.** In static systems, chiral edge modes can only exist in gaps between the bands, which are bounded in energy from below. **b.** Quasienergy bands in a periodically driven two-band system in the anomalous Floquet phase. Chiral edge modes can occur in the quasienergy gap at zero or between the Floquet copies of the bands, at quasienergy  $\varepsilon T/\hbar = \pi$ . As the bands are periodic with  $\hbar\omega$ , an edge mode can enter the lowest band from below and a situation can occur where chiral edge modes exist in the gaps although the Chern numbers of all bands are zero. The definition of the quasienergy gaps and the corresponding winding numbers, counting the number of chiral edge modes per gap, are denoted on the left and right. The sketch is based on a similar illustration in [41].

after a time-interval of  $T/4$  a particle has moved with probability 1 from one lattice site to the next. A possible sublattice energy offset can be added in a fifth part of the driving period to explicitly differentiate between the A- and B-sites, but in the case illustrated here, the potential is equal on both sublattices. After one period of the driving, a particle initially localized in the bulk (purple arrows in Fig. 2.3a) returns to its original position, corresponding to a completely trivial evolution of the bulk states with  $\hat{U}(T) = \mathbb{1}$ . Hence, the quasienergy spectrum of the bulk consists of two flat bands at zero energy (Fig. 2.3b). However, a particle at the edge of the sample hops by one lattice site during the driving period, performing a chiral motion, which yields linearly dispersing bands for the upper and lower edge. In the case depicted in Fig. 2.3, the system is finite along the vertical direction, but periodic along the horizontal direction, which results in two edge modes propagating along the upper and lower boundary. This example illustrates that the stroboscopic evolution at times  $t = nT$ ,  $n \in \mathbb{Z}$  does not contain all information necessary to fully describe an anomalous Floquet system.

**Winding numbers** The fact that the Chern number of a certain bulk band is given by the difference between the net number of edge modes above and below the band, is still valid in periodically driven systems, but the reverse conclusion does not hold any more, as illustrated above. Thus, the knowledge of the bulk Chern numbers alone is not sufficient to fully describe the system including the number of chiral edge modes. Instead, periodically driven systems can be characterized in terms of winding numbers

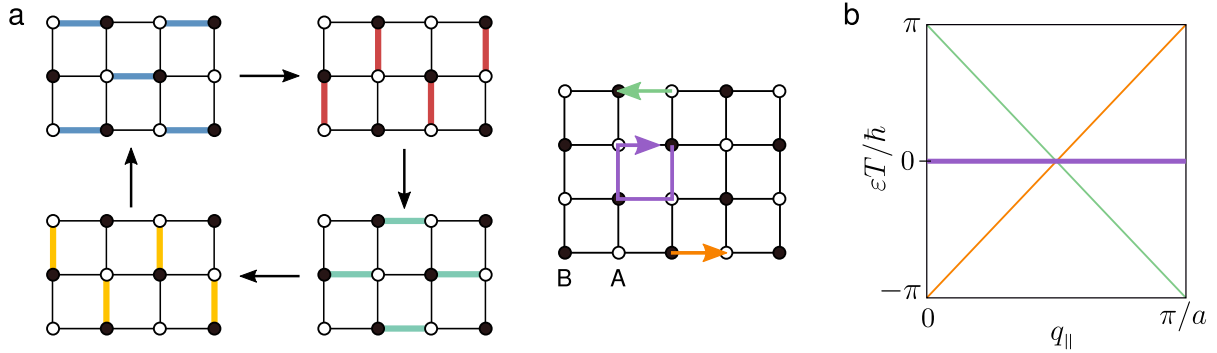


**Figure 2.3: Anomalous Floquet phase in a bipartite square lattice.** **a.** Sketch of the model introduced in [41]. The square lattice is comprised by two sublattices A and B and is assumed to be finite along the vertical but periodic along the horizontal direction. The driving period consists of 4 equal steps, in which tunneling along one bond direction is enabled, resulting in a trivial evolution of the bulk states but chiral motion along the boundary. **b.** Quasienergy spectrum containing two flat bands of the bulk states (purple) and two linearly dispersing edge modes (green and orange).

$W$ , which are related to the spatio-temporal winding structure of the time-evolution operator  $U(t)$ , including the full dynamics at all times within the driving period and not only at integer multiples of  $T$ . The winding numbers are integer valued quantities associated with the quasienergy gaps, meaning that a periodically driven system with  $N$  bands is characterized by  $N$  invariants, as there are  $N - 1$  gaps between the bands and the gap at the edge of the FBZ. In contrast,  $N$ -band static systems are fully described by  $N - 1$  Chern numbers, since  $\sum_{n=1}^N \mathcal{C}^n = 0$ . In Fig. 2.2b the quasienergy gaps and winding numbers are depicted for a two-band model. In this case, there are only two different quasienergy gaps: The gap  $g^0$  at zero quasienergy between the two bands, and the gap  $g^\pi$  at the edge of the FBZ, lying between the Floquet copies of the bands. The winding number  $W^j$  of a certain quasienergy gap  $g^j$  is equal to the number of edge modes in that gap, counted with a sign corresponding to their chirality [41]:

$$W^j = n_{\text{edge}}(g^j). \quad (2.41)$$

The winding numbers can be calculated explicitly from the general time-evolution operator  $\hat{U}(\mathbf{q}, t)$  depending on the quasimomentum  $\mathbf{q}$  and with  $t \in [0, T]$ , as derived in [41]. Considering a situation as in Fig. 2.3, with  $\hat{U}(T) = \mathbb{1}$ , there is basically one quasienergy gap at  $\varepsilon = \pi\hbar/T = \hbar\omega/2$ , as the two bulk bands collapse onto each other at  $\varepsilon = 0$ . The winding number associated with this gap is defined by

$$W(\hat{U}) = \frac{1}{8\pi^2} \int \text{tr}(\hat{U}^{-1} \partial_t \hat{U} [\hat{U}^{-1} \partial_{q_x} \hat{U}, \hat{U}^{-1} \partial_{q_y} \hat{U}]) dt dq_x dq_y, \quad (2.42)$$

where  $\hat{U} = \hat{U}(\mathbf{q}, t)$ . In a general setting with  $\hat{U}(T) \neq \mathbb{1}$ , the problem can be reduced to the above case for each gap at a certain quasienergy  $\varepsilon$ . It is possible to construct a

corresponding time-evolution operator  $\hat{U}^\varepsilon(\mathbf{q}, t)$ , which satisfies  $\hat{U}^\varepsilon(T) = \mathbb{1}$  and is smoothly connected to  $\hat{U}(\mathbf{q}, t)$  for every  $\mathbf{q}$  and  $t$ . The map between these operators preserves a quasienergy gap in the spectrum of  $\hat{U}$  at some value  $\tilde{\varepsilon}$ , which changes from  $\varepsilon$  to  $\pi\hbar/T$ . By constructing the appropriate interpolations, Eq. 2.42 can then be applied to each  $\hat{U}^\varepsilon(\mathbf{q}, t)$ , yielding the winding number  $W^\varepsilon$  in the gap at  $\varepsilon$ . The Chern number of a bulk band can be derived from the winding numbers in the quasienergy gaps above and below the band. Writing the Chern number of the  $n$ th band in terms of the operators  $\hat{P}^n$ , which project to the  $n$ th Floquet eigenstate

$$\mathcal{C}^n = \frac{1}{2\pi i} \int \text{tr}(\hat{P}^n [\partial_{q_x} \hat{P}^n, \partial_{q_y} \hat{P}^n]) dq_x dq_y, \quad (2.43)$$

it can be expressed in terms of the winding number in Eq. 2.42 for  $\hat{U}(T) = \mathbb{1}$  and thus also in the general setting [41].

The Chern number of the quasienergy band extending between  $[\varepsilon, \varepsilon']$  is given by

$$\mathcal{C}^{\varepsilon, \varepsilon'} = W(U^{\varepsilon'}) - W(U^\varepsilon). \quad (2.44)$$

In the case of a two-band system, where the Chern numbers of the first and second band are denoted by  $\mp$ , this yields

$$\mathcal{C}^\mp = \pm(W^0 - W^\pi). \quad (2.45)$$

As shown in [41], the number of edge modes in a certain quasienergy gap can be explicitly related to the winding number in Eq. 2.42 using similar expressions. Hence, a modified bulk-edge correspondence exists also for periodically driven systems, as the number of chiral edge modes that occur at the boundary of a finite system can be derived solely from bulk invariants - the winding numbers - which are also defined for an infinite system. Note, that the spectrum of the edge modes will be of course revealed directly, if the effective Hamiltonian is evaluated on a finite geometry with a boundary.

**Formulation in terms of phase bands** The topological properties of periodically driven systems are connected with the non-trivial evolution of the system during one driving period. This becomes more evident when considering the eigenvalues  $e^{-i\varphi_n(\mathbf{q}, t)}$  of the time-evolution operator  $\hat{U}(\mathbf{q}, t)$ , which are called the phase-bands [119]. At  $t = T$ , they coincide with the eigenvalues  $e^{-\frac{i}{\hbar}\varepsilon_n(\mathbf{q})T}$  of  $\hat{U}(T)$ . In this setting, the topology of a periodically driven system can be defined in terms of isolated degeneracies between the phase bands at the edge of the FBZ. As pointed out in [119], the phase bands can be smoothly changed as long as  $\hat{U}(T)$  is kept fixed. In particular, they can be deformed into equal flat bands for times  $0 \leq t < T - \delta t$ , followed by a linear increase to their final values within the small time-interval  $T - \delta t \leq t < T$ , describing an evolution equivalent to a static system. Band touchings which occur within the FBZ are thereby eliminated, as all bands collapse onto each other, and only the degeneracies between FBZs remain, which are thus identified as topologically protected singularities.

Each singularity at the edge of the FBZ can be assigned a charge, which is derived from the winding of  $\hat{U}(\mathbf{q}, t)$  in its neighborhood. The system with  $N$  phase bands can be characterized by the Chern numbers of the bands 1 to  $N - 1$  and the sum over the charges  $q^{\text{ZES}}$  of the zone-edge singularities:

$$\mathcal{C}^1, \dots, \mathcal{C}^{N-1}, \sum_i q_i^{\text{ZES}}. \quad (2.46)$$

The winding number of a gap  $g^j$  counting the chiral edge modes inside the gap, is then given by

$$W^j = \sum_{n=1}^j \mathcal{C}^n - \sum_i q_i^{\text{ZES}}. \quad (2.47)$$

### 2.3.2 Change of the winding numbers at band touching points

The winding number of a certain quasienergy gap is a topological invariant, which means that it can only change if the gap closes, defining a topological phase transition. These touchings between the quasienergy bands of  $\hat{H}_{\text{eff}}$  can be treated similarly to the degeneracies of the phase bands introduced above, by assigning them a charge  $Q_s$  which quantifies the change of the topological invariants at the singularity. For a linear closing of the gap  $g^j$ , the change of the corresponding winding number is defined as

$$\Delta W^j = Q_s^j. \quad (2.48)$$

In the following, a periodically driven system is considered which is characterized by a 2D quasimomentum  $\mathbf{q}$  and a parameter  $\lambda$  that represents the modulation parameters, e.g. being equal to the frequency  $\omega$ . In the vicinity of a gap closing point, the Hilbert space can be decomposed into the subspace spanned by the two touching bands and the remaining non-degenerate bands, which can assumed to be constant there [119]. Hence, the description of the singularity reduces to a two-band model and the effective Hamiltonian in the degenerate subspace can be written in terms of the Pauli matrices:

$$\hat{H}_{\text{eff}}(\mathbf{q}, \lambda) = \mathbf{h}_F(\mathbf{q}, \lambda) \cdot \hat{\boldsymbol{\sigma}}. \quad (2.49)$$

Possible energy offsets corresponding to terms  $\propto \hat{\sigma}_0$  are omitted here. The topological charge  $Q_s$  of a linear band-touching singularity at  $\mathbf{p}_s = (\mathbf{q}_s, \lambda_s)$  is determined by the winding of  $\mathbf{h}_F(\mathbf{q}, \lambda)$  around  $\mathbf{p}_s$  [119, 120]

$$Q_s = \text{sgn}(\det(J_F(\mathbf{p}_s))), \quad (2.50)$$

where  $J_F(\mathbf{p}_s)$  is the Jacobi matrix of  $\mathbf{h}_F$ . It can be related to the Berry flux through a closed surface around the singularity [121, 122], as derived below. Setting  $\mathbf{h}_F(\mathbf{p}_s) = 0$  without loss of generality, the Taylor expansion of  $\mathbf{h}_F(\mathbf{q}, \lambda)$  around  $\mathbf{p}_s$  up to first order reads:

$$\mathbf{h}_F(\mathbf{p}_s + \mathbf{p}) \approx J_F(\mathbf{p}_s)\mathbf{p} = \frac{\partial \mathbf{h}_F}{\partial q_x}(\mathbf{p}_s) q_x + \frac{\partial \mathbf{h}_F}{\partial q_y}(\mathbf{p}_s) q_y + \frac{\partial \mathbf{h}_F}{\partial \lambda}(\mathbf{p}_s) \lambda. \quad (2.51)$$

For linear, non-degenerate band touching points, the vectors  $\frac{\partial \mathbf{h}_F}{\partial p_j}$  are linearly independent and thus form a basis in the 3D parameter space. Without changing the topological invariants [121], these vectors can be chosen to coincide with the standard basis formed by the unit vectors  $\hat{q}_x, \hat{q}_y, \hat{\lambda}$ , up to orientation. The orientation  $O$  of the basis formed by  $\frac{\partial \mathbf{h}_F}{\partial p_j}$  is given by

$$O = \text{sgn} \left( \frac{\partial \mathbf{h}_F}{\partial q_x} \cdot \left( \frac{\partial \mathbf{h}_F}{\partial q_y} \times \frac{\partial \mathbf{h}_F}{\partial \lambda} \right) \right) = \text{sgn}(\det(J_F)). \quad (2.52)$$

Thus, Eq. 2.51 can be expressed as

$$\mathbf{h}_F(\mathbf{p}_s + \mathbf{p}) \cong O \left( \hat{q}_x q_x + \hat{q}_y q_y + \hat{\lambda} \lambda \right) = \text{sgn}(\det(J_F(\mathbf{p}_s))) \mathbf{p}, \quad (2.53)$$

and the effective Hamiltonian becomes:

$$\hat{H}_{\text{eff}}(\mathbf{p}) = \text{sgn}(\det(J_F(\mathbf{p}_s))) \mathbf{p} \cdot \hat{\boldsymbol{\sigma}}. \quad (2.54)$$

For a two-band Hamiltonian of the form  $\hat{H} = \mathbf{r} \cdot \hat{\boldsymbol{\sigma}}$ , exhibiting a singularity at  $\mathbf{r} = \mathbf{0}$  and  $E = 0$ , the Berry curvature is given by:

$$\boldsymbol{\Omega}^{\mp}(\mathbf{r}) = \pm \frac{\mathbf{r}}{2|\mathbf{r}|^3}, \quad (2.55)$$

where  $\mp$  denotes the first and second band lying below and above the degeneracy. Transforming to spherical coordinates, the Berry flux through a unit sphere containing the singularity can be evaluated as

$$\Phi^{\mp} = \int_S \boldsymbol{\Omega} \cdot d\mathbf{S} = \pm \frac{1}{2} \int_0^{2\pi} d\varphi \int_0^{\pi} d\vartheta r^2 \sin(\vartheta) \frac{\mathbf{r}}{|\mathbf{r}|^3} \cdot \frac{\mathbf{r}}{|\mathbf{r}|} = \pm 2\pi. \quad (2.56)$$

Using this identity, the Berry flux of the effective Hamiltonian in Eq. 2.54 can be directly related to the topological charge at the singularity inside the sphere:

$$\Phi^{\mp} = \pm \text{sgn}(\det(J_F(\mathbf{p}_s))) \int_S \frac{\mathbf{p}}{2|\mathbf{p}|^3} \cdot d\mathbf{S} = \pm 2\pi \text{sgn}(\det(J_F(\mathbf{p}_s))) = \pm 2\pi Q_s. \quad (2.57)$$

Hence, the sign of the topological charge, defining the change of the winding number, is given by the sign of the Berry flux through a closed surface around the singularity, employing the Berry curvature of the band lying below the degeneracy:

$$\text{sgn}(Q_s) = \text{sgn}(\Phi^-). \quad (2.58)$$

Equivalently, the Berry curvature of the band above the singularity can be used, leading to  $\text{sgn}(Q_s) = -\text{sgn}(\Phi^+)$ . This relation can be applied in experiments to measure the change of the winding number at a phase transition point, by probing the Berry curvature flux around it.

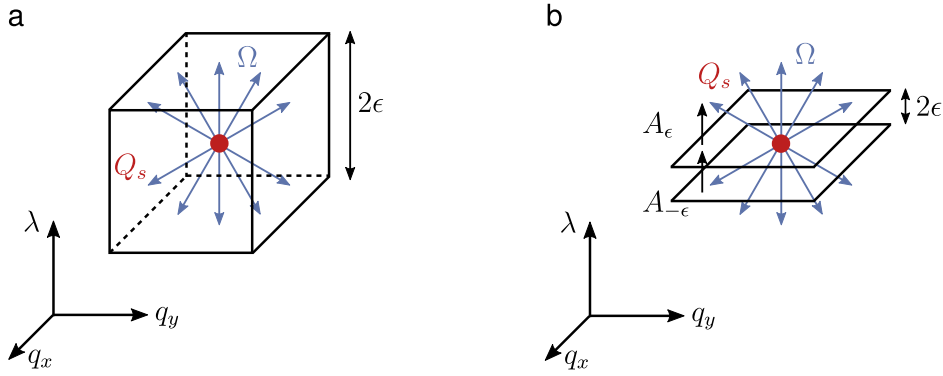


Figure 2.4: **Determination of the Berry flux around a band touching singularity.** **a.** Sketch of the singularity with charge  $Q_s$  in the 3D parameter space spanned by  $q_x$ ,  $q_y$  and  $\lambda$ . The sign of the total Berry curvature flux through a closed surface, represented by a cuboid with height  $2\epsilon$ , determines the topological charge. **b.** In the limit of  $\epsilon \rightarrow 0$ , the total flux is given by the contributions of the two surfaces  $A_\epsilon$  and  $A_{-\epsilon}$  above and below the singularity. In the experiments, both surfaces are oriented upwards.

The shape of the closed surface can be arbitrarily modified without changing the flux, as long as the singularity  $\mathbf{p}_s$  is still enclosed. In particular, it can be deformed into a cuboid of height  $2\epsilon$  (see Fig. 2.4a), where the flux through all 6 surfaces had to be probed [120]. In the limit of  $\epsilon \rightarrow 0$ , the determination of  $\Phi$  then reduces to the measurement of the flux through the two surfaces  $A_\epsilon$  and  $A_{-\epsilon}$  located at  $\lambda_s + \epsilon$  and  $\lambda_s - \epsilon$ . In the experiments, the Berry flux is probed in the  $q_x$ - $q_y$ -plane for  $\lambda_s + \epsilon$  and in the same way for  $\lambda_s - \epsilon$ , which corresponds to the two surfaces  $A_\epsilon$  and  $A_{-\epsilon}$  having the same orientation (Fig. 2.4b). Since the Berry curvature distribution is spherically symmetric and  $\epsilon \rightarrow 0$ , the flux is equally distributed between the two planes, and directed parallel to the upper and antiparallel to the lower surface for  $\Phi > 0$ , as depicted in Fig. 2.4b, such that

$$\begin{aligned} \text{sgn}(\Phi_{A_\epsilon}) &= +1, & \text{sgn}(\Phi_{A_{-\epsilon}}) &= -1, & \text{for } \Phi > 0 \\ \text{sgn}(\Phi_{A_\epsilon}) &= -1, & \text{sgn}(\Phi_{A_{-\epsilon}}) &= +1, & \text{for } \Phi < 0. \end{aligned} \quad (2.59)$$

Hence, the sign of the total flux can be obtained by comparing the sign of the flux through the surfaces located above and below the phase transition point. As the sign of the flux is directly given by the sign of the Berry curvature at the singularity, the topological charge can be determined as

$$\begin{aligned} Q_s &= \text{sgn}(\Phi^-) = \text{sgn}(\Phi_{A_\epsilon}^-) - \text{sgn}(\Phi_{A_{-\epsilon}}^-) \\ &= \text{sgn}(\Omega^-(\mathbf{q}_s, \lambda + \epsilon)) - \text{sgn}(\Omega^-(\mathbf{q}_s, \lambda - \epsilon)). \end{aligned} \quad (2.60)$$

For a periodically driven two-band system, as considered in this work, the topological charge of a band touching in the gap  $g^0$  or  $g^\pi$  can thus be derived from the sign change of the Berry curvature in the lower or upper band across the phase transition:

$$Q_s^0 = \text{sgn}(\Delta\Omega^-(\mathbf{q}_s)) \quad Q_s^\pi = \text{sgn}(\Delta\Omega^+(\mathbf{q}_s)). \quad (2.61)$$

In this way, the change of the winding numbers can be measured by comparing the sign of the Berry curvature at quasimomentum  $\mathbf{q}_s$  for modulation parameters  $\lambda$  just before and after the transition point  $\lambda_s$ . The application of Eq. 2.61 to experimentally determine the winding numbers in the anomalous Floquet regime is presented in chapter 5.

The singularities described above are non-degenerate, linear band touchings, characterized by the matrix  $J_F(\mathbf{p}_s)$  having full rank and corresponding to three linearly independent vectors  $\frac{\partial \mathbf{h}_F}{\partial p_j}$ . If the matrix  $J_F(\mathbf{p}_s)$  is not invertible, having a rank of  $3 - D$ , a  $D$ -dimensional manifold of degenerate touching points exists, which is in general not topologically protected [119]. By adding a perturbation, the degeneracy can either be lifted completely, or is reduced to a set of isolated singularities. There can also be parabolic band touching points [123–125], if the first derivative of  $\mathbf{h}_F$  is zero and the Taylor expansion is continued to the second order, as described in [121]. In this case, again a basis of three vectors can be identified and the topological charge equals two times the Berry flux around the singularity.

### 2.3.3 Anomalous Floquet phases in the presence of disorder and interactions

In view of exploring topological many-body phases, the question arises how periodic driving can be combined with interactions. In general, closed, interacting periodically driven quantum systems are expected to approach a featureless state in the thermodynamic limit, where eigenstates of all energies are mixed. The system constantly absorbs energy from the drive, which can not be released to an external bath, eventually heating up to infinite temperature. In cold atomic systems, this problem could be overcome in many-body localized (MBL) systems, where non-trivial stationary states can persist also at long times due to the presence of disorder [44, 45, 126, 127]. In this way, interacting topological systems could be stabilized, exhibiting a localized bulk and protected chiral edge modes at their boundaries.

However, in a system with energy bands having a non-zero Chern number, there are always delocalized bulk states accompanying the chiral edge modes, which can not be removed by disorder and prevent the system from being fully localized [43]. Consider a situation similar to the quantum Hall effect described in Sec. 2.1.2, but now defined in an annular geometry with additional magnetic flux piercing through the hole in the center [29]. If one full flux quantum  $\Phi_0$  is inserted into the sample, the overall spectrum returns to its original value, whereas the states at the boundary flow to a higher or lower energy, depending on their propagation direction. To terminate this flow, there must be extended bulk states connecting the edge modes on opposite sites [42, 128].

In a periodically driven system, the spectrum is periodic and there can be edge states which wrap around the complete FBZ and do not need to be terminated by a bulk state. This scenario is realized in the anomalous Floquet phase, where the same number of chiral edge states is present at all quasienergies, persisting also in the spectral region of the bulk, and thus fully winding around the FBZ and turning into themselves again. The equal value of all winding numbers necessarily implies  $\mathcal{C} = 0$  for all bands, enabling

the complete localization of the bulk states in the presence of disorder. In periodically driven systems with non-zero Chern numbers, the quasienergies are also periodic, but nevertheless, delocalized bulk states occur, as there must be chiral edge states exhibiting an unterminated spectral flow. The topological phase characterized by a fully localized bulk and propagating chiral edge modes is accordingly called the anomalous Floquet-Anderson insulator (AFAI) [42]. It is expected to be robust against perturbations up to a certain magnitude, which is defined by the disorder strength. Above that value, the mobility gap in the bulk closes leading to backscattering between the edge modes on opposite sites.

Adding disorder to an anomalous Floquet system will thus result in the AFAI phase described above, if the disorder is not too large. Increasing the disorder strength above a critical value will lead to the appearance of delocalized states sweeping through all quasienergies and thereby removing the edge modes. This results in the transition to a trivial phase with winding numbers equal to zero, where all of the bulk *and* edge states are localized. For systems with non-zero Chern numbers, increasing the disorder strength does not yield a complete localization of the bulk. The delocalized states move towards the energy gaps and finally annihilate, indicating the transition to the trivial phase.

The presence of interactions is expected to result in a coupling between the thermalizing edge states and the localized bulk states. The AFAI phase might persist for finite disorder and interaction strengths, leading to a MBL bulk with only minor leakage from the mobile edge states [58,59]. Hence, the anomalous Floquet phase constitutes a possible setting to stabilize interacting, periodically driven systems using disorder.

# Chapter 3

## Anomalous Floquet phases in a honeycomb lattice

In this chapter, the realization of anomalous and other Floquet topological phases in an optical honeycomb lattice is presented. First, the creation and characterization of the honeycomb lattice is described as well as the implementation of a sub-lattice energy offset or a lattice potential with broken rotational symmetry. In the second section, the driving scheme for the anomalous Floquet system, based on intensity modulation of the lattice beams, is introduced and the quasienergy bands and Berry curvature distribution of the effective Hamiltonian are calculated. The resulting phase diagram, hosting several topological phases, is discussed for the symmetric lattice and for the case of a non-zero sub-lattice offset. In view of calculating the energy bands in a semi-finite geometry, which directly reveals the dispersion of the edge states, a tight-binding description for the modulated honeycomb lattice is introduced in Sec. 3.3. Thereby, a two-band model is compared to an approach that includes also higher bands, which appear to influence the shape of the two lower Floquet bands. In the last section, the quasienergy bands are derived for a semi-finite system terminated by an armchair-edge, complementing the characterization of the different topological regimes.

### 3.1 The optical honeycomb lattice

Conservative potentials for neutral atoms can be created using intense, far detuned laser light. As described below, by interfering three running waves, a honeycomb lattice structure is realized. The properties of the lattice potential and the resulting energy bands are modified by changing the polarization or intensity of the beams. In this section, the experimental implementation of the optical lattice is described, as well as the theoretical methods to calculate the energy bands and the Berry curvature distribution in quasimomentum space for different configurations of the lattice.

### 3.1.1 Creation of the honeycomb lattice

The honeycomb lattice is created by interference of three, coplanar laser beams propagating at angles of  $120^\circ$  in the  $x$ - $y$ -plane, as depicted in Fig. 3.1a. The interaction of the oscillating electric field of the laser light with the dipole moment induced in a neutral atom results in a dipole potential, which is known as the *AC-Stark-effect*. The wavelength of the light is  $\lambda_L = 736.8$  nm, which is far blue-detuned from the  $D1$ - and  $D2$ -line of  $^{39}\text{K}$  at 770 nm and 767 nm. If the detuning is larger than the hyperfine splitting of the excited states, the corresponding levels are not resolved, and for alkali atoms, the dipole potential is given as [129]

$$V_{\text{dip}}(\mathbf{r}) = \frac{\pi c^2}{2} \left( \frac{\Gamma_{D2}}{\omega_{D2}^3} \frac{2 + g_F m_F \mathcal{P}}{\Delta_{D2}} + \frac{\Gamma_{D1}}{\omega_{D1}^3} \frac{1 - g_F m_F \mathcal{P}}{\Delta_{D1}} \right) I(\mathbf{r}) = U_0 I(\mathbf{r}), \quad (3.1)$$

where  $\omega_{D1(D2)}$  and  $\Gamma_{D1(D2)}$  denote the frequency and the natural linewidth of the  $D1(D2)$  transition,  $m_F$  and  $g_F$  the magnetic quantum number and the Landé-factor,  $c$  the speed of light and  $I(\mathbf{r})$  the spatially-dependent intensity. The detuning  $\Delta_{D1(D2)}$  is defined as

$$\frac{1}{\Delta_{D1(D2)}} = \frac{1}{\omega_L - \omega_{D1(D2)}} + \frac{1}{\omega_L + \omega_{D1(D2)}} \quad (3.2)$$

with  $\omega_L = \frac{2\pi\lambda_L}{c}$ . Hence, for blue detuned light with  $\omega_L > \omega_{D1(D2)}$ ,  $\Delta_{D1(D2)}$  is positive, corresponding to a repulsive potential, and the atoms are trapped in the intensity minima. The factor  $\mathcal{P}$  depends on the polarization of the light and is  $\mathcal{P} = 0$  for  $\pi$ - and  $\mathcal{P} = \pm 1$  for  $\sigma^\pm$ -polarization, defined in the plane perpendicular to the magnetic quantization axis. If  $\mathcal{P} = \pm 1$ , the potential contains a state-dependent part, which can be utilized for the creation of optical flux lattices [130, 131]. This part is mainly proportional to the difference of the detunings  $\Delta_{D1}$  and  $\Delta_{D2}$ , which is negligible for  $^{39}\text{K}$  and  $\lambda_L = 736.8$  nm. To calculate the intensity pattern, each lattice beam is described as a plane wave with frequency  $\omega_L$  propagating along the direction  $\mathbf{k}_j$ :

$$\mathbf{E}_j(\mathbf{r}, t) = \sqrt{I_j} e^{-i\omega_L t - i\mathbf{k}_j \cdot \mathbf{r}} (\cos(\theta_j) \mathbf{z} + \sin(\theta_j) e^{i\alpha_j} (\mathbf{z} \times \mathbf{k}_j)) = \mathbf{E}_{j,s} + \mathbf{E}_{j,p}. \quad (3.3)$$

The angle  $\theta_j$  describes the amplitudes of the  $s$ - and  $p$ -polarized parts and  $\alpha_j$  the relative phase shift between them, accounting for elliptical polarization, as illustrated in Fig. 3.1a. The propagation directions of the three beams are

$$\mathbf{k}_1 = k_L \begin{pmatrix} 0 \\ 1 \end{pmatrix}, \quad \mathbf{k}_2 = \frac{k_L}{2} \begin{pmatrix} -\sqrt{3} \\ -1 \end{pmatrix}, \quad \mathbf{k}_3 = \frac{k_L}{2} \begin{pmatrix} \sqrt{3} \\ -1 \end{pmatrix}, \quad k_L = \frac{2\pi}{\lambda_L}. \quad (3.4)$$

The total interference pattern, consisting of the  $s$ - and  $p$ -polarized part, is given by

$$\begin{aligned} I(\mathbf{r}) &= I_s(\mathbf{r}) + I_p(\mathbf{r}) \\ I_s(\mathbf{r}) &= |\mathbf{E}_s|^2 = \left| \sum_{j=1}^3 \mathbf{E}_{j,s} \right|^2 = \sum_{j,l=1}^3 \sqrt{I_j I_l} \cos(\theta_j) \cos(\theta_l) e^{-i\mathbf{k}_{jl} \cdot \mathbf{r}} \\ I_p(\mathbf{r}) &= |\mathbf{E}_p|^2 = \sum_{j,l=1}^3 \sqrt{I_j I_l} \sin(\theta_j) \sin(\theta_l) \cos(\eta_j - \eta_l) e^{-i\mathbf{k}_{jl} \cdot \mathbf{r}} e^{i\alpha_{jl}}, \end{aligned} \quad (3.5)$$

where  $\boldsymbol{\eta} = (0, 4\pi/3, 2\pi/3)$ ,  $\mathbf{k}_{jl} = \mathbf{k}_j - \mathbf{k}_l$  and  $\alpha_{jl} = \alpha_j - \alpha_l$ . If all beams are *s*-polarized and have equal intensities  $I_j = I_0$ , the intensity minima form a symmetric honeycomb lattice, which is shown in Fig. 3.1b. In this case, Eq. 3.5 can be simplified and the optical lattice potential with  $V_0 = U_0 I_0$  reads:

$$V(\mathbf{r}) = V_0 (3 + 2\cos(\mathbf{k}_{12}\mathbf{r}) + 2\cos(\mathbf{k}_{13}\mathbf{r}) + 2\cos(\mathbf{k}_{23}\mathbf{r})). \quad (3.6)$$

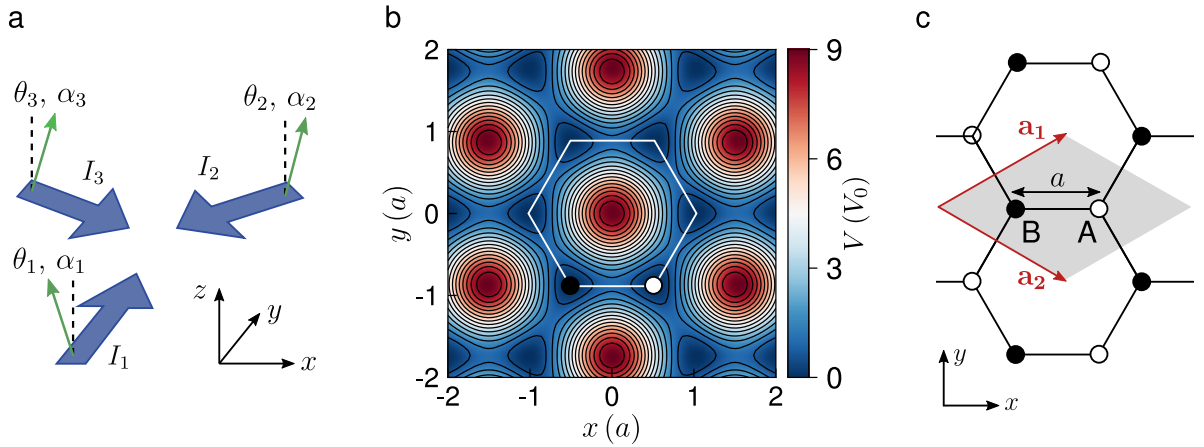


**Figure 3.1: Creation of the honeycomb lattice and real space potential.** **a.** The honeycomb lattice is generated by interference of three running waves in the  $x$ - $y$ -plane with polarizations described by  $\theta_j$ ,  $\alpha_j$ ,  $j = \{1, 2, 3\}$ . **b.** Lattice potential for *s*-polarized beams with equal intensities. Since the lattice wavelength is blue detuned to the atomic transitions, the potential is positive and the atoms are trapped in the minima, forming a honeycomb lattice, as depicted by the white hexagon. **c.** Lattice vectors  $\mathbf{a}_1$  and  $\mathbf{a}_2$  in real space forming the unit cell (gray area) which contains a single A- and B-site.

The unit cell of the honeycomb lattice is spanned by the two lattice vectors  $\mathbf{a}_1 = a(3/2, \sqrt{3}/2)$  and  $\mathbf{a}_2 = a(3/2, -\sqrt{3}/2)$ , as introduced in Sec. 2.1.3, and contains two inequivalent sites, denoted by A and B, which is illustrated in Fig. 3.1c. In the optical honeycomb lattice, the spacing is given by

$$a = \frac{4\pi}{3\sqrt{3}k_L} \approx 284 \text{ nm}. \quad (3.7)$$

### 3.1.2 Calculation of the energy bands and Berry curvature

The energy bands of the honeycomb lattice are usually described as functions of the quasimomentum. The first Brillouin zone (BZ) (see Fig. 3.2a) is spanned by the reciprocal lattice vectors (Sec. 2.1.3)

$$\mathbf{K}_1 = \frac{k_L}{2} \begin{pmatrix} \sqrt{3} \\ 3 \end{pmatrix} = \mathbf{k}_1 - \mathbf{k}_2 \quad \mathbf{K}_2 = \frac{k_L}{2} \begin{pmatrix} \sqrt{3} \\ -3 \end{pmatrix} = \mathbf{k}_3 - \mathbf{k}_1. \quad (3.8)$$

The honeycomb lattice potential as described in Eq. 3.6 exhibits inversion- ( $x \rightarrow -x$ ) and threefold rotational symmetry. There are certain quasimomenta in the first BZ, which are invariant under these transformations, and are accordingly called high-symmetry points. These are the  $\Gamma$ -point in the center of the hexagon, the  $M$ -point in the center of the edge and the Dirac points  $K$  and  $K'$  in the corners of the hexagon, as shown in Fig. 3.2b. The two  $K$ -points are in-equivalent, since they can not be mapped onto each other by a reciprocal lattice vector. The Schrödinger equation for the cell-periodic Bloch functions  $u_n^{\mathbf{q}}(\mathbf{r}) = u_n^{\mathbf{q}}(\mathbf{r} + \mathbf{R})$  in the honeycomb lattice is given by:

$$\left( \frac{(\hat{\mathbf{p}} + \hbar\mathbf{q})^2}{2m} + V(\mathbf{r}) \right) u_{\mathbf{q}}^n(\mathbf{r}) = E_{\mathbf{q}}^n u_{\mathbf{q}}^n(\mathbf{r}). \quad (3.9)$$

To solve the equation, the functions  $u_n^{\mathbf{q}}(\mathbf{r})$  are expanded in plane waves, whereas the corresponding wave vectors are multiples of reciprocal lattice vectors, due to the periodicity of  $u_n^{\mathbf{q}}(\mathbf{r})$  in real space:

$$u_{\mathbf{q}}^n(\mathbf{r}) = \sum_{\mathbf{K}} c_{\mathbf{K}}^{n,\mathbf{q}} e^{i\mathbf{Kr}}, \quad \mathbf{K} = l_1 \mathbf{K}_1 + l_2 \mathbf{K}_2, \quad l_1, l_2 \in \mathbb{Z}. \quad (3.10)$$

The plane wave expansion of the lattice potential corresponds to a two-dimensional (2D) Fourier transformation, again restricted to reciprocal lattice vectors:

$$V(\mathbf{r}) = \sum_{\mathbf{K}} V_{\mathbf{K}} e^{i\mathbf{Kr}} \Rightarrow V_{\mathbf{K}} = V_{l_1, l_2} = \sum_{\mathbf{r}} e^{i\mathbf{r}(l_1(\mathbf{k}_1 - \mathbf{k}_2) + l_2(\mathbf{k}_3 - \mathbf{k}_1))} V(\mathbf{r}), \quad (3.11)$$

where the reciprocal lattice vectors are expressed in terms of the lattice propagation directions, according to Eq. 3.8. Substituting the plane wave expansions into the Schrödinger equation, results in an eigenvalue equation for the coefficients  $c_{\mathbf{K}}^{n,q}$  (see also [73]):

$$\sum_{\mathbf{K}} H_{\mathbf{KK'}} c_{\mathbf{K}}^{n,\mathbf{q}} = E_{\mathbf{q}}^n c_{\mathbf{K'}}^{n,\mathbf{q}} \quad (3.12)$$

with

$$H_{\mathbf{KK'}} = \frac{\hbar^2(\mathbf{q} + \mathbf{K})^2}{2m} \delta_{\mathbf{K}, \mathbf{K'}} + V_{\mathbf{K'} - \mathbf{K}}. \quad (3.13)$$

The summation over the reciprocal lattice vectors corresponds to the summation over the double index  $l_1, l_2$ . Using Eq. 3.11 and 3.5, the Fourier coefficients of the lattice potential  $V_{l_1, l_2}$  can be calculated, leading to equations for the integers  $l_1$  and  $l_2$  depending on the values of the indices  $j, l$  in Eq. 3.5. Most of the Fourier coefficients evaluate to zero except for  $(l_1, l_2) = [(0, 0), (-1, 0), (1, 0), (0, 1), (0, -1), (1, 1)]$ . The Hamiltonian from Eq. 3.13

can be written in matrix form depending on the two double indices,  $l_1, l_2$  and  $l'_1, l'_2$

$$H_{l_1, l_2, l'_1, l'_2} = \begin{cases} (l_1 \mathbf{K}_1 + l_2 \mathbf{K}_2 + \mathbf{q})^2 + V_{00}, & l'_1 = l_1, l'_2 = l_2 \\ V_{01}, & l'_1 = l_1, l'_2 - l_2 = 1 \\ V_{0-1}, & l'_1 = l_1, l'_2 - l_2 = -1 \\ V_{10}, & l'_1 - l_1 = 1, l'_2 = l_2 \\ V_{-10}, & l'_1 - l_1 = -1, l'_2 = l_2 \\ V_{11}, & l'_1 - l_1 = 1, l'_2 - l_2 = 1 \\ V_{-1-1}, & l'_1 - l_1 = -1, l'_2 - l_2 = -1 \\ 0, & \text{otherwise.} \end{cases} \quad (3.14)$$

Here, the Hamiltonian is given in units of the recoil energy  $E_r = \frac{\hbar^2 k_L^2}{2m}$ . The coefficients of the lattice potential depend on the differences of the indices,  $l_1 - l'_1$  and  $l_2 - l'_2$ . Combining the prefactors of the optical potential with the beam intensities to  $V_j = U_0 I_j$ , the matrix entries are given as:

$$\begin{aligned} V_{00} &= V_1 + V_2 + V_3 \\ V_{01} = V_{0-1}^* &= \sqrt{V_1 V_3} \left( \cos(\theta_1) \cos(\theta_3) - \frac{1}{2} \sin(\theta_1) \sin(\theta_3) e^{i\alpha_{13}} \right) \\ V_{10} = V_{-10}^* &= \sqrt{V_2 V_1} \left( \cos(\theta_2) \cos(\theta_1) - \frac{1}{2} \sin(\theta_2) \sin(\theta_1) e^{i\alpha_{21}} \right) \\ V_{11} = V_{-1-1}^* &= \sqrt{V_2 V_3} \left( \cos(\theta_2) \cos(\theta_3) - \frac{1}{2} \sin(\theta_2) \sin(\theta_3) e^{i\alpha_{23}} \right). \end{aligned} \quad (3.15)$$

The energy bands and eigenstates are then obtained in the plane wave basis by diagonalization of the Hamiltonian matrix in Eq. 3.14, which is cut at some finite size. The indices run from  $-l_{max}$  to  $l_{max}$ , whereas the value of  $l_{max}$  has to be increased when considering bands with higher energy. For the calculations at a depth of  $V_0 = 6 E_r$ ,  $l_{max} = 7$  is used, resulting in a matrix of size  $225 \times 225$ . The BZ is described by a 2D rhombic grid of  $N \times N$  discrete points  $\mathbf{q}$ , with normally  $N = 61$ , defined along the directions of the lattice vectors  $\mathbf{K}_1$  and  $\mathbf{K}_2$  and centered around  $\mathbf{q} = \mathbf{0}$ :

$$\mathbf{q} = q_1 \mathbf{K}_1 + q_2 \mathbf{K}_2 - \frac{\sqrt{3}}{2} k_L \begin{pmatrix} 1 \\ 0 \end{pmatrix}, \quad q_1 = \frac{n_1}{N-1} \quad q_2 = \frac{n_2}{N-1}, \quad n_1, n_2 \in [0, \dots, N-1]. \quad (3.16)$$

Since the unit cell of the honeycomb lattice contains two lattice sites, the lowest band is split into two bands, which touch at the  $K$ - and  $K'$ -points, as depicted in Fig. 3.2b. These are usually called  $s$ -bands, since the wavefunctions in real space are expected to be approximately spherically symmetric. In the vicinity of the touching points, the energy dispersion is nearly linear and thus takes a form similar to the relativistic Dirac equation for electrons, as described in Sec. 2.1.3.

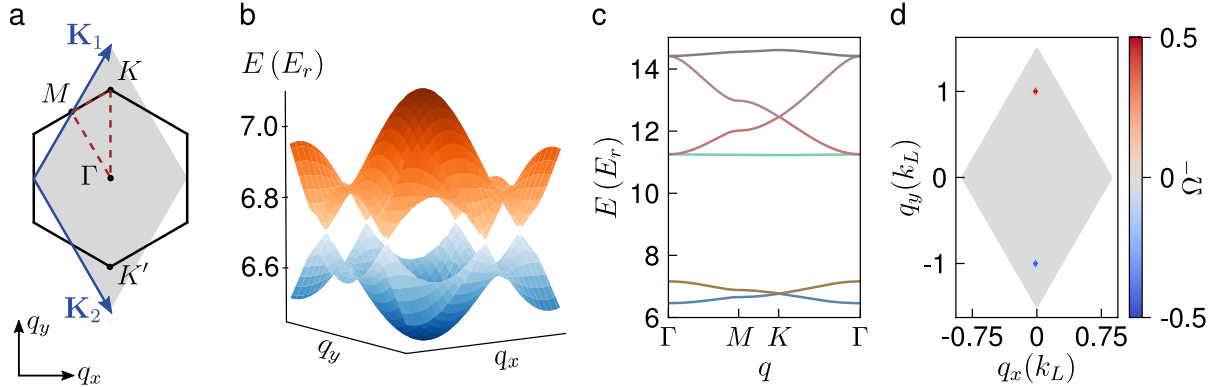


**Figure 3.2: Energy bands and Berry curvature in quasimomentum space.** **a.** Reciprocal lattice vectors  $\mathbf{K}_1$  and  $\mathbf{K}_2$  (blue arrows) spanning the first Brillouin zone (gray diamond). The high-symmetry points are sketched as well as the path  $\Gamma$ - $M$ - $K$ - $\Gamma$ , along which the energy bands are usually plotted (dashed, red line). **b.** The two lowest energy bands of the symmetric honeycomb lattice with  $V_0 = 6 E_r$  in 2D-quasimomentum space. The bands touch at the six Dirac points. **c.** The six lowest energy bands at the same lattice depth plotted along the high-symmetry line depicted in a. **d.** Berry curvature distribution of the lowest band for  $V_0 = 6 E_r$ , in the first BZ, exhibiting two sharp peaks at the  $K$ - and  $K'$ -points with opposite sign. For visual clarity, a small sublattice offset ( $\theta = 0.02$  rad, see Eq. 3.5) was used in the plot.

The next higher energy levels are separated by a large gap and form a group of four bands, which are pairwise degenerate at the Dirac points and at the  $\Gamma$ -point. These would be described as superpositions of  $p_x$ - and  $p_y$ -orbitals in real space, again doubled due to the two sites per unit cell. This is discussed in more detail in the context of a tight-binding model in Sec. 3.3. The first six energy bands of the honeycomb lattice are plotted in Fig. 3.2c for  $V_0 = 6 E_r$  along a line in quasimomentum space connecting the high-symmetry points  $\Gamma$ - $M$ - $K$ - $\Gamma$ .

To obtain the Berry curvature of the  $n$ th energy band on the discrete grid in momentum space, the method described in [132] is employed. Defining link variables  $U_1^n$  and  $U_2^n$  along the directions  $\mathbf{K}_1$  and  $\mathbf{K}_2$  as

$$U_1^n = \frac{\langle u^n(\mathbf{q}) | u^n(\mathbf{q} + \mathbf{e}_1) \rangle}{|\langle u^n(\mathbf{q}) | u^n(\mathbf{q} + \mathbf{e}_1) \rangle|} \quad U_2^n = \frac{\langle u^n(\mathbf{q}) | u^n(\mathbf{q} + \mathbf{e}_2) \rangle}{|\langle u^n(\mathbf{q}) | u^n(\mathbf{q} + \mathbf{e}_2) \rangle|}, \quad (3.17)$$

the Berry curvature is given by

$$\Omega^n(\mathbf{q}) = \ln (U_1^n(\mathbf{q}) U_2^n(\mathbf{q} + \mathbf{e}_1) U_2^n(\mathbf{q})^{-1} U_1^n(\mathbf{q} + \mathbf{e}_2)^{-1}). \quad (3.18)$$

This effectively approximates the state derivatives of Eq. 2.8 around a single plaquette by finite differences. The vectors connecting the points of the grid are defined as

$$\mathbf{e}_1 = \frac{1}{N-1} \mathbf{K}_1 \quad \mathbf{e}_2 = \frac{1}{N-1} \mathbf{K}_2, \quad (3.19)$$

whereas  $k_L = 1$  in the numerical calculations. In the symmetric honeycomb lattice, the degeneracy of the two lowest bands at the Dirac points gives rise to a Berry flux of  $\pm\pi$  concentrated at the singularity and a Chern number of zero. The formula in Eq. 3.18 is only valid for non-degenerate bands, but can be generalized to the case of band touching points [132]. The Berry curvature is usually calculated for the lowest band in cases where energy gaps have opened either due to lattice modulation or by breaking inversion symmetry, where Eq. 3.18 can be applied directly. To better visualize the Berry curvature distribution of the static lattice, it is plotted for a finite sublattice offset in Fig. 3.2d. In the remainder of this thesis, the numerically calculated Berry curvature will be plotted in units of  $1/(|\mathbf{e}_1| |\mathbf{e}_2|)$ , where the denominator corresponds to the size of the plaquette in reciprocal space.

### 3.1.3 Breaking of inversion or rotational symmetry

If all lattice beams are  $s$ -polarized and have equal intensities, the honeycomb lattice potential is fully symmetric, as described by Eq. 3.6 and plotted in Fig. 3.1b. In this case, the system exhibits inversion, threefold rotational and time-reversal symmetry, which constrains the existence of Dirac points to the positions of  $K$  and  $K'$  at the corners of the hexagon in reciprocal space [133–135].

Changing the polarizations or relative intensities of the lattice, either inversion symmetry can be broken by introducing an energy offset between the A- and B-sites or the lattice potential can be deformed, breaking threefold rotational symmetry. The sublattice energy offset can be realized using lattice beams with equal intensities and elliptical polarizations with  $\theta_1 = \theta_2 = \theta_3 = \theta$ . Now, the potential is given as the sum of the interference patterns from the  $s$ - and  $p$ -polarized components of the lattice beams, which read

$$\begin{aligned} V_s &= 3V_0 + 2V_0 \cos(\theta)^2 (\cos(\mathbf{k}_{12}\mathbf{r}) + \cos(\mathbf{k}_{13}\mathbf{r}) + \cos(\mathbf{k}_{23}\mathbf{r})) \\ V_p &= 3V_0 - V_0 \sin(\theta)^2 (\cos(\mathbf{k}_{12}\mathbf{r} - \alpha_{12}) + \cos(\mathbf{k}_{13}\mathbf{r} - \alpha_{13}) + \cos(\mathbf{k}_{23}\mathbf{r} - \alpha_{23})). \end{aligned} \quad (3.20)$$

While the  $s$ -part creates a honeycomb potential, the interference of three blue-detuned,  $p$ -polarized beams at  $120^\circ$  results in a triangular lattice. If the polarizations of all beams are linear with angle  $\theta$ , the lattice potential is still symmetric and only the depth is reduced, as shown in Fig. 3.3a. Making the polarization elliptical leads to a relative phase difference between the  $s$ - and  $p$ -polarized part of each individual beam. If the angles  $\alpha_j$  are different, the  $p$ -components of the corresponding beams are phase shifted relative to each other. The interference of the three  $p$ -polarized parts with relative phase offsets results in a triangular lattice moved in real space relative to the honeycomb pattern generated by the  $s$ -parts.

To create a potential difference between the A- and B-sites, the  $p$ -lattice is shifted such that it has a minimum at the positions of the A-sites in the  $s$ -lattice, and a maximum at the positions of the B-sites, resulting in a reduced potential at the B-sites compared to

the A-sites (see Fig. 3.3b). This can be realized by choosing

$$\alpha_1 = \frac{4\pi}{3} \quad \alpha_2 = 0 \quad \alpha_3 = \frac{2\pi}{3}, \quad (3.21)$$

which leads to a displacement of the  $p$ -interference pattern along the direction  $2\mathbf{k}_1 + \mathbf{k}_3$  by one lattice constant.

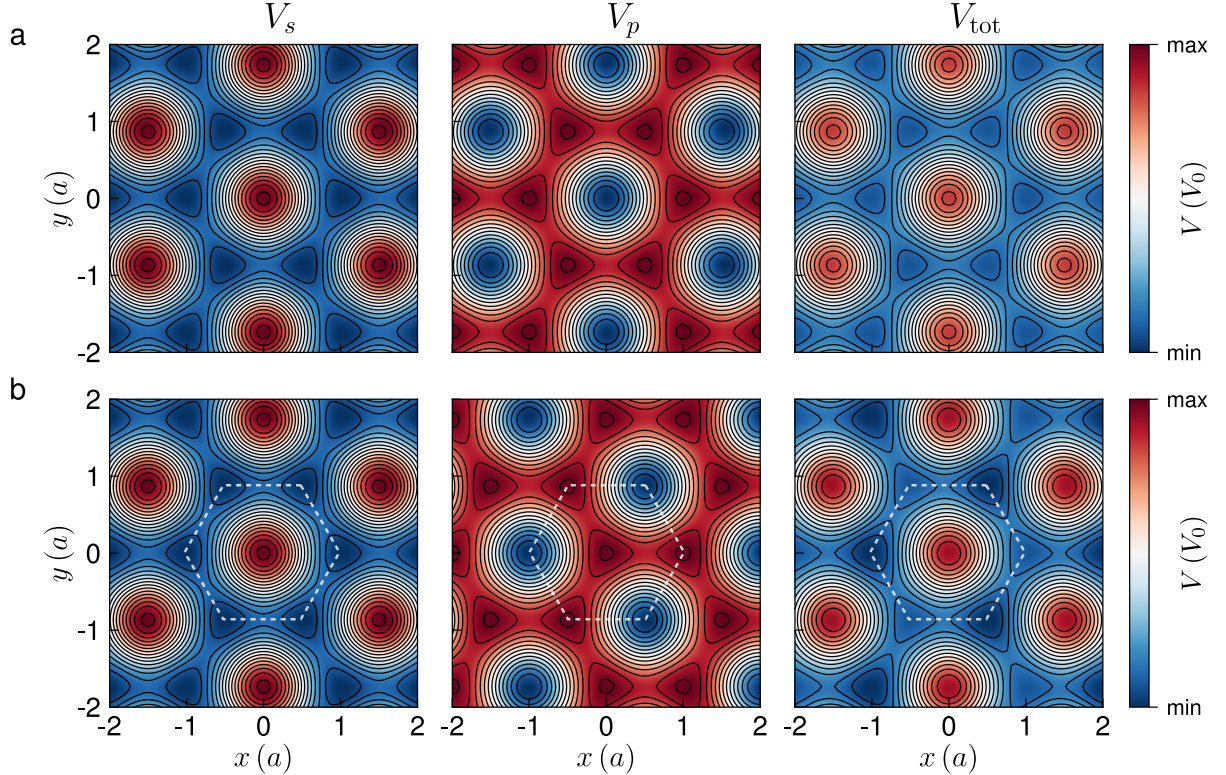


**Figure 3.3: Realization of a potential offset between the A- and B-sites.** Lattice potentials  $V_s$  and  $V_p$  arising from the  $s$ - and  $p$ -polarized parts of the lattice beams and total potential  $V_{\text{tot}} = V_s + V_p$  in real space. The limits of the colorbar are different for  $V_p$  for better visibility. **a.** Potentials for linear polarizations with  $\theta = \pi/4$  and  $\alpha_j = 0 \forall j$ , resulting in a honeycomb lattice with reduced depth. **b.** Potentials for elliptical polarization of two beams,  $\theta = \pi/4$  and  $\alpha_j$  according to Eq. 3.21, realizing a sublattice offset. The  $p$ -polarized part is shifted relative to the  $s$ -part by one lattice constant along  $(1/2, \sqrt{3}/2)$ , having a minimum at the location of the A-sites and a maximum at the B-sites of the honeycomb lattice, as indicated by the white, dashed line.

The magnitude of the sublattice offset is tuned by changing  $\theta \in [0, \pi/4]$  and its sign could be inverted e.g. by switching the polarizations of beam 2 and 3. The energy offset between the A- and B-sites leads to an opening of the energy gaps between the two lowest bands at the Dirac points, realizing a mass-term in the tight-binding description. The size of the energy gap at  $K$  and  $K'$  is approximately proportional to the sublattice energy

offset  $\Delta$  (see Eq. 2.23), which in turn is changed by the polarization angle  $\theta$  in a non-linear fashion (see next section). Another way to gap out the Dirac points is the breaking of time-reversal symmetry, which can be accomplished by time-periodic modulation of the lattice potential in a circular fashion, as described the next section and in chapters 2 and 6. If the lattice beams are linearly polarized but have unequal intensities, the real space potential is deformed (see Fig. 3.5), breaking threefold rotational symmetry. In this case, the Dirac points are shifted in quasimomentum space with increasing intensity imbalance and finally annihilate at a time-reversal-invariant quasimomentum  $\mathbf{q} = -\mathbf{q}$  [133, 136, 137].

## 3.2 Periodic intensity modulation

Anomalous Floquet systems can be realized with an optical honeycomb lattice by periodic modulation of the tunnelings, which is accomplished by imbalancing the intensities of the lattice beams. In this section, the modulation scheme is explained, followed by the numerical calculation of the Floquet band structure. The resulting topological phase diagram is derived for experimentally accessible parameters and the quasienergy bands and Berry curvature of the two lowest bands are discussed in the different phases. Finally, the phase diagram in the presence of a sublattice energy offset is shown, hosting a topological phase with Chern number  $C^\mp = \mp 2$ .

### 3.2.1 Lattice modulation scheme

As discussed in Sec. 2.3, anomalous Floquet systems have been generated on a bipartite square lattice, where the tunneling between neighboring sites is periodically switched on and off in a chiral fashion. A similar scheme has been proposed for the honeycomb lattice in [118], which is sketched in Fig. 3.4a and b. The nearest neighbor hopping  $J_0$  is enhanced by a factor  $\Lambda$  along each of the three bond directions during one third of the driving period  $T$ , leading to a chiral motion around the hexagonal plaquette. For small modulation amplitudes  $\Lambda > 1$ , the system is in a Haldane-like phase with  $C^- = 1$  and chiral edge modes exist in the quasienergy gap  $g^0$ , that opens at the Dirac points. Increasing the amplitude results in a phase transition to an anomalous Floquet phase at  $\Lambda_c \approx 3.3$ , exhibiting chiral edge modes in the quasienergy gaps at 0 and  $\pi$ , and  $C^- = 0$ .

In the optical honeycomb lattice, anisotropic tunnelings can be achieved by imbalancing the relative intensities of the lattice beams. If the intensity of beam  $j$  is increased, the potential well along the perpendicular tunneling direction is lowered, leading to a larger hopping amplitude along this bond. Since a stepwise switching of the laser intensities could lead to distortions and heating of the atomic cloud, the intensities are instead modulated smoothly in time according to (see Fig. 3.4c):

$$I_j(t) = I_0 (1 - m + m \cos(\omega t + \phi_j)), \quad \phi_j = \frac{2\pi}{3} j. \quad (3.22)$$

Here,  $m \in [0, 0.5]$  denotes the (relative) modulation amplitude and  $\omega = \frac{2\pi}{T}$ , with the driving period  $T$ .

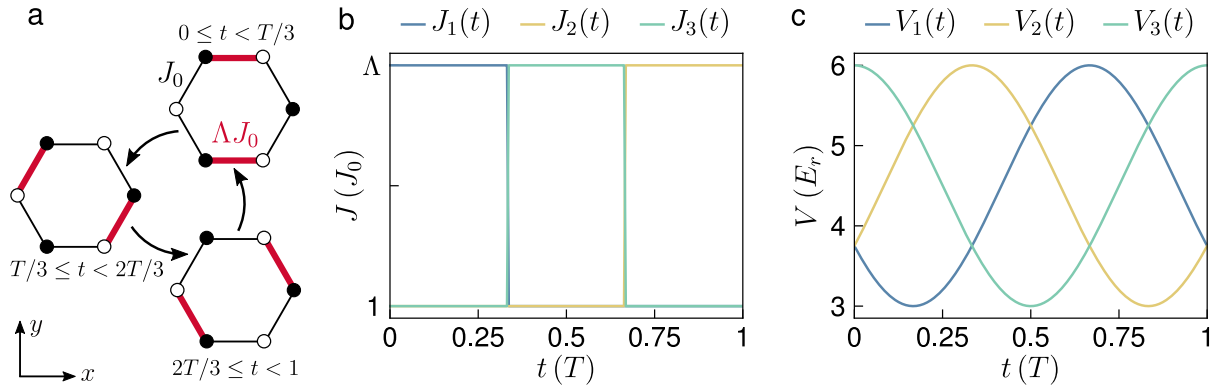


**Figure 3.4: Periodic modulation of the tunnelings with different protocols.** **a.** Stepwise modulation scheme proposed in [118]. The NN hopping is increased along each bond direction by  $\Lambda$  within one third of the driving period. For  $\Lambda > \Lambda_c \approx 3.3$ , an anomalous Floquet phase exists. **b.** Time-dependent hopping amplitudes for the stepwise modulation. **c.** Continuous modulation protocol used in the experiments, exhibiting similar topological phases as the scheme in **a**. The intensities of the lattice beams and hence the optical potentials  $V_j$  are periodically modulated according to Eq. 3.22, shown for  $V_0 = 6 E_r$  and  $m = 0.25$ .

This modulation protocol also breaks time-reversal symmetry and leads to similar topological phases as the stepwise model from [118], as shown explicitly in the next section. The imbalanced lattice potentials at different times within the modulation period are depicted in Fig. 3.5, illustrating the increased tunneling along the different bonds. It is important to note that the lattice beam intensities and hence the potentials associated with each beam are modulated in a cosine-fashion, but the tunnelings themselves exhibit a different time-dependence, nevertheless being periodic and chiral. The detailed time-dependence of the hopping amplitudes is discussed further in Sec. 3.3.

### 3.2.2 Floquet band structure calculation

In periodically driven systems, the bulk-edge correspondence is modified such that the number of chiral edge modes in a certain quasienergy gap is given by the winding number associated with the gap, which can be obtained from the sign change of the local Berry curvature across the phase transition (see Sec. 2.3). Thus, it is still possible to derive the existence of the edge modes solely from properties of the bulk bands, namely their quasienergy bands and Berry curvature. The bulk bands are described by the effective Hamiltonian, defined in Sec. 2.3 as the integral of the time-dependent Hamiltonian over one driving period:

$$H_{\text{eff}} = \frac{i\hbar}{T} \ln(U(T)), \quad U(T) = \mathcal{T} e^{-\frac{i}{\hbar} \int_0^T H(t) dt}, \quad (3.23)$$

where  $\mathcal{T}$  denotes time-ordering and  $\ln$  the matrix logarithm.

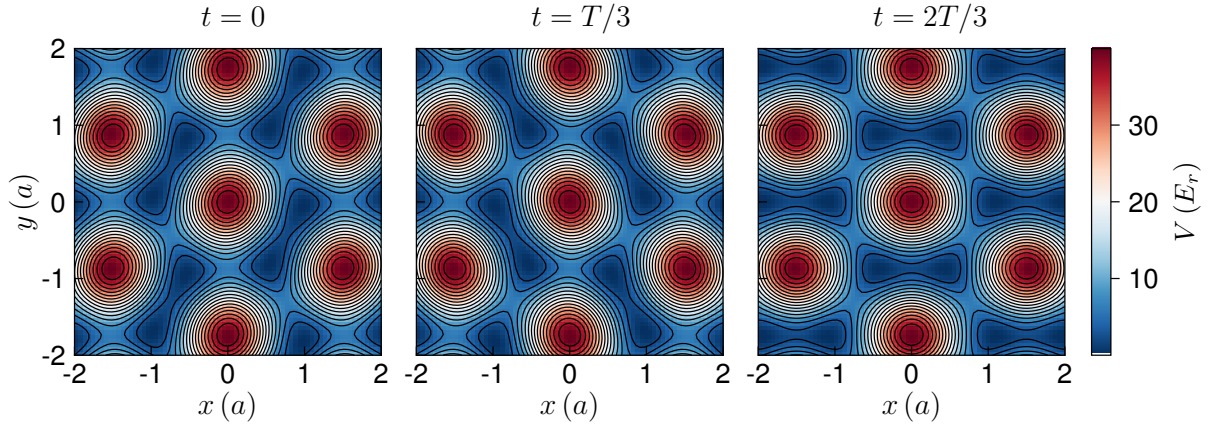


**Figure 3.5: Lattice potentials at different times within the driving period.** The real space potential is plotted at  $t = 0$ ,  $t = T/3$  and  $t = 2T/3$ , where the intensities  $I_3$ ,  $I_2$  and  $I_1$  are maximal, lowering the potential barrier in the perpendicular direction, which increases the hopping along this bond. The lattice depth is  $V_0 = 6 E_r$  and the modulation amplitude  $m = 0.25$ .

The topological properties discussed in chapter 2 are defined for a two-band system, which is represented by the two  $s$ -bands of the honeycomb lattice in this work. Hence, to obtain the phase diagram of the Floquet system, only the two lowest bands of the effective Hamiltonian need to be calculated. However, for certain modulation parameters used in the experiment, the shape of the effective  $s$ -bands is modified by coupling to higher bands during the driving period. To take these effects into account, mixing of the first six bands is allowed within one driving period by using  $6 \times 6$  matrices instead of  $2 \times 2$ . Increasing the size of the matrix even further does not change the resulting quasienergy bands any more for the modulation parameters considered in this work, which means that coupling to even higher bands than the  $p$ -bands can be neglected, which is also justified by the very good agreement between the numerical and experimental results (see chapter 5).

To calculate the effective Hamiltonian, the integral in Eq. 3.23 is approximated by a sum over  $N = 300$  discrete time steps of length  $\Delta t = 1/N$ :

$$-\frac{i}{\hbar} \int_0^T H(t) dt = -\frac{i}{\hbar} T \sum_{j=1}^N H(t_j) \Delta t. \quad (3.24)$$

Using Eq. 3.14, the instantaneous Hamiltonian  $H(t_j)$  at each time step  $t_j$  is derived for a certain modulation amplitude  $m$ , polarization angles  $\theta$ ,  $\alpha$ , and quasimomentum  $\mathbf{q}$ . To allow for coupling of the first six bands, each  $H(t_j, m, \mathbf{q})$  is projected to its eigenstates  $v_j^i$ ,  $i \in [1, 6]$ , corresponding to the six lowest eigenvalues (the polarization angles are omitted in the following)

$$H_p^*(t_j, m, \mathbf{q}) = M^\dagger(t_j, m, \mathbf{q}) \cdot H(t_j, m, \mathbf{q}) \cdot M(t_j, m, \mathbf{q}), \quad (3.25)$$

where  $\cdot$  denotes matrix multiplication and the columns of the matrix  $M$  are defined as the eigenvectors  $v_j^i$ :

$$M(t_j, m, \mathbf{q}) = \left( \begin{pmatrix} \vdots \\ v_j^1 \\ \vdots \\ v_j^2 \\ \vdots \\ v_j^3 \\ \vdots \\ v_j^4 \\ \vdots \\ v_j^5 \\ \vdots \\ v_j^6 \\ \vdots \end{pmatrix} \begin{pmatrix} \vdots \\ v_j^1 \\ \vdots \\ v_j^2 \\ \vdots \\ v_j^3 \\ \vdots \\ v_j^4 \\ \vdots \\ v_j^5 \\ \vdots \\ v_j^6 \\ \vdots \end{pmatrix} \begin{pmatrix} \vdots \\ v_j^1 \\ \vdots \\ v_j^2 \\ \vdots \\ v_j^3 \\ \vdots \\ v_j^4 \\ \vdots \\ v_j^5 \\ \vdots \\ v_j^6 \\ \vdots \end{pmatrix} \begin{pmatrix} \vdots \\ v_j^1 \\ \vdots \\ v_j^2 \\ \vdots \\ v_j^3 \\ \vdots \\ v_j^4 \\ \vdots \\ v_j^5 \\ \vdots \\ v_j^6 \\ \vdots \end{pmatrix} \right). \quad (3.26)$$

For the calculation of  $U(T)$ , the resulting  $6 \times 6$ -matrices  $H_p^*$  need to be transferred to a common basis, which is chosen to consist of the eigenstates  $v_0^i$ ,  $i \in [1, 6]$ , which belong to the first six eigenvalues of  $H(t = 0, m = 0, \mathbf{q} = 0)$ . In principle, any basis could be used, as long as it is independent of  $\mathbf{q}$  and  $t$ . The vectors  $v_0^i$  comprise the columns of a matrix  $M_0$ , similar as in Eq. 3.26, and the basis change of the Hamiltonian is performed by:

$$H_p(t_j, m, \mathbf{q}) = B(t_j, m, \mathbf{q}) \cdot H_p^*(t_j, m, \mathbf{q}) \cdot B^{-1}(t_j, m, \mathbf{q}) \quad (3.27)$$

with

$$B(t_j, m, \mathbf{q}) = M_0^\dagger \cdot M(t_j, m, \mathbf{q}). \quad (3.28)$$

The time-evolution operator  $U$  over one driving period is obtained from the projected Hamiltonians  $H_p(t_j, m, \mathbf{q})$ , according to Eqs. 3.23 and 3.24:

$$U(m, f, \mathbf{q}) = \prod_j e^{-\frac{i}{\hbar} H_p(t_j, m, \mathbf{q}) \frac{\Delta t}{f}}, \quad (3.29)$$

with the driving frequency  $f = 1/T = \omega/(2\pi)$ . The effective Hamiltonian in units of  $\hbar\omega$  is given by

$$H_{\text{eff}}(m, f, \mathbf{q}) = \frac{i}{2\pi} \ln(U(m, f, \mathbf{q})). \quad (3.30)$$

The eigenvalues of the matrix  $H_{\text{eff}}$  are bound to the interval  $[-0.5, 0.5] \hbar\omega$ , denoting the first Floquet Brillouin zone (FBZ). Due to the periodic driving, the quasienergies are only defined up to multiples of  $\hbar\omega$ , and the lowest band of the effective Hamiltonian at some quasimomentum  $\mathbf{q}$  is not associated with the smallest eigenvalue any more. However, in the limit of  $m \rightarrow 0$ , the dispersion of the static lattice has to be recovered, where the eigenstates of the first six bands are given by the corresponding unit vectors, when being written in the basis  $v_0^i$ . To extract the two lowest bands of the effective Hamiltonian, the quasimomentum is scanned over the discrete grid spanning the first BZ, and the eigenstates of  $H_{\text{eff}}(\mathbf{q})$  are compared at neighboring points by calculating their overlap. The overlap between two states  $|u(\mathbf{q}_i)\rangle$  and  $|u(\mathbf{q}_j)\rangle$  is given by the fidelity  $\mathcal{F}_{ij}$ :

$$\mathcal{F}_{ij} = |\langle u(\mathbf{q}_i) | u(\mathbf{q}_j) \rangle|^2. \quad (3.31)$$

At the first point of the grid, the two lowest bands are defined as the eigenvalues which eigenstates have the maximal overlap with the first two unit vectors, being the corresponding eigenstates in the static lattice. Here, the first (second) Floquet band can either be associated with the first (second) or the second (first) band of the static lattice, depending on the quasimomentum and the modulation parameters, as discussed in the next section. Then, for the following quasimomenta, the eigenstates having maximal overlap with the states of the first and second Floquet band from the previous step are determined, defining the first and second band at the current step. In Fig. 3.6, the eigenvalues of  $H_{\text{eff}}$  for  $m = 0.2$ ,  $f = 16 \text{ kHz}$  and  $f = 6 \text{ kHz}$  are plotted along the high-symmetry line in quasimomentum space, whereas the two lowest bands  $\varepsilon_1$  and  $\varepsilon_2$  are depicted by the black and gray dots, switching between the different eigenvalues (denoted by  $Ej$ ).

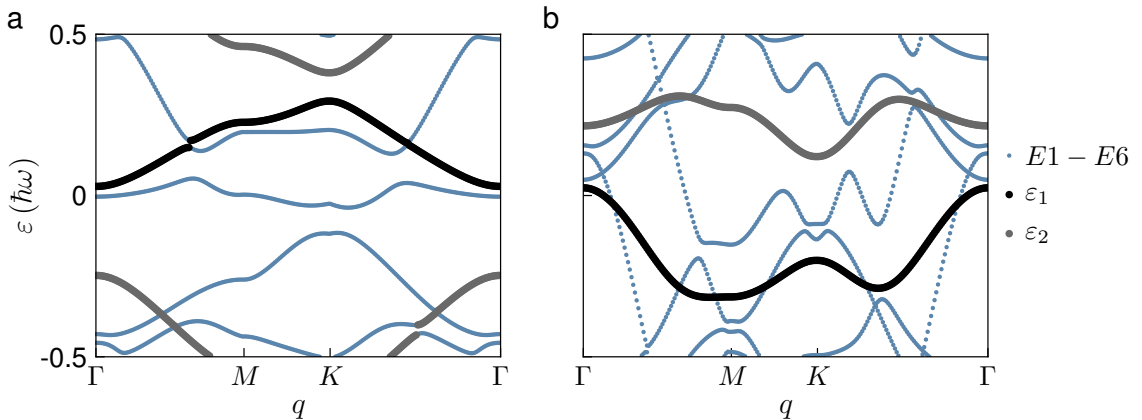


**Figure 3.6: Eigenvalues of  $H_{\text{eff}}$  and two lowest Floquet bands.** Eigenvalues and Floquet bands  $\varepsilon$  for different modulation parameters along the high-symmetry line in quasimomentum space for  $V_0 = 6 E_r$ . The eigenvalues (blue lines) are bound to the interval  $[-0.5, 0.5] \hbar\omega$ . The two lowest bands of  $H_{\text{eff}}$  (black and gray dots) are determined from the overlap between the eigenstates on neighboring points as described in the text. The association of each band with a certain eigenvalue depends on the quasimomentum and the modulation parameters. **a.**  $m = 0.2$  and  $f = 16 \text{ kHz}$ . Both Floquet bands exhibit jumps when passing an avoided crossing between the eigenvalues. **b.**  $m = 0.2$  and  $f = 6 \text{ kHz}$ .

The coupling of the  $s$ - and  $p$ -bands within the driving period leads to avoided crossings and to jumps in the Floquet bands when switching between the eigenvalues, which is also apparent in both bands in Fig. 3.6a. In the vicinity of the crossings, the overlap of the eigenstates with the first or second Floquet state from the previous step decreases and there can be several states having an overlap of similar magnitude. To avoid false attributions in these cases, the overlap with the unit vectors is used instead to determine the lowest bands, if the maximal overlap with the neighboring states drops below a certain threshold  $\nu$ . As the magnitude of these effects increases with the modulation frequency and amplitude, the value of this threshold depends on the modulation parameters. The optimal values of  $\nu$  are determined by checking the resulting Floquet bands in the first

BZ and along the high-symmetry line for each modulation amplitude and frequency. For small frequencies and amplitudes, the lowest bands are reliably obtained by using the overlap with the neighboring states everywhere, which corresponds to  $\nu = 0.5$ . When increasing the modulation parameters, values of  $\nu = 0.8$  to  $\nu = 0.9$  are normally used.

**Berry curvature** The Berry curvature of the first and second Floquet band is calculated from Eq. 3.18 using the corresponding eigenstates. From the definition of the Berry curvature  $\Omega$  it becomes apparent that regions in quasimomentum space with  $\Omega \neq 0$  are characterized by a state overlap between neighboring points being smaller than 1. On the other hand, in the vicinity of the avoided crossings described above, the overlap between neighboring eigenstates decreases, which leads to discontinuities in Berry curvature, consisting of a positive and a negative peak around that point. These peaks are not physical as they arise from the numerical calculation of the Berry curvature using Eq. 3.18, and the Chern number of the band is unchanged. Hence, to characterize the topological phases, the discontinuities could be neglected except for the case when they appear at high-symmetry points close to the phase transition, complicating the determination of the sign change. However, in the experiment, the Berry curvature is probed by Hall deflection measurements over an extended region in quasimomentum space (see Sec. 4.2.4). To be able to simulate the corresponding trajectories, a smooth distribution is needed. The discontinuities are detected by calculating the overlap between neighboring eigenstates in the complete BZ and finding the points where it becomes smaller than  $\sim 0.95$ , or where the first or second derivative of the Berry curvature diverges. These points are then removed from the distribution and replaced by cubic interpolation of the neighboring values. If a discontinuity appears at a quasimomentum where the Berry curvature is highly concentrated, e.g. at a Dirac point, the interpolation is not reliable any more. In these cases, the Berry curvature distribution of the other band needs to be multiplied by  $(-1)$  and can be used for the calculation of the deflections, since  $\Omega^-(\mathbf{q}) = -\Omega^+(\mathbf{q})$  for the two lowest bands.

The Berry curvature distributions of the Floquet bands are not perfectly sixfold rotational symmetric, as visible for example in Fig. 3.8. This arises mainly from the projection of the instantaneous Hamiltonian to its six lowest eigenstates. The quasienergy bands are fully symmetric and well described by the  $6 \times 6$  matrices used for the calculation. Since the effect of the asymmetry on the calculated transverse deflections is small compared to errorbars of the experimental data, the six-band calculation is sufficient. This is discussed in more detail in appendix A.

### 3.2.3 Phase diagram

The periodically modulated honeycomb lattice realizes different Floquet topological phases, depending on the modulation parameters and the sublattice energy offset. In this section, the phase diagram in the system without a sublattice offset is discussed, exhibiting inversion symmetry. In the parameter regime relevant for the experiments, three different topological phases occur, which are depicted in Fig. 3.7: ① A Haldane-like

phase with  $\mathcal{C}^- = 1$  in the lowest band and chiral edge modes in the quasienergy gap  $g^0$ , an anomalous Floquet phase ②, with  $\mathcal{C}^- = 0$  but chiral edge modes in both gaps, and a third phase ③ having  $\mathcal{C}^- = -1$  and chiral edge modes only in the gap  $g^\pi$  between FBZs. The transitions between the topological phases as well as the quasienergy dispersion and Berry curvature of the two lowest bands will be discussed in the following and are summarized in Fig. 3.8 for  $m = 0.2$  and different modulation frequencies.

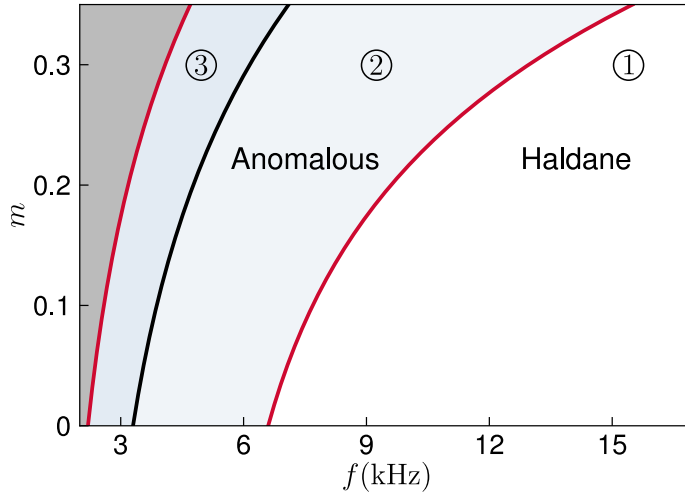


Figure 3.7: **Phase diagram of the modulated lattice.** Topological phases as a function of the modulation frequency  $f$  and modulation amplitude  $m$  for  $V_0 = 6 E_r$  in the parameter regime relevant for the experiment. The phase boundaries are determined by the quasienergy gap closings at  $\mathbf{q} = \Gamma$ , whereas the red lines denote a closing at  $g^\pi$  between FBZs and the black line a closing at  $g^0$  within a single FBZ. The gray shaded area depicts further topological regimes, which are not investigated in this work.

For large modulation frequencies, the system is in the Haldane regime, where quasienergy gaps have opened between the two lowest bands at both Dirac points, giving rise to positive Berry curvature in the lowest band, concentrated around  $K$  and  $K'$  (first row in Fig. 3.8). As already described in Sec. 2.1, the Chern number, given by the integral of the Berry curvature over the 2D BZ, equals  $\pm 1$  in the first (second) band. If the chirality of the modulation is switched, the Berry curvature distribution would be inverted, resulting in negative values at the Dirac points. The Haldane model can also be obtained analytically from a two-band tight-binding description of the modulated lattice in the limit of high modulation frequencies, which is shown in Sec. 3.3.4.

Increasing the modulation frequency reduces the gap at the Dirac points, which remains open though, and the bands do not touch anywhere else, meaning that the Haldane regime extends to the limit  $\omega \rightarrow \infty$ . The Floquet copies of the two lowest bands are spaced by  $\hbar\omega$  and hence, the gap between FBZs diverges in this limit, which means that no chiral edge mode can exist there, so  $W^\pi = 0$ . Relating the Chern numbers and

winding numbers as described in Sec. 2.3 by

$$\mathcal{C}^\mp = \pm(W^0 - W^\pi), \quad (3.32)$$

yields  $W^0 = 1$ , describing the chiral edge modes in the gap within the FBZ, that has opened at the Dirac points. In general, the size of the quasienergy gap at  $K$  and  $K'$  decreases for smaller modulation amplitudes, connecting the Haldane phase to the static lattice for  $m \rightarrow 0$ .

When the modulation frequency is decreased, the gap  $g^\pi$  between the Floquet copies of the bands is reduced. The transition to the anomalous phase occurs when  $\hbar\omega$  equals the effective width of the two lowest bands and the gap  $g^\pi$  closes at  $\mathbf{q} = \Gamma$ . This means that the first band and the lower Floquet copy of the second band touch, as depicted in the second row of Fig. 3.8 where  $f = 10\text{ kHz}$ . For a constant modulation frequency, the transition is reached by increasing the modulation amplitude, which increases the effective bandwidth until it equals  $\hbar\omega$ . Shortly before the transition, positive Berry curvature arises around  $\Gamma$  and is concentrated to a sharp peak when the transition is reached. At the band touching point, the sign of the peak changes from positive to negative, so it is characterized by a topological charge of  $Q^\pi = +1$ . The negative Berry curvature at  $\Gamma$  then spreads out in quasimomentum space in a ring-like shape, following the nearly degenerate minimum in the lowest band that is created by the hybridization with the Floquet copy of the second band (third row in Fig. 3.8 with  $f = 7\text{ kHz}$ ). The gap at the Dirac points remains open, so the winding number  $W^0 = 1$  is not changed and corresponding Berry curvature is still positive. Together with the negative Berry curvature around  $\Gamma$ , this results in  $\mathcal{C}^\mp = 0$ . The band touching at  $\Gamma$  creates a chiral edge mode in the  $g^\pi$  gap and  $W^\pi = 1$ , following from the sign change of the Berry curvature. In a setting with boundaries, there are now edge modes present in both quasienergy gaps  $g^0$  and  $g^\pi$ , constituting an anomalous Floquet phase, as introduced in chapter 2.

Reducing the modulation frequency further, leads to an increase of the quasienergy gaps within the FBZs at  $K$  and  $K'$  and the positive Berry curvature spreads out accordingly, similar to the ring minimum in the lowest band and the negative Berry curvature around  $\Gamma$ . Due to the modulation, the bands are deformed and touch again at  $\Gamma$ , now within the FBZ, when the modulation frequency equals half the effective bandwidth, as shown for  $f = 4.83\text{ kHz}$  in Fig. 3.8. Again, positive Berry curvature accumulates at  $\Gamma$  shortly before the gap closing occurs, which then turns into a negative peak and gives rise to a negative topological charge  $Q^0 = -1$ . Hence, the edge modes in the gap  $g^0$  are annihilated and  $W^0 = 0$ , while  $W^\pi = 1$  remains unchanged. The negative Berry curvature at  $\Gamma$  again spreads out in a ring-shape, now corresponding to a maximum in the lowest band (last row of Fig. 3.8) and  $\mathcal{C}^\mp = \mp 1$ . This regime looks similar to the Haldane phase, but hosts chiral edge modes in the gap  $g^\pi$  between FBZs, which does not exist in a static model. However, the system can be mapped to a Haldane-type model in a static setting by a gauge transformation.

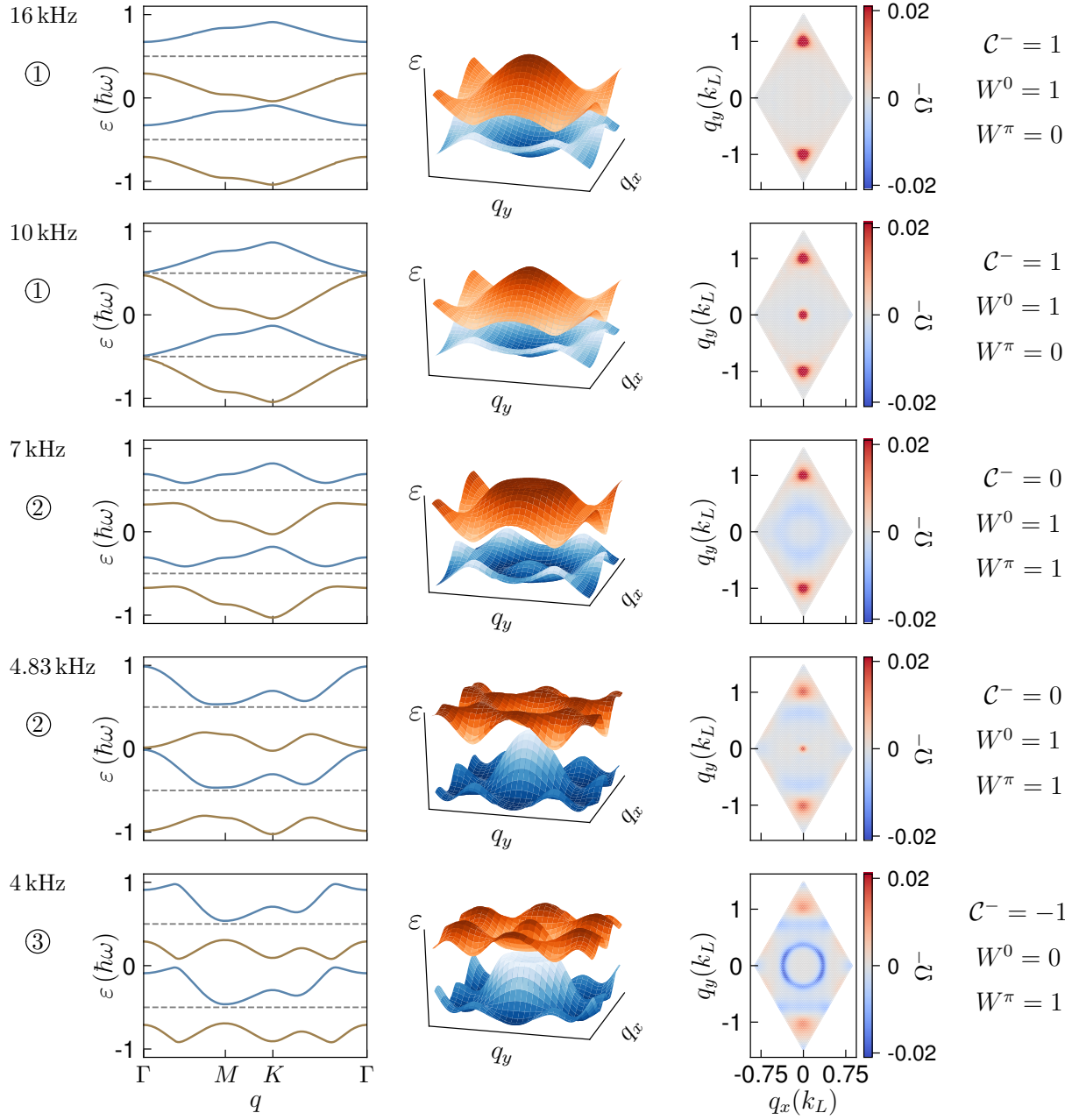
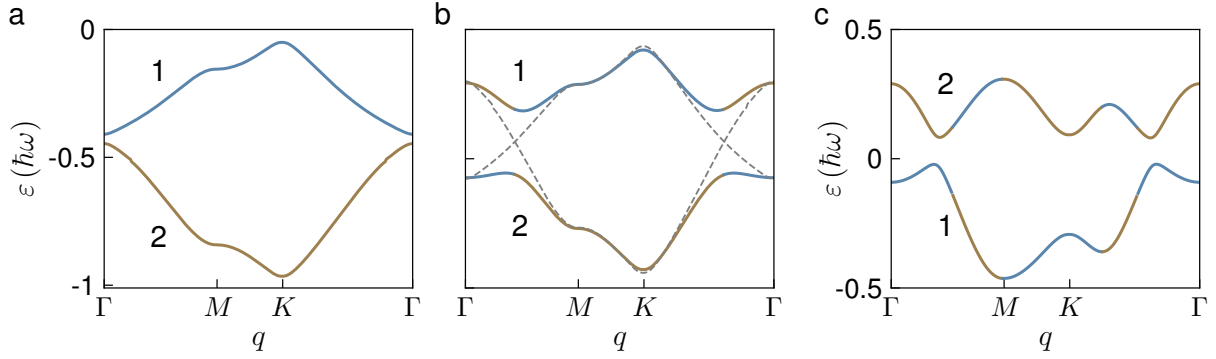


Figure 3.8: **Quasienergy bands and Berry curvature in the different topological phases.** First column: The two lowest quasienergy bands along the high-symmetry line  $\Gamma$ - $M$ - $K$ - $\Gamma$  in the extended zone scheme. Second column: Quasienergy bands as a function of the 2D quasimomentum in the reduced zone scheme. Third column: Berry curvature of the lowest band in the first BZ. The bands and Berry curvature are calculated for  $V_0 = 6 E_r$ ,  $m = 0.2$  and modulation frequencies  $f = (16, 10, 7, 4.83, 4)$  kHz, scanning the Haldane, anomalous and third phase. The Chern and winding numbers are noted on the right of each row.

For small modulation frequencies  $f \lesssim 2$  kHz or larger amplitudes  $m \gtrsim 0.3$ , further topological phases occur, which are not discussed in this work, as these parameter regimes are difficult to characterize in the experiment, which is described in Sec. 5.1. The third regime ends with a closing of the  $g^\pi$  gap at  $\Gamma$ , as depicted by the second red line in Fig. 3.7, which is followed by another closing of the  $g^\pi$  gap, now at the Dirac points.



**Figure 3.9: Connection of the quasienergy bands to the static lattice.** **a.** Floquet bands in the Haldane phase shortly before the first phase transition. **b.** The quasienergy bands in the anomalous phase emerge from shifting the former bands into each other (gray dashed lines) and opening gaps at the crossing points. Hence, the lowest band consists of the former second band at quasimomenta around  $\Gamma$ , where the bands have already hybridized, which is depicted by the brown color. These parts are connected to the second band of the static lattice in the limit of  $m \rightarrow 0$ . **c.** In the third phase, the bands have again touched at  $\Gamma$ , now at quasienergy 0, and the first band is again connected to the first band of the static lattice around  $\Gamma$ , indicated by the blue color. Due to the band dispersion, the level of band mixing depends on  $\mathbf{q}$ , changing the ‘character’ of the bands within the first BZ, as illustrated by the color change along the lines. The quasienergy bands are calculated for  $m = 0.2$  and frequencies  $f = (10, 7, 4)$  kHz from left to right. The numbers denote the first and second band in the respective phase.

The lowest quasienergy band in the anomalous phase arises from mixing of the first band in the Haldane phase with the lower Floquet copy of the second band, which is shifted by  $\hbar\omega$ . At the intersection points, the old bands hybridize and gaps open, which increase in magnitude with the modulation amplitude. Lowering the modulation frequency effectively moves the two bands further into each other, shifting the intersection points away from  $\Gamma$ . In the Haldane phase, the first band has positive curvature around  $\Gamma$ , whereas the curvature of the second band is negative there, which leads to a minimum and maximum in the first and second band in the anomalous phase at the avoided crossings. This is illustrated in Fig. 3.9a and b, where the formation of the quasienergy bands in the anomalous phase from the shifted bands before the transition is illustrated for  $m = 0.2$ . If the modulation amplitude is lowered, the size of the gaps at the avoided crossings decreases. For modulation frequencies  $f \in [3.3, 6.6]$  kHz, the limit of  $m \rightarrow 0$  corresponds to the static lattice with its bands being shifted by  $\hbar\omega$  and crossing each other. Hence, in the anomalous phase, the part of the lowest band around  $\Gamma$ , which

originates from the former second band, is adiabatically connected to the second band of the static lattice in the limit of  $m \rightarrow 0$ . This is illustrated by the changing colors of the quasienergy bands in the anomalous phase Fig. 3.9b.

At the second phase transition, the bands touch again at  $\Gamma$ , but now in the gap  $g^0$ . Similar to the anomalous phase, the bands after the transition can be viewed as the former bands being shifted into each other with gaps opened at the intersection points. Hence, in the third phase, the first band is again connected to the first band of the static lattice around  $\Gamma$  (blue color in Fig. 3.9). These considerations are of practical interest, as the connection to the bands of static lattice is used in the experiments to load the atoms into the second band of the modulated lattice, by starting with  $f \in [3.3, 6.6]$  kHz at  $m = 0$  and ramping up the modulation amplitude, which is discussed in Sec. 5.3.

### 3.2.4 Topological phases with a sublattice offset

In the experiments presented in this work, the topological regimes of the honeycomb lattice without a sublattice energy offset are characterized, which have been described in the previous section. Combining the lattice modulation with a time-independent sublattice offset  $\Delta$  results in additional topological phases, including a regime with a Chern number of  $\mathcal{C}^\mp = \mp 2$ , as depicted in Fig. 3.10. In general, the energy offset leads to the opening of a topologically trivial energy gap at the Dirac points with Berry curvature of opposite sign at the  $K$  and  $K'$  point. This corresponds to a mass term  $\propto \pm m\hat{\sigma}_z$  in the two-band tight-binding Hamiltonian of the honeycomb lattice, having equal sign at both points (see Sec. 2.1.3).

On the contrary, the gap that opens at the Dirac points due to the lattice modulation results in a Berry curvature of the same sign, representing mass terms of opposite signs at  $K$  and  $K'$ , as described in the context of the Haldane model. Since the Chern number in the lowest band equals  $+1$  in the Haldane phase, the lattice modulation corresponds to the case of positive complex hopping  $\sin(\phi) > 0$  in Eq. 2.23, giving  $m > 0$  at  $K$ . The size of the topological gap increases with the modulation amplitude and the size of the trivial gap with the sublattice energy offset, which depends on the polarization angle  $\theta$  of the lattice beams. In the following,  $\theta > 0$  corresponding to  $\Delta > 0$ , which results in positive Berry curvature at the  $K$ -point and negative Berry curvature at the  $K'$ -point. Hence, adding a sublattice offset to the modulated lattice increases the size of the gap at  $K$ , whereas the gap at  $K'$  is decreased for larger values of  $\theta$ , until it closes within the FBZ, resulting in a sign change of the Berry curvature from positive to negative values. Being in the Haldane regime, the system undergoes a transition to a topologically trivial phase, where the edge mode in the gap  $g^0$  is annihilated, as  $\Delta W^0 = \text{sgn}(\Delta\Omega^-) = -1$  at  $K'$ . The phase boundary, given by the closing of  $g^0$  at  $K'$ , is depicted by the blue line in Fig. 3.10a, where the phase diagram is shown as a function of the modulation frequency and amplitude for  $\theta = 0.1$  rad. The other transition lines, defined by the gap closings at  $\Gamma$ , are similar as for  $\theta = 0$ , but slightly shifted to higher modulation frequencies, since the effective bandwidth of the two lowest bands is increased by the sublattice offset. As the polarization angle is the relevant quantity for the experiments, the phase diagram

is presented in terms of  $\theta$  rather than in terms of the sublattice energy offset  $\Delta$  (see Fig. 3.12b for the conversion from  $\theta$  to  $\Delta$ ).

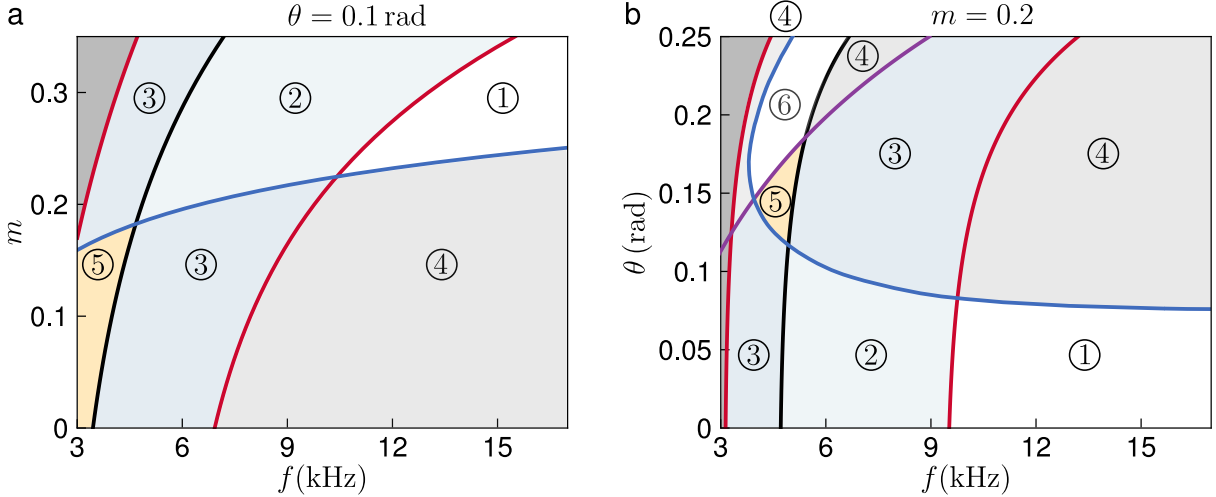


**Figure 3.10: Topological phases with a sublattice energy offset for  $V_0 = 6 E_r$ .** **a.** Phase diagram as a function of the modulation frequency and amplitude for  $\theta = 0.1 \text{ rad}$ . The red and black lines denote gap closings of the  $\pi$ - and 0-gap at  $\Gamma$  and the blue line the closing of the 0-gap at  $K'$ . For large modulation amplitudes, the quasienergy gap at  $K'$  induced by the modulation is larger than the gap that would arise from the sublattice offset and the system exhibits the same topological phases as for  $\theta = 0$ . If the modulation amplitude is small, the sublattice gap at  $K'$  has not closed and a trivial phase ④ is realized for larger modulation frequencies followed by phases ③ and ⑤ with  $\mathcal{C}^- = -1$  and  $\mathcal{C}^- = -2$ . **b.** Phase diagram as a function of the modulation frequency and the polarization angle  $\theta$  for  $m = 0.2$ . The regimes described in **a** are obtained in reversed order and additional phases occur due to the closing of the  $\pi$ -gap at  $K$ , which is depicted by the purple line. This gives rise to two further topologically trivial regions ④ at large  $\theta$ , and a Haldane-like phase with  $\mathcal{C}^- = -1$  denoted by ⑥.

Starting from the trivial phase ④ with  $\mathcal{C}^- = 0$  and  $W^0 = 0 = W^\pi$  and reducing the modulation frequency, the bands touch in the  $\pi$ -gap at  $\Gamma$ , creating negative Berry curvature there, which brings the system into the third topological regime with  $\mathcal{C}^- = -1$  and  $W^\pi = 1$ , again denoted by ③. For smaller modulation frequencies, the second touching at  $\Gamma$  in the 0-gap results in a phase with  $\mathcal{C}^- = -2$ , again adding a negative Berry curvature peak. Now,  $W^0 = -1$  and  $W^\pi = 1$ , which means that a pair of chiral edge modes is created in the gap  $g^0$ , but with opposite sign as the edge modes at  $g^\pi$ . This phase ⑤ is expected to have similar properties as the Haldane like phases ①, ③ and ⑥, regarding the localization of the bulk states in the presence of disorder: There is no winding of the edge modes around the complete FBZ, as the winding numbers of  $g^0$  and  $g^\pi$  have opposite sign, and the non-zero Berry curvature necessarily results in delocalized bulk states, as discussed in Sec. 2.3. If the modulation amplitude is increased, the energy gap at  $K'$  decreases until it closes and reopens, which leads then to the same phases as for

$\theta = 0$ , including the anomalous Floquet phase for intermediate modulation frequencies.

In Fig. 3.10b, the phase diagram is shown as a function of the modulation frequency and the polarization angle  $\theta$  for a fixed modulation amplitude of  $m = 0.2$ . Here, the original phases ①-③ appear in the lower part of the diagram, as they are realized when the sublattice offset is small compared to the modulation amplitude. Increasing  $\theta$  leads to the closing of  $g^0$  at  $K'$  (blue line) and the same phases as discussed above. But in addition, as the bands are deformed by the sublattice offset, the  $\pi$ -gap at  $K$  closes for larger polarization angles, which is illustrated by the purple line. Depending on the modulation frequency, this happens before the second and third gap closings at  $\Gamma$  (black and second red line), resulting in a trivial phase ④ and another Haldane-like phase ⑥ with  $C^- = -1$  and  $W^0 = -1$ ,  $W^\pi = 0$  at large values of  $\theta$ . In the phase diagrams of Fig. 3.10a and Fig. 3.7, the closing of  $g^\pi$  at  $K$  takes place at smaller modulation frequencies lying outside the parameter range accessible in the experiments (dark gray shaded areas).

The quasienergy bands and Berry curvature in the lowest band for the different phases ③-⑥ are presented in Fig. 3.11 for  $m = 0.2$ , first following a line at  $\theta = 0.15$ , which passes the regimes of ④, ③, ⑤ and ④ with  $f = (14, 8, 4.5, 3.7)$  kHz, and in addition at  $\theta = 0.2$  and  $f = 5$  kHz representing phase ⑥. The quasienergy bands (first column) are evaluated along the two high-symmetry paths  $\Gamma$ - $M$ - $K$ - $\Gamma$  (solid lines) and  $\Gamma$ - $M$ - $K'$ - $\Gamma$  (dashed lines) and are also shown as 3d-plots in the second column. In the trivial phase, the gap at zero quasienergy is larger at  $K$  than at  $K'$ , as described above, resulting in the positive Berry curvature at  $K$  being spread out further as the negative contribution from  $K'$ . After the transition to phase ③, where  $\Delta W^\pi = 1$ , the negative Berry curvature at  $\Gamma$  again spreads out, but now, due to the broken inversion symmetry, in a triangular shape along the directions  $\Gamma$ - $K$  (second row in Fig. 3.11). Originally, the lowest band exhibits two maxima at  $K$  and  $K'$ . Reducing the modulation frequency leads to a flattening of the maximum at  $K$ , which can already be observed for  $f = 8$  kHz, resulting in a complete spread of the corresponding positive Berry curvature. In contrast, the maximum at  $K'$  becomes more pronounced and the negative Berry curvature is contracted further, as the quasienergy gap here is reduced until it closes at  $\theta = 0.15$  and  $f \approx 4$  kHz.

The second gap closing at  $\Gamma$ , now at zero quasienergy, results again in a negative Berry curvature peak, which also spreads in a triangular pattern, now along the directions  $\Gamma$ - $K'$ , as visible in the third row of Fig. 3.11 for  $f = 4.5$  kHz. The negative Berry curvature from the previous transition, moving along with minima in the lowest band, has accumulated at the  $K$ -points, where the lowest band now exhibits a minimum. The additional Berry curvature from the second transition is located at maxima in the lowest band, similar as in phase ③ for  $\theta = 0$ . These two triangular parts together with the opposite contributions from the Dirac points in the trivial phase constitute  $C^- = -2$  with  $W^0 = -1$ ,  $W^\pi = 1$ . For  $f = 3.7$  kHz, two gap closings have occurred at both Dirac points. At  $K$ , the minimum of the lowest band touches the maximum in the lower copy of the upper band, so the gap is closing at energy  $\pi$ . Shortly before this transition, a sharp negative peak of Berry curvature arises at  $K$ , which then turns to a positive peak in addition to the negative contributions from  $\Gamma$  that have accumulated there. Hence,  $\Delta W^\pi = -\text{sgn}(\Delta\Omega^-) = -1$ , so the edge mode in the gap  $g^\pi$  is annihilated.

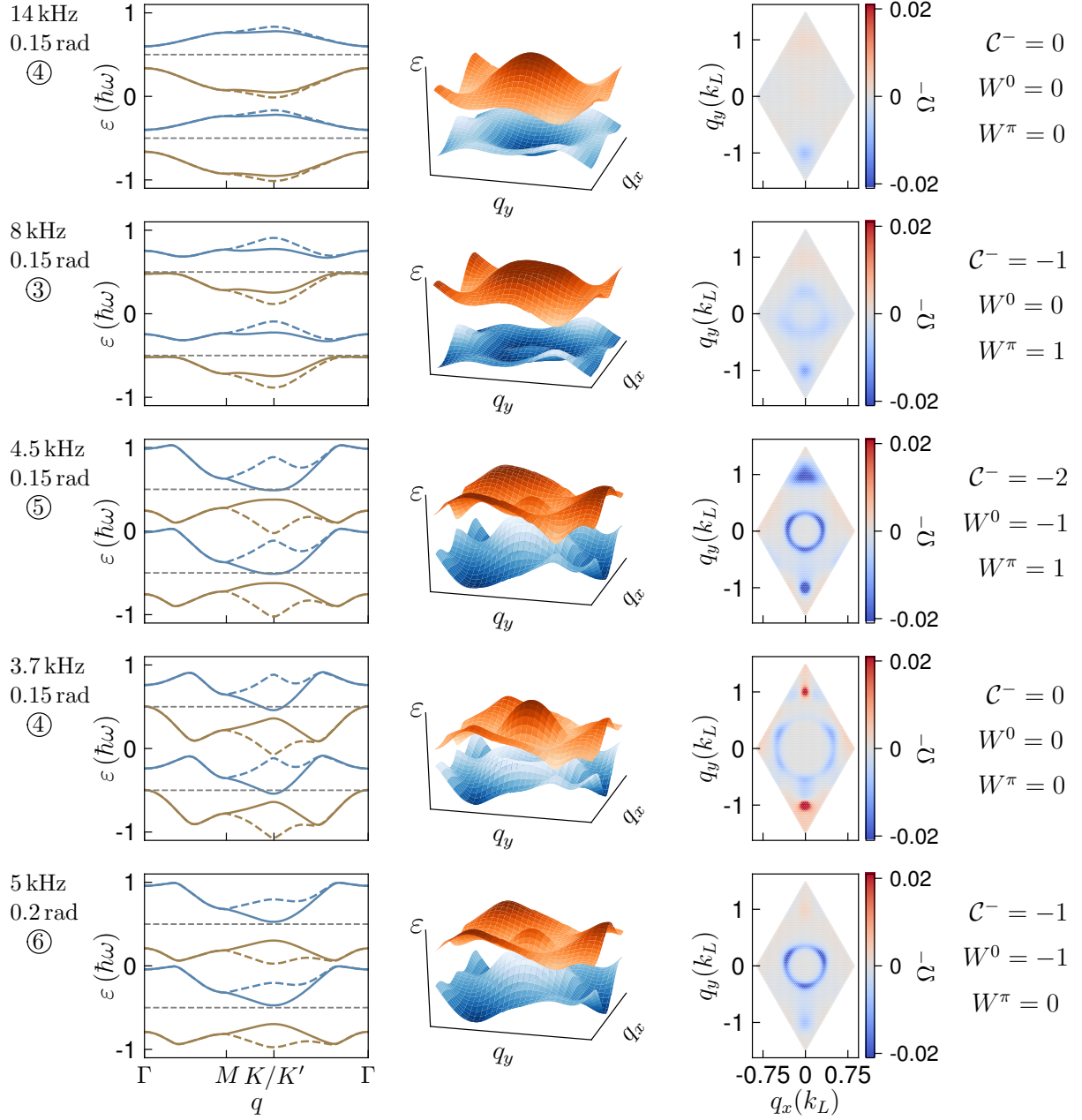


**Figure 3.11: Quasienergy bands and Berry curvature with a sublattice offset.** First column: The two lowest quasienergy bands along the high-symmetry lines  $\Gamma$ - $M$ - $K$ - $\Gamma$  (solid lines) and  $\Gamma$ - $M$ - $K'$ - $\Gamma$  (dashed lines) in the extended zone scheme. Second column: Quasienergy bands as a function of the 2D quasimomentum, plotted in the reduced zone scheme. Third column: Berry curvature in the first BZ. The bands and Berry curvature are calculated for  $V_0 = 6 E_r$ ,  $m = 0.2$  and  $f = (14, 8, 4.5, 3.7, 5)$  kHz with  $\theta = (0.15, 0.2)$  rad, scanning across the additional phases depicted in Fig. 3.10b. The Chern and winding numbers are noted on the right of each row.

At  $K'$ , the maximum of the lowest band touches in the minimum of the second band within the FBZ. Here, the original negative Berry curvature has completely collapsed along with the decreasing of the gap, and is turned into a positive peak, removing the edge mode in the zero gap since  $\Delta W^0 = \text{sgn}(\Delta\Omega^-) = 1$  which leads to  $W^0 = 0$ ,  $W^\pi = 0$ .

The positive and negative Berry curvature at the Dirac points in the trivial phase can be described by having a weight of 1/2, in contrast to the new contributions arising from the gap closings at  $\Gamma$  and at  $K$ , which have a weight of 1. As the Chern number in the Haldane phase is equal to 1, each of the two positive peaks at  $K$  and  $K'$  carries a weight of 1/2 and at the transition to the trivial phase, the weight of the peak at  $K'$  turns from +1/2 to -1/2. Hence, the transition at  $K'$  is qualitatively different from the other transitions encountered here, as a Berry curvature peak being already present before concentrates and changes sign, whereas in the other cases, a new peak appears in addition to the other contributions. Accordingly, in the trivial phase at  $f = 3.7$  kHz, there are now two positive parts with weight 1/2, and the new positive peak at  $K$  with weight 1, which indeed sum up to  $\mathcal{C}^- = 0$  together with the two negative contributions of weight 1 from the transitions at  $\Gamma$ . In the Haldane-like phase ⑥, depicted in the last row of Fig. 3.11, the gap  $g^\pi$  at  $K$  has already closed, but  $g^0$  at  $K'$  remains open. Hence,  $W^\pi = 0$  but  $W^0 = -1$ , leading to  $\mathcal{C}^- = -1$ , constituted by the two negative triangles of Berry curvature originating from  $\Gamma$  and the positive Berry curvature from  $K$ , in addition to the two contributions from the Dirac points in the trivial phase. For  $f = 5$  kHz and  $\theta = 0.2$  rad, as shown in the plot, the Berry curvature at  $K$ , as well as the accumulated parts from the first gap closing at  $\Gamma$  are already quite distributed, whereas the triangle from the second transition at  $\Gamma$  is clearly visible. For large values of  $\theta$  the gap closing at  $K$  occurs at larger modulation frequencies than the second gap closing at  $\Gamma$ , giving rise to a trivial phase again, since the edge mode at energy  $\pi$ , being present in phase ③, is annihilated as  $\Delta W^\pi = -1$ .

### 3.3 Tight-binding description of the modulated honeycomb lattice

In the previous section, the numerical calculation of the effective Hamiltonian in the periodically modulated honeycomb lattice has been described. The resulting quasienergy bands and Berry curvature distributions are used to derive the energy gaps and transverse deflections, which can be directly compared to experimental data. As presented in chapter 5, the theoretical values based on the numerical six-band calculation are in general in very good quantitative agreement with the measured data over the full parameter range. The bulk properties of the modulated lattice are well described by this model in all three topological regimes considered in this work. Nevertheless, in view of probing the localization properties of the system in the anomalous Floquet regime, a direct measurement of the chiral edge modes is desirable, as further explicated in chapter 7. In this regard, the quasienergy dispersion of the edge modes needs to be derived, determining the group velocity of the atoms at the edge, which can be directly accessed in experiments.

Moreover, the influence of the harmonic trapping potential on the edge modes can be studied.

So far, a sensible and numerically feasible model of a finite, or semi-finite lattice system is usually composed of a tight-binding description. In this way, the specific shape of the edge in real space can be accounted for. To provide quantitative information about the edge mode dispersion, first, a tight-binding description of the infinite, modulated honeycomb lattice is introduced, and based on this, the corresponding model on a semi-finite geometry will be discussed in the next section.

The current section starts with a two-band tight-binding model [3.3.1], which aims to describe the instantaneous Hamiltonian at every time step during one modulation period, to finally calculate an effective Hamiltonian by integration, similar to the numerical calculation in the previous section. In this context, different methods are discussed to obtain the optimal tight-binding parameters, including the use of an eight-band model [3.3.2]. The quasienergy bands in the Haldane phase can directly be fitted with the model from Sec. 2.1.3, providing an adequate description in this regime [3.3.3]. Finally, the direct mapping between the modulated lattice and the Haldane model is derived analytically in the limit of high modulation frequencies [3.3.4].

### 3.3.1 Two-band tight-binding model

The general form of a tight-binding model for the honeycomb lattice has been introduced in Sec. 2.1.3. The system is described in the basis of wavefunctions localized on the A and B sublattice sites. If the two lowest bands are considered, there is only one type of orbital at each site, being approximately spherically symmetric and thus called *s*-orbital. Similar as in the Haldane model, nearest neighbor (NN) and next-nearest neighbor (NNN) hopping is taken into account, whereas all tunneling amplitudes are assumed to be real-valued here. To calculate the effective Hamiltonian, the system needs to be described at every time step within the modulation period, hence, a tight-binding version of the imbalanced honeycomb lattice is needed, revealing  $\hat{H}(t)$  for the two lowest bands. Due to the intensity imbalance, the location of the lattice sites changes periodically in time, as depicted in Fig. 3.5 and it is not possible to find a co-moving reference frame, in contrast to the case of lattice shaking, where the whole potential is moved (see chapter 6). However, there is a reference frame, where all A-sites or all B-sites are at rest and the sites of the respective other sublattice move along trajectories in real space having the shape of rounded triangles, similar to a Reuleaux-triangle. In fact, the vectors  $\delta_j$  connecting nearest neighbors (see Fig. 2.1b), namely A- and B-sites, become time-dependent, whereas the lattice vectors  $\mathbf{a}_j$ , which connect next-nearest neighbors, remain constant.

In the imbalanced honeycomb lattice, the NN and NNN tunneling amplitudes depend on the bond direction and on time, whereas the bonds themselves are additionally changing in the former case. The two-band tight-binding Hamiltonian of the imbalanced lattice

at a time  $t$  during the driving period can be written as

$$\hat{H}(t) = \sum_{\mathbf{r}_A} \left[ \sum_{j=1}^3 J_j(t) (\hat{a}_{\mathbf{r}_A}^\dagger \hat{a}_{\mathbf{r}_A + \delta_j(t)} + h.c.) + \frac{\Delta}{2} (\hat{a}_{\mathbf{r}_A}^\dagger \hat{a}_{\mathbf{r}_A} - \hat{a}_{\mathbf{r}_A + \delta_1}^\dagger \hat{a}_{\mathbf{r}_A + \delta_1}) \right. \\ \left. + \sum_{j=1}^3 (\tilde{J}_j(t) \hat{a}_{\mathbf{r}_A}^\dagger \hat{a}_{\mathbf{r}_A + \mathbf{a}_j} + h.c.) + \sum_{j=1}^3 (\tilde{J}_j(t) \hat{a}_{\mathbf{r}_A + \delta_1}^\dagger \hat{a}_{\mathbf{r}_A + \delta_1 - \mathbf{a}_j} + h.c.) \right], \quad (3.33)$$

where the sublattice offset  $\Delta$  is time-independent and the locations of the B-sites have been expressed in terms of the A-sites. Performing a Fourier transform similar as in Sec. 2.1.3,

$$\hat{a}_{\mathbf{r}_A}^\dagger = \sum_{\mathbf{q}} e^{-i\mathbf{q}\cdot\mathbf{r}_A} \hat{a}_{\mathbf{q}}^\dagger \quad \hat{a}_{\mathbf{r}_A + \delta_j}^\dagger = \sum_{\mathbf{q}} e^{-i\mathbf{q}\cdot(\mathbf{r}_A + \delta_j)} \hat{b}_{\mathbf{q}}^\dagger, \quad (3.34)$$

yields the Hamiltonian in quasimomentum space:

$$\hat{H}(t) = \sum_{\mathbf{q}} \left[ \sum_{j=1}^3 J_j(t) \left( e^{i\mathbf{q}\cdot\delta_j(t)} \hat{a}_{\mathbf{q}}^\dagger \hat{b}_{\mathbf{q}} + e^{-i\mathbf{q}\cdot\delta_j(t)} \hat{b}_{\mathbf{q}}^\dagger \hat{a}_{\mathbf{q}} \right) \right. \\ \left. + \sum_{j=1}^3 \tilde{J}_j(t) 2 \cos(\mathbf{q} \cdot \mathbf{a}_j) (\hat{a}_{\mathbf{q}}^\dagger \hat{a}_{\mathbf{q}} + \hat{b}_{\mathbf{q}}^\dagger \hat{b}_{\mathbf{q}}) + \frac{\Delta}{2} (\hat{a}_{\mathbf{q}}^\dagger \hat{a}_{\mathbf{q}} - \hat{b}_{\mathbf{q}}^\dagger \hat{b}_{\mathbf{q}}) \right]. \quad (3.35)$$

The Schrödinger equation  $\hat{H}(t)|\psi(t)\rangle = E(t)|\psi(t)\rangle$  can then be solved for every quasimomentum and time by making the ansatz

$$|\psi(\mathbf{q}, t)\rangle = c_A(\mathbf{q}, t)|\phi_A^s(\mathbf{q})\rangle + c_B(\mathbf{q}, t)|\phi_B^s(\mathbf{q})\rangle = c_A(\mathbf{q}, t)\hat{a}_{\mathbf{q}}^\dagger|0\rangle + c_B(\mathbf{q}, t)\hat{b}_{\mathbf{q}}^\dagger|0\rangle, \quad (3.36)$$

where the superscript  $s$  illustrates the assumption of spherically symmetric  $s$ -orbitals. Using the bosonic commutation relations

$$[\hat{a}_{\mathbf{q}}, \hat{a}_{\mathbf{q}'}^\dagger] = \delta_{\mathbf{q}, \mathbf{q}'}, \quad [\hat{b}_{\mathbf{q}}, \hat{b}_{\mathbf{q}'}^\dagger] = \delta_{\mathbf{q}, \mathbf{q}'}, \quad (3.37)$$

with all other commutators being equal to zero, leads to the eigenvalue equation for the coefficients  $c_A$  and  $c_B$  with the Hamiltonian being represented by a  $2 \times 2$  matrix for each  $\mathbf{q}$  and  $t$ :

$$\hat{H}_{\mathbf{q}}(t) = \begin{pmatrix} \frac{\Delta}{2} + \sum_{j=1}^3 \tilde{J}_j(t) 2 \cos(\mathbf{q} \cdot \mathbf{a}_j) & \sum_{j=1}^3 J_j(t) e^{i\mathbf{q}\cdot\delta_j(t)} \\ \sum_{j=1}^3 J_j(t) e^{-i\mathbf{q}\cdot\delta_j(t)} & -\frac{\Delta}{2} + \sum_{j=1}^3 \tilde{J}_j(t) 2 \cos(\mathbf{q} \cdot \mathbf{a}_j) \end{pmatrix} \quad (3.38)$$

**Fitting the tight binding parameters** The time-dependent connection vectors  $\delta_j$  are obtained by numerically evaluating the minima of the lattice potential defined in Eq. 3.5 within one unit cell at every time  $t$ . The length and angle of each vector varies

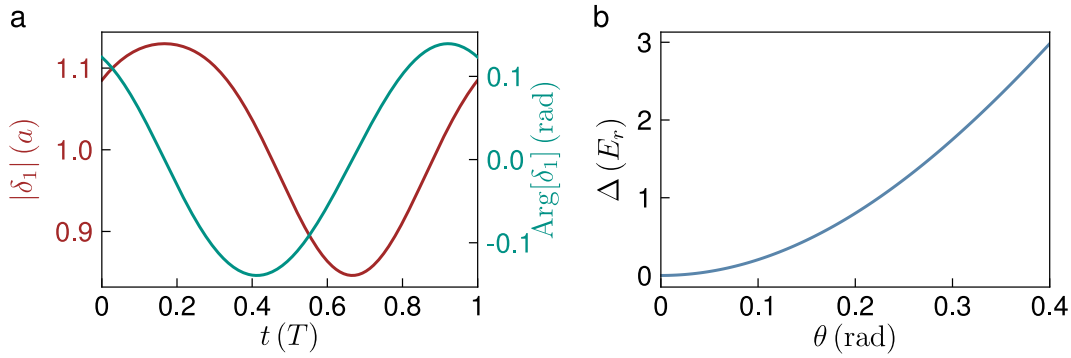


**Figure 3.12: Time-dependence of the connection vector  $\delta_1$  and sublattice offset in the tight-binding model for  $V_0 = 6 E_r$ .** **a.** Length  $|\delta_1|$  and angle  $\text{Arg}[\delta_1] = \arctan(\delta_1^y/\delta_1^x)$  of the vector connecting A- and B-sites along bond direction 1, being parallel to the  $x$ -direction in the symmetric lattice, during one period of the lattice modulation for  $m = 0.25$ . The connection vectors are derived by evaluating the minima of the imbalanced lattice potential at every time step  $t$ . The length and angle of  $\delta_2$  and  $\delta_3$  vary similarly but are phase shifted by  $2\pi/3$  and  $4\pi/3$ . **b.** Sublattice energy offset  $\Delta$  as a function of the polarization angle  $\theta$  obtained from fitting the tight-binding model to the bands of the symmetric, static lattice. The relation can be described by a polynomial as defined in Eq. 3.39.

periodically in time, as depicted in Fig. 3.12a for  $\delta_1$ , whereas the curves for the other two vectors are similar, but phase shifted by  $2\pi/3$  and  $4\pi/3$ .

The magnitude of the oscillations increases with the modulation amplitude  $m$  and the connection vectors are derived for each value of  $m$  separately. The sublattice offset  $\Delta$  is time-independent and not modified by the intensity imbalance. Its relation to the polarization angle  $\theta$  of the lattice beams is derived by fitting the energy bands from the tight-binding model in Eq. 3.38 for  $J_j(t) = J$ ,  $\tilde{J}_j(t) = \tilde{J}$  to the two lowest bands of the symmetric, static lattice for a given value of  $\theta$ , both evaluated on a grid spanning the complete 2D BZ. Here, the free fit parameters are  $J$ ,  $\tilde{J}$  and  $\Delta$ . The resulting values of the sublattice offset depending on the polarization angle are plotted in Fig. 3.12b for a lattice depth of  $V_0 = 6 E_r$ . They can be described by a polynomial function

$$\Delta(\theta) = A_\Delta \theta^2 + B_\Delta \theta^4, \quad (3.39)$$

where the prefactors for  $V_0 = 6 E_r$ , derived from fitting this function to the curve in Fig. 3.12b, are  $A_\Delta = 20.456(8) E_r/\text{rad}^2$  and  $B_\Delta = -11.38(6) E_r/\text{rad}^4$ .

The tunneling amplitudes are obtained in a similar manner, namely by fitting the tight-binding bands at every  $t$  to the bands of the imbalanced lattice calculated from Eq. 3.14 for a certain modulation amplitude  $m$ , including the direction dependence of the hoppings and using the corresponding time-dependent connection vectors. Thereby, a higher weight is assigned especially to the  $\Gamma$ -, but also to the  $K$ -points, to ensure that the dispersion at these points is reproduced as precise as possible. If a sublattice offset is

considered, the bands need to be fitted separately for each value of  $\Delta$ , as it changes the width and dispersion of the bands.

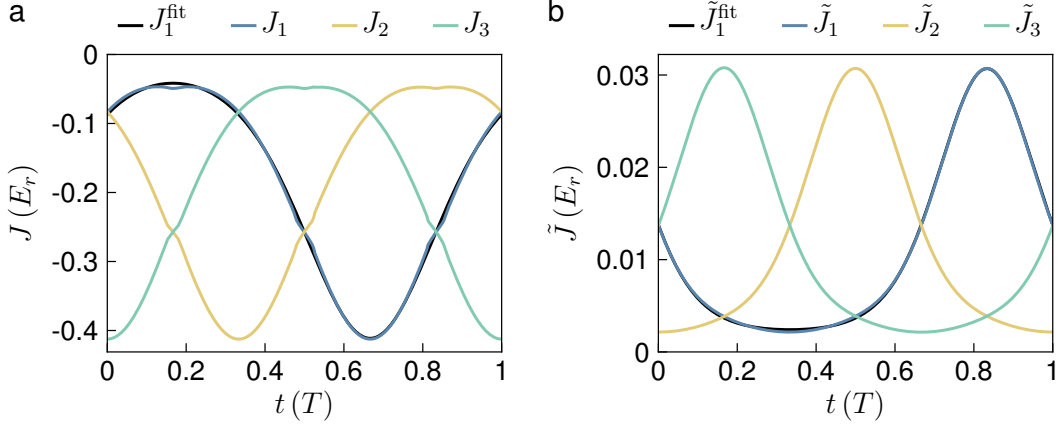


**Figure 3.13: Time- and direction-dependent hopping amplitudes in the modulated lattice for  $V_0 = 6 E_r$ ,  $m = 0.25$  and  $\Delta = 0$ .** **a.** NN tunneling amplitudes along the different bond directions obtained by fitting the energy bands of the tight-binding model in Eq. 3.38 to the two lowest bands of the full Hamiltonian in Eq. 3.14. The black line denotes a fit to  $J_1(t)$  using Eq. 3.40, resulting in  $A = -0.204(2) E_r$ ,  $B = 0.813(7)$  and  $C = 0.049(2) E_r$ . **b.** NNN hopping amplitudes from the same band fit as in **a**. The parameters of the fitted function (black line) are  $\tilde{A} = 5.16(3) \cdot 10^{-3} E_r$ ,  $\tilde{B} = -1.733(5)$  and  $\tilde{C} = 1.50(2) \cdot 10^{-3} E_r$ .

Again, the fit is performed on a 2D grid corresponding to the first BZ. The NN hopping amplitude along a certain bond direction  $j$  is expected to be proportional to  $1/|\delta_j|$ , as the tunneling probability between two lattice sites increases when the distance between the sites is reduced. In Fig. 3.13a, the resulting NN hoppings along the different directions are shown for a modulation amplitude of  $m = 0.25$  and  $\Delta = 0$ , indeed following the inverted length of the connection vectors. The NNN tunnelings, depicted in Fig. 3.13b, are about one order of magnitude smaller and exhibit a similar time-dependence. The evolution of the tunneling amplitudes can be described by the following functions:

$$\begin{aligned} J_j(t) &= A e^{B \cos(\omega t + \phi_j)} + C, \quad \phi_j = \frac{2\pi}{3} j, \\ \tilde{J}_j(t) &= \tilde{A} e^{\tilde{B} \cos(\omega t + \tilde{\phi}_j)} + \tilde{C}, \quad \tilde{\phi}_j = \frac{2\pi}{3} (j+1), \quad j = \{1, 2, 3\}. \end{aligned} \quad (3.40)$$

The form of the curves is motivated by the fact that the intensities of the lattice beams are modulated according to Eq. 3.22, and thus the height of the potential barrier between two sites is  $\propto \cos(\omega t)$  and the corresponding tunneling probability  $\propto e^{\cos(\omega t)}$ . As depicted by the black lines in Fig. 3.13, being fits of Eq. 3.40 to the values  $J_1(t)$  and  $\tilde{J}_1(t)$ , the time-dependence of the hoppings is in general well described by this approach. For increasing modulation amplitudes and larger sublattice offsets, the small kinks deviating from the fit functions become more pronounced, restricting the use of Eq. 3.40 to  $m \lesssim 0.3$  and

$\theta \lesssim 0.12$  rad. Nevertheless, in any case the values of  $J_j$ ,  $\tilde{J}_j$  obtained from the fit to the full bands can be used directly for the calculation of the effective Hamiltonian, provided that they are evaluated at sufficiently many time steps.

As the orbitals are assumed to be spherically symmetric, the change of the connection vectors could in principle be completely absorbed into the time-dependence of the hopping amplitudes. Indeed, fitting the bands with a tight-binding model incorporating constant vectors  $\delta_{j,0}$  being equal to their counterparts in the symmetric lattice, leads to the same values for all  $J_j(t)$  and  $\tilde{J}_j(t)$ . However, as discussed below, even if the resulting bands look similar, leading to the same fit parameters, the corresponding tight-binding Hamiltonian  $\hat{H}(t)$  is different, as it explicitly depends on  $\delta(t)$ , changing the resulting Floquet bands.

**Floquet bands** Using the time-dependent tight-binding parameters, the Hamiltonian at every time step  $t$  can be determined according to Eq. 3.38. The time-evolution operator over one period of the driving is calculated numerically, again by replacing the integral in Eq. 3.23 with a sum over  $N = 300$  discrete time steps. Since the tight-binding Hamiltonian is represented in the basis of the time-independent, localized wavefunctions  $|\phi_A^s\rangle$  and  $|\phi_B^s\rangle$ , no projection or basic change is necessary. The resulting effective Hamiltonian is accordingly a  $2 \times 2$  matrix and the first and second Floquet band are identical to the lower and higher eigenvalues for most quasimomenta. Otherwise, the correct assignment of the bands can be obtained by again tracking the maximal overlap with the eigenstate at the previous quasimomentum, as described in Sec. 3.2.2.

In Fig. 3.14, the quasienergy gaps obtained from the two-band tight-binding model for  $m = 0.25$  and  $\Delta = 0$  (blue lines) are compared to the results from the full calculation (black lines) introduced in the previous section for different modulation frequencies in the third and anomalous regime along the high-symmetry line  $\Gamma$ - $M$ - $K$ - $\Gamma$  in quasimomentum space. In this way, the applicability of the tight-binding description is benchmarked with the bulk dispersion, which is reproduced well by the full band calculation, to be thereupon used for the calculations in the semi-finite system. The dashed, blue lines denote the resulting gaps for time-independent connection vectors  $\delta_j(t) = \delta_{j,0}$  in the tight-binding Hamiltonian, while employing the same hopping amplitudes as before. In addition, the quasienergy gaps derived from an eight-band tight-binding model are shown (red lines), which partly incorporates the coupling of the  $s$ -bands to higher bands. As described in detail in Sec. 3.3.2, more than six tight-binding orbitals are necessary to correctly reproduce the lowest six bands of the honeycomb lattice with  $V_0 = 6 E_r$ . For the corresponding quasienergy gaps in Fig. 3.14, the first eight bands of the full model are fitted in the 2D BZ, and the resulting hopping amplitudes for the  $s$ -bands are inserted in the two-band tight-binding model from eq. 3.38, employing time-dependent connection vectors. Hence, all tight-binding results presented in Fig. 3.14 are obtained from an effective  $2 \times 2$  Hamiltonian.

At the  $\Gamma$ -point, the quasienergy gap is best described by the eight-band fit for larger modulation frequencies in the anomalous phase, but by the two-band model in the third phase. Here, the two versions of the two-band description using  $\delta(t)$  and  $\delta_0$  coincide. The gap at the  $K$  point is matched well by the models with time-dependent connection

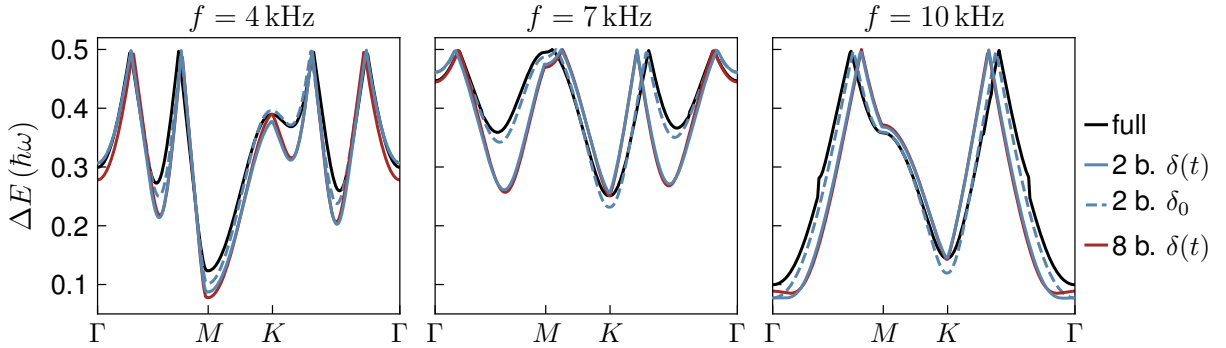


Figure 3.14: **Quasienergy gaps for  $V_0 = 6 E_r$ ,  $m = 0.25$  and  $\Delta = 0$ .** Quasienergy gaps in the anomalous ( $f = (7, 10)$  kHz) and third ( $f = 4$  kHz) regime, plotted along the high-symmetry line in quasimomentum space. The results obtained from the full band calculation (black lines) are compared to different tight-binding models (blue and red lines), all incorporating an effective  $2 \times 2$  Hamiltonian, but using tight-binding parameters derived from fitting either two or eight bands (see Sec. 3.3.2). At the high-symmetry points  $\Gamma$  and  $K$ , the values from the full band model are altogether best described by the two-band tight-binding model employing time-dependent connection vectors (solid, blue lines).

vectors  $\delta(t)$ , whereas the two-band model with  $\delta_0$  deviates significantly from the full model at this point. Along the lines  $\Gamma$ - $M$  and  $K$ - $\Gamma$  however, it fits best to the gap from the full band calculation, which becomes especially apparent for  $f = 7$  kHz.

**Quasienergy gaps vs. modulation frequency** In Fig. 3.15a and b, the quasienergy gaps at  $\Gamma$  and  $K$  calculated using the different models are shown as a function of the modulation frequency, extending over all three topological regimes. In addition to the tight-binding models mentioned above, the quasienergy gaps obtained from a two-band calculation using the full Hamiltonian are presented (dashed, gray lines). In this case, the calculation proceeds as described in the previous section, but the Hamiltonian is projected to its two lowest eigenstates at each time step. Remarkably, this yields no improvement compared to the two-band tight-binding model, it fits even worse at the  $K$ -point. This justifies the use of a tight-binding description in general, as the important drawbacks seem to be connected to the fact that only two bands are employed rather than to the application of a tight-binding model.

The quasienergy gap at  $\Gamma$ , determining the phase transition points, is captured equally well by the different tight-binding models at low modulation frequencies. In the Haldane phase and for larger frequencies in the anomalous phase, using the parameters from the eight-band fit performs slightly better (see also inset of Fig. 3.15a showing the first phase transition), but its difference to the pure two-band fits is negligible compared to the overall deviation from the full band calculation. At the  $K$ -point, the gaps from the two-band model with  $\delta(t)$  differ from the results employing constant vectors nearly over

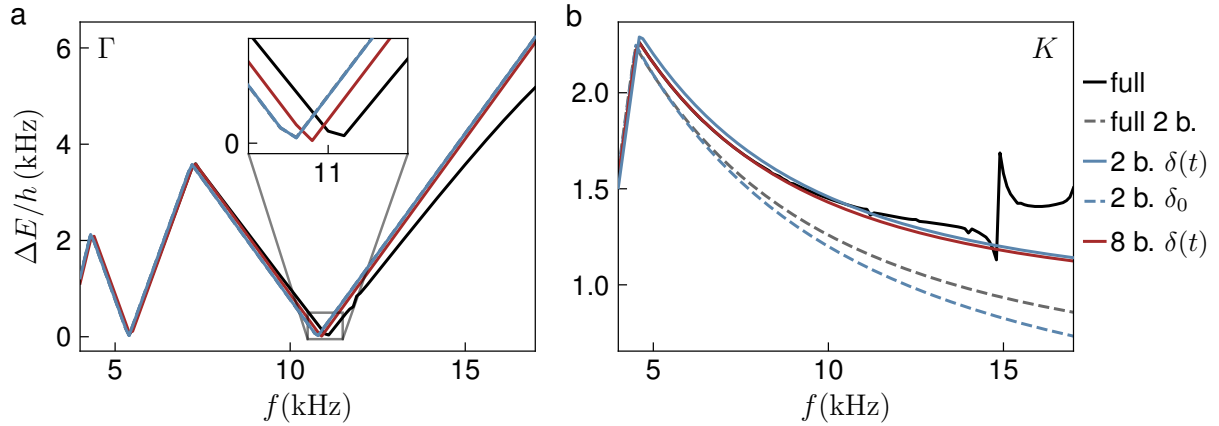


Figure 3.15: **Energy gaps at  $\Gamma$  and  $K$  for  $V_0 = 6 E_r$ ,  $m = 0.25$  and  $\Delta = 0$  as a function of the modulation frequency.** The gaps obtained from the full band calculation (black lines) are compared to different tight-binding models (blue and red lines), all incorporating a  $2 \times 2$  effective Hamiltonian, but using tight-binding parameters obtained from fitting either two or eight bands, and to a full band calculation using only two bands (dashed, gray lines). **a.** All effective two-band models describe the gap at  $\Gamma$  well for small modulation frequencies, but deviate for large  $f$ , suggesting the use of a different approach in the Haldane phase. **b.** At the  $K$ -point, the models using time-dependent connection vectors fit the full band calculation much better, except for the jump at high modulation frequencies, which could only be reproduced by a model incorporating six bands within the time-integration.

the complete frequency range, but especially at large modulation frequencies. The jump of the gap in the full model, resulting from avoided crossings between the  $s$ -bands and higher bands (also being observed in the experiments), is not captured by any of the tight-binding models, since they all employ a two-band Hamiltonian, just incorporating parameters obtained from fitting a different number of bands.

Nevertheless, the models using  $\delta(t)$  describe the overall development of the quasi-energy gap at  $K$  sufficiently well, which is also verified for a larger modulation amplitude of  $m = 0.3$  in Sec. 5.2.1. As apparent in Fig. 3.15, the Haldane regime occurring for high modulation frequencies is in general not captured well by the models employing a  $2 \times 2$  Hamiltonian, as the direct coupling to higher bands during the modulation period is increased in this parameter range. However, the Haldane phase can be described by an effective, time-independent Hamiltonian, as derived in Sec. 2.1.3, which is used to provide a tight-binding description in this regime, as further illustrated in Sec. 3.3.3. In conclusion, the quasienergy bands and gaps in the anomalous and third regime can be well described by a two-band tight-binding model, employing fitted time-dependent hopping amplitudes and time-dependent connection vectors.

### 3.3.2 Eight-band tight-binding model

The shape of the two lowest bands of the effective Hamiltonian is influenced by coupling to the  $p$ -bands during the modulation period, especially at high modulation frequencies and amplitudes. In particular, in the full band calculation, the effective Hamiltonian is obtained by multiplication of  $6 \times 6$  matrices which are in general not diagonal, as they are transformed to a common basis. To provide a complete description of the Hamiltonian at every time step, a six-band tight-binding model would be desirable, embedding the coupling between  $s$ - and  $p$ -bands. However, at a lattice depth of  $V_0 = 6 E_r$  as used in the experiments and hence in the calculations, it is not possible to find a model that describes all of the first six bands of the imbalanced honeycomb lattice correctly by employing only six tight-binding orbitals, as illustrated below.

**Tight-binding description of the p-bands** Using the localized basis introduced above, the eigenstates of the next four bands are expressed in terms of  $p_x$ - and  $p_y$ -orbitals on the A- and B-sites, analogously to the description of the hydrogen atom, being projected to the  $x$ - $y$ -plane. These orbitals are not spherically symmetric but oriented along the  $x$ - and  $y$ -direction (see Fig. B.1).

To describe hopping along a certain bond, directed orbitals are constructed from linear combinations of  $p_x$  and  $p_y$ , being either oriented along the respective bond or perpendicular to it [138]. For NN hopping, the prefactors are given by the  $x$ - and  $y$ -coordinates of the normalized connection vectors  $\hat{\delta}_j(t)$  or the corresponding unit vectors  $\hat{\gamma}_j(t)$  perpendicular to them:

$$\begin{aligned} |\phi_{A(B)}^{j\parallel}(t)\rangle &= \hat{\delta}_j^x(t)|\phi_{A(B)}^{p_x}\rangle + \hat{\delta}_j^y(t)|\phi_{A(B)}^{p_y}\rangle, & \hat{\delta}_j(t) &= \frac{\boldsymbol{\delta}_j(t)}{|\boldsymbol{\delta}_j(t)|}, \\ |\phi_{A(B)}^{j\perp}(t)\rangle &= \hat{\gamma}_j^x(t)|\phi_{A(B)}^{p_x}\rangle + \hat{\gamma}_j^y(t)|\phi_{A(B)}^{p_y}\rangle, & \hat{\gamma}_j(t) \cdot \hat{\delta}_j(t) &= 0, & j &= \{1, 2, 3\}. \end{aligned} \quad (3.41)$$

In general, the hopping  $p\parallel$ - $p\parallel$  is expected to be much larger than  $p^\perp$ - $p^\perp$ , whereas the amplitude vanishes for  $p\parallel$ - $p^\perp$ . The NNN hopping is described by orbitals oriented along the lattice vectors  $\pm \mathbf{a}_j$  for A- and B-sites, which are chosen to be  $-\mathbf{a}_1, \mathbf{a}_2, \mathbf{a}_3$  as depicted in Fig. 2.1, and hopping of perpendicular orbitals is not accounted for as its amplitude is negligible. The corresponding oriented orbitals are time-independent and read:

$$|\tilde{\phi}_{A(B)}^{j\parallel}\rangle = \pm \hat{a}_j^x|\phi_{A(B)}^{p_x}\rangle \pm \hat{a}_j^y|\phi_{A(B)}^{p_y}\rangle, \quad \hat{a}_j = \frac{\mathbf{a}_j}{|\mathbf{a}_j|}. \quad (3.42)$$

Moreover, tunneling between  $s$  and  $p\parallel$  orbitals is taken into account on the NN-level, whereas the amplitude for  $s$ - $p^\perp$  is zero and NNN- $s$ - $p\parallel$  is negligible for the lattice configurations considered here. Using the oriented orbitals, a tight-binding Hamiltonian can be constructed analogously to the two-band case, being represented by a  $6 \times 6$  matrix at every  $\mathbf{q}$  and  $t$  in the basis of the localized orbitals. Then, the tight-binding parameters for this model could be fitted at each time step to derive an effective Hamiltonian.

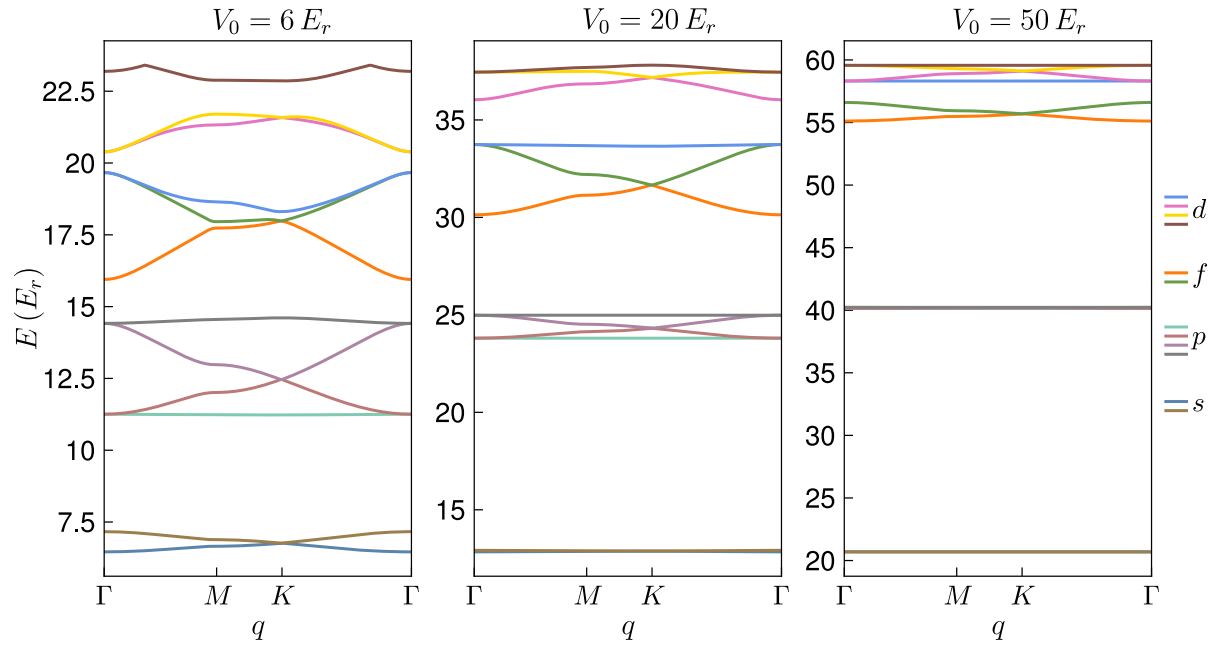
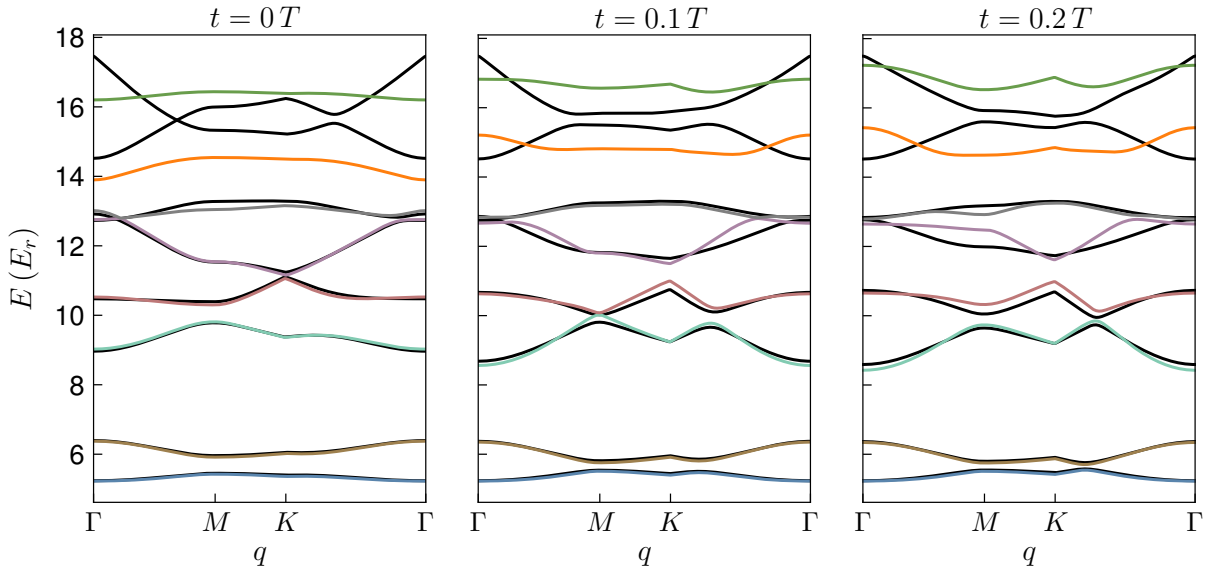


Figure 3.16: **Energy bands of the symmetric honeycomb lattice.** The first 12 energy bands plotted along the high-symmetry line for different lattice depths. The  $f$ - and  $d$ -bands are highly mixed for  $V_0 = 6 E_r$  and strongly couple to the  $p$ -bands. The bands for  $V_0 = 20 E_r$  already exhibit a larger gap above the  $p$ -bands. At  $V_0 = 50 E_r$ , the grouping of the  $f$ - and  $d$ -bands becomes apparent.

**Coupling to higher bands in the symmetric lattice for  $V_0 = 6 E_r$**  The  $p$ -bands of the honeycomb lattice at  $V_0 = 6 E_r$  are however not well described by the model described above, not even in the symmetric lattice, as illustrated in Fig. B.1c. To correctly reproduce the bands of the full model, higher orbitals must be included, at least the next two bands, which correspond to two  $f$ -orbitals. The reason for this becomes apparent in Fig. 3.16, where the first 12 bands of the symmetric honeycomb lattice are compared for different lattice depths.

At  $V_0 = 6 E_r$ , there is a significant gap between the  $s$ - and  $p$ -bands, indicating the vanishing  $s$ - $p$ -coupling in the symmetric case. However, above the  $p$ -bands, there is only a small gap to the next higher bands, which are themselves highly mixed and do not appear to be arranged in groups of even numbers of bands, as expected from having two sites per unit cell. This already suggests that there is a non-negligible coupling between these bands and the  $p$ -bands. To disentangle the higher bands into groups of orbitals, the lattice depth has to be increased considerably to about  $50 E_r$ , where the  $s$ - and  $p$ -bands are nearly flat and the higher bands are well separated from them. These appear in a group of two bands, being described by 6-fold rotational  $f_{x(x^2-3y^2)}$ -orbitals and a group of four bands, corresponding to  $d_{xy}$ - and  $d_{x^2-y^2}$ -orbitals, which exhibit 4-fold rotational symmetry [139], as depicted in Fig. B.1a.



**Figure 3.17: Fitted energy bands from the eight-band tight-binding model at different time steps.** Energy bands using the fitted tight-binding parameters (colorful lines) compared to the bands from the full model (black lines) along the high-symmetry line for  $V_0 = 6 E_r$ . The  $s$ -bands are described well at all time steps, whereas the agreement of the  $p$ -bands decreases with higher energy, especially for  $t = 0.2 T$ . In general, the fitted bands match well again at  $t = T/3$ ,  $t = 2T/3$  and  $t = T$  and deviate the most at  $t \sim 0.2 T$ ,  $t \sim 0.5 T$  and  $t \sim 0.8 T$ . As the  $f$ -bands are described incompletely in the eight-band tight-binding model, they strongly deviate from the full calculation.

**Eight-band model including f-orbitals** Including the  $f$ -orbitals in the tight-binding model provides a reasonable description of the  $p$ -bands in the symmetric lattice (see Fig. B.1d) and to some extent also in the imbalanced case (Fig. 3.17). In addition to the  $s$ - and  $p$ -hopping terms described above, this eight-band model contains NN hopping in the  $f$ -bands and between  $p$ - and  $f$ -orbitals. The coupling of  $s$ - and  $f$ -bands can be neglected. The  $f$ -orbital considered here has lobes which are oriented along the vectors  $\delta_j$ , so no linear combinations need to be formed to describe NN hopping, if the direction change of the orbitals is neglected.

In principle, this would need to be taken into account, as well as possible NNN hopping of the  $f$ - $f$  and  $p$ - $f$ -orbitals, if one would aim for a correct representation of the  $f$ -bands. As the coupling between  $f$ - and  $d$ -orbitals is apparently even larger than between  $p$  and  $f$  though, a complete description of the  $f$ -bands is anyway only possible if the  $d$ -bands would be taken into account. Hence, at a lattice depth of  $6 E_r$ , in principle only the  $s$ -bands can be described by a tight-binding model which contains solely coupling between these orbitals. All higher bands are mixed with the next higher bands to some extent, preventing the development of a tight-binding model that correctly reproduces the properties of all participating bands. A full description of the eight-band tight-binding Hamiltonian is given in appendix B.

The corresponding hopping amplitudes for  $s$ - $s$ ,  $s$ - $p$ ,  $p$ - $p$ ,  $p$ - $f$  and  $f$ - $f$  coupling can be obtained by fitting the lowest eight bands of the imbalanced lattice in the 2D BZ at every time step with the tight-binding model outlined above and defined by Eq. B.4. The resulting bands are plotted along the high-symmetry line  $\Gamma$ - $M$ - $K$ - $\Gamma$  at different times during the driving period along with the bands of the full model (black lines) in Fig. 3.17. The  $s$ -bands and the lowest  $p$ -band are captured well at all times, whereas the fitted higher bands still deviate, especially at  $t = 0.2T$ . The  $f$ -bands from the tight-binding fit are entirely different than in the full model, owing to their incomplete description which misses the coupling with the  $d$ -bands. Including these would lead to similar problems, as described above, and as the degree of band mixing increases for higher energies, incorrect  $d$ -bands would in turn lead to wrong  $f$ - $d$ -coupling and hence corrupt the  $f$ -bands.

Calculating the effective Hamiltonian in the eight-band tight-binding model using the fitted parameters leads to incorrect Floquet bands, which strongly deviate from the full model compared to the results from the two-band tight-binding approach. The reason for this is on the one hand the wrong  $f$ -bands, leading to corrupted  $p$ - $f$  coupling terms, and on the other hand the hoppings of the  $p$ -bands themselves, which are not entirely correct at all times, as apparent in Fig. 3.17. Projecting down the Hamiltonian to its six lowest eigenstates does not improve the calculation, as the initial eight-band Hamiltonian is already not correct and misses the contributions from all higher bands, which are in contrast apparent in the full band calculation, emanating from a large Hamiltonian matrix at every time step.

**Employing the parameters from the eight-band fit in a two-band model** The resulting tight-binding parameters for the  $s$ -bands can nevertheless be incorporated in a two-band tight-binding model, which leads to slight improvements in the shape of the resulting Floquet bands and gaps, as illustrated in Figs. 3.14 and 3.15. This is accounted for by the finite  $s$ - $p$ -hopping terms arising in the imbalanced lattice, which represent the coupling between these bands, finally leading to the avoided crossings in the Floquet bands at larger modulation frequencies and amplitudes. Even if these terms are not contained in the time-dependent Hamiltonian, the NN and NNN tunneling amplitudes of the  $s$ -bands, which are modified indirectly due to a finite coupling to  $p$ -bands, slightly differ from the values obtained in a pure two-band fit, as depicted in Fig. 3.18.

There is only a small difference between the resulting NN hopping amplitudes, mostly close to their maximum, but this already leads to an improvement in the description of the quasienergy gap at  $\Gamma$ , as mentioned in the last section. The relative deviation between the NNN terms is more obvious, but as they are about one order of magnitude smaller than the NN contributions, this difference can in principle be neglected. Using the NN hopping from the eight-band fit along with NNN hoppings from the two-band fit results basically in the same bands as when using the eight-band NNN terms. Depending on the situation and the degree of accuracy needed to describe the quasienergy gaps of the Floquet bands, using the  $s$ -band parameters from the eight-band fit could constitute a helpful improvement of the tight-binding description.

Considering the fitted tight-binding parameters as a function of time, they obey the

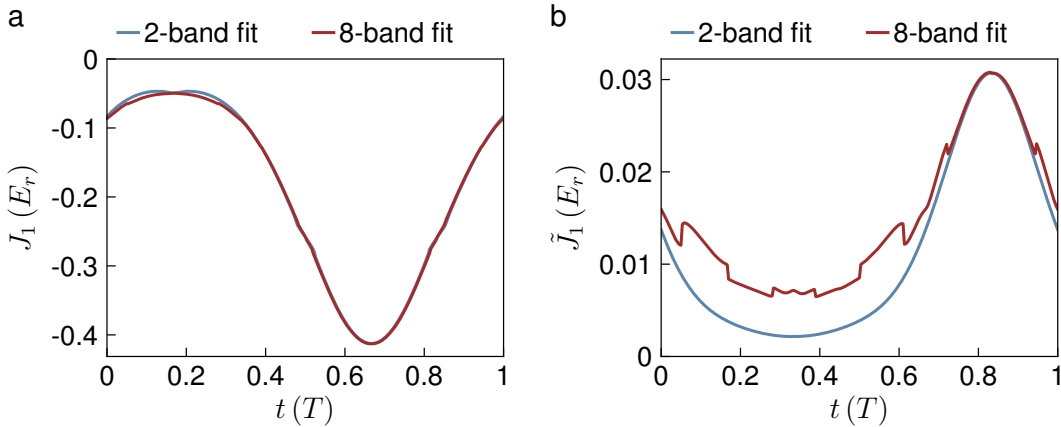


Figure 3.18: **Fitted hopping amplitudes of the  $s$ -bands from the eight-band and two-band models along  $\delta_1$  for  $V_0 = 6 E_r$ .** **a.** NN tunneling within one driving period. Although the resulting values mostly coincide, the slight differences lead indeed to an improved description of the Floquet bands at  $\Gamma$ , when using the parameters from the eight-band fit, which includes  $s$ - $p$ -coupling. **b.** The relative difference between the NNN tunneling is larger, though having only little influence on the shape of the Floquet bands, as the contributions are about one order of magnitude smaller than the NN hoppings.

expected periodicity and phase shifts, when comparing hopping amplitudes along different directions, but not all of them appear as smooth curves, as apparent for the NNN  $s$ -band hopping in Fig. 3.18b. One reason for this could be a non-optimal basis choice. Alternatively, a tight-binding description could also be carried out in a basis of Wannier functions which are localized only to the range of a unit cell and not to a single site. These form a basis of energy eigenstates instead of single orbitals corresponding to A- and B-sites. The hopping amplitudes can then be calculated directly as overlap integrals between functions on neighboring unit cells, leading to a  $6 \times 6$  matrix assigned to each pair of sites when considering  $s$ - and  $p$ -bands. This might result in tunneling amplitudes being smooth functions of time, it does however not solve the general problem of coupling to higher bands. Truncating the model at 6-bands again leads to an incorrect description of the  $p$ -bands and thus to erroneous Floquet bands, as the large coupling to the  $f$ -bands is neglected.

### 3.3.3 Fitting the effective bands in the Haldane phase

The Floquet bands obtained by employing a two-band tight-binding Hamiltonian at every time step, using the fitted, time-dependent hopping amplitudes, deviate from the full bands for high modulation frequencies. To provide an adequate tight-binding description in the Haldane regime, enabling the derivation of the edge mode dispersion, the Floquet bands from the full band calculation are directly fitted with the two-band model defined in Eq. 2.18.

The topological Haldane phase can be described by an effective static model, as there

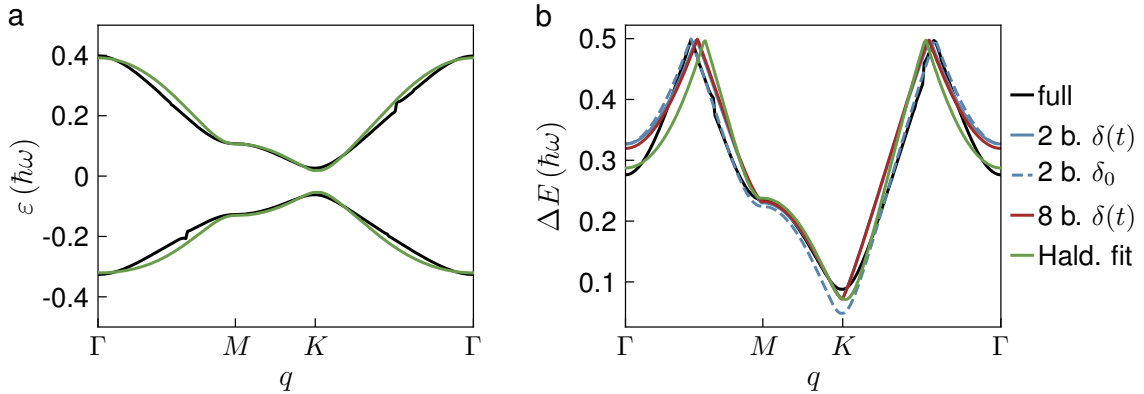


Figure 3.19: **Quasienergy bands and gaps in the Haldane phase for  $V_0 = 6 E_r$ .** **a.** Floquet bands from the full model (black lines) and the bands obtained by directly fitting them with the two-band Haldane model from Eq. 2.18, for  $m = 0.25$ ,  $f = 16$  kHz and  $\Delta = 0$  (green lines), plotted along the high-symmetry line. The fitted hopping amplitudes are  $J = 0.116 E_r$ ,  $t = -0.018 E_r$  and  $\phi = 1.241$  rad. **b.** Corresponding quasienergy gaps, compared also to the results from the two-band and eight-band fits (blue and red lines), where the Hamiltonian at every time step during the driving period is approximated by a tight-binding model.

are only chiral edge modes in the gap at zero quasienergy, which will be reproduced when evaluating the Haldane model on a finite geometry. The quasienergy bands are described by an isotropic, real-valued NN hopping  $J$  and complex NNN hopping  $\tilde{J} = t e^{i\phi}$ , expressed in terms of its absolute value and phase. In addition, the tight-binding bands are shifted by a constant energy offset to resemble the Floquet bands lying in the interval  $[-\hbar\omega/2, \hbar\omega/2]$ . The Haldane-tight-binding model is fitted to the quasienergy bands from the full model on the 2D BZ, whereas this procedure needs to be repeated for each modulation amplitude and frequency. The resulting quasienergy bands and gaps for  $m = 0.25$  and  $f = 16$  kHz are plotted along the high-symmetry line  $\Gamma$ - $M$ - $K$ - $\Gamma$  in Fig. 3.19 (green lines). Overall, the fitted quasienergy bands coincide well with the full Floquet bands, especially at the high-symmetry points. Considering the energy gap, the deviations along the  $\Gamma$ - $M$  and  $K$ - $\Gamma$  lines become more obvious, compared to the tight-binding approach using time-independent connection vectors. However, at  $\Gamma$  and  $K$ , the gap is best described by the Haldane fit.

### 3.3.4 Derivation of the Haldane model in the high-frequency limit

The two-band tight-binding description of the modulated honeycomb lattice directly resembles the Haldane model from Eq. 2.18 in the limit of large modulation frequencies, validating the use of this model to fit the quasienergy bands in this regime. As described in Sec. 2.2.2, the effective Hamiltonian can be approximated by a series expansion up to first order for  $\hbar\omega \gg 1$ , containing the Fourier components  $\hat{H}_n$  of the time-dependent

Hamiltonian (see Eq. 2.38):

$$\hat{H}_{\text{eff}} \approx \hat{H}_0 + \frac{1}{\hbar\omega} \sum_{n=1}^{\infty} \frac{1}{n} [\hat{H}_n, \hat{H}_{-n}] + \mathcal{O}\left(\frac{1}{(\hbar\omega)^2}\right). \quad (3.43)$$

Using the expressions for the time-dependent hoppings given in Eq. 3.40 and neglecting the time-dependence of the NN connection vectors, being valid for small modulation amplitudes, the Hamiltonian defined in Eq. 3.35 can be written in terms of Pauli matrices for each quasimomentum  $\mathbf{q}$ :

$$\begin{aligned} \hat{H}(\mathbf{q}, t) = & \sum_{j=1}^3 \left[ 2 \cos(\mathbf{q} \cdot \mathbf{a}_j) \left( \tilde{A} e^{\tilde{B} \cos(\omega t + \tilde{\phi}_j)} + \tilde{C} \right) \right] \hat{\sigma}_0 \\ & + \sum_{j=1}^3 \left[ \cos(\mathbf{q} \cdot \boldsymbol{\delta}_j) (A e^{B \cos(\omega t + \phi_j)} + C) \right] \hat{\sigma}_x \\ & - \sum_{j=1}^3 \left[ \sin(\mathbf{q} \cdot \boldsymbol{\delta}_j) (A e^{B \cos(\omega t + \phi_j)} + C) \right] \hat{\sigma}_y + \frac{\Delta}{2} \hat{\sigma}_z. \end{aligned} \quad (3.44)$$

The Fourier components are obtained by employing the relation

$$e^{ir \sin(\vartheta)} = \sum_{n=-\infty}^{+\infty} \mathcal{J}_n(r) e^{in\vartheta}, \quad (3.45)$$

where  $\mathcal{J}_n$  denotes the Bessel function of the first kind of integer order  $n$ . Thus, the time-dependent part of the hopping-amplitudes can be expressed as

$$e^{B \cos(\omega t + \phi_j)} = e^{i(-iB) \sin(\omega t + \phi_j + \pi/2)} = \sum_{n=-\infty}^{+\infty} \mathcal{J}_n(-iB) e^{in(\omega t + \phi_j + \pi/2)}, \quad (3.46)$$

and the Fourier components of the time-dependent Hamiltonian are read off as the pre-factors of the terms  $\propto e^{in(\omega t)}$ . The commutator of the  $n$ th and  $-n$ th component evaluates to:

$$[\hat{H}_n, \hat{H}_{-n}] = -2 (\mathcal{J}_n(-iB))^2 A^2 (-1)^n 2 \sum_{j=1}^3 \sin(\mathbf{q} \cdot \mathbf{a}_j) \sin(n\xi_j) \hat{\sigma}_z. \quad (3.47)$$

Here, the differences of the NN connection vectors  $\boldsymbol{\delta}_j$  have been expressed in terms of the lattice vectors  $\mathbf{a}_j$ , defined as  $-\mathbf{a}_1$ ,  $\mathbf{a}_2$  and  $\mathbf{a}_3$  and the angles  $\xi_j$  describe the corresponding differences in the modulation phases:

$$\boldsymbol{\xi} = (\phi_1 - \phi_3, \phi_2 - \phi_1, \phi_3 - \phi_2) = \left( \frac{2\pi}{3}, \frac{2\pi}{3}, -\frac{4\pi}{3} \right). \quad (3.48)$$

By inserting this result into Eq. 3.43, the effective Hamiltonian becomes:

$$\begin{aligned} \hat{H}_{\text{eff}}(\mathbf{q}) = & \sum_{j=1}^3 \left[ 2 \cos(\mathbf{q} \cdot \mathbf{a}_j) (\tilde{A} \mathcal{J}_0(-i\tilde{B}) + \tilde{C}) \right] \hat{\sigma}_0 \\ & + \sum_{j=1}^3 [\cos(\mathbf{q} \cdot \boldsymbol{\delta}_j) (A \mathcal{J}_0(-iB) + C)] \hat{\sigma}_x - \sum_{j=1}^3 [\sin(\mathbf{q} \cdot \boldsymbol{\delta}_j) (A \mathcal{J}_0(-iB) + C)] \hat{\sigma}_y \\ & + \left[ \frac{\Delta}{2} - \sum_{j=1}^3 \left( 2 \sin(\mathbf{q} \cdot \mathbf{a}_j) \frac{2A^2}{\hbar\omega} \sum_{n=1}^{\infty} \frac{(-1)^n}{n} (\mathcal{J}_n(-iB))^2 \sin(n\xi_j) \right) \right] \hat{\sigma}_z. \end{aligned} \quad (3.49)$$

This form of the Hamiltonian can be directly compared to Eq. 2.21, resembling a two-band model with real-valued, isotropic NN hoppings  $J' = A \mathcal{J}_0(-iB) + C$  and complex NNN tunneling amplitudes, which are also independent of the bond direction:

$$\tilde{J}' = (\tilde{A} \mathcal{J}_0(-i\tilde{B}) + \tilde{C}) + i \left( \frac{2A^2}{\hbar\omega} \sum_{n=1}^{\infty} \frac{(-1)^n}{n} (\mathcal{J}_n(-iB))^2 \sin\left(n\frac{2\pi}{3}\right) \right). \quad (3.50)$$

The zeroth order Bessel function  $\mathcal{J}_0(-iB)$  has a global minimum at  $B = 0$  and is real and positive for all  $B$ , meaning that the absolute value of the NN tunneling monotonically increases with the modulation amplitude, where  $m \in [0, 0.4]$  corresponds approximately to  $B \in [0, 1]$ . This confirms the observation that the effective bandwidth is increasing with  $m$ , shifting the phase transition points at  $\Gamma$  to higher frequencies for larger amplitudes. The higher order Bessel functions  $\mathcal{J}_n(-iB)$  are purely imaginary for odd  $n$  and real for even  $n$ , leading to an overall positive contribution from  $n = 1$  and a negative contribution from  $n = 2$ , being however more than one order of magnitude smaller. Thus, the sum in Eq. 3.50 evaluates to a real and positive number. For NNN hopping,  $\tilde{B} < 0$ , but since  $\mathcal{J}_0(-ix)$  is symmetric with respect to  $x = 0$  and  $\tilde{A}, \tilde{C} > 0$ , the real part of  $\tilde{J}'$  is also positive. Hence, the renormalized complex hopping has a positive real and imaginary part corresponding to  $\phi > 0$  in the Haldane model, resembling a Chern number of  $\mathcal{C}^- = +1$  in the lowest band for  $\Delta > 0$ , as also occurring in the numerical calculations. The contributions from the different Bessel functions are also shown in Fig. 6.7, being compared to the corresponding terms for a phase modulated lattice introduced in chapter 6.

### 3.4 Calculation of the edge mode dispersion

The quasienergy dispersion of the edge modes is obtained by calculating the effective Hamiltonian on a stripe-geometry, being periodic along one direction but finite along the other direction. To incorporate the specific shape of the edge, a two-band tight-binding model is used and the corresponding parameters are derived from fitting the bulk bands, as described in the previous sections. The honeycomb lattice can exhibit several kinds of edges, depending on the spatial direction along which it is cut [140]. In the following, the armchair-termination will be considered, which occurs when the lattice is assumed to be

finite along the  $y$ -direction. The zigzag-geometry, corresponding to a system being finite along the  $x$ -direction, is discussed in appendix C.

### 3.4.1 Tight-binding model in the stripe-geometry

The system considered in the following is periodic along the  $x$ -direction and consists of  $2N$  lattice sites along the  $y$ -direction, as depicted in Fig. 3.20. The effective unit cell is indicated by the gray shaded area, having a width of  $a_{\text{eff}} = 3a$  and extending over the complete length of the system along the  $y$ -direction. The effective Hamiltonian of the modulated lattice is obtained by numerical integration of the tight-binding Hamiltonian at every time step during the modulation period. To describe the imbalanced lattice within the modulation period as well as the Haldane phase, real-valued, direction-dependent NN tunneling is considered, employing the time-dependent connection vectors  $\delta(t)$  derived for each modulation amplitude. The NNN hopping amplitudes are in general assumed to be complex and also depend on the bond direction. Thereby, the time-dependent hopping parameters derived previously from fitting the bulk bands of the infinite system are used, yielding the dispersion of both the bulk and edge states when being evaluated on the stripe-geometry. In the Haldane regime, the Floquet bands are calculated directly with the parameters obtained from fitting the Haldane model to the bulk bands. The semi-finite system is described by pairs of lattice sites  $(mA, mB)$  located inside a single unit cell with  $m \in \mathbb{N} \in [1, N]$ . Depending on the bond direction and the site index, the tunneling connects sites within the same unit cell or sites in neighboring cells.

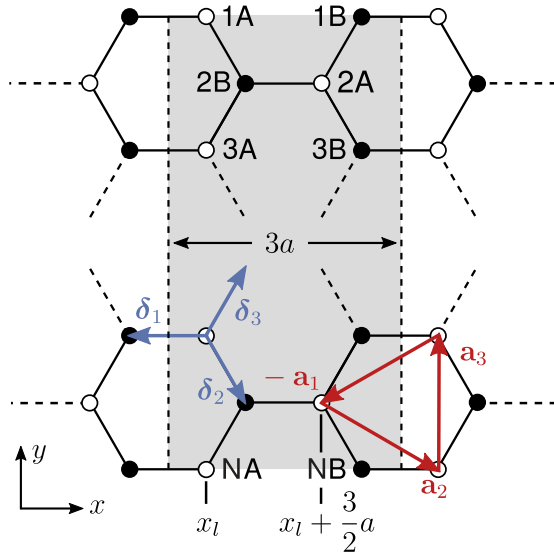


Figure 3.20: **Sketch of the armchair-geometry.** Honeycomb lattice being periodic along the  $x$ -direction and finite along  $y$ . The unit cell (gray shaded area) consists of  $N$  A- and  $N$  B-sites and has a width of  $3a$ . The locations of the odd and even A-sites in the  $l$ th unit cell are denoted by  $x_l$  and  $x_l + \frac{3}{2}a$ .

The corresponding tight-binding Hamiltonian reads:

$$\begin{aligned}
\hat{H}(t) = & \sum_l \left[ J_1(t) \left( \sum_{m \text{ odd}} \hat{a}_l^\dagger(m) \hat{b}_{l-1}(m) + h.c. + \sum_{m \text{ even}} \hat{a}_l^\dagger(m) \hat{b}_l(m) + h.c. \right) \right. \\
& + \sum_m J_2(t) \left( \hat{a}_l^\dagger(m) \hat{b}_l(m+1) + h.c. \right) + J_3(t) \left( \hat{a}_l^\dagger(m) \hat{b}_l(m-1) + h.c. \right) \\
& + \sum_{m \text{ odd}} \left( \tilde{J}_1(t) \hat{a}_l^\dagger(m) \hat{a}_{l-1}(m+1) + \tilde{J}_1(t) \hat{b}_l^\dagger(m) \hat{b}_{l+1}(m-1) + h.c. \right. \\
& \quad \left. + \tilde{J}_2(t) \hat{a}_l^\dagger(m) \hat{a}_l(m+1) + \tilde{J}_2(t) \hat{b}_l^\dagger(m) \hat{b}_l(m-1) + h.c. \right) \\
& + \sum_{m \text{ even}} \left( \tilde{J}_1(t) \hat{a}_l^\dagger(m) \hat{a}_l(m+1) + \tilde{J}_1(t) \hat{b}_l^\dagger(m) \hat{b}_l(m-1) + h.c. \right. \\
& \quad \left. + \tilde{J}_2(t) \hat{a}_l^\dagger(m) \hat{a}_{l+1}(m+1) + \tilde{J}_2(t) \hat{b}_l^\dagger(m) \hat{b}_{l-1}(m-1) + h.c. \right) \\
& + \sum_m \left( \tilde{J}_3(t) \hat{a}_l^\dagger(m) \hat{a}_l(m-2) + \tilde{J}_3(t) \hat{b}_l^\dagger(m) \hat{b}_l(m+2) + h.c. \right. \\
& \quad \left. + \frac{\Delta}{2} \left( \hat{a}_l^\dagger(m) \hat{a}_l(m) - \hat{b}_l^\dagger(m) \hat{b}_l(m) \right) \right), \tag{3.51}
\end{aligned}$$

where the operators  $\hat{a}_l^\dagger(m)$  and  $\hat{b}_l^\dagger(m)$  create a particle on the  $m$ th A- and B-site in the unit cell denoted by  $l$ .

Since the lattice is periodic along  $x$ , a one-dimensional (1D) Fourier transform of the operators can be performed in this direction:

$$\hat{a}_l^\dagger(m) = \sum_q e^{-iqx_{l,mA}} \hat{a}_q^\dagger(m) \quad \hat{b}_l^\dagger(m) = \sum_q e^{-iqx_{l,mB}} \hat{b}_q^\dagger(m). \tag{3.52}$$

In the following, the A-sites are assumed to be at rest, and the locations of the B-sites are thus time-dependent and can be derived using the normalized connection vectors:

$$\begin{aligned}
m \text{ odd:} \quad & x_{l,mA} = x_l & x_{l-1,mB}(t) = x_{l,mA} + \hat{\delta}_1^x(t) \\
& x_{l,(m+1)B}(t) = x_{l,mA} + \hat{\delta}_2^x(t) & x_{l,(m-1)B}(t) = x_{l,mA} + \hat{\delta}_3^x(t) \\
\\
m \text{ even:} \quad & x_{l,mA} = x_l + \frac{3}{2}a & x_{l,mB}(t) = x_{l,mA} + \hat{\delta}_1^x(t) \\
& x_{l,(m+1)B}(t) = x_{l,mA} + \hat{\delta}_2^x(t) & x_{l,(m-1)B}(t) = x_{l,mA} + \hat{\delta}_3^x(t). \tag{3.53}
\end{aligned}$$

The site-locations appearing in the NNN hopping-terms can be directly expressed using the geometry of the symmetric lattice, as depicted in Fig. 3.20, since the lattice vectors are time-independent. This yields phase factors containing the differences in the  $x$ -coordinates of the vectors  $\mathbf{a}_j$ , which would otherwise also emerge from subtracting the connection vectors, using the definitions in Eq. 3.53. Analogously to the infinite system,

the Schrödinger equation can be solved by the ansatz

$$|\psi_q\rangle = \sum_m \left( c_{mA} \hat{a}_q^\dagger(m) + c_{mB} \hat{b}_q^\dagger(m) \right) |0\rangle. \quad (3.54)$$

Using the commutation relations between operators for different quasimomenta and site numbers

$$[\hat{a}_q(m), \hat{a}_{q'}^\dagger(m')] = \delta_{q,q'} \delta_{m,m'}, \quad [\hat{b}_q(m), \hat{b}_{q'}^\dagger(m')] = \delta_{q,q'} \delta_{m,m'}, \quad (3.55)$$

and shifting the indices  $m \rightarrow m \pm 1$ , the prefactors of  $\hat{a}_q^\dagger(m)$  and  $\hat{b}_q^\dagger(m)$  can be read off on both sides of the equation. This yields the eigenvalue equations for the coefficients  $c_{mA(B)}$ :

$$\begin{aligned} E c_{mA} &= J_1(t) e^{iq\hat{\delta}_1^x(t)} c_{mB} + J_2(t) e^{iq\hat{\delta}_2^x(t)} c_{(m+1)B} + J_3(t) e^{iq\hat{\delta}_3^x(t)} c_{(m-1)B} \\ &\quad + \left( \tilde{J}_1(t) e^{-iq\frac{3}{2}a} + \tilde{J}_2(t) e^{iq\frac{3}{2}a} \right) c_{(m+1)A} + \left( \tilde{J}_1^*(t) e^{iq\frac{3}{2}a} + \tilde{J}_2^*(t) e^{-iq\frac{3}{2}a} \right) c_{(m-1)A} \\ &\quad + \tilde{J}_3^*(t) c_{(m+2)A} + \tilde{J}_3(t) c_{(m-2)A} + \frac{\Delta}{2} c_{mA}, \\ E c_{mB} &= J_1(t) e^{-iq\hat{\delta}_1^x(t)} c_{mA} + J_2(t) e^{-iq\hat{\delta}_2^x(t)} c_{(m-1)A} + J_3(t) e^{-iq\hat{\delta}_3^x(t)} c_{(m+1)A} \\ &\quad + \left( \tilde{J}_1(t) e^{iq\frac{3}{2}a} + \tilde{J}_2(t) e^{-iq\frac{3}{2}a} \right) c_{(m-1)B} + \left( \tilde{J}_1^*(t) e^{-iq\frac{3}{2}a} + \tilde{J}_2^*(t) e^{iq\frac{3}{2}a} \right) c_{(m+1)B} \\ &\quad + \tilde{J}_3(t) c_{(m+2)B} + \tilde{J}_3^*(t) c_{(m-2)B} - \frac{\Delta}{2} c_{mB}. \end{aligned} \quad (3.56)$$

In the basis of the coefficients, being defined as  $(c_{1A}, c_{1B}, c_{2A}, c_{2B}, \dots, c_{NA}, c_{NB})$ , the Hamiltonian can be written as a  $2N \times 2N$  matrix for every quasimomentum  $q$ . The first BZ in the armchair-geometry is given by  $q_x \in [-\frac{\pi}{3a}, \frac{\pi}{3a}]$ . Using the time-dependent hoppings obtained from the bulk band fits, the Hamiltonian can be derived at every time step  $t$ , and the effective Hamiltonian is accordingly also represented by a  $2N \times 2N$  matrix. Hence, there are  $2N$  quasienergy bands for each quasimomentum. Analogously, the bands in the Haldane regime are given by the eigenvalues of the Hamiltonian in Eq. 3.56, when employing the corresponding time-independent, isotropic tunnelings and the static connection vectors.

### 3.4.2 Quasienergy dispersion

In Fig. 3.21, the quasienergy bands in the armchair geometry are shown for  $m = 0.25$  and  $f = (5, 9, 16)$  kHz, representing the third, anomalous and Haldane regime. In the first case, a pair of chiral edge modes is visible in the quasienergy gap at the FBZ edge, whereas the bands are gapped at zero energy, as expected from the bulk winding numbers being  $W^\pi = 1$  and  $W^0 = 0$ . In the anomalous regime, two pairs of edge modes appear in both energy gaps, confirming both winding numbers being equal to 1, and in the Haldane

phase, only the edge mode in the  $g^0$ -gap remains. Since the stripe considered here has an upper and a lower boundary, pairs of counter-propagating edge modes are created. In the armchair-geometry, the  $\Gamma$ - and  $K$ -points both correspond to  $q_x = 0$ , thus the edge states appear in the center of the BZ in all cases.

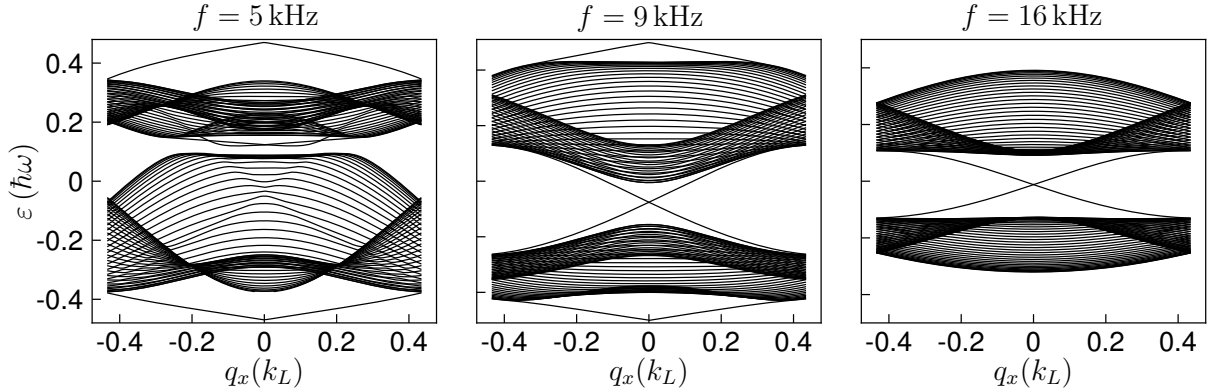


Figure 3.21: **Quasienergy bands in the armchair-geometry.** Quasienergy bands for  $V_0 = 6 E_r$ ,  $m = 0.25$  and  $f = (5, 9, 16)$  kHz as a function of the 1D quasimomentum along the  $x$ -direction, resembling the third, anomalous and Haldane regime. The calculations are performed without a harmonic trap and for  $N = 50$  pairs of sites.

The semi-finite system considered so far has a well defined, sharp edge and the two states having energies in the gap of the bulk bands directly correspond to the edge modes. In the experiment, the edge of the system is defined by the harmonic trapping potential, resembling a soft boundary. The trap can be included as a 1D potential along the finite  $y$ -direction, maintaining the periodicity of the lattice in the  $x$ -direction. This corresponds to adding diagonal terms to the Hamiltonian in Eq. 3.56, which depend on the distance of the corresponding site to the center, which is assumed to be located at  $y = 0$ , so  $m = N/2$ . Averaging over the time-dependence of the connection vector  $\delta_1$ , the  $m$ th A- and B-site have the same distance  $\Delta y(m)$  to the center of the unit cell, as in the symmetric case. The energy offset for the  $m$ th pair of sites is thus given by

$$U_T(m) = \frac{1}{2} m_K \omega_T^2 (\Delta y(m))^2. \quad (3.57)$$

In general, this describes a system exhibiting an infinitely steep wall at its upper and lower end with an additional harmonic confinement. To simulate the effect of the smooth boundary set by the trap and not only of the numerical edge, the system size needs to be increased considerably above  $N = 50$  which is used in Fig. 3.21.

In [141], the effect of different trapping potentials has been investigated in a 2D system being finite along both directions. The dispersion of the edge modes is expected to flatten when adding a soft confinement, like a harmonic trap, and auxiliary states appear in the gaps which nevertheless do not change the topological invariants. However, when using a harmonic confinement, the effective edge region is extended in real space and it becomes more difficult to distinguish the bulk from the edge states. One possibility

is to define the edge as the point in real space where no states have energetic overlap with the eigenstates in the center of the trap. Replacing the harmonic trapping potential with a steeper confinement leads to a better separation of the bulk and edge states, already in the case of a quartic potential [141]. The possible realization of a sharp edge in the experiment will be discussed in chapter 7.



# Chapter 4

## Overview of the experimental setup and techniques

In this chapter, the experimental setup and techniques are described that have been used for the measurements presented in this work. The first section provides an overview of the creation and detection of an ultracold atomic gas [4.1.1, 4.1.2], the optical lattice setup [4.1.3 and 4.1.5] and the optical dipole trap [4.1.4]. The experimental methods needed for the characterization of the different Floquet systems are illustrated in the second section, starting with the change of the quasimomentum by lattice acceleration [4.2.1]. This is used to measure the band gaps in the static or modulated lattice employing Stückelberg interferometry [4.2.2]. Moreover, it enables the determination of the atomic cloud's extent in quasimomentum space [4.2.3] and the application of an effective force to probe the Berry curvature distribution by Hall deflection measurements [4.2.4].

### 4.1 Experimental setup

All measurements reported in this work have been performed with a Bose-Einstein condensate (BEC) of  $^{39}\text{K}$ . The preparation of the BEC and technical details of the setup are described in great detail in other works [73, 75, 142, 143], hence only a short overview of the most relevant experimental steps is given in the first section. To detect either the real space position or momentum of the atomic cloud, absorption imaging is employed insitu or after a time-of-flight (TOF), as described in the second part. Subsequently, the loading of the atoms into the optical honeycomb lattice and its characterization using TOF measurements is presented as well as the determination of the harmonic trapping frequencies in the combined potential generated by the optical dipole trap and the honeycomb lattice. In addition to the two-dimensional (2D) honeycomb lattice in the  $x$ - $y$ -plane, there is also a one-dimensional (1D) lattice along the  $z$ -direction, which is not used in the measurements presented here, but can be an important tool for future experiments, as discussed in chapters 7 and 9. The optical setup and characterization of the vertical lattice is described in Sec. 4.1.5, as well as first attempts to load the atoms into a three-dimensional (3D) lattice configuration.

### 4.1.1 Creation of the BEC

The experimental setup allows for the creation of either a  $^{39}\text{K}$ - or  $^{87}\text{Rb}$ -BEC. The measurements reported here have been performed with  $^{39}\text{K}$ , since it exhibits an experimentally accessible Feshbach resonance, which allows for tuning of the inter-particle interactions, as described further below. Nevertheless, to prepare the  $^{39}\text{K}$  BEC, atoms of both species are employed to enable sympathetic cooling of  $^{39}\text{K}$  with  $^{87}\text{Rb}$ , thereby reducing the amount of  $^{39}\text{K}$  atoms that is lost during the cooling process.

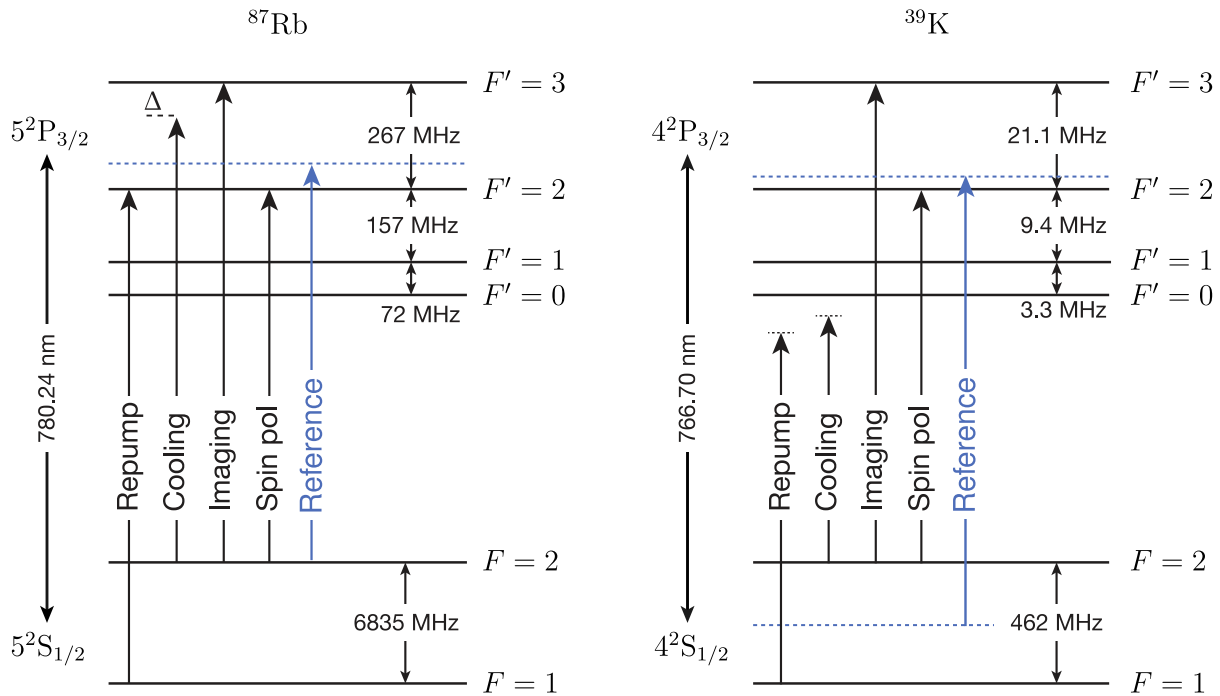


Figure 4.1: **Hyperfine levels of the D2-lines of  $^{87}\text{Rb}$  and  $^{39}\text{K}$ .** The optical transitions used in the experiment are sketched with black arrows. The reference transition (blue arrow) is used for locking the other lasers to this line. The data are taken from [144, 145].

The sequence starts with precooling of  $^{39}\text{K}$  and  $^{87}\text{Rb}$  in a double-species 2D<sup>+</sup> magneto-optical trap (MOT), where the atoms are optically cooled by counter-propagating laser beams and magnetically trapped along the transverse directions [146]. Another beam traveling along the longitudinal direction provides further axial cooling [147]. Subsequently, the atoms are pushed by an additional beam [148] into the next chamber, which is connected by a differential pumping section to maintain a lower pressure of  $\sim 10^{-10}$  mBar. Here, a 3D MOT [149, 150] is imposed on the atoms, which is loaded for  $\sim 3$  s in the case of  $^{87}\text{Rb}$  and during the last  $\sim 0.4$  s for  $^{39}\text{K}$ . The level structure of Potassium and Rubidium with the corresponding transitions used for cooling and imaging is shown in Fig. 4.1. After the 3D MOT phase the cloud is compressed [151] by increasing the magnetic field gradients and detuning the laser frequencies to prepare it for subsequent further cooling

by optical molasses [149, 150, 152], where the magnetic fields are switched off.

The next cooling steps are performed in the science chamber which is separated from the 3D MOT by another differential pumping section. The atoms are transported there by magnetic transport [153]: A series of overlapping coils is subsequently switched on in the Anti-Helmholtz-configuration to produce an adiabatically moving quadrupole potential, trapping the atoms and pulling them into the next chamber. To trap the atoms in the quadrupole fields, both species are transferred to the low field seeking state  $|F = 2, m_F = 2\rangle$  by a resonant light pulse. After recapturing the atoms in the quadrupole field of the 3D MOT coils, the transport is started. Due to the small diameter of the differential pumping section connecting the MOT and science chamber, a low pressure of  $\sim 6 \cdot 10^{-12}$  mBar is achieved in the latter. On the other hand, this reduces the transport efficiency, since about 80% of the  $^{87}\text{Rb}$  and 90% of the  $^{39}\text{K}$  atoms are lost when entering the differential pumping section.

In the science chamber, evaporative cooling is performed first in a magnetic quadrupole trap and afterwards in an optical dipole trap. To avoid Majorana spin-flips in the center of the magnetic trap, where  $B = 0$ , a tightly-focused, blue detuned plug beam is sent in laterally, repelling the atoms from that region [154, 155]. In this magnetic trap,  $^{87}\text{Rb}$  is cooled by forced microwave evaporation [156]: A microwave field is applied for a duration of  $\sim 10$  s, selectively transferring hot atoms from  $|F = 2, m_F = 2\rangle$  to the antitrapped state  $|F = 1, m_F = 1\rangle$ , and thus removing them from the trap. The energy levels are shifted by the Zeeman-effect depending on the position of the atoms in the magnetic field. Hence, the frequency of the microwave is swept to continuously match the resonance of the hot atoms, which are first located in the outer regions of the trapping potential and then approach the center of the trap during the evaporation. The microwave field is only acting on  $^{87}\text{Rb}$ , which sympathetically cools  $^{39}\text{K}$  [157], necessitating the rather long evaporation ramp due to the small inter-species scattering length of  $\sim 36 a_0$  [158].

To reach temperatures below the  $\mu\text{K}$ -regime, the evaporation continues in an optical dipole trap [129], formed by superimposing two laser beams with  $\lambda = 1064$  nm propagating at angles of  $90^\circ$  along the directions denoted by  $X$  and  $Y$ , as depicted in Fig. 4.2a. The polarizations of the beams are perpendicular and they are additionally shifted in frequency relative to each other by 200 MHz, thus preventing cross interference. The atoms are trapped in the intensity maximum due to the AC-Stark-effect (see 3.1), whereas the total potential is additionally bent along the vertical direction by gravitation. While the quadrupole field is ramped down, the intensity of the dipole trap beams is simultaneously increased to its maximal value, which is held for 1 s. During the last 70 ms of the quadrupole ramp-down, a small bias-field along the vertical direction is switched on to keep the atoms spin-polarized. To avoid possible spin-changing collisions in the subsequent evaporation,  $^{87}\text{Rb}$  and  $^{39}\text{K}$  are then both transferred to their ground state  $|F = 1, m_F = 1\rangle$  by microwave and radio-frequency sweeps, respectively. An additional laser pulse resonant with the  $F = 2 \rightarrow F' = 3$  transition removes remaining atoms in  $|F = 2, m_F = 2\rangle$ .

After switching off the quadrupole field, the current in the coils is ramped up again, now in the Helmholtz-configuration, realizing a homogeneous magnetic field directed

along the vertical axis which is used to tune the scattering lengths during the evaporation via Feshbach resonances (see below). In a first evaporation ramp, the intensity of the dipole trap beams is reduced exponentially within 6 s, and the inter-species scattering length is increased to  $\sim 90 a_0$ , utilizing the Feshbach resonance between  $^{87}\text{Rb}$  and  $^{39}\text{K}$  at 317.9(5) G [158], to enhance the sympathetic cooling of  $^{39}\text{K}$  [157, 159]. Since the mass of a Rubidium atom is about two times larger than the mass of a Potassium atom, it experiences a weaker total trapping potential and at the end of this first part, nearly all  $^{87}\text{Rb}$ -atoms are evaporated from the trap. Then, the evaporation continues for another 5 s with Potassium alone, increasing the K-K scattering length to  $\sim 150 a_0$  by exploiting the Feshbach resonance in the  $|F = 1, m_F = 1\rangle$  state at 403.3(7) G [160]. At the end, the atoms are held in the low potential for about 1 s to create the BEC.

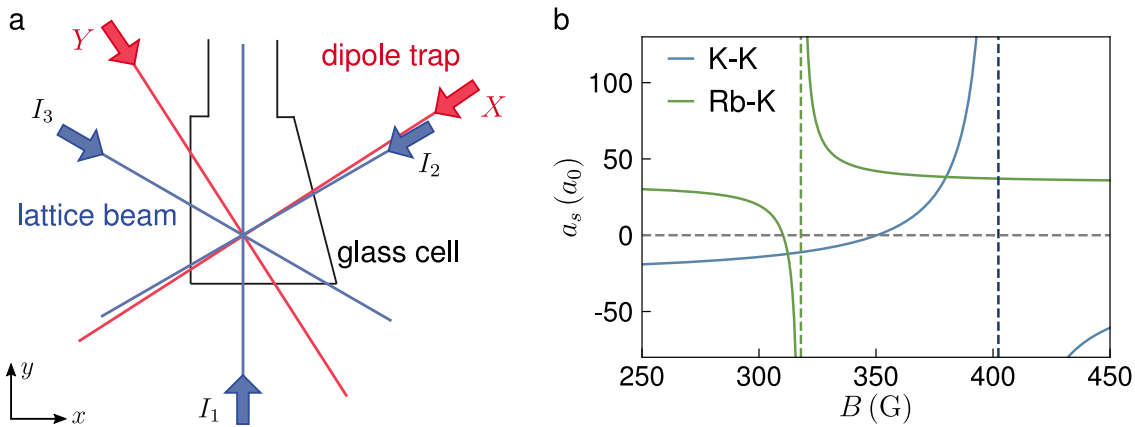


Figure 4.2: **Sketch of the optical setup and Feshbach resonances.** **a.** Sketch of the science chamber with the optical dipole trap beams (red) and the lattice beams (blue), denoted by  $I_j$ . The atoms enter the chamber from the top and the BEC is located at the intersection point of the beams. **b.** Calculated scattering lengths between  $^{39}\text{K}$ - $^{39}\text{K}$  (blue lines) and  $^{87}\text{Rb}$ - $^{39}\text{K}$  (green lines) depending on the magnetic field strength according to Eq. 4.1. The parameters are:  $B_0 = 403.3(7)$  G,  $\Delta B = 52$  G and  $a_{bg} = -29 a_0$  [160] for  $^{39}\text{K}$ - $^{39}\text{K}$  and  $B_0 = 317.9(5)$  G,  $\Delta B = 7.6$  G and  $a_{bg} = 34 a_0$  [158] for  $^{87}\text{Rb}$ - $^{39}\text{K}$ .

**Feshbach resonances** An important tool in experiments with ultracold gases are Feshbach resonances, which allow for the tuning of the s-wave scattering length  $a_s$  using magnetic or optical fields [161, 162]. The resonances between  $^{87}\text{Rb}$ - $^{39}\text{K}$  and  $^{39}\text{K}$ - $^{39}\text{K}$  are both induced by magnetic fields. The mechanism of a Feshbach resonance can be understood by considering the scattering process of two atoms with initial total energy  $E$ , being the sum of the internal energies of both atoms as well as their relative kinetic energy. In general, for cold bosonic atoms, it is sufficient to consider elastic s-wave scattering [161]. After the collision process, the system can either be in a scattering state or a molecular bound state. If the total energy of the final state is smaller than  $E$ , it is called an open channel, and if it is larger than  $E$ , the state is called a closed channel.

In the presence of a magnetic field, the internal states of the atoms are described by the projection of their angular momentum to the field axis. If the spin states of the individual atoms are different after the collision, while maintaining their total angular momentum projection, they generally possess a different magnetic moment compared to the initial state. Hence, by changing the magnetic field, the energy levels of the final and initial state can be shifted relative to each other. When the molecular bound state of a closed channel is shifted in energy such that it equals the initial energy of the two scattering atoms, the two channels strongly mix leading to a large increase in the scattering length [163, 164]. The resulting s-wave scattering length for a magnetic Feshbach resonance can be described as follows [161, 165]:

$$a_s(B) = a_{bg} \left( 1 - \frac{\Delta B}{B - B_0} \right), \quad (4.1)$$

where  $a_{bg}$  denotes the background scattering length in the absence of the magnetic field,  $\Delta B$  the width of the resonance and  $B_0$  its position. In Fig. 4.2b, the corresponding curve is shown for the two Feshbach resonances between  $^{87}\text{Rb}$ - $^{39}\text{K}$  and  $^{39}\text{K}$ - $^{39}\text{K}$ . Both resonances are located at rather high magnetic fields where in principle  $F$  and  $m_F$  are not good quantum numbers any more, since the electron and nuclear spin decouple and the system should be described in terms of  $J$  and  $I$  (*Paschen-Back-regime* [144]). Nevertheless, in the context of Feshbach resonances, the participating states are usually named after the zero-field eigenstates which they are connected to [161]. In the case of  $^{39}\text{K}$ , the ground state in the presence of the Feshbach field is  $|m_J = -1/2, m_I = +3/2\rangle$ , which is connected to  $|F = 1, m_F = 1\rangle$  at  $B = 0$ .

### 4.1.2 Imaging techniques

To obtain information about the BEC, absorption images [166] are taken either while the cloud is held in the lattice and the harmonic trap, or after releasing it from all potentials during TOF. For this purpose, a resonant light pulse is sent through the cloud along the vertical direction and is detected on a charge-coupled device (CCD) chip. When imaging in TOF, the dipole trapping potential and the lattice are switched off, and subsequently the Feshbach field is ramped down within 1 ms while the atoms fall. Depending on the purpose of the experiment, the TOF is varied between 3.5 ms and 15 ms. The imaging light is resonant with the  $F = 2 \rightarrow F' = 3$  transition (see Fig. 4.1), so the atoms are transferred to the  $|F = 2\rangle$  state by a repumper beam just before the imaging. In most measurements reported here, the atoms are imaged in the  $x$ - $y$ -plane, but it is also possible to take images along the propagation directions of the dipole trap, lattice and plug beams, mainly for alignment purposes.

The intensity of the light is reduced after traveling through the atomic cloud with density  $n$ , according to the *Beer-Lambert law* [167]:

$$I(x, y) = I_0 e^{-\sigma_0 \int n(x, y, z) dz} = I_0 e^{-\sigma_0 n_{\text{col}}(x, y)}, \quad (4.2)$$

where  $\sigma_0$  is the resonant scattering cross section for a two-level atom and  $n_{\text{col}}(x, y)$  denotes the column density. To determine the column density in the experiment, three images are taken: The first one contains the shadow cast by the atoms, the second image is taken with the same imaging pulse but without the atoms, and for the third image the light is switched off to determine the background of the CCD. The initial intensity distribution without the atoms,  $I_i(x, y)$ , is obtained by subtracting the dark image from the second image. For the final distribution  $I_f(x, y)$  after passing the atoms, the dark image is subtracted from the first image. Then, by employing these two difference images, the column density is obtained as:

$$n_{\text{col}}(x, y) = -\frac{1}{\sigma_0} \ln \left( \frac{I_f(x, y)}{I_i(x, y)} \right). \quad (4.3)$$

Using TOF imaging, the quasimomentum of the cloud in the lattice can be measured, as described in the next section. To obtain the real-space distribution of the atoms, insitu images are taken with the harmonic trap, lattice and Feshbach field being on - hence, the atoms are now imaged in the presence of a high magnetic field, shifting the resonance frequency. As mentioned in the last section, magnetic field strengths of around 400 G are used here, so the eigenstates of the atoms are described by their quantum numbers  $J$  and  $I$  with  $|m_J = -1/2, m_I = +3/2\rangle$  being the ground state. The imaging light has  $\sigma^-$ -polarization and as it does not change the nuclear spin, the only excited state that can be addressed is  $|m'_J = -3/2, m'_I = +3/2\rangle$ , forming a cyclic transition, since radiative decay into  $|m_J = +1/2, m_I = +3/2\rangle$  is dipole-forbidden. Due to the scattering of the imaging light, the atoms acquire a recoil velocity which leads to an increase in the cloud size if many photons are scattered [149]. To reliably determine the size and shape of the cloud insitu, the duration of the imaging pulse is reduced to  $2 \mu\text{s}$ , compared to  $40 \mu\text{s}$  used for the TOF images. This necessitates an increase of the light intensity far above the saturation intensity  $I_{\text{sat}}$ , to obtain useful images on the CCD, taking into account the relatively large magnification of  $\sim 16$  of the imaging system. In principle, the expression for the column density in Eq. 4.3 is now modified according to [168]:

$$n_{\text{col}}(x, y) = -\alpha \ln \left( \frac{I_f(x, y)}{I_i(x, y)} \right) + \frac{I_i(x, y) - I_f(x, y)}{I_{\text{sat}}}, \quad (4.4)$$

where the parameter  $\alpha$  is a generalization of the resonant cross section  $\sigma_0$  for a two-level atom, taking into account imperfections of the imaging beam as well as the level-structure of the ground and excited states. To obtain the full column density,  $\alpha$  would need to be calibrated experimentally [168]. However, in the measurements reported here, the insitu images are only used to determine either the width or the center-of-mass position of the cloud, whereas the actual density distribution is not relevant and moreover, the actual absorption due to the atoms is small in case of the insitu imaging. Hence, the second term can be neglected in the imaging processing, since it does not modify the resulting position or width of the cloud.

### 4.1.3 Honeycomb lattice setup

As described in chapter 3 and also shown in Fig. 4.2a, the optical honeycomb lattice is created by interfering three laser beams in the  $x$ - $y$ -plane with  $\lambda_L = 736$  nm. Since the lattice wavelength is blue detuned to the atomic resonances, it generates a repulsive potential and the  $X$ - $Y$ -dipole trap needs to be switched on in order to hold the atoms against gravity. The focus of both trap beams is elliptical with  $w_{xy} \sim 10 \cdot w_z$ , creating a relatively flat BEC, which could facilitate the loading of the atoms into a single plane of a vertical lattice, that is described in more detail in Sec. 4.1.5. The lattice beam foci have a similar extent in the  $x$ - $y$ -plane, but the waist along the vertical direction is only smaller by a factor of  $\sim 3$ . Thus, the confinement in the vertical direction is determined by the  $X$ - $Y$ -dipole trap beams, whereas in the  $x$ - $y$ -plane it can be adjusted by a third dipole beam, traveling along the  $z$ -direction. Since this beam is not involved in the creation of the BEC, a lower power of  $\sim 800$  mW is sufficient, compared to a maximum value of  $\sim 8 - 9$  W in each of the trapping beams. In the experiments characterizing the different Floquet topological systems, the  $X$ - $Y$ -trap is increased again after the evaporation, to compensate for the anticonfinement of the lattice. After that, the  $z$ -dipole beam is ramped up close to its maximum value and subsequently the lattice is ramped up exponentially within 200 ms to adiabatically load the BEC from its ground state in the harmonic trap into the lowest band of the lattice at  $\mathbf{q} = \Gamma$ .

**Lattice alignment and balancing** To align the lattice beams onto the BEC, the atoms can be imaged along each of the beam directions by combining resonant light with the lattice light on a beam-splitter. Owing to the larger atom number, the quality of the insitu images is better for  $^{87}\text{Rb}$  than for  $^{39}\text{K}$ , especially when imaging along the lattice directions, where the resolution is much lower than in the  $x$ - $y$ -plane. In order to align the lattice, the  $^{87}\text{Rb}$ -BEC is imaged insitu along each direction and afterwards the beams are moved to the corresponding position on the camera using motorized mirrors. Since the lattice light has a different wavelength than the imaging light and the imaging system is optimized for the latter, the position and size of the lattice beam foci will in general not be imaged correctly due to optical aberrations. Nevertheless, since the waist of the lattice beams is rather large compared to the extent of the BEC, this technique provides sufficiently good alignment. The position of the dipole trap minimum is slightly shifted when changing the trap depth, probably due to a small tilt of the focus of one beam. Hence, to maximize its depth, the lattice has to be aligned to the trap position which is used in the experiments. When creating a  $^{87}\text{Rb}$ -BEC, the final value of the dipole trap has to be higher than for  $^{39}\text{K}$  to compensate for the larger gravitational sag. The insitu images of the  $^{87}\text{Rb}$ -BEC are taken with the  $z$ -dipole trap at maximum and the  $X$ - $Y$ -trap being set to its final value, which is two times larger than the evaporation value of  $^{39}\text{K}$ , and roughly coincides with the evaporation value of  $^{87}\text{Rb}$ .

Due to drifts of the optical components over time, the alignment of the lattice slightly changes on a daily basis, leading to unequal intensities at the position of the atoms. This effect could be reduced by increasing the focus sizes, reducing however the maximal

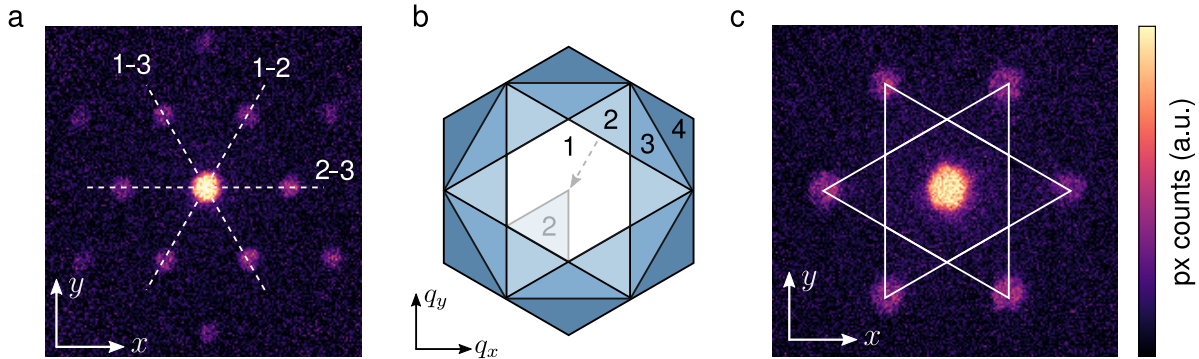


**Figure 4.3: Diffraction peaks and bandmapping in the honeycomb lattice.** **a.** Diffraction peaks of  $^{39}\text{K}$  at  $a_0 = 6 a_0$  after abruptly switching off the honeycomb lattice with  $V_0 = 6 E_r$  and  $t_{\text{TOF}} = 3.5$  ms. The white dashed lines illustrate the axes corresponding to the overlap between adjacent beams as denoted by the numbers, used for balancing of the lattice. **b.** Sketch of the first four Brillouin zones (BZs) of the honeycomb lattice (numbers), and the unfolding of the second BZ during bandmapping. **c.** Absorption image of  $^{39}\text{K}$  at  $a_0 = 6 a_0$  with  $t_{\text{TOF}} = 3.5$  ms after performing bandmapping at  $\mathbf{q} = \Gamma$  in the honeycomb lattice, exhibiting populations in several bands.

lattice depth available, which is already quite small with  $7 E_r$ , limited by the maximal output power of the Ti:sapphire (TiSa) laser. Instead, the imbalance is compensated by slightly modifying the relative intensities of the lattice beams. To measure the imbalance effect, the atoms are loaded into the lattice with nearly maximal depth and are then released by abruptly switching off the lattice and the dipole trap beams. The resulting density distribution after free expansion reflects the quasimomentum of the atoms in the lattice [169]. For a cloud exhibiting perfect phase coherence and hence being represented by a  $\delta$ -function at  $\mathbf{q} = \Gamma$  in reciprocal space, the pattern would consist of sharp peaks with a spacing corresponding to the width of the first BZ. In the experiment, the BEC is extended around  $\mathbf{q} = \Gamma$ , leading to a slight broadening of the peaks, as visible in the absorption image shown in Fig. 4.3a. If the lattice beams have unequal intensities at the position of the BEC, the visibility of the diffraction peaks is reduced along the directions of lower intensity. As denoted in Fig. 4.3a, the axes of the first order peaks can be assigned to the overlap of the two beams propagating along the adjacent directions. The relative intensity of each beam is obtained by summing up all pixels of the corresponding four first order diffraction peaks it contributes to and dividing the result by the total sum. Due to vibrations of the components and air flow on the table, the relative intensities also vary from shot to shot, so the relative weights are averaged over  $\sim 5 - 10$  images and then the intensities of the beams are adapted accordingly.

**Bandmapping** By switching off the lattice abruptly and imaging the cloud after free expansion, information about the quasimomentum of the atoms in the lattice can be obtained, but not about their energy. To quantify the amount of atoms being in a certain

energy band, the lattice potential is ramped down to perform bandmapping [170]. This corresponds to an unfolding of the periodic BZs, converting the energy bands back to the dispersion of a free particle. In this way, higher bands are mapped to larger momenta and atoms occupying different energy levels can be separated from each other by expansion. The first four BZs of the honeycomb lattice and their folding is illustrated in Fig. 4.3b. The points corresponding to  $\mathbf{q} = \Gamma$  in the second to sixth band are mapped to the same position, coinciding with the location of the first order diffraction peaks. In Fig. 4.3c an absorption image after bandmapping is shown, exhibiting atoms in the lowest band around  $\mathbf{q} = \Gamma$ , represented by the center peak, and atoms in the second to sixth band, distributed over the outer peaks. In the experiments, bandmapping is mostly performed at  $\mathbf{q} = \Gamma$ . Hence, it can not be directly inferred from the images in which of the bands 2-6 the atoms have been. But usually, only the relative population of the first two bands is of interest and it can be deduced from the relevant energy scales that excitations to the  $p$ -bands are negligible.

#### 4.1.4 Dipole trapping frequencies

Close to the center of the dipole trap, the generated potential can be approximated by a harmonic function. In the deflection measurements explained in Sec. 4.2.4, the atomic cloud is displaced in real space which leads to a restoring force of the harmonic trap, changing the position and quasimomentum of atoms. Hence, to correctly solve the equations of motion, the trapping frequencies need to be determined for the configuration used in the experiments, i.e. in the presence of the honeycomb lattice with  $V_0 = 6 E_r$  and the  $z$ -dipole beam. The dipole trapping frequencies are measured by exciting a breathing mode of the BEC, which can be observed insitu as oscillations of the width of the cloud. For an oblate cloud, the trapping frequency  $f$  can be obtained from the frequency  $\tilde{f}$  of the breathing oscillation according to [171]:

$$f = \sqrt{\frac{3}{10}} \tilde{f}. \quad (4.5)$$

The atoms are first loaded into the honeycomb lattice and dipole traps as described above, then the intensity of the  $z$ -dipole beam is lowered to 0 within  $10 \mu\text{s}$ , held there for  $3 \text{ ms}$  and ramped up again in  $10 \mu\text{s}$ . Due to the fast change of the confinement, a breathing oscillation is generated. The BEC is imaged insitu after a variable hold time and the width of the cloud is extracted by fitting a 2D Gaussian function to the absorption images. Hereby, the principle axes are oriented perpendicular to the propagation directions of the two trap beams, capturing the width of the Gaussian along the axis of the corresponding focus. From the fits, the Gaussian widths  $\sigma_X$  and  $\sigma_Y$  are extracted and plotted as a function of the hold time, as shown in Fig. 4.4. To obtain the oscillation frequencies, a damped cosine function is fitted to the oscillation:

$$\sigma(t) = A e^{-t/\tau} \cos(2\pi \tilde{f} t + \phi) + \sigma_0. \quad (4.6)$$

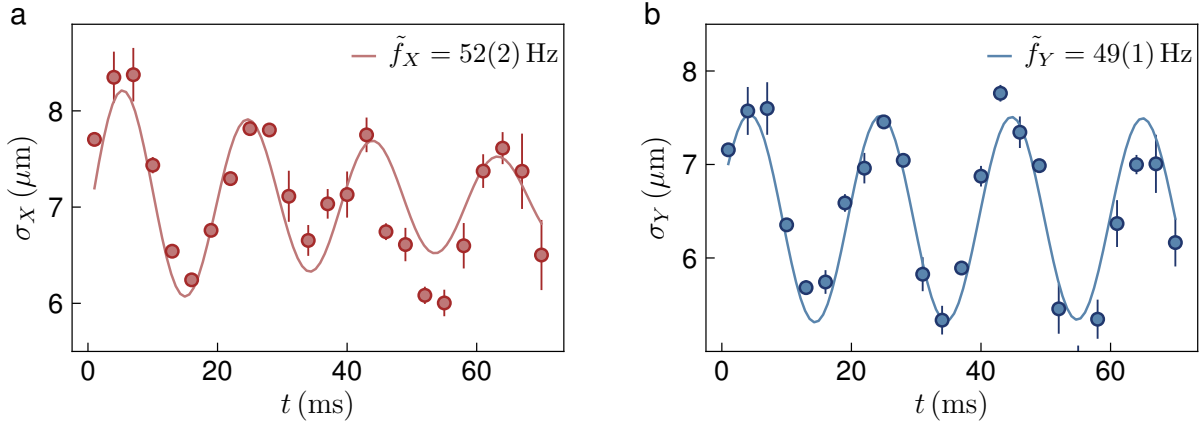


**Figure 4.4: Breathing mode in the dipole trap.** The oscillation of the insitu width (data points) along the directions of the dipole beam foci, denoted by  $\sigma_X$  and  $\sigma_Y$ , is measured after a fast ramp-down and -up of the in-plane confinement. The oscillation frequency  $\tilde{f}$  is extracted by fitting a damped cosine (solid lines) and the trapping frequency can be obtained from Eq. 4.5. Each data point is an average over 2-3 individual images and the errorbars denote the standard error. The measurement is performed with  $^{39}\text{K}$  at  $a_0 = 6 a_0$  in the presence of the honeycomb lattice at  $V_0 = 6 E_r$ , and the dipole beams are set to their corresponding values used in the experiments.

From the frequencies of the breathing modes, the trapping frequencies are obtained as

$$f_X = 27.9(7) \text{ Hz} \quad f_Y = 26.8(4) \text{ Hz}, \quad (4.7)$$

which are rather similar along both directions. Hence, in the calculations of the transverse deflections, the weighted arithmetic mean of

$$f_T = \frac{f_X/\sigma_{f_X}^2 + f_Y/\sigma_{f_Y}^2}{1/\sigma_{f_X}^2 + 1/\sigma_{f_Y}^2} = 27.0 \text{ Hz}, \quad \sigma_{f_T} = \sqrt{\frac{1}{1/\sigma_{f_X}^2 + 1/\sigma_{f_Y}^2}} = 0.4 \text{ Hz} \quad (4.8)$$

is used.

#### 4.1.5 Vertical lattice

In the experiments with the honeycomb lattice, the confinement along the vertical direction is mainly determined by the focus size of the optical dipole trap beams traveling along the  $X$ - and  $Y$ -directions, as described above. Hence, the system is not truly 2D, but each lattice site is effectively extended along the  $z$ -direction ('tubes'). This does not affect the topological properties of the Floquet systems studied in this work, as they are defined for 2D systems. Nevertheless, as discussed in chapter 7, increasing the vertical confinement by adding another lattice will be necessary to study strongly-interacting systems where the onsite-interaction energy is comparable to or larger than the tunneling.

Moreover, restricting the degrees of freedom in the transverse direction could help to reduce scattering processes and extend the lifetime of ultracold bosonic gases in modulated optical lattices (see chapter 9).

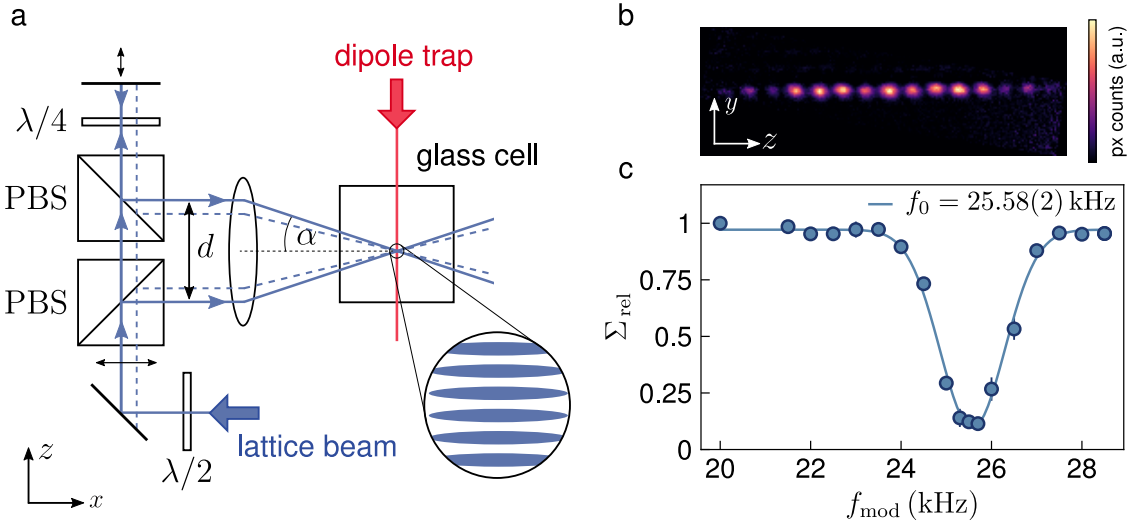


**Figure 4.5: Vertical lattice setup and characterization measurements.** **a.** Sketch of the setup used to create the vertical optical lattice. The lattice beam (blue line) is split into two parts with equal intensity with a relative distance of  $d$ , that interfere under an angle  $\alpha$ . Moving the beam on the first polarizing beam splitter (PBS) changes the distance and results in a different lattice spacing (dashed blue line). The  $z$ -dipole beam defining the confinement in the  $x$ - $y$ -plane is depicted as the red line. **b.** Diffraction peaks of  $^{39}\text{K}$  with  $a_s = 50 a_0$  imaged from the side after  $t_{\text{TOF}} = 15$  ms, used to determine the lattice spacing. The colorbar indicates the pixel sum. **c.** Calibration of the vertical lattice via parametric heating (see text). The relative pixel sum (data points) is measured as a function of the modulation frequency with a relative modulation amplitude of  $\sim 1\%$  and  $a_s = 50 a_0$ . The solid line indicates a Gaussian fit resulting in a resonance frequency of  $f_0 = 25.58(2)$  kHz which corresponds to  $V_Z = 360 E_{rZ}$ . The pixel sum is obtained from absorption images taken in the  $x$ - $y$ -plane after ramping down the lattice and  $t_{\text{TOF}} = 15$  ms. Each point is an average over 4 individual images and the errorbars denote the standard error.

**Setup** To realize a 1D lattice along the vertical direction, two blue-detuned laser beams with  $\lambda_L = 740$  nm enter the chamber from the side with a distance  $d$  and interfere under an angle  $\alpha$ , as depicted in Fig. 4.5a. This creates interference fringes along the  $z$ -direction with a lattice spacing of

$$a_Z = \frac{\lambda_L}{2 \sin(\alpha)}. \quad (4.9)$$

Compared to sending in two counter-propagating beams from above and below, this arrangement has the advantage, that the spacing of the lattice can be varied by changing

the distance between the beams, which is why it is often called 'accordion lattice' [172, 173]. The two beams are created out of a single one by splitting it at a polarizing beam splitter (PBS). To achieve equal intensities, a half-wave-plate is put before the first cube rotating the incoming linear polarization to  $45^\circ$ . The light being transmitted through the first PBS is then again transmitted at the second PBS, passes a quarter-wave-plate and is back-reflected at the top. The quarter-wave-plate is rotated such that after the second transit the polarization of the light propagating downwards is rotated by  $90^\circ$ , so that it is now reflected at the second PBS. The top mirror is mounted on a piezo, to enable active stabilization of the relative phase of the two beams, which was however not used so far.

Behind the cubes, the two beams are propagating parallel to each other, and are then focused onto the atoms by an aspheric lens with a focal length of  $f = 10\text{ cm}$  placed at a distance of  $\sim 9.34\text{ cm}$  to the atoms. After passing through the chamber the light is collected again by a similar lens and imaged onto a camera (not shown in Fig. 4.5a). To properly align the lattice beams to the position of the BEC, a part of the imaging light for  $^{39}\text{K}$  and  $^{87}\text{Rb}$  is sent through the same fiber as the lattice light. Then, the position of the BEC is imaged on the camera behind the lattice for each of the two beams separately and afterwards the corresponding beam is moved to this position, similar to the alignment of the honeycomb lattice.

To vary the lattice spacing, the entering beam can be moved on the first cube by a motorized mirror, which shifts the two beams relative to each other, as indicated by the dashed, blue line in Fig. 4.5a. This setup offers the possibility of changing the lattice spacing dynamically during the experiment to load the atoms into a single plane of the vertical lattice, realizing a true 2D system. In this case, the sequence would start with a large lattice spacing to fit the BEC into a single lattice site, and then the spacing is reduced adiabatically to compress the cloud into a plane, which was realized in [172]. As pointed out there, the compression needs to be performed carefully not to heat up the cloud.

In the setup presented here, it is technically possible to change the lattice spacing dynamically, but keeping the proper alignment of the beams during the compression is rather challenging. The vertical lattice has been added after the honeycomb lattice and dipole setup, so the available space on the experimental table is rather limited. This demands for a very compact setup as shown in Fig. 4.5a, which in turn offers less control, for example it is not possible to place additional mirrors behind the cubes to modify the paths of the two beams independently. Since it is not necessary to load a single plane to study the effects mentioned above, the spacing of the lattice is kept fixed close to its minimal value, corresponding to the maximal distance between the beams.

**Characterization of the vertical lattice** To determine the lattice spacing, the lattice is pulsed on within  $1\text{ ms}$  and the dipole trap is switched off simultaneously, leading to diffraction of the BEC, similar as described above for the honeycomb lattice. The interference pattern is recorded by absorption imaging after TOF. The momentum imparted on the atoms in the  $j$ th maximum is  $p_j = \frac{2\pi\hbar}{a_Z} j$ . Hence, by measuring the distance  $\Delta s$

between the maxima, the lattice spacing can be obtained as

$$a_Z = \frac{2\pi\hbar}{\Delta s m_K} t_{\text{TOF}}. \quad (4.10)$$

An example of such interference peaks is shown in Fig. 4.5b, measured at  $t_{\text{TOF}} = 15$  ms, which yields a lattice spacing of  $a_Z = 1.91 \mu\text{m}$ . The large lattice spacing results in a much smaller recoil energy compared to the honeycomb lattice of  $E_{rZ} \approx 371.6 \text{ Hz} \cdot h \approx 0.04 E_r$  for Potassium and accordingly higher lattice depths. When the atoms are loaded into the vertical lattice, the  $X$ - $Y$ -trap can be lowered or even switched off, since gravity is compensated by the lattice, and only the confinement in the  $x$ - $y$ -plane provided by the  $z$ -dipole beam is needed.

The lattice depth is calibrated via parametric heating [174, 175]: By weak modulation of the lattice intensity the atoms can be excited to a higher band if the frequency of the modulation matches the corresponding energy gap. Here, the modulation is treated as a time-dependent perturbation to the static lattice potential, allowing for transitions from the first band to higher bands with the same parity, i.e. the 3rd, 5th, 7th, band, etc. The width of the resonance is determined by the bandwidth of the participating bands, which makes this technique suitable for deep lattices where the bands are more flat. The amplitude of the modulation should not be too large in order to stay in the perturbative regime and to avoid deformation of the bands. In the experiment, the transition from the first to the third band is measured as atom loss, since the energy of the excited atoms is high enough to leave the trap.

The atoms are loaded into the lowest band of the vertical lattice by ramping up the laser intensity exponentially within 100 ms while all dipole beams are kept at constant values. Then, the lattice intensity is modulated with a relative amplitude of  $\sim 1\%$  for 100 ms and subsequently the atoms are held in the static lattice for another 50 ms before the lattice is ramped down linearly within 100 ms. Afterwards, the harmonic trapping potentials are switched off and the cloud is imaged after  $t_{\text{TOF}} = 15$  ms in the  $x$ - $y$ -plane. The number of atoms remaining in the trap is measured as a function of the modulation frequency, by summing up the pixel counts in a region-of-interest (ROI) containing the BEC. To obtain the resonance position, an inverted Gaussian is fitted to the pixel sum normalized by the counts far away from the resonance,  $\Sigma_{\text{rel}}$ , as shown in Fig. 4.5c. By comparing the measured resonance frequency to band structure calculations, the lattice depth is determined.

**Combination with the honeycomb lattice** To load the BEC into the 3D lattice, the respective intensities are ramped up after another, combined with ramping of the dipole trapping potential, in order to minimize heating effects due to fast compression of the cloud, which is illustrated in Fig. 4.6a. First, the  $z$ -dipole intensity is increased up to its final value followed by ramping up the vertical lattice while reducing the  $X$ - $Y$ -trap potential to 0. The cloud is held in this configuration for  $\sim 100$  ms to allow for redistribution in the planes of the vertical lattice. Then, the honeycomb lattice is ramped up exponentially within 100 ms together with the  $X$ - $Y$ -dipole beams, which are

either increased back to their initial magnitude (red curve), which is the final value of the evaporation, or to a lower value (dashed, green line) resulting in a lower overall confinement. The  $z$ -dipole trap is usually held at an intermediate value being about two times smaller than in the experiments with the honeycomb lattice alone. The honeycomb lattice is then calibrated, as described in the next section, in the presence of the vertical lattice. While the depth of the honeycomb lattice is slightly modified by the vertical lattice, the depth of the deep, vertical lattice, obtained from parametric heating, remains practically unchanged. Hence, the values derived from the calibration presented above can be used.

In general, the lifetimes of the  $^{39}\text{K}$ - and  $^{87}\text{Rb}$ -BEC in the 3D lattice are strongly reduced compared to loading the atoms only into the honeycomb or the vertical lattice. The loading scheme presented above has been optimized regarding the durations and shapes of the ramps as well as the depth of the confining dipole potentials, all of which has had only minor effects on the lifetimes. Similar results are obtained, for example, when ramping up the honeycomb and the vertical lattice simultaneously or keeping the dipole trap at a fixed value. In Fig. 4.6b, two measurements of the lifetime of the  $^{39}\text{K}$ -BEC are shown, performed at two different final values of the  $X$ - $Y$ -dipole ramp (red and green data points, corresponding to the red and green curves for  $V_{\text{dxy}}$  in Fig. 4.6a), with lattice depths  $V_Z = 120 E_r Z$  and  $V_{\text{hex}} = 4 E_r$ .

Both lattices are ramped up as described in Fig. 4.6a, then the atoms are held in the 3D lattice for a time  $t$ , and afterwards all potentials are switched off suddenly, resulting in interference peaks of the BEC, which are recorded in the  $x$ - $y$ -plane after a TOF of 7 ms. For the green data points, denoted by 'shallow trap', the overall confinement is reduced compared to the red data points, resulting in lower densities of the cloud. The decay of the pixel sum in the central peak, representing the atom number in the BEC, is rather comparable in both cases, and accordingly the lifetimes obtained from an exponential fit are very similar. In principle, the density of the cloud is increased in the 3D lattice compared to loading into the honeycomb or vertical lattice alone, but not as much as to cause heating effects due to three-body losses. This can be directly seen from the fact that changing the confinement (as in Fig. 4.6b) or the atom number in the BEC (by reducing the duration of the 3D MOT by a factor of 2) does not influence the lifetimes much. Moreover, if three-body-losses were present, the decay of the atom number should be fast in the beginning and then slow down, since the density is reduced by the atom losses, exhibiting a kink. However, the observed decay is rather purely exponential, as in Fig. 4.6b, or even linear. Increasing the scattering length has also reduced the lifetimes even more, although the density of the cloud is decreased in this case.

To further examine the cause of the reduced lifetime, the number of remaining atoms is measured as a function of the two lattice depths, when holding in the 3D lattice for a fixed time of 50 ms, which is shown in Fig. 4.7a. The ramp-up and detection are the same as in the lifetime measurements in Fig. 4.6b, whereas now the mean pixel sum is normalized to the maximum value, which occurs at  $V_{\text{hex}} = 0.5 E_r$  and  $V_Z = 120 E_r Z$ . In the left panel, the depth of the vertical lattice is scanned while  $V_{\text{hex}} = 4 E_r$ . Increasing the depth of the vertical lattice first results in a slight reduction of the atom number, but

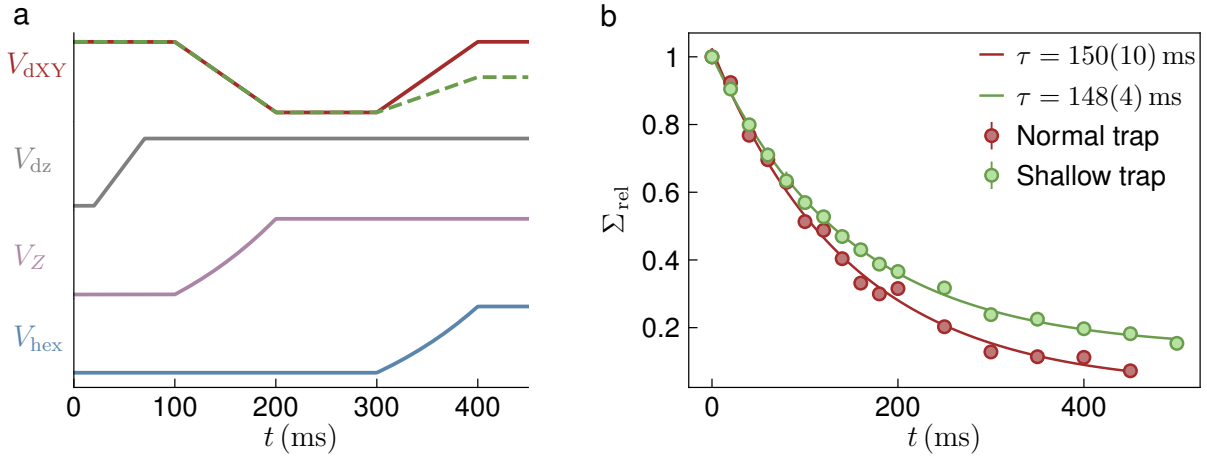


**Figure 4.6: Loading scheme and lifetimes in the 3D lattice.** **a.** Sketch of the sequence for ramping up the vertical lattice  $V_Z$  and the honeycomb lattice  $V_{\text{hex}}$ , combined with changes in the  $X$ - $Y$ -dipole trap  $V_{\text{dXY}}$  to allow for redistribution of the atoms after loading into the vertical lattice. The final confinement is varied by changing  $V_{\text{dXY}}$ . **b.** Lifetimes measured in the 3D lattice with  $V_Z = 120 E_{rZ}$  and  $V_{\text{hex}} = 4 E_r$  for  $^{39}\text{K}$  at  $a_s = 80 a_0$ . All potentials are switched off suddenly, and the cloud is imaged in the  $x$ - $y$ -plane after  $t_{\text{TOF}} = 7 \text{ ms}$ . Each data point represents the pixel sum in the central peak averaged over 3 individual images, normalized to the value at  $t = 0$ , the errorbars denote the standard error. For the green data points,  $V_{\text{dXY}}$  is reduced by a factor of two compared to the red data points, where the evaporation value was used. The lines denote an exponential decay fit to extract the lifetimes.

then it remains more or less constant for  $V_Z \gtrsim 200 E_{rZ}$ . In contrast, the atom number decreases almost linearly with the honeycomb depth, as shown in the right panel, which means that the reduction of the lifetime is more likely connected to the honeycomb and not the vertical lattice. This is confirmed by monitoring the cloud insitu while being held in the 3D lattice, which is performed with  $^{87}\text{Rb}$  to obtain a larger signal. In Fig. 4.7b, absorption images of the  $^{87}\text{Rb}$ -BEC are shown for increasing hold times, either in both lattices (first row), only the honeycomb lattice (second row) or only in the vertical lattice (last row), again with  $V_Z = 120 E_{rZ}$  and  $V_{\text{hex}} = 4 E_r$ . Holding in the 3D lattice results in heating of the cloud, which is only slightly reduced when just the honeycomb lattice is switched on. However, the atoms remain much colder even after 2 s hold time, when they are loaded only into the vertical lattice. From this it can be concluded that the main reason for the reduced lifetimes in the 3D must be connected to the honeycomb lattice. Moreover, the insitu images show that the atoms are primarily heated in the trap rather than directly lost from it.

Due to the different setup geometry and lattice spacings, a much higher laser power ( $\sim 700 \text{ mW}$  per beam) is necessary to reach the depth of  $4 E_r$  in the honeycomb lattice than for  $V_Z = 120 E_{rZ}$  in the vertical lattice ( $\sim 20 \text{ mW}$  per beam). Hence, the photon scattering rate from the honeycomb lattice is larger and detrimental effects due to

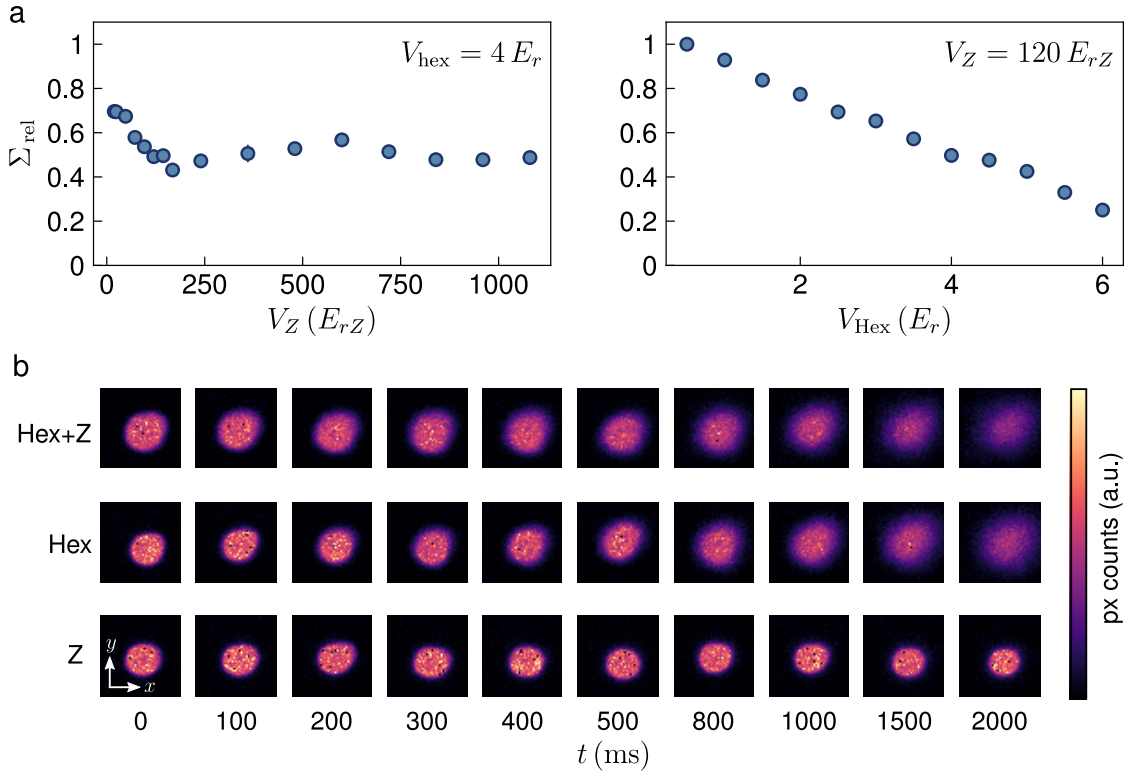


**Figure 4.7: Probing the effect of the honeycomb and vertical lattice separately.**

**a.** Mean relative pixel sum in the central diffraction peak after holding the  $^{39}\text{K}$ -BEC at  $a_s = 80 a_0$  in the 3D lattice for 50 ms as a function of the individual lattice depths. Each point is an average over 3 individual images, being normalized to the maximum sum occurring at  $V_{\text{hex}} = 0.5 E_r$  and  $V_Z = 120 E_{rZ}$ , the errorbars denote the standard error. The images are taken after suddenly switching off all potentials and  $t_{\text{TOF}} = 7 \text{ ms}$ , the dipole trapping potentials and the loading scheme are similar to the lifetime measurements in Fig. 4.6. Left panel: Scan of the vertical lattice depth at  $V_{\text{hex}} = 4 E_r$ , showing only small changes of the atoms number. Right panel: Increasing the honeycomb lattice depth for  $V_Z = 120 E_{rZ}$  strongly reduces the relative counts. **b.** In situ absorption images of the  $^{87}\text{Rb}$ -BEC taken in the  $x$ - $y$ -plane when being held in both lattices, only the honeycomb lattice, or only in the vertical lattice, (first to last row) with  $V_Z = 120 E_{rZ}$  and  $V_{\text{hex}} = 4 E_r$ . The hold time in the lattice is increased from left to right and denoted by the numbers below the last row. Heating of the BEC in the trap is observed, mainly when being loaded into the honeycomb lattice.

amplitude- or phase-noise of the laser beams are more pronounced. The intensity of all laser beams is actively stabilized by monitoring a small portion of the light exiting the optical fiber on the experimental table and comparing it to a reference value. The intensity spectrum of all lattice beams has been measured by Fourier transforming the signal of the control photodiodes resulting in a single peak at  $f \approx 60 \text{ kHz}$ , being present for the honeycomb and vertical lattice beams. Since this peak is also observed in the light

directly after the output of the TiSa-lasers, it must originate from there. However, the observed heating of the cloud in the trap can not be caused by this amplitude-noise, since the frequency of 60 kHz is too large: After absorbing a single energy quantum the atoms would directly be lost from the trap. The heating must originate from some source exhibiting frequencies in the lower kHz-regime, in order to heat up the BEC while keeping it trapped. Hence, the most probable reason for the heating in the 3D lattice is phase-noise from the honeycomb lattice beams. So far, the frequency of two beams can be shifted using acousto-optic modulators (AOMs), but the relative phases of the three beams are not stabilized. There are definitely drifts of the relative phase present due to the fibers, the different path lengths on the optical table, vibrations of the components, possible drifts of the optical breadboards and a constant air flow on the table from the top, due to the temperature stabilization.

When measuring the lifetime in the honeycomb lattice alone, the relative phase drifts of the lattice beams are negligible and the lifetimes are sufficient to perform the experiments described in this work, even when additionally modulating the intensity or phase to realize topological systems. However, to be able to use the 3D lattice configuration for future experiments, the implementation of an active phase stabilization for the honeycomb lattice is planned. In the intended setup, each lattice beam will be synthesized out of a right- and left-circular polarized part, of which the relative phase and intensity are actively stabilized [176, 177]. Referencing these for all three lattice beams will allow for precise and dynamic control of the polarization of each lattice beam, and at the same time will provide phase stability of the beams relative to each other.

## 4.2 Measurement techniques

In this section, the experimental techniques which are used for the characterization of the Floquet topological systems are presented. By acceleration of the lattice potential relative to the atoms, as described in Sec. 4.2.1, the quasimomentum of the cloud can be changed either adiabatically or diabatically. This is employed to probe the energy gaps in the static and modulated lattice [4.2.2], as well as to determine the extent of the cloud in momentum space [4.2.3] and to perform Hall deflection measurements. In Sec. 4.2.4 the deflection measurements as well as the corresponding theoretical simulations will be discussed.

### 4.2.1 Lattice acceleration: Creating a gradient

Since the honeycomb lattice is created by combination of three running waves, the interference pattern can be shifted in space by detuning the frequency of one or two beams relative to the others using AOMs. The frequency difference between the waves leads to a time-dependent phase shift  $\Delta\omega t$ , which corresponds to a moving pattern. If the frequency of the  $j$ th lattice beam has a constant offset of  $\Delta f_j = \Delta\omega_j/(2\pi)$ , the lattice

potential moves along the propagation direction of the beam with a constant velocity of

$$v_j = \frac{2}{3} \lambda_L \Delta f_j. \quad (4.11)$$

By changing the frequency detuning linearly in time, the interference pattern is accelerated with a constant acceleration

$$a_j = \frac{2}{3} \lambda_L \frac{\Delta f_j}{\Delta t}. \quad (4.12)$$

In the reference frame co-moving with the lattice, the atoms experience a force  $F_j = m a_j$  along the direction of the  $j$ th beam, which can be seen by transformation of the time-dependent Hamiltonian. In the lab frame, the Hamiltonian for a lattice potential moving by  $\mathbf{R}(t)$  reads:

$$\hat{H}(t) = \frac{\hat{\mathbf{p}}^2}{2m} + V_L(\hat{\mathbf{r}} - \mathbf{R}(t)). \quad (4.13)$$

The transformation into the co-moving frame is described by the unitary operator [73]

$$\hat{U} = e^{-i \frac{m}{\hbar} \dot{\mathbf{R}}(t) \cdot \hat{\mathbf{r}}} e^{\frac{i}{\hbar} \mathbf{R}(t) \cdot \hat{\mathbf{p}}}, \quad (4.14)$$

accounting for the changing position and momentum of the atoms. The time-dependent Schrödinger equation  $i\hbar\dot{\psi} = \hat{H}\psi$  in the co-moving frame is given by  $i\hbar\dot{\psi}' = \hat{H}'\psi'$  with  $\psi' = U\psi$ . The Hamiltonian is transformed as

$$\hat{H}' = U\hat{H}U^\dagger + i\hbar UU^\dagger. \quad (4.15)$$

Using the commutation relations between the position and momentum operator yields:

$$U\hat{H}U^\dagger = \frac{\hat{\mathbf{p}}^2}{2m} + V(\hat{\mathbf{r}}) + \frac{m\dot{\mathbf{R}}(t)^2}{2} + \dot{\mathbf{R}}(t) \cdot \hat{\mathbf{p}} \quad (4.16)$$

$$i\hbar UU^\dagger = m\ddot{\mathbf{R}}(t) \cdot \hat{\mathbf{r}} - \dot{\mathbf{R}}(t) \cdot \hat{\mathbf{p}} - m\dot{\mathbf{R}}(t)^2, \quad (4.17)$$

which leads to the following expression for the Hamiltonian in the co-moving frame:

$$\hat{H}' = \frac{\hat{\mathbf{p}}^2}{2m} + V(\hat{\mathbf{r}}) + m\ddot{\mathbf{R}}(t) \cdot \hat{\mathbf{r}} - \frac{m\dot{\mathbf{R}}(t)^2}{2}. \quad (4.18)$$

The term  $m\ddot{\mathbf{R}}(t) = -\mathbf{F}$  describes the fictitious force that the atoms experience in the moving inertial frame which is directed opposite to the motion of the interference pattern. This induces a translation in quasimomentum space along the direction of the force [62]:

$$\mathbf{F} = \hbar \frac{\Delta \mathbf{q}}{\Delta t}. \quad (4.19)$$

The measurements are performed in the lab frame, where the interference pattern of the lattice and hence the Brillouin zone is moving relative to the atoms, whereas the opposite

happens in the lattice frame, as depicted in Fig. 4.8. Since both reference frames are equivalent, the atoms can be effectively shifted through the Brillouin zone by accelerating the lattice.

The last term in Eq. 4.18 corresponds to the kinetic energy of the atoms moving with a velocity of  $\dot{\mathbf{R}}(t)$  along with the lattice, thus into the opposite direction of the force. In general, the atoms will perform Bloch oscillations in real- and momentum space under the influence of the force [62]. If the quasimomentum reaches the edge of the BZ, the velocity of the atoms is reversed and performs a periodic oscillation in time. The velocity from the lattice motion has the opposite sign and counteracts the Bloch velocity when the latter is positive. Hence, if bandmapping is performed at a finite quasimomentum in the first BZ, the atoms appear at  $\mathbf{q} = \Gamma$  and when the quasimomentum is increased across the edge of the BZ, they are mapped to  $\mathbf{q} = \Gamma$  in the next BZ. Due to the motion of the atoms relative to the harmonic trap, a non-negligible restoring force occurs when the lattice acceleration is applied for a long time, as described further in Sec. 4.2.4.

By comparing Eq. 4.12 and 4.19, the change in quasimomentum along the direction of lattice beam  $j$  can be related to the frequency detuning:

$$\Delta q_j = \frac{2\lambda_L m \Delta f_j}{3\hbar}. \quad (4.20)$$

For  ${}^{39}\text{K}$  and a laser wavelength of  $\lambda_L = 736.8 \text{ nm}$ , a frequency shift of  $\Delta f = 28.297 \text{ kHz}$  corresponds to  $\Delta q = 1 k_L$ . In the experiment, the frequencies of two laser beams can be modulated, allowing for the application of forces along arbitrary directions in the 2D BZ. The total quasimomentum is then given as the vector sum of the individual quasimomenta along the propagation directions of the corresponding lattice beams. For a certain final quasimomentum, the magnitude of the force is set independently by the duration  $\Delta t$  of the frequency ramp. Hence, compared to the application of a magnetic gradient, much larger forces can be realized by lattice acceleration, which can also be changed rather quickly and point along an arbitrary direction.

### 4.2.2 Stückelberg interferometry

As described in the last section, the quasimomentum of the atoms can be changed by lattice acceleration. This is applied to measure the energy gap between the two lowest bands of the honeycomb lattice depending on the quasimomentum using Stückelberg interferometry [178, 179]: Starting in the lowest band of the lattice at  $\mathbf{q} = \Gamma$ , the atoms are driven to the quasimomentum  $\mathbf{Q}$ , where the gap should be measured, as depicted in Fig. 4.8b. The applied force is large compared to the energy gap between the two bands (but smaller than the gap to the third band), which coherently transfers some atoms from the first to the second band during the acceleration. The initial state is denoted by  $|\psi_{\Gamma}^1\rangle$ , with all atoms being in the lowest band. After the acceleration, the state at  $\mathbf{Q}$  is a superposition of the two bands:

$$|\Psi_2(\mathbf{Q})\rangle = a_1 |\psi_{\mathbf{Q}}^1\rangle + a_2 |\psi_{\mathbf{Q}}^2\rangle. \quad (4.21)$$

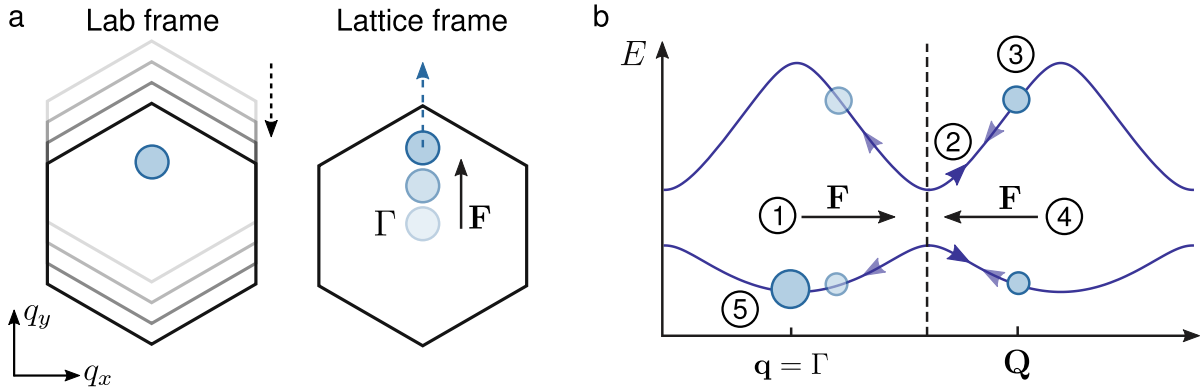


**Figure 4.8: Effect of the lattice acceleration and Stückelberg sequence.** **a.** In the lab frame, the Brillouin zone is moved across the atoms by the lattice acceleration, which leads to a change in quasimomentum in the reference frame co-moving with the lattice. **b.** Schematics of the Stückelberg interferometry used to probe the energy gaps. The atoms are loaded into the lowest band at  $\mathbf{q} = \Gamma$ , then a force is applied (1) to drive the atoms non-adiabatically to the desired quasimomentum  $\mathbf{Q}$ . The second band is populated during the acceleration (2) and then the atoms are held at  $\mathbf{Q}$  (3), acquiring different dynamical phases in the two bands. Afterwards, the force is reverted (4), and bandmapping is performed at  $\mathbf{q} = \Gamma$  (5) to measure the relative population in the lowest band.

Then, the atoms are held at  $\mathbf{Q}$  for a time  $t$ , acquiring a dynamical phase that depends on the energy band they are occupying:

$$|\Psi_3(\mathbf{Q})\rangle = a_1 e^{-\frac{i}{\hbar}E_1(\mathbf{Q})t} |\psi_{\mathbf{Q}}^1\rangle + a_2 e^{-\frac{i}{\hbar}E_2(\mathbf{Q})t} |\psi_{\mathbf{Q}}^2\rangle. \quad (4.22)$$

The atoms are driven back to  $\mathbf{q} = \Gamma$  with the same force applied in the opposite direction, leading again to a split of the populations in each band.

$$|\Psi_4(\mathbf{Q})\rangle = a_1 e^{-\frac{i}{\hbar}E_1(\mathbf{Q})t} (b_1 |\psi_{\Gamma}^1\rangle + b_2 |\psi_{\Gamma}^2\rangle) + a_2 e^{-\frac{i}{\hbar}E_2(\mathbf{Q})t} (c_1 |\psi_{\Gamma}^1\rangle + c_2 |\psi_{\Gamma}^2\rangle). \quad (4.23)$$

At the end of the sequence, bandmapping is performed at  $\mathbf{q} = \Gamma$  and the relative population in the lowest band is measured, which is given by

$$\begin{aligned} n^1(\mathbf{Q}) &= |\langle \psi_{\Gamma}^1 | \Psi_4(\mathbf{Q}) \rangle|^2 = |e^{-\frac{i}{\hbar}E_1(\mathbf{Q})t} (a_1 b_1 + a_2 c_1 e^{-\frac{i}{\hbar}(E_2(\mathbf{Q}) - E_1(\mathbf{Q}))t})|^2 \\ &= |a_1 b_1|^2 + |a_2 c_1|^2 + 2|a_1 b_1 a_2 c_1| \cos \left( \frac{E_2(\mathbf{Q}) - E_1(\mathbf{Q})}{\hbar} t + \phi \right). \end{aligned} \quad (4.24)$$

Hence, the population in the lowest band (and similarly in the second band) oscillates with a frequency that equals the energy gap at the quasimomentum  $\mathbf{Q}$ . In the experiment, the relative population is obtained from the bandmapping images by counting the pixels corresponding to the lowest band and dividing the result by the total pixel sum of both bands. In Fig. 4.9a, an example image is shown. The atoms in the lowest band appear

in the central peak and the atoms in the second band are distributed over the 6 outer peaks, as explained in the last section. To account for inhomogeneities in the background, arising from the spatially dependent intensity of the imaging beam, the pixel sum  $\Sigma_j$  of a certain peak is obtained by subtracting the background at the position of the peak. The pixels are summed inside a circular ROI with radius  $r$ , containing only the peak (yellow circles in Fig. 4.9a), and inside a larger ROI with radius  $r' = \sqrt{2}r$  and hence twofold area (white circles). Then, the pixel sum of the  $j$ th peak is defined as  $\Sigma_j = 2\Sigma_r - \Sigma_{r'}$  and the relative population in the lowest band is given by dividing  $\Sigma_0$  by the total pixel sum over all peaks. The energy gap  $\Delta E(\mathbf{Q})$  is obtained by fitting a damped cosine function to the population oscillation and extracting the frequency:

$$n^1(t) = A e^{-\frac{t-t_0}{\tau}} \cos(2\pi f(t - t_0)) + n_0. \quad (4.25)$$

To calibrate the depth of the honeycomb lattice, the energy gap at  $\mathbf{Q} = \Gamma$  is measured with Stückelberg interferometry and compared to bandstructure calculations. In principle, the gap could be measured at any point in the BZ, but at  $\Gamma$  the gap is maximal, which allows for shorter hold times  $t$  and leads to a higher amplitude of the population oscillation. In Fig. 4.9b, an example of a lattice calibration is shown, yielding an energy gap of  $\Delta E(\Gamma) = 6.67(4)$  kHz ·  $h$  which corresponds to a lattice depth of  $V_0 = 5.97 E_r$ . The lattice calibration is performed at  $a_s = 6 a_0$  with the dipole trap beams being set to their values used in the experiments and  $t_{\text{TOF}} = 3.5$  ms.

### 4.2.3 Momentum space width

In the following and in the next section, the BEC is represented as a semiclassical wavepacket. Due to finite temperatures and spatial confinement, the atomic cloud can not be described by a perfect  $\delta$ -function, but is broadened in momentum space. Since the involved mechanisms can be captured by single-particle physics, the measurements for the characterization of the Floquet systems are performed at a small but finite scattering length of  $a_s = 6 a_0$ , which also increases the extent in reciprocal space. The density distribution of the BEC in momentum space is described by a symmetric, two-dimensional Gaussian profile.

When a force is applied by lattice acceleration, the quasimomentum of the center-of-mass (CoM) in reciprocal space is changed according to Eq. 4.20. For the energy gap measurements, the overall quasimomentum can be approximated by the CoM-momentum, as the observed population oscillation is well described by a single cosine wave, rather than by a superposition of oscillations with different frequencies, which would correspond to the simultaneous probing of multiple energy gaps. In principle, the effect of the momentum space width also depends on the quasimomentum at which the energy gaps should be probed. Around the  $\Gamma$ -point, as used in the lattice calibrations, the dispersion is relatively flat, which facilitates the measurements compared e.g. to the  $M$ -point, where the steeper dispersion can lead to instabilities when holding the atoms there for a long time. Nevertheless, apart from measuring very small energy gaps, using Stückel-

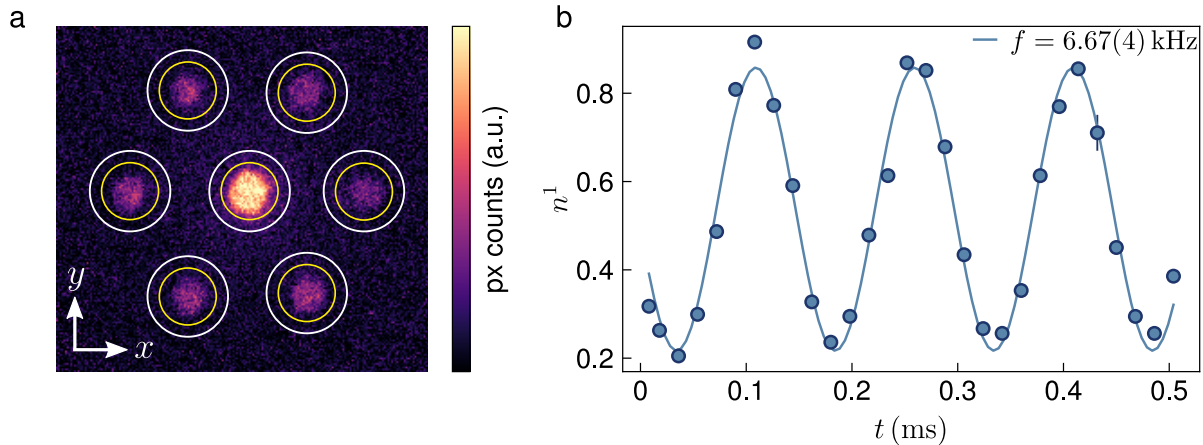
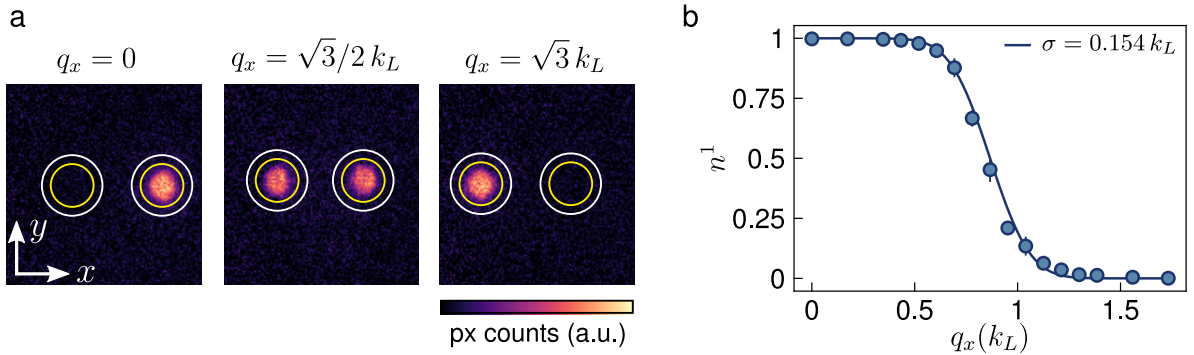


Figure 4.9: **Measuring energy gaps with Stückelberg interferometry.** **a.** Counting of the pixel sums to obtain the relative population in the lowest band after bandmapping. For each peak, the total counts are given by subtracting the pixel sum in the white circle from two times the pixel sum inside the yellow circle, effectively subtracting the background around the peak. The relative population in the lowest band is then obtained by dividing the pixel counts of the central peak by the total sum over all peaks. **b.** Stückelberg oscillation at  $\mathbf{Q} = \Gamma$  to calibrate the lattice. The frequency is determined from fitting Eq. 4.25 and corresponds to  $V_0 = 5.97 E_r$ . Each data point is an average over 1-2 individual images, the errorbars denote the standard error.

berg interferometry allows for an accurate determination of the energy gaps, also in the modulated lattice, as discussed in Sec. 5.1.1.

When probing the Berry curvature using Hall deflection measurements, the momentum space extent of the BEC has to be taken into account. Depending on the width of the cloud compared to the spread of the Berry curvature distribution, either not all atoms might experience a transverse deflection or only a certain part of the Berry curvature could be probed. In the experiments, the CoM position of the cloud in real space is detected, being the average over all quasimomenta (neglecting any scattering events), as described in the next section. Hence, to be able to theoretically simulate the deflections measured in the experiments, the width in momentum space needs to be determined. The momentum space extent slightly changes over time, mainly due to fluctuations of the atom number, and therefore it is probed along with every deflection measurement presented in this work and used in the corresponding calculations (see Sec. 5.1.1).

The momentum space width is determined by a knife-edge measurement, where the cloud is moved across the edge of the first BZ and the transfer into the second BZ is observed. A small force of  $Fa/h = 204$  Hz is applied along the  $x$ -direction, changing the CoM-quasimomentum adiabatically in small steps up to one reciprocal lattice vector. After every step, bandmapping is performed at the corresponding quasimomentum along the path, so the lattice intensity is ramped down while keeping a constant frequency offset. Since the images are taken in the lab frame, the atoms appear at  $\mathbf{q} = \Gamma$  as long as they



**Figure 4.10: Measurement of the momentum space width** **a.** Bandmapping images after  $t_{\text{TOF}} = 3.5 \text{ ms}$  when adiabatically changing the quasimomentum along the  $x$ -direction, crossing the edge of the first BZ at  $q_x = \sqrt{3}/2 k_L$  (second image). The relative population in the first BZ is obtained by dividing the pixel sum in the right peak by the total sum. The pixel sums for both peaks are counted by subtracting the background similarly as for the Stückelberg oscillations, using the ROIs depicted by the white and yellow circles. **b.** Relative population in the first band as a function of the CoM-quasimomentum, representing an integration of the Gaussian density distribution in momentum space inside the first BZ. Each data point is an average over 6 individual images and the errorbars denote the standard error. The momentum space width  $\sigma$  is extracted by fitting an errorfunction according to Eq. 4.26.

are still in the first BZ, due to the velocity from the moving lattice. When some atoms reach the edge of the BZ, they are mapped to  $\mathbf{q} = \Gamma$  in the next BZ, as mentioned in the last section. Hence, in the bandmapping images, two peaks appear and the population is gradually transferred from the first to the second one, as shown in Fig. 4.10a. The relative population in the first peak is determined by dividing the corresponding pixel sum by the total pixel sum in both peaks, whereas the counts of each peak are again obtained by subtracting the background at the position of the peak, as described in the last section (yellow and white circles in Fig. 4.10a). Plotting the relative population in the first peak as a function of the quasimomentum corresponds to integrating the Gaussian density distribution in reciprocal space within the first BZ, which is described by an error function:

$$n^1(q_x) = -\frac{1}{2} \left[ \text{erf} \left( \frac{q_x - \frac{\sqrt{3}}{2} k_L}{\sqrt{2}\sigma} \right) + 1 \right] + 1. \quad (4.26)$$

To obtain the momentum space width  $\sigma$ , this function is fitted to the measured relative populations in the first BZ, as shown in Fig. 4.10b.

#### 4.2.4 Deflection measurements and simulations

The Berry curvature associated with a certain energy band can be probed by Hall deflection measurements. This is used in the characterization of the Floquet systems to extract

the sign change of the local Berry curvature in the lowest band across the phase transition, which determines the change of the corresponding winding number (see Secs. 2.3, 5.1.3 and 5.1.4). In the experiments, a small force is applied to the atoms via lattice acceleration and they are moved adiabatically within a single band through the domain where the Berry curvature should be probed. The Berry curvature acts like a magnetic field in quasimomentum space [102, 103, 180, 181], adding a transverse component to the velocity of the atoms, which is directly proportional to it. Hence, by detecting the displacement in real space perpendicular to the direction of the force, a signal corresponding to the total amount of Berry curvature traversed in quasimomentum space is obtained. The full dynamics in real- and quasimomentum space can be described by the semiclassical equations of motion [182]:

$$\begin{aligned}\dot{x} &= \frac{1}{\hbar} \frac{\partial \varepsilon}{\partial q_x}(\mathbf{q}) - \frac{1}{\hbar} \left( F_y - \frac{\partial V_{\text{trap}}}{\partial y} \right) \Omega(\mathbf{q}) + \frac{F_x}{m_K} t \\ \dot{y} &= \frac{1}{\hbar} \frac{\partial \varepsilon}{\partial q_y}(\mathbf{q}) + \frac{1}{\hbar} \left( F_x - \frac{\partial V_{\text{trap}}}{\partial x} \right) \Omega(\mathbf{q}) + \frac{F_y}{m_K} t \\ \dot{q}_x &= \frac{1}{\hbar} \left( F_x - \frac{\partial V_{\text{trap}}}{\partial x} \right) \\ \dot{q}_y &= \frac{1}{\hbar} \left( F_y - \frac{\partial V_{\text{trap}}}{\partial y} \right),\end{aligned}\tag{4.27}$$

where  $\varepsilon(\mathbf{q})$  and  $\Omega(\mathbf{q})$  denote the energy dispersion and Berry curvature of the band and the terms  $\frac{F_j}{m_K} t$  describe the velocity of the atoms along the direction of the force due to the lattice acceleration. The harmonic trapping potential with radial trapping frequency  $f_T$  is given by:

$$V_{\text{trap}} = \frac{1}{2} m_K (2\pi f_T)^2 (x^2 + y^2).\tag{4.28}$$

To measure the transverse deflections, the atoms are first loaded at  $\mathbf{q} = \Gamma$  into the band that should be probed, which is the lowest band in most cases. Then, the quasimomentum is changed adiabatically to move through the Berry curvature, with the force being small compared to the energy gap to the next band in order to avoid excitations. The real space position of the cloud after the acceleration is detected by taking absorption images insitu at the final quasimomentum and the CoM-position is extracted from a 2D Gaussian fit. In order to obtain a more robust signal, the differential deflection is evaluated: The measurement is repeated with opposite chirality of the modulation, which inverts the Berry curvature and hence the transverse deflection. Measuring additionally the initial position of the cloud without applying a force enables the derivation of the displacement with respect to the bisecting axis, as depicted in Fig. 4.11a, which is defined as the differential deflection  $s_\perp$ .

The insitu position of the BEC on the camera changes from shot to shot due to the air flow on the table and vibrations of the optical components, with the largest contribution arising from the  $z$ -dipole beam: It mainly determines the position and width of the

cloud, and, at the same time, the beam path is rather long to be able to enter the experimental chamber from the top, which makes it especially susceptible to distortions. Since the scatter of the position between two single images can be larger than the expected transverse deflections, typically 30 – 40 experimental realizations are averaged to obtain the initial CoM-position and similarly for each of the final positions. This results in a standard error of the mean lying well below the absolute value of the differential deflection, allowing for reliable probing of the Berry curvature. The observed position scatter is not isotropic, but larger along the direction of the  $X$ -dipole beam, which propagates nearly parallel with lattice beam 2 (see Fig. 4.2a). A possible reason for this asymmetry is, that the focus of this dipole beam is slightly tilted out of the horizontal plane with respect to the other beam, which also leads to a shift of the potential minimum when changing its depth, as mentioned in Sec. 4.1.3. In the measurements presented in this work, the energy bands and the Berry curvature are sixfold rotational symmetric, so the Berry curvature can be probed around any of the high-symmetry points in the BZ. To minimize the errors in the transverse directions, the forces are directed approximately along the axis of the largest position scatter. When probing the Berry curvature around the  $\Gamma$ -point, the force is applied along the negative  $x$ -direction, measuring at  $\mathbf{q} = (-\sqrt{3}, 0) k_L$ . To probe a  $K$ -point, it is directed towards  $\mathbf{q} = (-\sqrt{3}/2, 1/2) k_L$ .

**Calculation of the transverse deflections** To calculate the transverse deflections, Eq. 4.27 is solved numerically in the time interval  $\Delta t$  used in the experiments, yielding the trajectories in real- and momentum space. The probing of the  $\Gamma$ - and  $K$ -point is simulated by a force directed along the  $x$ - and  $y$ -axis, respectively. The theoretical Berry curvature distribution is originally defined on a rhombic grid spanning the first BZ. To cover the full range of the trajectory including the momentum space extent of the BEC, it is then interpolated on a quadratic grid spanning several BZs with a step size of  $0.0145 k_L$ . This is the largest value at which the resulting transverse deflections do not change any more with the step size. The transformation from the rhombic to the quadratic grid gives rise to a factor of  $\sqrt{3}/2$  when expressing the Berry curvature in SI units. Accordingly, in Fig. 4.11b and c, the Berry curvature is plotted in units of  $1/(\sqrt{3}/2 |\mathbf{e}_1| |\mathbf{e}_2|)$ , with  $|\mathbf{e}_1| = |\mathbf{e}_2| = \sqrt{3} k_L$  (see Eq. 3.19 and Sec. 3.1.2).

To take into account the momentum space width, the equations of motion are integrated for about 7300 different initial points in momentum space lying inside a circle with radius  $r = 0.5 k_L$  centered around the starting point of the trajectory. Each point is assigned a weight according to the Gaussian density distribution in momentum space with width  $\sigma$ , as depicted by the green shading in Fig. 4.11b. The CoM positions in real- and momentum space are then calculated as the weighted average over the corresponding final points. In Fig. 4.11c, the trajectories along the transverse direction and the Berry curvature probed along the path are shown as a function of the quasimomentum set by the force, for different initial positions in quasimomentum space, which are indicated by the green arrows in Fig. 4.11b. Here, the calculation of the transverse deflection is illustrated for a force directed along the  $y$ -axis, probing the Berry curvature around the  $K$ -point in the Haldane regime.

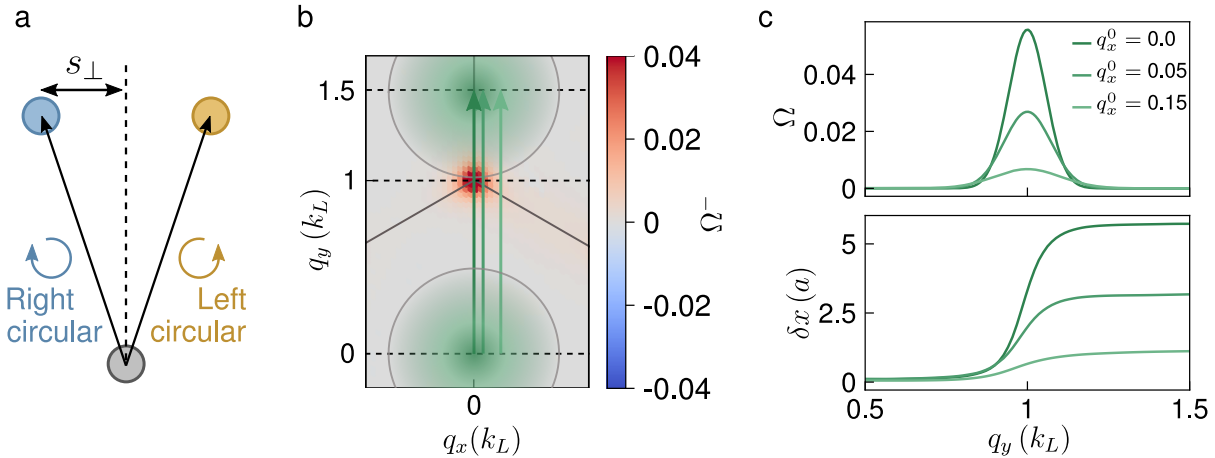


**Figure 4.11: Measurement and calculation of the transverse deflections.** **a.** Definition of the differential deflection  $s_{\perp}$ . The CoM position of the cloud is determined from insitu images without applying a force (gray circle) and after moving through the Berry curvature in reciprocal space for opposite chiralities of the modulation (blue and yellow circle), leading to opposite deflections. This gives a larger signal being more robust against position scatter (see text). The differential deflection is defined as half the distance between the two final points, measured perpendicular to the bisecting axis (dashed line). **b.** Calculation of the transverse deflection, illustrated for probing the Berry curvature around  $K$  in the Haldane regime with the force being directed along the  $y$ -axis. The equations of motion are solved numerically for various initial points (green arrows) in quasimomentum space lying inside a circle with  $r = 0.5 k_L$  (gray circle) and being weighted according to the momentum space width (green shading). The CoM positions are obtained as the weighted average over all final values. **c.** Berry curvature and calculated transverse position along different paths in quasimomentum space with initial positions of  $q_x^0 = (0, 0.05, 0.15) k_L$  and  $q_y^0 = 0$ , corresponding to the arrows in **b**, as a function of the quasimomentum along the path.

From the equations of motion it can be seen that the transverse velocity in real space is determined by the Berry curvature and the derivative of the energy dispersion along this direction. In the deflection measurements, the CoM in momentum space is moved along high-symmetry paths in the BZ, connecting e.g.  $\Gamma$  and  $K$ . The transverse derivative of the energy dispersion is symmetric with respect to these lines and vanishes for quasimomenta lying on the path. Since the momentum distribution is symmetric with respect to the center point, the derivative along the center part is zero and the contributions from the neighboring paths cancel each other. This means that without the harmonic trap the transverse velocity would only be affected by the Berry curvature when probing along high-symmetry lines. In the presence of the trapping potential, a displacement from the trap minimum in real space leads to a change of the quasimomentum along the corresponding direction. Hence, due to the transverse deflection initially induced by the Berry curvature, the transverse quasimomentum acquires a finite value and the path

starts to deviate from the high-symmetry line, now being affected by the derivative of the dispersion. Overall, this means that the transverse deflection is not only proportional to the Berry curvature any more.

Since the force in the deflection measurements is small, the lattice acceleration is applied for a long time  $\Delta t$ , which leads to large longitudinal displacements and to a significant effect of the harmonic trap along this direction, as discussed in Sec. 5.1.3. However, along the transverse direction, the displacements are small and thus the restoring force of the trap has only a minor effect. The simulated final transverse CoM-quasimomenta are  $q_{\perp} < 0.005 k_L$  for all experimental parameters used in this work. Thus it can be assumed that the measured transverse deflections are indeed directly proportional to the Berry curvature, allowing for the determination of the sign changes of the Berry curvature from sign changes of the deflections.



# Chapter 5

## Characterization of the Floquet topological regimes

Anomalous Floquet settings have been realized experimentally in photonic systems [100, 101, 115, 117, 183]. These platforms turned out to be especially useful for studying the propagation of chiral edge modes, since the system can be initialized in a state where mainly the edge states are populated. However, a full experimental characterization of the anomalous Floquet topological phase, including the properties of the bulk and edge states, is still missing. So far, an experimentally feasible scheme has been presented to realize a variety of topological regimes, including anomalous Floquet systems, by periodic modulation of the tunnel couplings in an optical honeycomb lattice. In this chapter the invariants describing the different topological regimes are obtained experimentally by energy gap and local deflection measurements using the techniques described in the last chapter. Moreover, the complete two-dimensional (2D) phase diagram is mapped out and the mixing of the two lowest bands across the phase transitions is used to load and probe also the second band. The chapter concludes with measurements of the condensate lifetime at the  $\Gamma$ -point in all regimes.

### 5.1 Determination of the winding numbers

Floquet topological phases are characterized by winding numbers associated with the different quasienergy gaps which give the net number of chiral edge modes crossing the respective gap. As described in Sec. 2.3.2, a phase transition occurs when a quasienergy gap  $g^j$  within or between Floquet Brillouin zones (FBZs) is closing, which changes the winding number in this gap by  $\Delta W^j$ :

$$\Delta W^j = Q_s^j, \quad (5.1)$$

where the topological charge  $Q_s^j$  of the band touching point at  $(\mathbf{q}_s, \lambda_s)$  is given by the sign change of the local Berry curvature across the phase transition. Hence, to determine the phase boundaries and the development of the winding numbers, the quasienergy gap closings and the change of the local Berry curvature at these points need to be probed.

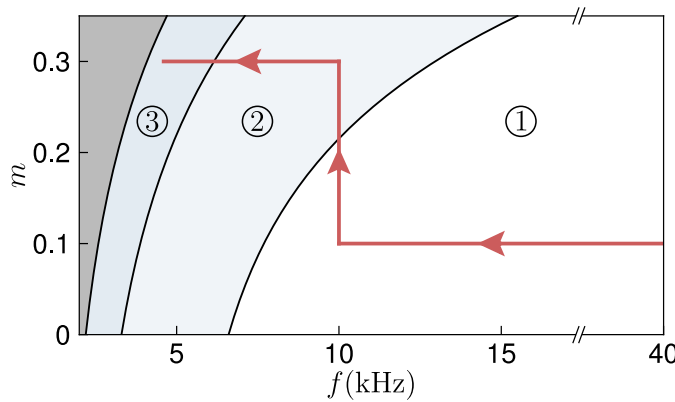


Figure 5.1: **Phase diagram of the modulated lattice as a function of the modulation frequency  $f$  and modulation amplitude  $m$ .** The blue shadings indicate the different topological phases: ① The Haldane phase, ② anomalous phase and ③ the third phase. The red line marks the path along which the modulation parameters are varied to determine the winding numbers in the different topological regimes.

To locate the phase transitions, the quasienergy gap between the two lowest bands is measured at various quasimomenta and modulation parameters. The latter are varied along a path in  $f$ - $m$ -space, where  $f$  denotes the modulation frequency and  $m$  the relative modulation amplitude, which traverses all three topological regimes characterized here, as depicted by the red line in Fig. 5.1. The path starts in the high frequency limit where the quasienergy gap between the FBZs is much larger than the gaps within a single FBZ, at a modulation amplitude and frequency of  $m = 0.1$  and  $f = 40$  kHz. Then, the frequency is reduced to 10 kHz while keeping  $m$  fixed, traversing the Haldane regime. The transition to the anomalous regime is crossed by increasing the modulation amplitude to  $m = 0.3$  at a constant frequency of 10 kHz. Finally, the parameter regime of the third phase is entered by decreasing the frequency to 4.6 kHz at  $m = 0.3$ . In this way, the modulation parameters are varied along a smooth path connecting the high frequency limit, where the properties of the system are known, to the other topological regimes. The specific shape of the path is chosen mainly for technical reasons: At high modulation frequencies, small amplitudes are favorable due to longer lifetimes and reduced coupling to the  $p$ -bands, both of which will be discussed later in this chapter. The third regime is probed for a larger modulation amplitude, since for  $m = 0.1$  the modulation frequency would need to be reduced to very small values below  $f \approx 3.8$  kHz, where the gap sizes that can be probed using Stückelberg interferometry are restricted, as described in the next section.

The scan of the modulation parameters is performed at three different quasimomenta:  $\Gamma$ ,  $K$  and  $M$ . In the inversion-symmetric, 2D honeycomb lattice the phase transitions can only occur via energy gap closings at the high-symmetry points in the first Brillouin zone (BZ) [184], so it is sufficient to probe these points for the modulation scheme investigated in this chapter. After determination of the modulation parameters  $\lambda_s$  and quasimomenta  $\mathbf{q}_s$ , at which the phase transitions occur, the change of the Berry curvature is probed

across the transitions. The quasimomentum is fixed at  $\mathbf{q} = \mathbf{q}_s$ , whereas the modulation parameters are varied and the Berry curvature is compared before and after each phase transition:

$$\Delta\Omega^\mu(\mathbf{q}_s) = \Omega^\mu(\mathbf{q}_s, \lambda_s + \epsilon) - \Omega^\mu(\mathbf{q}_s, \lambda_s - \epsilon), \quad (5.2)$$

with  $\mu$  denoting the upper or lower band and  $\lambda$  the modulation frequency or amplitude, respectively. Depending on the quasienergy gap that is closing, the topological charge of the corresponding singularity is determined by the Berry curvature change in the lower or upper band (see Eq. 2.61)

$$Q_s^0 = \text{sgn}(\Delta\Omega^-(\mathbf{q}_s)) \quad Q_s^\pi = \text{sgn}(\Delta\Omega^+(\mathbf{q}_s)). \quad (5.3)$$

Since the Berry curvature of the upper band equals the inverse Berry curvature of the lower band,  $\Delta\Omega^+ = -\Delta\Omega^-$ , the winding numbers can be obtained by probing any of the two bands. In the experiments presented in this section, the Berry curvature is measured in the lower band. This is realized by performing Hall deflection measurements, as described in the previous chapter: The cloud is driven through the phase transition point  $\mathbf{q}_s$  and the differential transverse deflection  $s_\perp^-$  at the end of the path is recorded, being proportional to the total amount of Berry curvature traversed along the path. Hence, the sign change of the Berry curvature across the phase transitions, and therefore the topological charge, can directly be inferred from the sign change of the transverse deflection:

$$Q_s^0 = \text{sgn}(\Delta s_\perp^-(\mathbf{q}_s)) \quad Q_s^\pi = -\text{sgn}(\Delta s_\perp^-(\mathbf{q}_s)), \quad (5.4)$$

where

$$\Delta s_\perp^-(\mathbf{q}_s) = \text{sgn}[s_\perp^-(\mathbf{q}_s, \lambda_s + \epsilon)] - \text{sgn}[s_\perp^-(\mathbf{q}_s, \lambda_s - \epsilon)]. \quad (5.5)$$

Using the deflection measurements, the topological charges of the band touching points are derived, which enables the determination of both winding numbers in all three topological regimes using the connection to the high-frequency limit.

### 5.1.1 Stückelberg interferometry in the modulated lattice

The quasienergy gap between the two lowest bands is probed using Stückelberg interferometry. As mentioned above, the gaps are measured at the  $\Gamma$ -,  $K$ -, and  $M$ -point for different modulation parameters. The starting point for all following measurements is the Bose-Einstein-Condensate (BEC) at  $\mathbf{q} = \Gamma$ , adiabatically loaded into the lowest band of the static honeycomb lattice with  $V_0 = 6 E_r$ . Then, the intensity modulation of the lattice beams is ramped up within  $t_r = 5T$  for all modulation frequencies used here, held for an integer number of periods and ramped down again within  $t_r$ , as depicted in Fig. 5.2a. For all quasienergy gap measurements, the modulation amplitude is ramped up and down linearly in time at a constant modulation frequency (Fig. 5.2c and d). The final values  $m_f$  and  $f_f$  are varied according to the path in parameter space shown in Fig. 5.1.

To probe the quasienergy gap at a certain point  $\mathbf{Q}$  in the BZ, a large force is applied to the atoms by accelerating the lattice simultaneously with the intensity modulation,

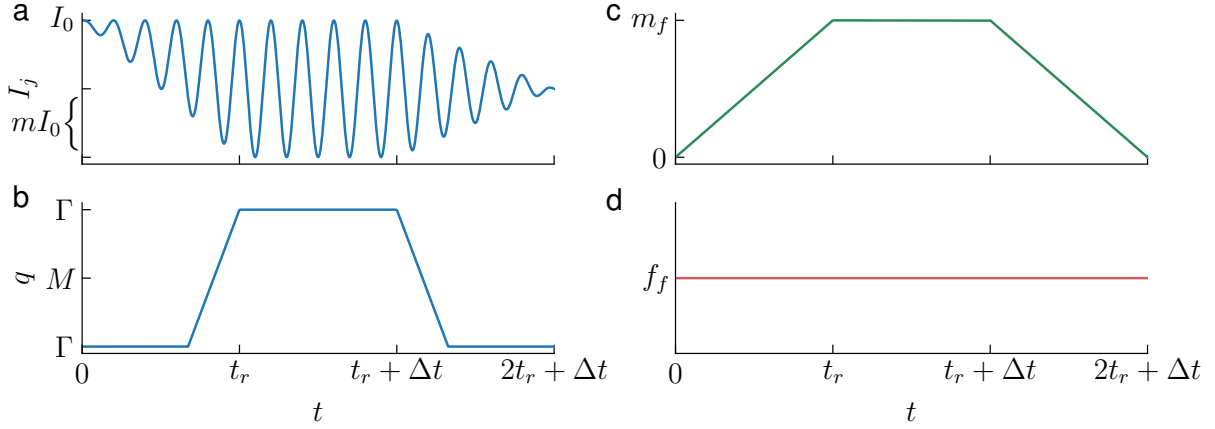


**Figure 5.2: Schematics of the lattice intensity and quasimomentum ramps to measure the quasienergy gaps via Stückelberg interferometry.** **a.** The intensity modulation  $I_j(t)$  of each lattice beam is ramped up within  $t_r = 5T$ , starting at  $I_j = I_0$ , held for  $\Delta t = NT$ ,  $N \in \mathbb{N}$ , and then ramped down within  $t_r$ , now ending at  $I_j = I_0 - mI_0$ . Subsequently, the intensity of all beams is ramped down to 0 to perform bandmapping (not shown). Here,  $\Delta t = 5T$  and  $j = 1$  is illustrated. The intensities of the other two beams follow the same trace but phase shifted by  $2\pi/3$  and  $4\pi/3$ , respectively. **b.** Non-adiabatic change of the cloud's quasimomentum to perform the Stückelberg interferometry at  $\mathbf{Q} = \Gamma$ . The ramp starts with a delay such that the final quasimomentum is reached when the intensity ramp is finished, similarly for the ramp-down. **c** and **d**. Ramp of the modulation amplitude  $m$  and modulation frequency  $f$  used in the Stückelberg interferometry. The amplitude is changed linearly to its final value  $m_f$  at constant frequency  $f = f_f$ .

changing their quasimomentum non-adiabatically from  $\Gamma$  to  $\mathbf{Q}$ . Since the force is large compared to the quasienergy gaps between the two lowest bands, a coherent superposition between the first and second band is created, as described in Sec. 4.2.2. To probe the quasienergy bands, being eigenvalues of the effective Hamiltonian, the hold time  $\Delta t$  at  $\mathbf{Q}$  is set to integer multiples of the modulation period  $T$ . The time needed to move the atoms to  $\mathbf{Q}$  is usually smaller than  $t_r$ , so the lattice acceleration starts later, such that it finishes simultaneously with the modulation ramp-up (Fig. 5.2b). After the hold time at  $\mathbf{Q}$  in the modulated lattice, the atoms are accelerated back to  $\Gamma$  while ramping down the modulation. Subsequently, the lattice is ramped down to perform bandmapping and the relative population in the first band is counted (see Sec. 4.2.2).

The hold times are varied between  $\Delta t = 0$  and  $\Delta t = 22T$ , providing 23 points for the oscillation fit for each quasienergy gap that is measured. In all gap measurements presented in Sec. 5.1.2, a force of  $Fa/h \approx 4.081$  kHz is used. The time needed to accelerate the atoms by one reciprocal lattice vector from  $\Gamma$  to  $\Gamma$  is  $t_\Gamma \approx 0.163$  ms, to probe the other high symmetry points the acceleration times are  $t_M \approx 0.082$  ms and  $t_K \approx 0.094$  ms. For most modulation frequencies, the ramp time  $t_r = 5T$  is larger than the acceleration times, but for very high modulation frequencies they are comparable (i.e.  $t_r = 0.125$  ms

for  $f = 40$  kHz). The start of the lattice acceleration is then shifted forward or backward in time accordingly.

The band gap at a certain quasimomentum is determined by fitting a cosine function to the oscillation of the relative population  $n^1(t)$  in the lowest band and extracting the frequency (Sec. 4.2.2). In the periodic spectrum of the modulated lattice, the quasienergy differences can be measured between bands within the same FBZ or between bands in different FBZs. In the experiments performed here, the gap between the two lowest bands and their lowest order Floquet copies are probed. But at high modulation frequencies and amplitudes, the coupling to the Floquet copies of the  $p$ -bands increases, which means that more than two bands can be populated in the Stückelberg sequence. This leads to an oscillation of the lowest band population with several frequencies, which is taken into account by fitting a sum of two cosines:

$$n^1(t) = e^{-(t-t_1)\gamma} A_1 \cos(\omega_1(t-t_1)) + A_2 \cos(\omega_2(t-t_2)) + n_0^1. \quad (5.6)$$

Here,  $A_1, A_2, \omega_1, \omega_2, t_1, t_2, \gamma, n_0^1$  are all free fit parameters and the main oscillation frequency corresponding to the quasienergy gap between the two lowest bands is defined as having the larger amplitude. For most modulation parameters,  $A_2 \ll A_1$ , confirming that normally the oscillation is well described by a single quasienergy gap being probed. The damping constant  $\gamma$  takes into account heating and depletion effects, as well as dephasing due to the finite momentum space width of the cloud. These effects are visible in the time-of-flight (TOF) images at long hold times, i.e. when probing the quasienergy gaps at low modulation frequencies where  $T$  is large. They arise predominantly when the atoms are held for long times at a maximum of the quasienergy dispersion, as it appears in the first band at  $K$  in the Haldane regime. Since the ramp-up of the modulation starts at  $\Gamma$ , the atoms will be transferred to the second band when probing the anomalous or third regime, as the quasienergy gap is closing. However, since the atoms will be populating the second band anyway during the Stückelberg sequence, this simply adds an offset to the population oscillation.

Due to the extent of the cloud in momentum space, the quasienergy gaps are actually probed in a finite region around the center point set by the lattice acceleration. The population oscillation  $n^1(t)$  would correspond to a sum of several oscillations with similar frequencies close to the gap frequency. However, the measured oscillations are better described by a sum of two cosines with unequal frequencies as in Eq. 5.6 (see also Fig. 5.13b), whereas the momentum space width mainly leads to a damping of the oscillation due to dephasing, as mentioned above. This is also confirmed by the very good agreement of the measured gaps with the theoretical calculations, which take into account only the Center-of-mass (CoM) of the cloud in momentum space.

Starting with the atoms in the first band, the quasienergy gap between the first and second band,  $g^0$ , or between the the first band and the lower copy of the second band,  $g^\pi$ , can be measured. To probe the spectrum of the effective Hamiltonian, the hold times are integer multiples of the modulation period, so the gap oscillation is scanned with time steps of size  $T$ . The cosine wave needs to be sampled with at least two points per cycle (*Nyquist–Shannon sampling theorem*), which means that the minimal gap oscillation

period that can be probed is  $2T$ . Hence, the maximal gap frequency that can be measured in this way is

$$\omega_{\max} = \frac{\omega}{2}. \quad (5.7)$$

This complicates on the one hand the measurements at low modulation frequencies, restricting the accessible range of quasienergy gaps. On the other hand, it can be used to determine which of the two possible quasienergy gaps,  $g^0$  or  $g^\pi$ , is probed. Since  $g^0 + g^\pi = \hbar\omega$ , if the first gap is smaller than  $\hbar\omega_{\max}$ , the other one is necessarily larger, so in the experiment the measured gap is

$$\Delta E_{\text{exp}} = \min(g^0, g^\pi). \quad (5.8)$$

Starting in the high frequency limit where  $g^\pi \gg g^0$ , the gap within the zone, i.e.  $g^0$ , is probed. Reducing the modulation frequency decreases  $g^\pi$  until  $g^\pi = g^0 = \hbar\omega/2$ , after what  $g^\pi$  is measured. This is used in the next section to detect not only the phase transitions, but also to deduce which of the two quasienergy gaps is closing.

### 5.1.2 Measurement of the phase transition points

The quasienergy gaps between the two lowest bands are probed for various modulation parameters along the path depicted in Fig. 5.1, covering the three different topological regimes. For each set of modulation parameters, Stückelberg interferometry measurements are performed at the high symmetry quasimomenta  $\Gamma$ ,  $K$  and  $M$ , consisting of 23 population measurements per oscillation, each of which is averaged over 3-4 individual images. The oscillations are fitted according to Eq. 5.6 and the main oscillation frequency, corresponding to the minimal gap  $\min(g^0, g^\pi)$ , is plotted against the modulation parameters to detect the phase transitions indicated by gap closings. The resulting relative gaps  $\Delta E/(\hbar\omega)$  at  $\Gamma$  are presented in Fig. 5.3 together with the theoretical values (solid lines), calculated using the six-band model introduced in Sec. 3.2.2. The results at  $K$  and  $M$  are shown in Fig. 5.4.

At the  $\Gamma$ -point, the quasienergy gap closes two times, indicating two phase transitions, at  $f = 10$  kHz around  $m = 0.2$  and close to  $f = 6.4$  kHz and  $m = 0.3$ . At the  $K$ - and  $M$ -point, the quasienergy gaps remain open for all modulation parameters, confirming that the band touchings at  $\Gamma$  constitute the only phase transitions that occur in this range. Moreover, the measured quasienergy gaps are in excellent quantitative agreement with the theoretical calculations for all quasimomenta and modulation parameters. At high modulation frequencies, where  $\hbar\omega$  is much larger than the combined width of the two lowest bands,  $g^\pi \gg g^0$ , and hence  $g^0$  is measured, as indicated by the gray arrow in the upper right area of Fig. 5.3. The first two quasienergy bands in the high frequency limit are plotted in the upper right panel of Fig. 5.3 for  $f = 30$  kHz and  $m = 0.1$ , illustrating the large separation between the Floquet copies of the lowest bands. Reducing the modulation frequency decreases  $g^\pi$ , while  $g^0/(\hbar\omega)$  increases, until  $g^0 = g^\pi = \hbar\omega/2$  at the cusp around  $f = 15$  kHz. For lower modulation frequencies,  $g^\pi < g^0$ , and  $g^\pi$  is measured in the Stückelberg interferometry. The subsequent increase of the modulation

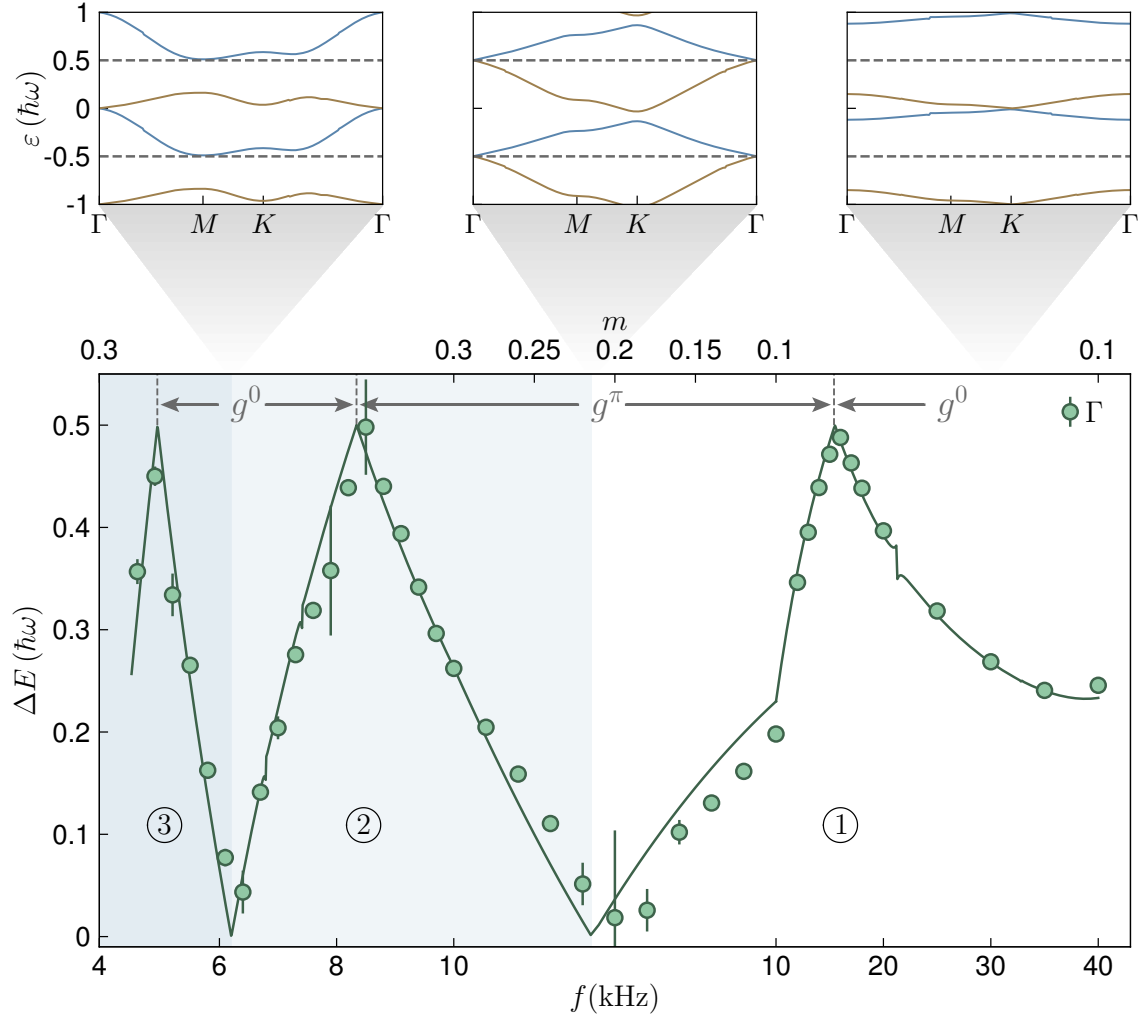


**Figure 5.3: Quasienergy gaps at  $\Gamma$  across the phase transitions.** Measured relative quasienergy gaps (data points) at  $\mathbf{Q} = \Gamma$  and theoretical values (solid lines) as a function of the modulation amplitude and frequency. Every data point is the result of a fit to the Stückelberg population oscillation consisting of 23 points, each being an average over 3-4 individual images. The errorbars denote fitting errors. The blue shadings and the numbers illustrate the different topological phases separated by the closings of the relative gap. The gap maxima signal if the gap  $g^0$  or  $g^\pi$  is measured, as indicated by the gray arrows and annotations. Upper panels: Calculated dispersion of the two lowest bands in the extended zone scheme for  $m = (0.3, 0.215, 0.1)$  and  $f = (6.2, 10, 30)$  kHz, from left to right. The first two plots show the band touchings at quasienergies 0 and  $\pi$ , marking the phase transitions, the last plot illustrates the high frequency limit.

amplitude reduces  $g^\pi$  further since the effective bandwidth increases, until the lowest band and the lower Floquet copy of the upper band touch, as depicted in the central upper panel of Fig. 5.3. Hence, at the first phase transition, the quasienergy gap at  $\Gamma$

closes between FBZs which means that  $W^\pi$  is changing. For even higher modulation amplitudes and lower frequencies, the bands cross and hybridize at the Floquet zone edge and the gap reopens and increases again until  $g^\pi = g^0 = \hbar\omega/2$  at the second maximum around  $f = 8.2$  kHz and  $m = 0.3$ . Now, the relative gap within the FBZ is smaller again and closes at the second phase transition, which means that now  $W^0$  is changed. The following cusp then signals again a change of the measured quasienergy gap as indicated in the plot. By measuring the quasienergy gaps, the phase transition

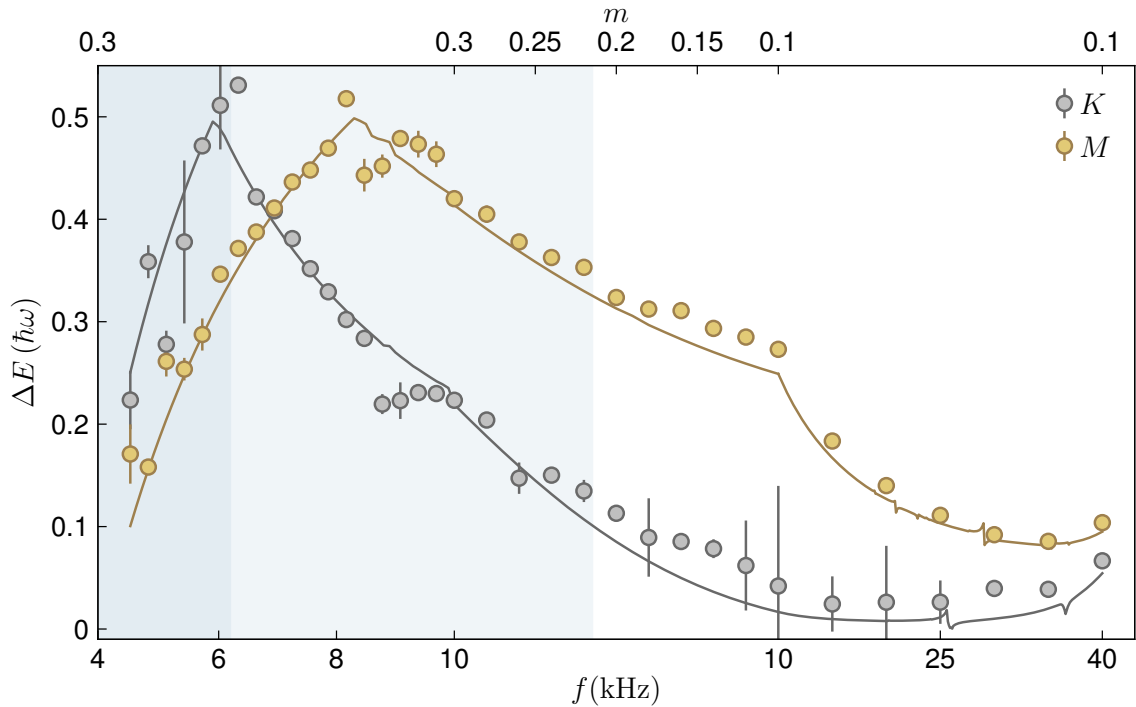


**Figure 5.4: Quasienergy gaps at  $K$  and  $M$  across the phase transitions.** Measured relative quasienergy gaps at  $\mathbf{Q} = K$  (gray data points) and  $\mathbf{Q} = M$  (yellow data points) and theoretical values (solid lines) as a function of the modulation amplitude and frequency. Every data point is the result of a fit to the Stückelberg population oscillation consisting of 23 points, each being an average over 3-4 individual images. The errorbars denote fitting errors. The blue shadings again illustrate the different topological phases obtained from the gap closings at  $\Gamma$ . The quasienergy gaps at  $K$  and  $M$  remain open over the full range of modulation parameters scanned here.

points are detected as gap closings at  $\mathbf{q} = \Gamma$  and the modulation parameters at which they occur are determined. Following the maxima of the relative gap allows for identification of whether the gap is closing within or between FBZs and hence which of the winding numbers  $W^0$  and  $W^\pi$  is changing at which set of modulation parameters. In the next two sections, the measurements of the local Berry curvature are described, quantifying the amount by which the respective winding numbers are changed at the phase transitions and thus completing the characterization of the topological regimes.

### 5.1.3 Deflection measurements in the lowest band

To determine the topological charges at the phase transition points, the sign change of the local Berry curvature is probed via Hall deflection measurements as described in Sec. 4.2.4. Due to the extend of the cloud in reciprocal space, the Berry curvature integrated over the corresponding area is probed. To characterize the topological regimes, the deflection measurements are performed along paths in reciprocal space traversing the  $\Gamma$ -point or both Dirac points,  $K$  and  $K'$ , once with the complete cloud.

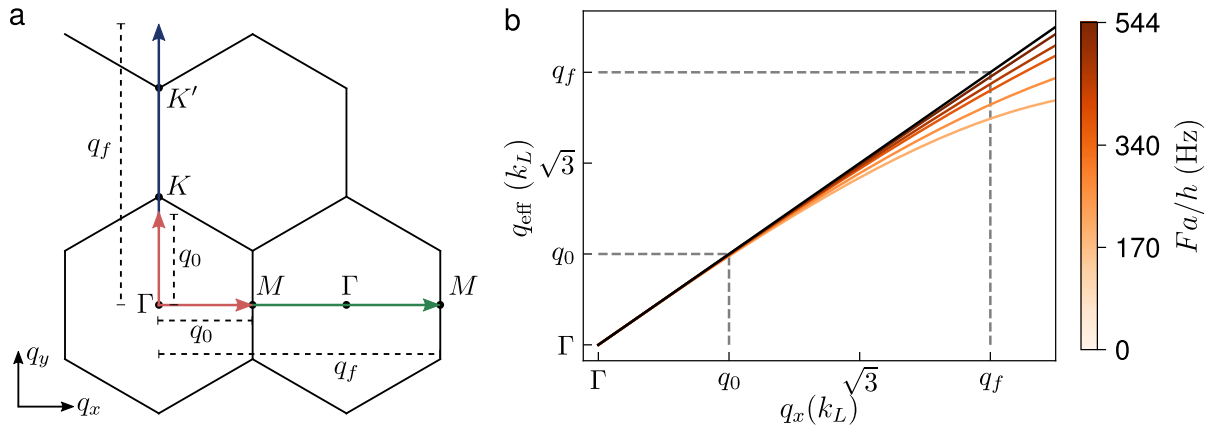


**Figure 5.5: Schematics of the paths in reciprocal space and calculated final quasimomenta including the harmonic trap. a.** Paths in quasimomentum space traversed to probe the Berry curvature at  $\Gamma$  (green arrow) or at  $K$  and  $K'$  (blue arrow) in the Haldane and anomalous regime, denoted as  $\Gamma$ - and  $K$ -directions in the text. The cloud is accelerated to the final value  $\Delta q = q_f$  along the direction of the force and the modulation is ramped up during the first part of the path (red arrows), ending at a distance of  $\Delta q = q_0$ . **b.** Effective longitudinal quasimomentum in the presence of the harmonic trap with  $f_T = 27.0(4)$  Hz calculated using Eq. 4.27 as a function of the quasimomentum  $q_x$ , set by the lattice acceleration when driving along the  $\Gamma$ -direction. The colors represent different forces and the black line depicts the values without the trap, i.e.  $q_{\text{eff}} = q_x$ . The gray dotted lines mark the quasimomentum after the modulation ramp-up at  $q_x = q_0$  and at the final point of  $q_x = q_f = 1.5\sqrt{3}k_L$ , used for measuring the Berry curvature in the Haldane and anomalous regime.

The measurements start at the  $\Gamma$ -point in the first BZ and the quasimomentum is changed by an amount  $\Delta q = q_f$  along the respective direction using lattice acceleration, as depicted in Fig. 5.5a by the green and blue trajectories. To avoid excitations to the second band during the acceleration, the forces are chosen to be much smaller than the quasienergy gaps that occur along the path. In turn, this leads to large displacements in real space along the longitudinal direction in the range of  $\sim 100 \mu\text{m}$  and hence to significant restoring forces of the harmonic trap, counteracting the lattice acceleration in real and momentum space. Thus, the length of the path in reciprocal space is reduced from  $q_f$ , the value set by the lattice acceleration, to an effective value  $q_{\text{eff}}$ . The change of

the quasimomentum along the path due to the harmonic trap is shown in Fig. 5.5b for different forces, calculated using Eq. 4.27. Here, the black line represents the ideal values  $q_x = q_f$  without the harmonic trap. Along the transverse direction, the displacements in real space are small and the effect of the harmonic trap is negligible, which means that the transverse quasimomentum is essentially unchanged and the cloud is still driven along the high-symmetry paths in reciprocal space, as described in Sec. 4.2.4. Hence, the contribution of the transverse dispersion derivative is vanishing and the measured deflections are indeed directly proportional to the integrated Berry curvature.

Since the energy gap at  $\Gamma$  is closing at both phase transitions, the atoms will be excited to the second band when ramping up the modulation amplitude in the anomalous or third regime while the cloud resides at  $\Gamma$ . To prevent these excitations and load the complete BEC into the lowest band in each of the topological sectors, different ramp-up-schemes are used depending on the modulation parameters. The general idea is to move the cloud in quasimomentum space by  $\Delta q = q_0 = 0.5\sqrt{3}k_L$  while the modulation is ramped up, to avoid the gap closing at  $\Gamma$  (see Fig. 5.7 and red arrows in Fig. 5.5a). The corresponding schemes are chosen such that no transverse deflection is expected during the ramp-up. Hence, the Berry curvature is effectively probed along paths from  $q_0$  to  $q_{\text{eff}}$  along the respective directions, traversing the  $\Gamma$ - and both  $K$ -points approximately once with the cloud. The effect of the harmonic trap during the ramp-up is minor, since the longitudinal displacement is still small when accelerating by  $q_0$ , even for the smallest force of  $Fa/h = 170$  Hz used in this work. So the absolute value of the quasimomentum after the ramp-up can be assumed as  $q \approx q_0$ , which is also shown in Fig. 5.5b, where the lines for all forces coincide at  $q_x = q_0$ .

**Ramp-up scheme for large modulation frequencies** To probe the Berry curvature in the Haldane regime and for large modulation frequencies in the anomalous regime, the modulation amplitude is ramped up linearly from  $m = 0$  to  $m = m_f$  within a time  $t_r$ , while the cloud is accelerated by  $q_0$  along the  $\Gamma$ - or  $K$ -direction. When measuring along the  $\Gamma$ -direction, this corresponds to probing the Berry curvature along the line  $M-\Gamma-M$ . The ramp-up time  $t_r$  is determined by rounding up the time  $\Delta t$  that is needed to change the quasimomentum by  $q_0$  with a given force to full cycles of the modulation. The modulation frequency is held at a constant value  $f_f$ . The ramp-up scheme is presented in Fig. 5.6 for  $f = 10$  kHz and  $m = 0.16$ . The values of the modulation amplitude and frequency during the course of the ramp-up are drawn as a white line in the quasienergy plot in Fig. 5.6d, with the final quasimomentum after the ramp-up noted at its end. The procedure is applied when measuring along the  $\Gamma$ - as well as along the  $K$ -directions.

This ramp-up scheme is used for probing the Berry curvature in the Haldane and anomalous regime for modulation frequencies  $f_f > f_{\text{lim}}$ , whereas the value of  $f_{\text{lim}}$  depends on the modulation amplitude: For  $m < 0.3$ , it is set to  $f_{\text{lim}} = 7$  kHz and for  $m = 0.3$  to  $f_{\text{lim}} = 8$  kHz, which is discussed in more detail in appendix D. For frequencies smaller than  $f_{\text{lim}}$ , the overall quasienergy gaps at the quasimomenta of the moving BEC during the ramp-up become too small to avoid excitations to the second band. Moreover, with decreasing modulation frequency, the modulation parameters will cross the phase

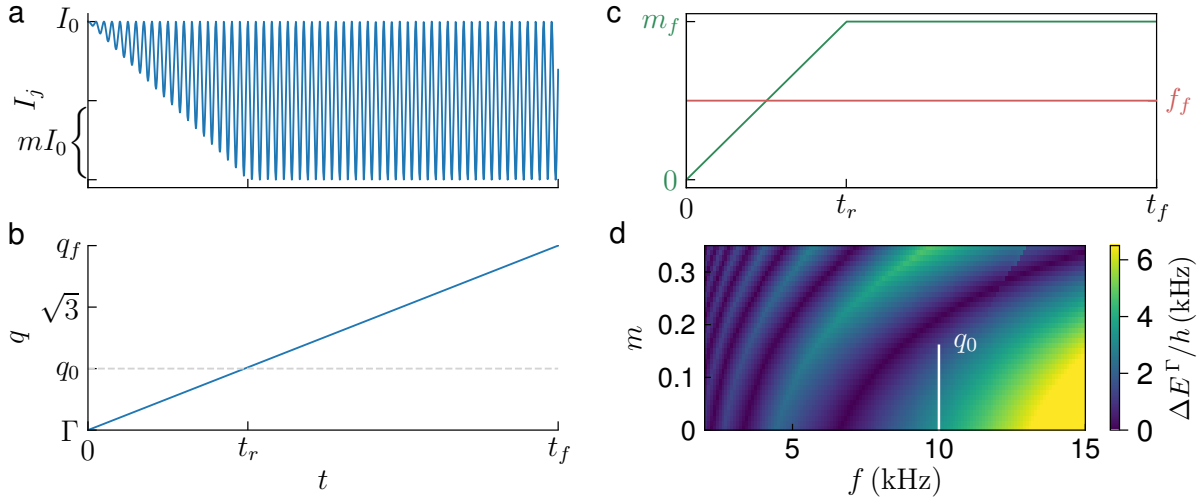


**Figure 5.6: Ramp-up sequence in the Haldane and anomalous regime.** Time-dependent parameters to probe the Berry curvature of the first band in the Haldane regime and for large frequencies in the anomalous regime along the  $\Gamma$ - and  $K$ -direction, illustrated for  $f = 10$  kHz and  $m = 0.16$ . **a.** Time-dependent intensity  $I_j$  of a single beam, the modulation of the other two beams is similar but phase shifted by  $\frac{2\pi}{3}$  and  $\frac{4\pi}{3}$ , respectively. The atoms are imaged insitu at  $t = t_f$  in the modulated lattice and afterwards the modulation, the lattice and the trap are switched off abruptly. **b.** Linear quasimomentum change during the ramp-up and the subsequent crossing of the Berry curvature between  $t_r$  and  $t_f$ . **c.** Time-dependent modulation amplitude (green) and frequency (red). The amplitude is ramped up linearly to  $m_f$  within  $t_r$ , while the frequency is constant at its final value  $f_f$ . **d.** Calculated energy gaps  $\Delta E^\Gamma$  at  $\Gamma$  depending on the modulation parameters, resembling the phase diagram. The ramp-up path in parameter space is depicted as the white line, ending at a quasimomentum of  $q = q_0$ .

transition at earlier times in the interval  $[0, t_r]$ , which means that the cloud is still close to the  $\Gamma$ -point at the moment of the gap closing. This favors excitations and can lead to a transverse deflection during the ramp-up, since the cloud potentially overlaps with the Berry curvature spreading around  $\Gamma$  in reciprocal space after the phase transition. The changing Berry curvature distribution when ramping across the phase transition together with the BEC moving in it along the  $\Gamma$ -direction is shown in Fig. 5.7 for  $f = 8$  kHz and  $m = 0.2$ . Here, no overlap in reciprocal space occurs between the cloud and the Berry curvature, avoiding transverse deflections during the ramp-up.

When measuring deep in the Haldane regime, where no Berry curvature is present at  $\Gamma$ , the modulation amplitude could also be ramped up while keeping the cloud at  $\Gamma$  and then starting to probe from here. However, to provide a consistent measurement scheme and assure comparability between the results in the different topological sectors, the ramp-up scheme described here is chosen for all modulation parameters in the Haldane regime.

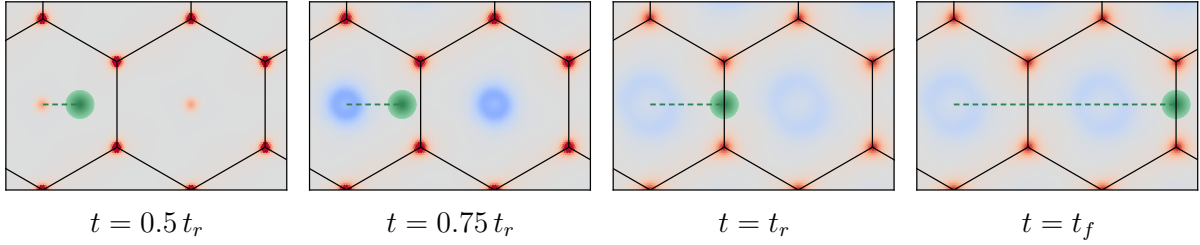


**Figure 5.7: Moving the atoms in reciprocal space during the modulation ramp-up.** Berry curvature and BEC in reciprocal space when measuring along the  $\Gamma$ -direction for  $f = 8\text{ kHz}$  and  $m = 0.2$ . The modulation amplitude is ramped up linearly in time while the cloud is accelerated to the  $M$ -point, as illustrated by the green dashed lines. The BEC is depicted by the green circles with radius  $R = \bar{\sigma} = 0.153 k_L$  being the mean over all measured momentum space widths. At the beginning of the ramp-up the modulation parameters lie in the Haldane regime exhibiting no Berry curvature at  $\Gamma$ , and the transition to the anomalous regime at  $m = 0.12$  is passed at  $t = 0.6 t_r$ . Shortly before the phase transition at  $t = 0.5 t_r$ , positive Berry curvature concentrated at  $\Gamma$  arises which is not probed by the cloud being already at a different quasimomentum. At the phase transition, the Berry curvature at  $\Gamma$  becomes negative and then starts to spread when increasing the modulation amplitude further to its final value ( $t = 0.75 t_r$  and  $t = t_r$ ). Then, the Berry curvature distribution around the  $\Gamma$ -point in the next BZ is probed (last image).

**Ramp-up scheme for small modulation frequencies in the anomalous regime**  
For final modulation frequencies  $f_f \leq f_{\lim}$  in the anomalous regime, the frequency and amplitude of the modulation are changed simultaneously during the ramp-up. The modulation amplitude is still increased linearly in time from 0 to  $m_f$ , but the frequency is ramped from  $f_0$  to  $f_f$  according to an exponential function:

$$f(t) = f_0 + \left( \frac{f_f - f_0}{e^{p \cdot m_f} - 1} \right) (e^{p \cdot m(t)} - 1), \quad m(t) = \frac{m_f}{t_r} t. \quad (5.9)$$

This functional form is motivated by the shape of the phase boundaries in  $m$ - $f$ -space, which approximately follow  $f(m) \propto e^m$  for  $\theta = 0$ , and is used for optimizing the ramp-up paths to load the atoms into the lowest band in the third regime, as described later. The ramp-up time  $t_r$  is chosen close to the time needed to accelerate by  $q_0$ , but ending at full cycles of the modulation. For all modulation parameters in the anomalous regime with  $f_f \leq f_{\lim}$ ,  $p = 20$  and the initial modulation frequency is  $f_0 = 13.3\text{ kHz}$ , where the relative quasienergy gap at  $\Gamma$  is maximal for  $m \rightarrow 0$ . In Fig. 5.8 the ramp-up and probing scheme for the  $\Gamma$ -and  $K$ -directions is illustrated for  $m = 0.3$  and  $f = 7\text{ kHz}$ , with similar plots as in Fig. 5.6. Due to the exponential change of the modulation frequency, the phase transition is now crossed at later times during the ramp-up as compared to the case where the frequency would be held constant at  $f(t) = f_f$ . This ensures that the cloud has already moved away far enough from  $\Gamma$  in reciprocal space and neither probes

the Berry curvature arising there nor traverses through points with small quasienergy gaps.

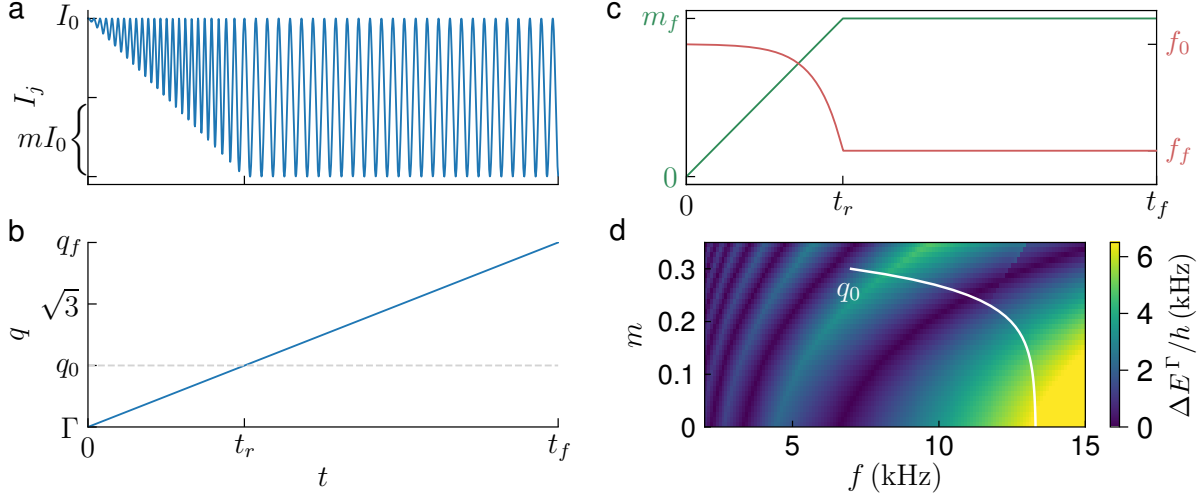


**Figure 5.8: Ramp-up sequence in the anomalous regime at small frequencies.** Time-dependent parameters to probe the Berry curvature of the first band in the anomalous regime for modulation frequencies  $f_f \leq f_{\text{lim}}$  along the  $\Gamma$ - and  $K$ -direction, illustrated for  $f = 7$  kHz and  $m = 0.3$ . **a.** Time-dependent intensity  $I_j$  of a single beam. **b.** Linear quasimomentum change during the full sequence. **c.** Time-dependent modulation amplitude (green) and frequency (red). The amplitude is ramped up linearly to  $m_f$  within  $t_r$ , while the frequency is changed exponentially from  $f_0 = 13.3$  kHz to  $f_f$ . **d.** Calculated energy gaps  $\Delta E^\Gamma$  at  $\Gamma$  depending on the modulation parameters with the ramp-up path in parameter space (white line), ending at a quasimomentum of  $q = q_0$ .

To calculate the transverse deflections, the real space positions and quasimomenta after the modulation ramp-up are used as starting points for the trajectories, with  $q_\parallel = q_0$ ,  $q_\perp = 0$  and  $r_\parallel = 0$ . The longitudinal offset  $r_\parallel$  in real space is obtained by solving Eq. 4.27 numerically including the momentum space width (as described in Sec. 4.2.4), while applying the respective force for a time  $\Delta t = t_r$  and setting  $\Omega(\mathbf{q}) = 0$ . Here, the quasienergy dispersion for the final modulation parameters is used. This gives similar results as when employing the changing dispersion during the ramp-up, which has been tested numerically.

**Measured deflections during the modulation ramp-up and test of adiabaticity**  
To further confirm that there is no Berry curvature probed when driving the atoms by  $q_0$  during the linear or exponential ramp-up of the modulation, the corresponding transverse deflection is measured for  $m = 0.25$  and modulation frequencies  $f \in [6, 16]$  kHz scanning the Haldane and anomalous regime, as presented in Fig. 5.9a. For  $f \leq 7$  kHz the exponential frequency ramp is applied, in the other cases the modulation frequency is constant during the amplitude ramp-up. The cloud is accelerated by  $q_0$  along the  $\Gamma$ - or  $K$ -direction (green and gray data points) with a force of  $Fa/h = 204$  Hz while

the modulation parameters are changed to their final values as just described. Indeed, there is no significant transverse deflection observed along both directions, verifying the ramp-up schemes presented above.

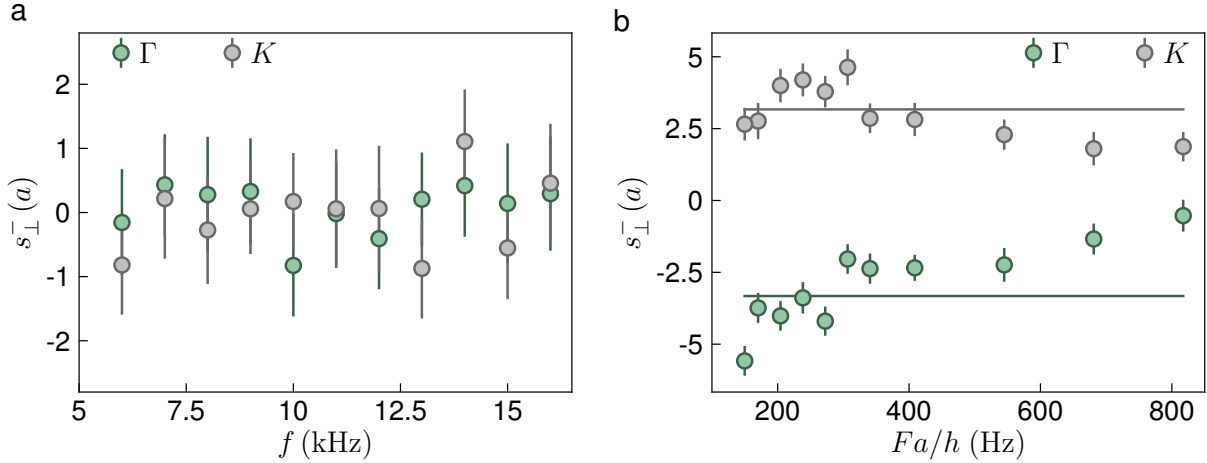


**Figure 5.9: Measured transverse deflections during the modulation ramp-up and as a function of the applied force.** **a.** Deflections after the modulation ramp-up for  $m = 0.25$  and various modulation frequencies in the Haldane and anomalous regime. The cloud is accelerated by  $q_0$  with  $Fa/h = 204\text{ Hz}$  along the  $\Gamma$ - (green data points) and  $K$ -direction (gray data points), while the modulation amplitude is increased linearly and the modulation frequency is either held constant or, for  $f \leq 7\text{ kHz}$ , changed exponentially according to the schemes presented before. The data points represent the differential deflection evaluated from three measurements, each being an average over 30-40 experimental realizations, the errorbars denote the standard error of the mean (SEM). **b.** Transverse deflections along the  $\Gamma$ - and  $K$ -direction (green and gray data points) in the anomalous regime ( $f = 10\text{ kHz}$ ,  $m = 0.24$ ) for the path  $q_0 \rightarrow q_{\text{eff}} \approx 1.25\sqrt{3}k_L$  and different applied forces. The lattice acceleration is adapted to reach the same value of  $q_{\text{eff}}$  for all forces, the data points and errorbars are obtained similarly as in **a**.

As mentioned earlier, excitations to the second band could not only occur during the loading of the atoms into the modulated lattice, but also when changing the quasi-momentum to probe the Berry curvature for  $t > t_r$ , if the applied force is too large compared to the quasienergy gaps along the path. The forces used in this work for the deflection measurements are chosen such that they are at least two times smaller than the smallest quasienergy gaps occurring along the path, except for some points very close to the phase transitions (see Fig. 5.12), where the force is of similar magnitude as the quasienergy gap at  $\Gamma$ . Nevertheless, the magnitude of the force is tested experimentally by probing the transverse deflections along the  $\Gamma$ - and  $K$ -directions for different forces, shown in Fig. 5.9b.

The modulation parameters lie in the anomalous regime,  $f = 10\text{ kHz}$  and  $m = 0.24$ , and the final quasimomentum set by the lattice acceleration is adapted such that  $q_{\text{eff}} \approx 1.25\sqrt{3}k_L$  for all forces investigated here. The solid lines denote the theoretical values

including the momentum space width measured along with the data set. Along the  $\Gamma$ -direction, the measured deflections are smaller than the theoretical predictions for  $Fa/h > 300$  Hz, indicating excitations: The second band has opposite Berry curvature and hence the CoM-deflection is reduced, representing a superposition of atoms in both bands. Along the  $K$ -direction, the transverse deflection does not drop until  $Fa/h > 400$  Hz, which is explained by the larger quasienergy gaps traversed here. Since the modulation parameters are relatively close to the phase transition, the quasienergy gap at  $\Gamma$ ,  $\Delta E^\Gamma/h = 1110(70)$  Hz, is smaller than the gap at  $K$ ,  $\Delta E^K/h = 1500(30)$  Hz, requiring smaller forces. In the deflection measurements at these modulation parameters, forces of  $Fa/h = 170$  Hz and  $Fa/h = 204$  Hz are used, being sufficiently small as confirmed by the data presented here.

**Ramp-up schemes in the third regime** When loading the atoms into the first band in the third regime, the phase transition points can not be avoided by acceleration of the cloud, since the quasienergy gap at  $\Gamma$  closes two times when starting in the Haldane regime. Instead, the modulation ramp-up is directly performed in the parameter regime corresponding to the third phase. As discussed in Sec. 3.2.3, in the limit of  $m \rightarrow 0$ , at  $\Gamma$ , the first band of the static lattice is connected to the first band of the modulated lattice in the Haldane and third phase, but connected to the second band in the anomalous phase. Hence, by choosing an initial modulation frequency in the range of  $f \in [2.2, 3.3]$  kHz, the atoms are directly loaded into the lowest band of the modulated lattice in the third topological regime. To avoid excitations to the second band during the ramp-up, the modulation frequency is changed exponentially from  $f_0 = 2.7$  kHz to  $f_f$  according to Eq. 5.9, but now the parameter  $p$ , characterizing the shape of the curve in  $m$ - $f$ -space, is optimized to maximize the quasienergy gap at  $\Gamma$  along the ramp-up path in parameter space. At the initial frequency  $f_0$ , the relative quasienergy gap at  $\Gamma$  for  $m \rightarrow 0$  is maximal. The modulation amplitude is increased linearly in time and the atoms are held at  $\Gamma$  during the ramp-up. The ramp-up time  $t_r$  is chosen to be similar as in the other two regimes, again rounded to full modulation cycles.

To probe the Berry curvature around  $\Gamma$ , the cloud is then accelerated by  $\Delta q = \sqrt{3} k_L$  along the path  $\Gamma$ - $M$ - $\Gamma$ . In this way, for the modulation parameters used in this work, the same Berry curvature distribution is traversed as along  $M$ - $\Gamma$ - $M$ , which is used in the Haldane and anomalous regime when measuring around  $\Gamma$ . This has also been verified numerically by comparing the calculated transverse deflections for both paths. However, the situation is different when measuring along the  $K$ -direction. Driving by  $\Delta q = \sqrt{3} k_L$  from  $\Gamma$  probes only one of the Dirac points and not both, as in the other two regimes, and in addition the negative Berry curvature around  $\Gamma$  in the first BZ is traversed. To get comparable results, the transverse deflection is measured for accelerating by  $q_f = 1.5\sqrt{3} k_L$  and then, in a second set of measurements, for accelerating by  $q_0 = 0.5\sqrt{3} k_L$ . In the end, the resulting differential deflections are subtracted to resemble the path  $q_0 \rightarrow q_f$ , which is probed in the Haldane and anomalous regime.

The rampup-scheme is illustrated in Fig. 5.10, where the orange line in Fig. 5.10b indicates the larger quasimomenta when probing along the  $K$ -direction, extending to

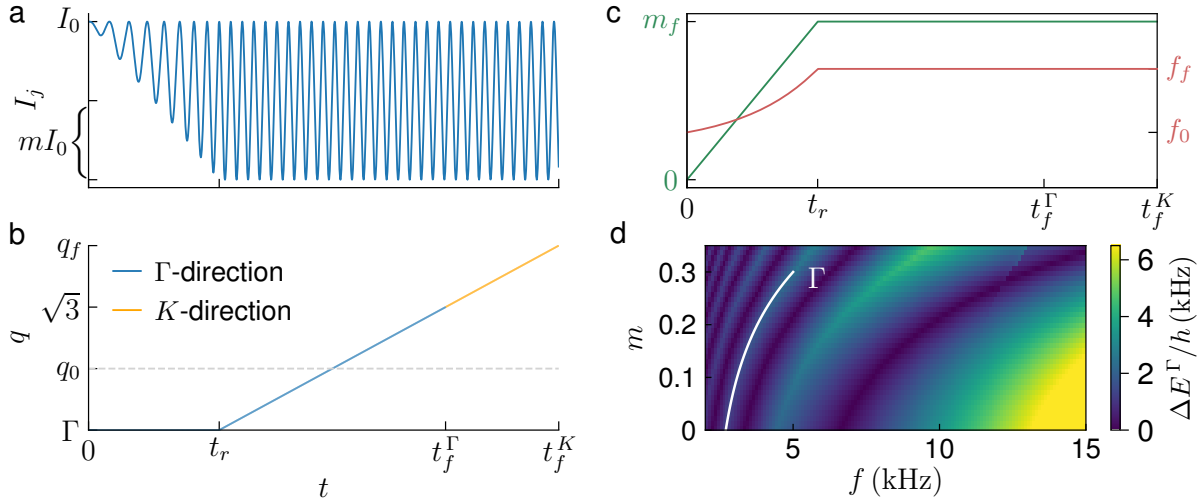


**Figure 5.10: Ramp-up sequence in the third regime.** Time-dependent parameters to probe the Berry curvature of the first band in the third regime along the  $\Gamma$ - and  $K$ -direction, illustrated for  $f = 5$  kHz and  $m = 0.3$ . **a.** Time-dependent intensity  $I_j$  of a single beam. **b.** Linear quasimomentum change during the ramp-up and the subsequent crossing of the Berry curvature between  $t_r$  and  $t_f$ . When measuring along the  $\Gamma$ -direction (blue line), the Berry curvature is probed for  $\Gamma \rightarrow \Gamma$ , giving similar results as  $M \rightarrow M$ . Along the  $K$ -direction (orange line), the deflections for  $\Gamma \rightarrow q_f = 1.5\sqrt{3}k_L$  and  $\Gamma \rightarrow q_0 = 0.5\sqrt{3}k_L$  are subtracted, effectively probing  $q_0 \rightarrow q_f$ . Since the same force is used, the measurement times are different:  $t_f^K > t_f^\Gamma$ . **c.** Time-dependent modulation amplitude (green) and frequency (red). The amplitude is ramped up linearly to  $m_f$  within  $t_r$ , while the frequency is changed exponentially from  $f_0 = 2.7$  kHz to  $f_f$ . **d.** Calculated energy gaps  $\Delta E^\Gamma$  at  $\Gamma$  depending on the modulation parameters with ramp-up path in parameter space (white line), while the cloud remains at  $\Gamma$ .

$q = q_f$ , whereas the path ends at  $q = \sqrt{3}k_L$  when probing along the  $\Gamma$ -direction. The ramp-up path in Fig. 5.10d (white line), maximizing  $\Delta E^\Gamma$ , exhibits a similar shape as the phase transition lines, motivating the functional form of Eq. 5.9.

### 5.1.4 Derivation of the winding numbers

The change of the winding numbers across the topological phase transitions, which are detected as quasienergy gap closings at  $\Gamma$  in Sec. 5.1.2, is given by the topological charges of the corresponding band touching singularities. The topological charge is measured as the sign change of the local Berry curvature at the singularity. Hence, to determine the change of the winding numbers, the Berry curvature of the lowest band is probed using transverse deflection measurements along the  $\Gamma$ -direction for modulation parameters following the same path as in the quasienergy gap measurements, which is depicted in Fig. 5.1.

**Haldane regime** The absolute values of the winding numbers are derived by exploiting the connection to the high-frequency limit: Starting from the Haldane regime and sending  $f \rightarrow \infty$ , the quasienergy gap between FBZs,  $g^\pi$ , diverges and necessarily  $W^\pi = 0$ , which holds everywhere in the Haldane sector, since  $g^\pi$  remains open. The winding number  $W^0$  can then be deduced from the well known properties of the Haldane model, which has been tested in several experiments [96, 99, 103, 104], exhibiting a Chern number of  $\mathcal{C}^- = 1$  in the lowest band (see Sec. 3.3 for the derivation of the Haldane model in the limit of large modulation frequencies):

$$W_1^\pi = 0 \quad W_1^0 = \mathcal{C}^- + W_1^\pi = 1. \quad (5.10)$$

The Chern number of the lowest band in the Haldane regime is verified experimentally by measuring the transverse deflections along all  $\Gamma$ - and  $K$ -directions, as illustrated by the green and blue dashed lines in Fig. 5.11a.

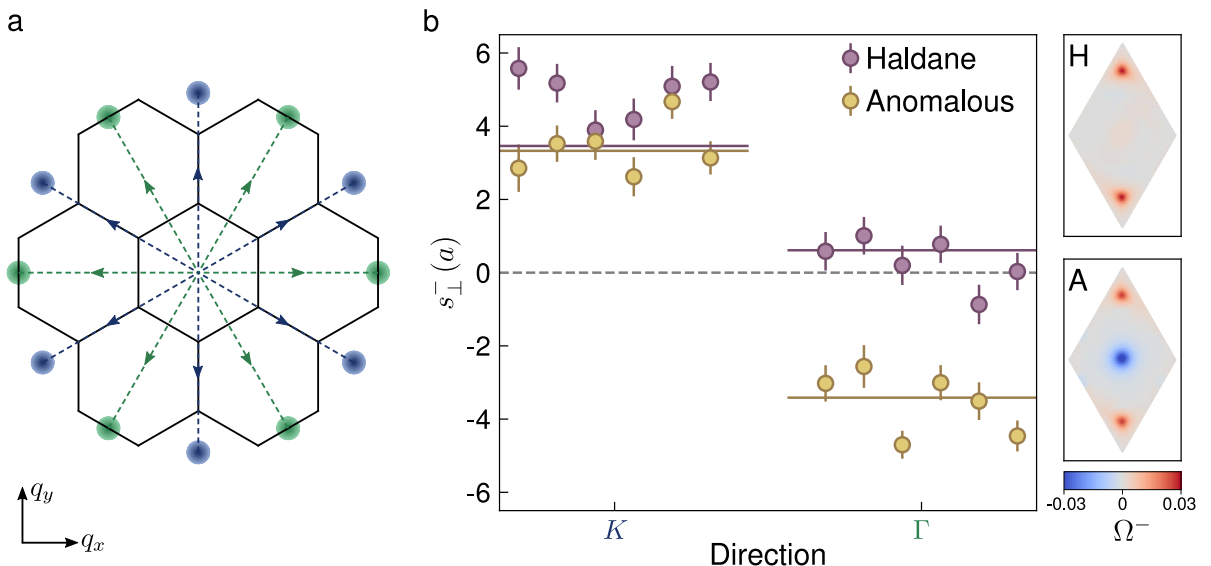


Figure 5.11: **Transverse deflections measured in units of the lattice constant  $a$  along all  $\Gamma$ - and  $K$ -directions.** **a.** Sketch of the paths traversed in quasimomentum space, probing the Berry curvature around the  $\Gamma$ - (dashed green lines) or  $K$ - and  $K'$ -directions (dashed blue lines). The BEC is illustrated by the green and blue circles with radius  $R = \bar{\sigma} = 0.153 k_L$ . **b.** Measured transverse deflections along all directions depicted in **a**, in the Haldane regime at  $f = 16$  kHz and  $m = 0.25$  (purple data points) and in the anomalous regime at  $f = 10$  kHz and  $m = 0.24$  (yellow data points) for  $q_0 \rightarrow q_{\text{eff}} \approx 1.33\sqrt{3} k_L$  using  $Fa/h = 204$  Hz. The data points represent differential deflections derived from three measurement points, each being an average over 30-40 experimental realizations, the errorbars denote the SEM. The calculated deflections including the measured momentum space widths are plotted as solid purple and yellow lines. Right panel: Corresponding calculated Berry curvature distributions in the lowest band.

The modulation parameters are chosen to lie deep in the Haldane regime,  $f = 16$  kHz and  $m = 0.25$ , such that the Berry curvature is mainly concentrated around the Dirac points (see upper right panel of Fig. 5.11b). Accelerating by  $q_f = 1.5\sqrt{3} k_L$  with  $Fa/h = 204$  Hz moves the center of the cloud by  $q_{\text{eff}} \approx 1.33\sqrt{3} k_L$ , hence traversing the Berry curvature at both Dirac points and around  $\Gamma$  once with all atoms ( $\sigma = 0.159 k_L$  in this measurement). The modulation amplitude is ramped up linearly at a constant frequency while driving by  $q_0$ , as described in Sec. 5.1.3. This effectively probes the Berry curvature of the entire first BZ, corresponding to the Chern number.

The measured transverse deflections (purple data points in Fig. 5.11b) reach large, positive values along all  $K$ -directions and small positive values along the  $\Gamma$ -directions, confirming the expected Berry curvature distribution. The Chern number of 1 is moreover verified by the good agreement with the theoretical calculations (purple solid lines) employing the lowest band with  $C^- = 1$  and the momentum space width. In contrast, in the anomalous regime for  $f = 10$  kHz and  $m = 0.24$  (yellow data points and solid lines), the transverse deflection turns to large negative values along all  $\Gamma$ -directions and to slightly smaller positive values at the  $K$ -directions, as compared to the Haldane regime. This resembles the negative Berry curvature arising at  $\Gamma$  behind the phase transition and the still positive Berry curvature at the  $K$ -points (see lower right panel of Fig. 5.11b), adding up to a Chern number of zero. Also here, the measured values coincide well with the corresponding theory lines. The Haldane regime could also be characterized by adding a sublattice energy offset and starting in the trivial region of the phase diagram with a small modulation amplitude and large frequency (see Sec. 3.2.4). By increasing the amplitude, the closing of the 0-gap at  $K'$  could be observed along with the sign change of the corresponding Berry curvature from negative to positive values, resembling  $\Delta W^0 = 1$ .

**Anomalous and third regime** The winding numbers in the other two regimes can now be derived by detecting the sign changes of the transverse deflection at the phase transitions (see Eq. 5.4) in combination with the winding numbers in the Haldane regime. The measured transverse deflections along the  $\Gamma$ -direction are shown in Fig. 5.12, the modulation parameters are varied in the same way as for the gap measurements in Fig. 5.3. The modulation ramp-up is performed according to the different schemes presented in Sec. 5.1.3, depending on the topological regime that is probed. The cloud is accelerated by  $q_f = 1.5\sqrt{3} k_L$  with a force of  $Fa/h = 170$  Hz, hence moving by  $q_{\text{eff}} \approx 1.25\sqrt{3} k_L$ , for all measurements in the Haldane and anomalous regime. In the third regime, the quasimomentum is not changed during the ramp-up and the Berry curvature is probed for  $\Gamma \rightarrow q_{\text{eff}} \approx 0.93\sqrt{3} k_L$ , using the same force. The blue shaded areas and the numbers denote the different topological regimes with the boundaries derived from the gap closing points at  $\Gamma$ .

In the Haldane regime, the transverse deflections are positive everywhere and rise when approaching the first gap closing point, which is traversed by changing the modulation amplitude. For  $m > 0.2$ , the deflections then turn to negative values with a pronounced minimum around  $m = 0.24$ , resembling the Berry curvature at  $\Gamma$ , which is jumping from positive to negative values (see upper panels of Fig. 5.3). Hence, at the first phase

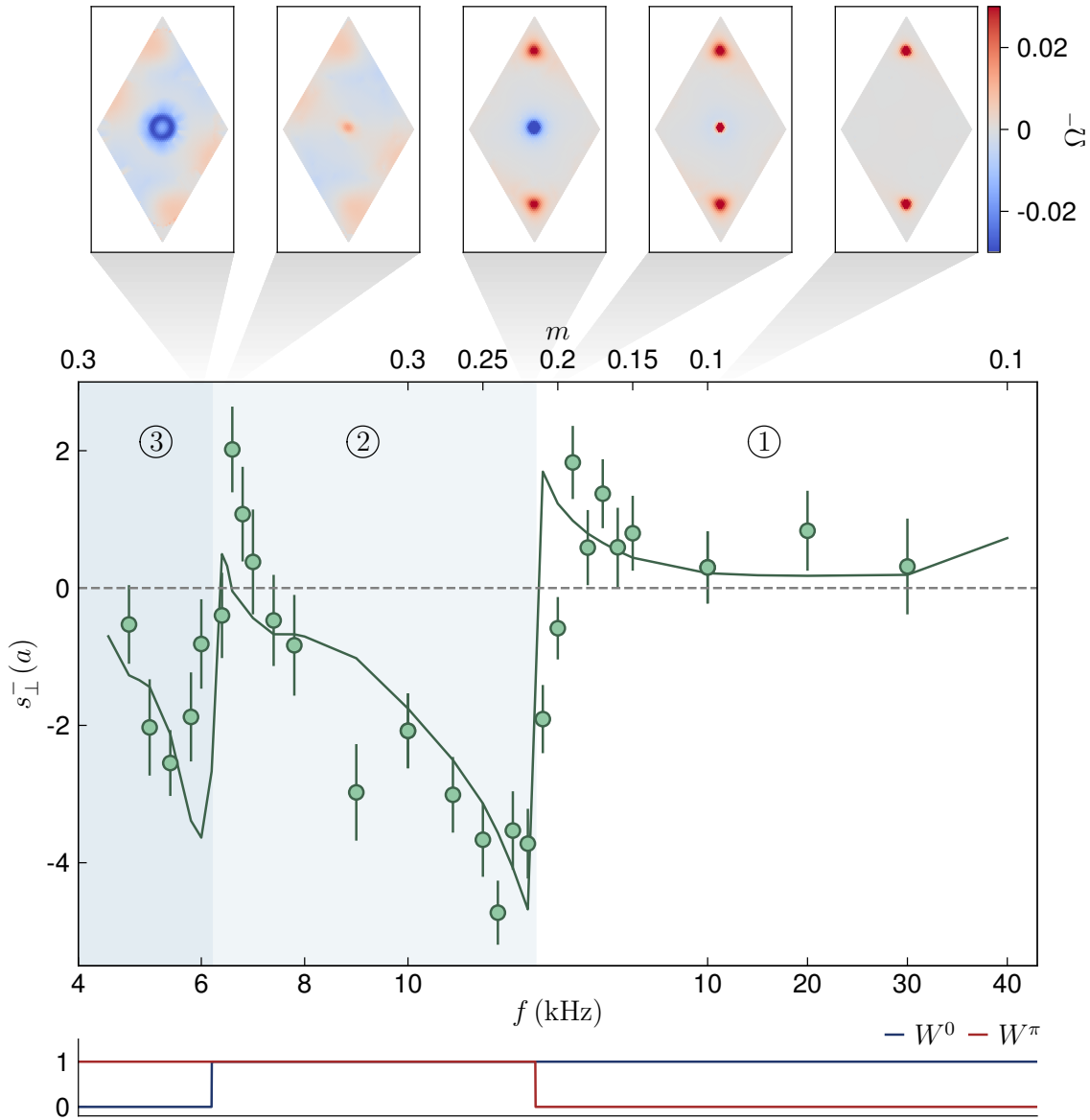


**Figure 5.12: Probing the Berry curvature across the phase transitions.** Measured transverse deflections  $s_{\perp}$  in the lowest band along the  $\Gamma$ -direction (data points) and theoretical values (solid green line, see Sec. 3.2.2) as a function of the modulation amplitude and frequency. The Berry curvature is probed for  $q_0 \rightarrow q_{\text{eff}} \approx 1.25\sqrt{3}k_L$  in the Haldane and anomalous regime and for  $\Gamma \rightarrow q_{\text{eff}} \approx 0.93\sqrt{3}k_L$  in the third regime using  $Fa/h = 170$  Hz. Every data point is derived from three measurement points, each being an average over 30-40 experimental realizations, the errorbars denote the SEM. The blue shaded areas and the numbers illustrate the different topological regimes. Upper panel: Calculated Berry curvature distributions in the first BZ for  $f = (6, 6.4, 10, 10, 10)$  kHz and  $m = (0.3, 0.3, 0.22, 0.21, 0.1)$  from left to right. Lower panel: Winding numbers derived from the sign change of the measured transverse deflections.

transition, characterized by the closing of  $g^\pi$ , the winding number  $W^\pi$  is increased by +1, whereas  $W^0$  remains unchanged, which is also plotted in the lower panel of Fig. 5.3:

$$\Delta W^\pi = Q_s^\pi = -\text{sgn}(\Delta s_\perp^-(\Gamma)) = 1 \quad \Rightarrow W_2^\pi = 1 \quad W_2^0 = 1, \quad (5.11)$$

corresponding to  $\mathcal{C}^- = W^0 - W^\pi = 0 = \mathcal{C}^+$ . Thus, an additional pair of chiral edge modes is created in the quasienergy gap  $g^\pi$ , while the edge modes at  $g^0$  are still present, constituting the realization of an anomalous Floquet system.

When tuning the modulation parameters further into the anomalous regime, the Berry curvature around  $\Gamma$  spreads, indicated by the negative transverse deflection which is decreasing in magnitude, since the area of the Berry curvature ring is not fully covered by the momentum space extent of the BEC any more. For modulation frequencies close to 7 kHz, the deflections become positive again and after passing through a pronounced maximum,  $s_\perp^-$  turns to negative values for  $f \geq 6.4$  kHz, also confirming the position of the second phase transition determined from the gap measurements. The negative Berry curvature at  $\Gamma$  spreads out again (first upper panel of Fig. 5.3), leading to a decrease in absolute value of the transverse deflections when turning the parameters deeper into the third regime. At the second phase transition, the energy gap  $g^0$  is closing, which now changes the winding number  $W^0$ :

$$\Delta W^0 = Q_s^0 = \text{sgn}(\Delta s_\perp^-(\Gamma)) = -1 \quad \Rightarrow W_3^\pi = 1 \quad W_3^0 = 0. \quad (5.12)$$

The measured transverse deflections coincide well with the theoretical values (solid green line), which are calculated as described in Sec. 4.2.4. The momentum space width is measured along with each data point in Fig. 5.12 and used in the calculation of the corresponding  $s_\perp^-$ -value. The theoretical deflections are also evaluated for parameters in between the measured points, especially in the vicinity of the phase transitions. Here, the momentum space width of the nearest experimental point is used.

Close to the phase transitions, for  $f = 10$  kHz,  $m \in [0.2, 0.22]$  and  $f \in [6.4, 5.8]$  kHz,  $m = 0.3$ , the experimental deflections are reduced compared to the theoretically expected positive and negative peaks. Since the quasienergy gap at  $\Gamma$  is very small at these points, some atoms can be excited to the second band when moving the cloud through that region in quasimomentum space, even for the small force used here. There are also modulation parameters at which the measured deflections exceed the theoretical values. In addition to possible drifts of the relative beam positions influencing the balancing and depth of the lattice, this might be explained by excitations to Floquet copies of  $p$ -bands which exhibit different Berry curvature distributions than the  $s$ -bands.

To directly probe the band touching point, the Berry curvature would need to be measured exactly at  $\mathbf{q} = \Gamma$  for modulation parameters being infinitely close to the transition, hence sending  $\epsilon \rightarrow 0$  in Eq. 5.5. Due to the vanishing quasienergy gaps, it is not possible to measure the deflections at modulation parameters arbitrarily close to the phase transition. Moreover, the Berry curvature integrated over a region around  $\Gamma$  is probed, because of the cloud's extent in quasimomentum space. Nevertheless, the topological charge of the band touching singularity can indeed be determined from these measurements, since

it is given by the sign change of the Berry curvature which can unambiguously be defined from a sign change of the transverse deflections. In addition, the good quantitative agreement of the experimental values with the numerical calculations justifies the change of the winding numbers by  $\pm 1$ , being characteristic of linear, non-degenerate band touching points. Hence, using deflection measurements in the Haldane regime and across the phase transitions enables the derivation of the winding numbers, and provides a complete characterization of the different topological regimes investigated in this work. Moreover, the existence of chiral edge modes can be revealed, even in a system with smooth boundaries, as it is used in the experiments presented here.

## 5.2 Probing the phase diagram

To further confirm the observations from the previous section and benchmark the theoretical model presented in Sec. 3.2.2, the phase diagram of Fig. 5.1 is explored in a larger parameter range. For modulation frequencies  $f \in [5, 16]$  kHz and amplitudes  $m \in [0.2, 0.3]$  the quasienergy gaps and Berry curvature at  $\Gamma$  and  $K$  are studied systematically to obtain the phase boundaries and confirm the change of the winding numbers.

### 5.2.1 Quasienergy gaps

The phase boundaries are located by measuring the quasienergy gaps at  $\Gamma$  when varying the modulation frequency within  $f \in [5, 16]$  kHz while keeping the modulation amplitude constant at  $m = (0.2, 0.22, 0.25, 0.27, 0.3)$ , thus scanning the phase diagram in Fig. 5.1 along horizontal lines. The quasienergy gaps are also probed at  $K$ , to further test the theoretical calculations and to determine the correct forces for the deflection measurements (Sec. 5.2.2), matching the minimal gaps. The measurements are again performed using Stückelberg interferometry in the same way as described in Sec. 5.1.1, now with a force of  $Fa/h = 1360$  Hz. For larger forces, excitations to higher bands occur, when probing the gaps for high modulation frequencies ( $f \gtrsim 12$  kHz) and amplitudes ( $m \gtrsim 0.25$ ) along both directions. In the previous band gap measurements presented in Sec. 5.1.2, the modulation parameters have been chosen to avoid combinations of high  $f$  and  $m$ , thus enabling the use of a larger force.

An example of Stückelberg oscillations at  $\Gamma$  is shown in Fig. 5.13a for  $m = 0.25$ . The relative population in the lowest band is plotted as a function of the hold time and the modulation frequency. Since the hold times are integer multiples of the modulation period, with  $t \in [0, 22] T$ , the width of the time steps decreases with increasing modulation frequency. The oscillations for each modulation frequency are clearly visible as well as the decrease and increase of the oscillation frequency when approaching the phase transitions around  $f \approx 11$  kHz and  $f \approx 5.5$  kHz. The gap frequencies presented in Fig. 5.14 are obtained by fitting Eq. 5.6 to the oscillation for each set of modulation parameters. Usually the contribution of the second component arising from excitations to  $p$ -bands is small, and the oscillation is well described by a single, damped sine wave. This is illustrated when computing the fast Fourier transform (FFT) of the time-dependent

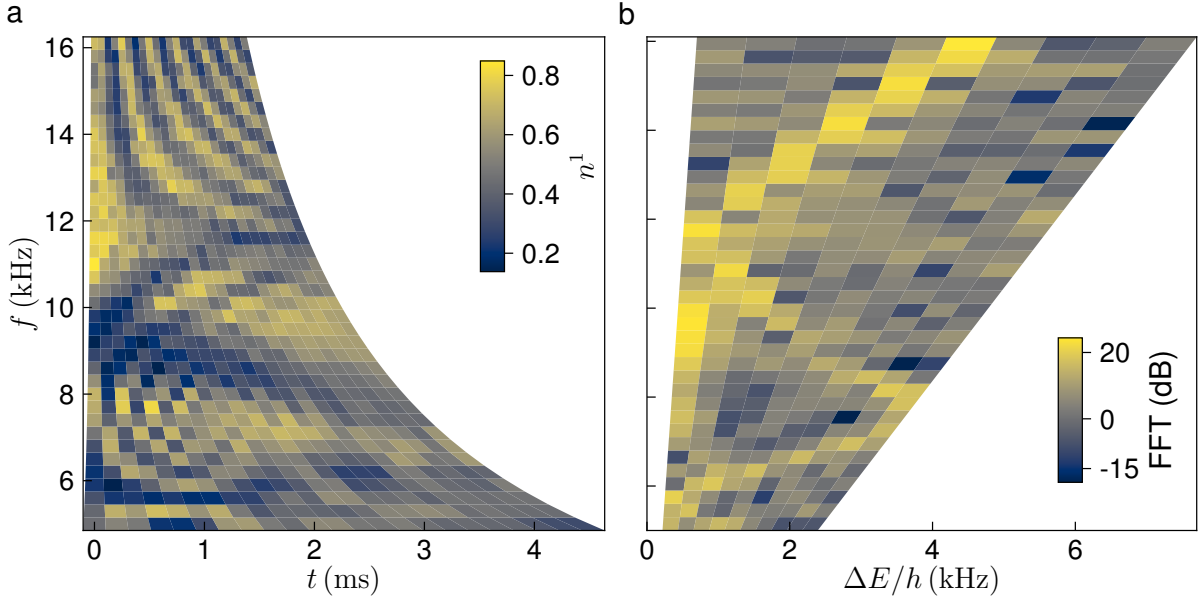
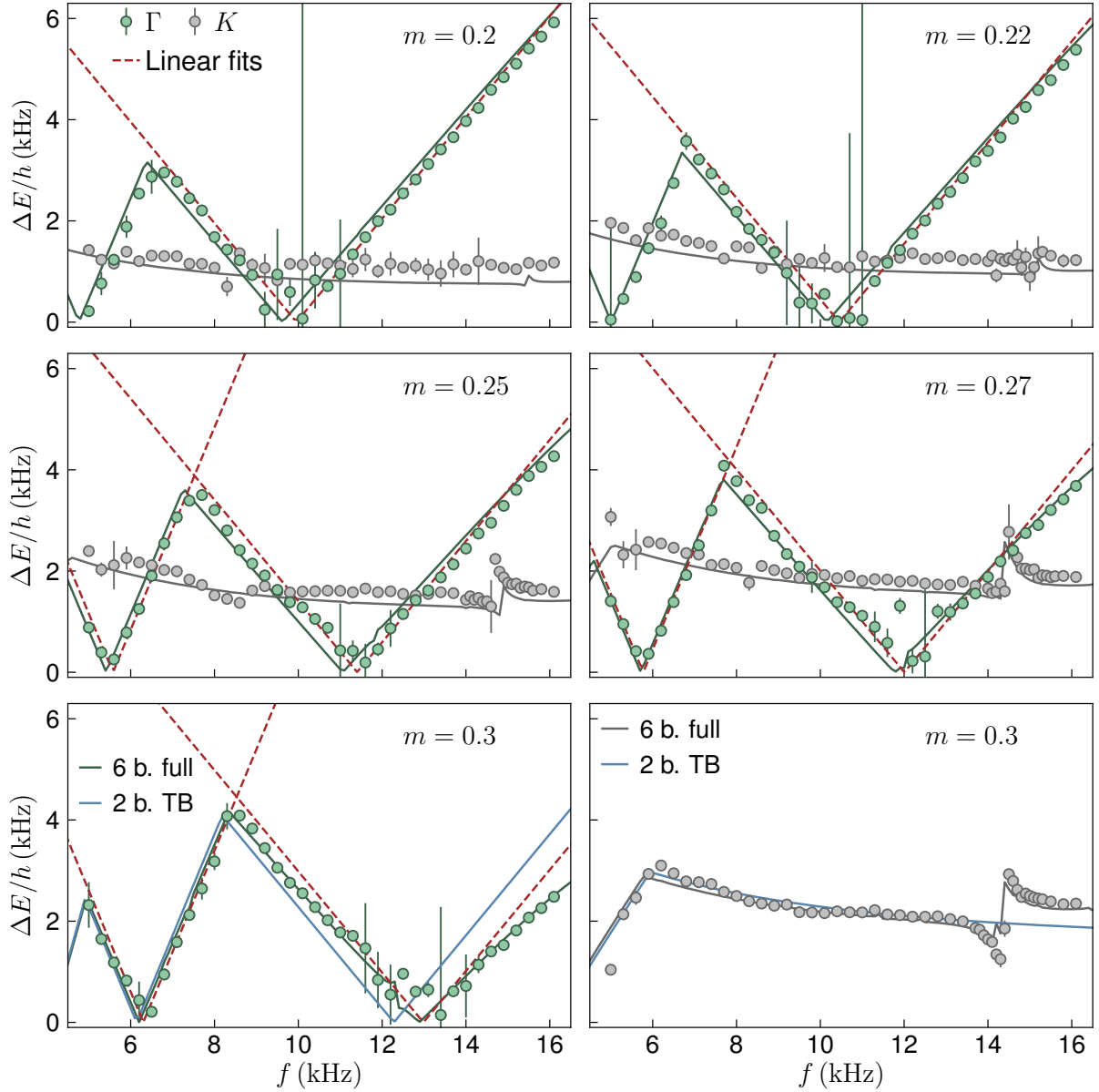


Figure 5.13: **Population oscillations and FFT.** **a.** Measured relative population  $n^1(t)$  in the lowest band depending on the hold time and the modulation frequency for  $f \in [5, 16]$  kHz and  $m = 0.25$ . Each data point is an average over 3 – 4 individual images, with the average SEM being  $\bar{\Sigma} = 0.030(4)$ . **b.** Fast Fourier transform (FFT) of the population signal in **b**, signaling the opening and closing of the energy gaps. The DC component is not displayed for clarity.

population signals in Fig. 5.13a, which is shown in Fig. 5.13b. For most values of  $f$ , there is a single maximum in the FFT signal, corresponding to the main oscillation frequency in Eq. 5.6. Only for some values close to the first phase transition, a second component arises at small gap frequencies. In general, the opening and closing of the quasienergy gaps is clearly visible already in the raw data and its FFT, highlighting the applicability of Stückelberg interferometry to experimentally determine the band gaps with great quantitative precision.

In Fig. 5.14, the resulting gap frequencies at  $\Gamma$  and  $K$  are plotted as a function of the modulation frequency (green and gray data points) for the different modulation amplitudes, along with the theoretical calculations employing the six-band model presented in Sec. 3.2.2 (green and gray lines). For  $m = 0.3$ , the data is also compared to a two-band tight-binding calculation, as introduced in Sec. 3.3, which incorporates the change of the vectors connecting nearest neighbor lattice sites,  $\delta_j(t)$  (blue lines).

The quasienergy gaps calculated using the six-band model are in excellent agreement with the experimental values for both quasimomenta and all modulation parameters considered here. The two-band calculation describes the gaps well at low modulation frequencies and amplitudes where the coupling to the  $p$ -bands is weak, as already discussed in Sec. 3.3. But for increasing modulation parameters, the quasienergy gaps at  $\Gamma$  and hence the phase transition lines are shifted, as visible in the lower left panel of Fig. 5.14.



**Figure 5.14: Quasienergy gaps as a function of the modulation frequency and amplitude.** Quasienergy gaps at  $\Gamma$  and  $K$  (green and gray data points) vs. modulation frequency for increasing modulation amplitude measured using Stückelberg interferometry with  $Fa/h = 1360$  Hz. The solid green and gray lines show the calculated gaps employing the six-band model, for the blue solid lines at  $m = 0.3$ , the two-band tight-binding model introduced in Sec. 3.3 is used including time-dependent connection vectors  $\delta_j(t)$ . The dashed, red lines are linear fits to the gaps at  $\Gamma$  to determine the phase transition points (see text). The data points are the frequencies resulting from fits to the Stückelberg population oscillations consisting of 23 points, each of which is an average over 3-4 individual images. The errorbars denote fitting errors.

The difference between the two models becomes also apparent for the quasienergy gaps at  $K$ , which exhibit jumps at high modulation frequencies that increase in height with the modulation amplitude. These originate from avoided crossings with the  $p$ -bands and are well captured by the six-band model, also indicating that it is not necessary to include more than six bands in the calculation for the modulation parameters considered here. Accordingly, they do not appear in the two-band model, which predicts a monotonically decreasing gap at  $K$  with higher modulation frequencies. However, apart from the missing jumps, the values of the measured quasienergy gaps at  $K$  are in general also well described by the two-band tight-binding model.

For very small gap frequencies, the measurement of the quasienergy gaps using Stückelberg interferometry becomes more difficult, since the hold times needed to observe a full period of the population oscillation diverge. As described earlier, at long hold times, heating effects start to play a role, limiting the minimal gap that can be measured also for large modulation frequencies, which is indicated by the increasing fitting errors at the gap minima. Hence, the phase transition points are not read-off directly, but determined by applying linear fits to the quasienergy gaps at  $\Gamma$  in the vicinity of the transition, where the measurements are more reliable. The gap frequencies increase and decrease linearly with the modulation frequency around the closing point. At the first phase transition, where the modulation frequency equals the effective bandwidth,  $\hbar\omega = W_{\text{eff}}$ , the gap changes with a slope of 1 and at the second phase transition ( $2\hbar\omega = W_{\text{eff}}$ ) with a slope of 2. For modulation amplitudes  $m \geq 0.25$ , both phase transitions are obtained by fitting  $\Delta E/h = n \cdot |f - f_n^{\text{PT}}|$  with  $n = \{1, 2\}$  to the measured gaps lying at lower and higher frequencies around the minima. Since the transition frequencies move to smaller values with decreasing modulation amplitude, for  $m < 0.25$ , only the first phase transition is determined. The fits are shown as dashed, red lines in Fig. 5.14. The errors of the phase transition frequencies  $f_n^{\text{PT}}$  are derived as a combination of the standard deviations from the linear fit,  $\Sigma_{\text{fit}}$ , and systematic errors,  $\Sigma_{\text{sys}}$ :

$$\Sigma_{\text{tot}} = \sqrt{\Sigma_{\text{fit}}^2 + \Sigma_{\text{sys}}^2}. \quad (5.13)$$

The latter are given by the step size of the modulation frequency used in the measurements in Fig. 5.14,  $\Sigma_{\text{sys}} = 300$  Hz, and dominating over the fitting errors being in the range of  $\Sigma_{\text{fit}} \in [20, 70]$  Hz. The resulting phase transition points are plotted in Fig. 5.17 (dark gray data points), matching the theoretically expected phase boundaries.

This is also illustrated in Fig. 5.15a, where the measured relative quasienergy gaps at  $\Gamma$ ,  $\Delta E^\Gamma/(\hbar\omega)$ , are plotted in the  $m$ - $f$  parameter space, resembling the phase diagram very well, which is derived from the theoretical quasienergy gaps at  $\Gamma$  (Fig. 5.15b). The maxima of the relative gap at  $\Delta E^\Gamma/(\hbar\omega) = 0.5$  indicate the change from measuring  $g^\pi$  to measuring  $g^0$  and vice versa (see Sec. 5.1.2). For modulation frequencies in the Haldane regime, the gap between FBZs is measured, which is deduced from the comparison with theory, as the corresponding maxima occur at higher modulation frequencies that lie outside the parameter range considered here. In the gap measurements in Fig. 5.3, the Haldane regime is probed for a small modulation amplitude of  $m = 0.1$ , where the phase boundaries are shifted to smaller frequencies, enabling the observation of this first

maximum there. In Fig. 5.15a, the maximum line obtained for  $f \in [6, 8]$  kHz accordingly signals the change from probing  $g^\pi$  to probing  $g^0$ . Hence, the points obtained for the first phase transition at larger modulation frequencies describe the closing of  $g^\pi$  and the second phase transition for smaller modulation frequencies occurs as a closing of  $g^0$ . Overall, the positions of the gap closings as well as of the gap maxima match the values expected from theory.

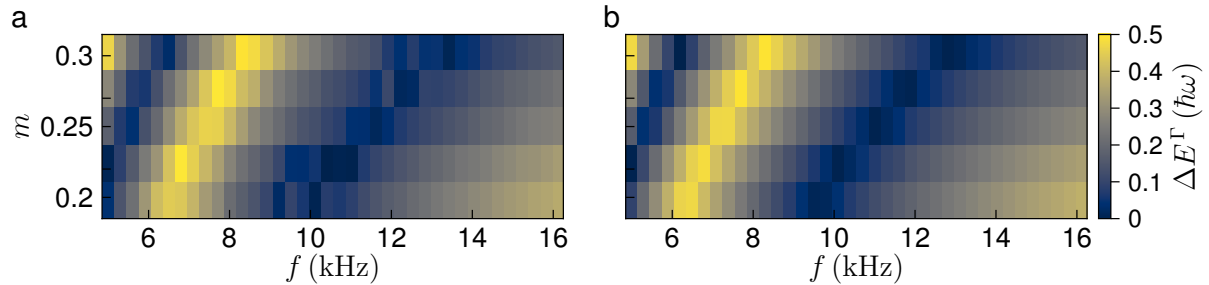


**Figure 5.15: Relative quasienergy gaps at  $\Gamma$  depending on the modulation frequency and amplitude.** **a.** Measured values using Stückelberg interferometry. The same data points as in Fig. 5.14 are used. **b.** Calculated quasienergy gaps using the six-band model for the same modulation parameters as the experimental values. The phase boundaries are given by the gap closings.

**Quasienergy gaps along the high-symmetry line** To further study the different topological regimes, the quasienergy gaps are also probed at different quasimomenta along the high-symmetry line  $\Gamma$ - $M$ - $K$ - $\Gamma$ , which is presented in Fig. 5.16. In these experiments, the lattice acceleration is divided into two parts: First, the cloud is moved along  $\Gamma$ - $M$  (gray path in Fig. 5.16a). Then, a second lattice frequency ramp is performed to either drive to different quasimomenta along the axis  $M$ - $\Gamma$  (green arrows) and  $M$ - $K$  (blue arrows), or to points lying on the connection line  $\Gamma$ - $K$  (red arrows), reached by changing the angle of the path. The lattice acceleration starts with a delay in time, such that it finishes simultaneously with the modulation ramp-up performed within  $t_r = 5 T$ . The resulting quasienergy gaps along all three segments are combined in Fig. 5.16b and Fig. 5.16c, probing the Haldane and anomalous regime for  $m = 0.25$ ,  $f = 14$  kHz and  $f = 7$  kHz, respectively. The measured values agree well with the calculated gaps, thus validating the model also for quasimomenta lying in between the high-symmetry points. The cusp-like maxima indicate again the change of the measured gap from  $g^\pi$  to  $g^0$  or vice versa, now depending on the quasimomentum instead of the modulation parameters (gray and white backgrounds). In the plots, the absolute quasienergy gaps are shown, but since each data set is measured at constant  $f$ , the relative quasienergy gaps along the path would look similar, but rescaled to the range  $[0, 0.5]$ .

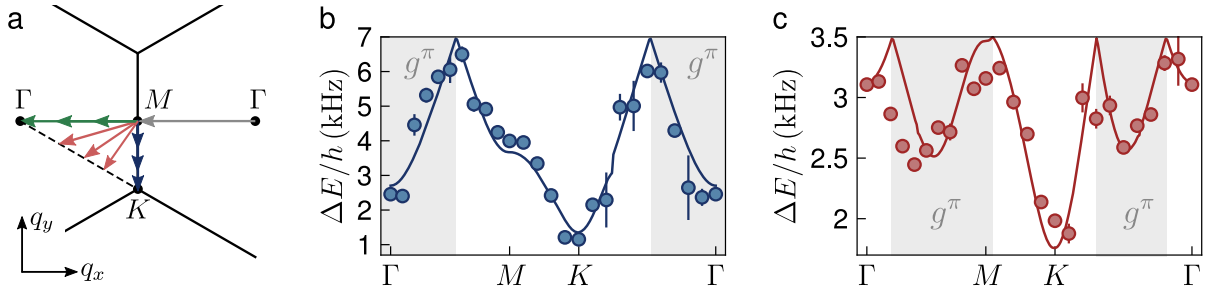


**Figure 5.16: Quasienergy gaps along high-symmetry lines in reciprocal space.**

**a.** Sketch of the paths along which the atoms are accelerated to measure the at the quasi-momenta lying on the connections lines  $\Gamma$ - $M$  (green arrows),  $M$ - $K$  (blue arrows) and  $K$ - $\Gamma$  (red arrows).

**b.** Measured quasienergy gaps along the complete path  $\Gamma$ - $M$ - $K$ - $\Gamma$  in the Haldane regime for  $f = 14$  kHz and  $m = 0.25$ , using  $Fa/h = 1360$  Hz, and corresponding theory values (blue line).

**c.** Measured quasienergy gaps in the anomalous regime for  $f = 7$  kHz and  $m = 0.25$  with  $Fa/h = 6801$  Hz, the theoretical gaps are depicted by the red line. The gray (white) shaded areas denote the regions where the quasienergy gap  $g^\pi$  ( $g^0$ ) is probed. All data points are obtained from a fit to the Stückelberg population oscillations consisting of 23 points, each being an average over 3-4 individual images, errorbars denote fitting errors.

### 5.2.2 Berry curvature

From the measured quasienergy gaps at  $\Gamma$ , the phase boundaries in the  $m$ - $f$  parameter space are obtained by linear fits, as described in the last section. To obtain the topological properties of the different sectors, the Berry curvature around  $\Gamma$  and  $K$  is probed, enabling the determination of the topological charge along the phase transitions. The local Berry curvature is again measured by performing Hall deflection measurements in the lowest band, employing the ramp-up schemes presented in Sec. 5.1.3. The forces that are used to move the cloud in quasimomentum space depend on to the modulation parameters. In the anomalous and third regime,  $Fa/h = 204$  Hz is used for all modulation frequencies and amplitudes, hence probing the Berry curvature for  $q_0 \rightarrow q_{\text{eff}} \approx 1.33\sqrt{3} k_L$  in the anomalous and along  $K$  in the third regime (here, the contributions from  $\Gamma \rightarrow q_{\text{eff}} \approx 1.33\sqrt{3} k_L$  and  $\Gamma \rightarrow q_0$  are subtracted). Along the  $\Gamma$ -direction in the third regime, the modulation is ramped up at  $\Gamma$  and hence the path  $\Gamma \rightarrow q_{\text{eff}} \approx 0.95\sqrt{3} k_L$  is measured.

In the Haldane regime for  $m = 0.2$ ,  $0.22$  and  $0.27$ , the deflections are also measured with  $Fa/h = 204$  Hz, probing  $q_0 \rightarrow q_{\text{eff}} \approx 1.33\sqrt{3} k_L$ . For  $m = 0.25$  and  $m = 0.3$ , at certain high modulation frequencies deep in the Haldane regime, large positive deflections at  $\Gamma$  have been observed, comparable to the values at  $K$ , when using a force of  $Fa/h = 204$  Hz or smaller. Since the coupling to higher bands is increased at these parameters, it might be that some of the atoms are transferred to  $p$ -bands via avoided crossings at which the lower band exhibits a jump, but the atoms are driven into another band which is resonant. This can be prevented by slightly increasing the force to  $Fa/h = 272$  Hz for  $m = 0.25$  and  $Fa/h = 340$  Hz for  $m = 0.3$ , moving the cloud along  $q_0 \rightarrow q_{\text{eff}} \approx 1.40\sqrt{3} k_L$ .

and  $q_0 \rightarrow q_{\text{eff}} \approx 1.33\sqrt{3}k_L$ , whereas in the latter case, the quasimomentum is set to  $q_f = 1.381\sqrt{3}k_L$  by the lattice acceleration, to compensate for the effect of the harmonic trap.

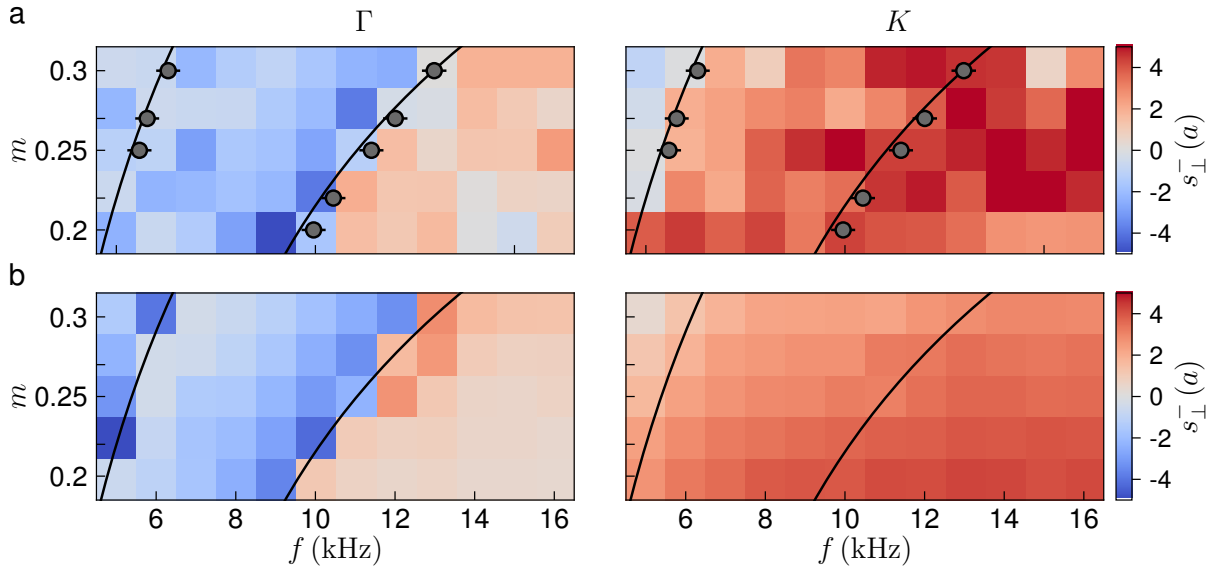


**Figure 5.17: Probing the Berry curvature as a function of the modulation frequency and amplitude.** Transverse differential deflections along the  $\Gamma$ - and  $K$ -directions (left and right panel) in units of the lattice constant, depending on the modulation frequency and amplitude. **a.** Measured deflections (colored pixels) and phase transition points (gray data points) which are obtained from linear fits to the measured quasienergy gaps at  $\Gamma$ . The solid black lines depict the theoretical phase boundaries. For the deflections, every data point is derived from three measurement points, each being an average over 30-40 experimental realizations. The mean SEMs along the  $\Gamma$ - and  $K$ -directions are  $\bar{\Sigma}_\Gamma = 0.72(4)a$  and  $\bar{\Sigma}_K = 0.78(5)a$ . The used forces and effective path lengths are denoted in the text. **b.** Calculated transverse deflections from the six-band model using the measured momentum space widths at each point and the corresponding forces. The black lines show again the theoretical phase boundaries.

The resulting transverse deflections along the  $\Gamma$ - and  $K$ -directions are presented in the left and right panel of Fig. 5.17a. The phase transition points obtained from the gap measurements are plotted as dark gray data points, following the theoretically expected phase boundaries quite well (black solid lines). The calculated deflections using the forces and momentum space widths from the experiments, are shown in the left and right panels of Fig. 5.17b. Across the first phase transition, the measured deflections at  $\Gamma$  change sign from positive to negative for all amplitudes, similar to the measurements in Fig. 5.12, indicating  $\Delta W^\pi = 1$  everywhere. The observed variation in the transverse deflection is in very good agreement with the theoretical calculations. At the second phase transition, observed for  $m \geq 0.25$ , the sign change of  $s_\perp^-$  is less pronounced than in Fig. 5.12, and for  $m = 0.25$  and  $m = 0.3$  it is hardly visible. This is partly due to the larger step size

of 1 kHz that is used for the modulation frequency, effectively jumping over the sharp peaks around the phase transition, which is also apparent in the calculations: Before the second phase transition, the theoretical deflections are still close to zero, since the narrow positive peak, as visible in Fig. 5.12, occurs at modulation frequencies lying in between the values probed here. Moreover, the magnitude of the negative deflection behind the transition might be reduced due to small excitations to the second band, as also observed in Fig. 5.12, since the corresponding quasienergy gaps at  $\Gamma$  are very small.

Along the  $K$ -direction, the measured transverse deflections are positive mostly everywhere as expected from the theoretical calculations shown below. The energy gap at  $K$  increases for larger modulation amplitudes and with decreasing modulation frequency across the Haldane and anomalous regime (see Fig. 5.14), which corresponds to a spread of the Berry curvature around  $K$ . The increasing area over which the Berry curvature is distributed can not be probed entirely by the cloud, leading to the decrease in the transverse deflections. Close to the second phase transition (probed for  $m \geq 0.25$ ), there is nearly no transverse deflection observed around  $K$  any more. The positive deflections at  $K$  together with the changing deflections at  $\Gamma$  illustrate again the change from  $\mathcal{C}^- = 1$  in the Haldane regime to  $\mathcal{C}^- = 0$  in the anomalous regime. Apart from the small modulation frequencies close to the second phase transition, the measured transverse deflections at  $\Gamma$  and  $K$  coincide well with the calculated values, confirming the theoretical model and the winding numbers previously derived for the different topological regimes.

## 5.3 Deflection measurements in the second band

The Berry curvature distribution in the lowest band and the quasienergy gaps between the first two bands have been probed, enabling the full characterization of the three topological regimes considered in this work in terms of the winding numbers. As described in Sec. 5.1.3, by combining the lattice acceleration with carefully chosen ramp-up schemes for the intensity modulation, the atoms can be loaded into the lowest band for all modulation parameters. Exploiting the limit of  $m \rightarrow 0$ , which connects the modulated lattice to the static lattice, it is also possible to load the atoms adiabatically into the second band and to measure the Berry curvature there, which will be described consecutively.

### 5.3.1 Loading into the second band

At the transition from the Haldane to the anomalous regime, the quasienergy gap  $g^\pi$  is closing at  $\Gamma$ . Subsequently, gaps open at avoided crossings, which are formed between the two lowest bands being shifted into each other. As discussed in Sec. 3.2.3, in the region in quasimomentum space around  $\Gamma$ , where the bands have already hybridized, the new lowest band in the anomalous regime is connected to the second band of the static lattice for  $m \rightarrow 0$  and vice versa. Hence, by starting the modulation ramp-up at  $\Gamma$  with initial frequencies  $f_0 \in [3.3, 6.6]$  kHz, lying in the anomalous regime at  $m \rightarrow 0$ , the atoms are loaded from the first band of the static lattice into the second band of the modulated lattice.

In Fig. 5.18, the ramp-up scheme for measuring the second band in the Haldane regime is presented for  $f = 10$  kHz and  $m = 0.16$ . In the first part of the ramp-up, the modulation amplitude is always increased linearly up to  $m = 0.3$ , while the frequency is ramped exponentially according to Eq. 5.9 from  $f_0 = 4.4$  kHz (maximal gap for  $m \rightarrow 0$ ) to  $f_f$ . In order to minimize excitations to the first band, the parameter  $p$  characterizing the ramp is again optimized to yield a maximum quasienergy gap  $\Delta E^\Gamma$  during the ramp-up.

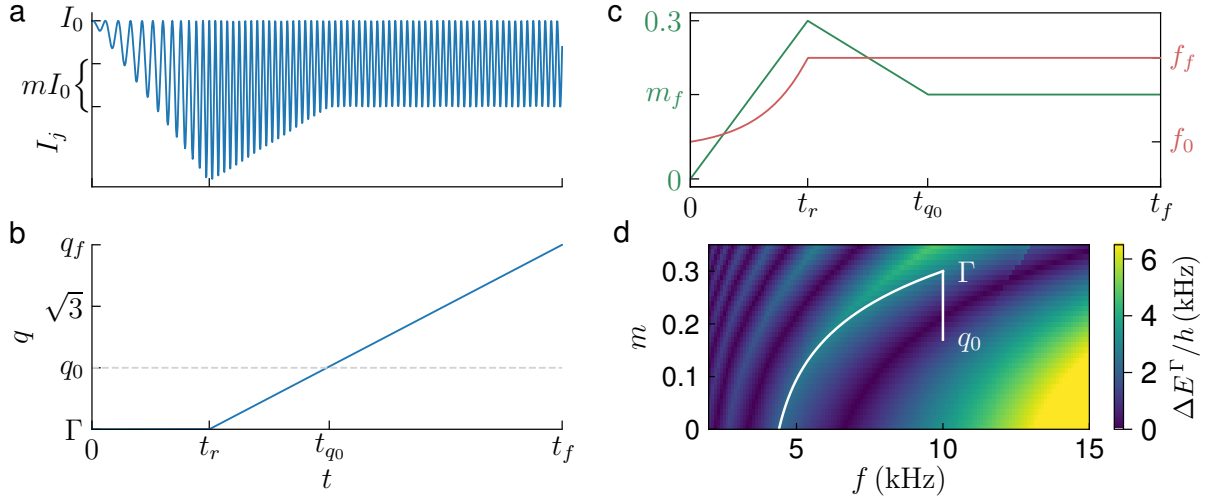


**Figure 5.18: Ramp-up sequence to load the second band in the Haldane regime.** Time-dependent parameters to probe the Berry curvature of the second band in the Haldane regime along the  $\Gamma$ - and  $K$ -direction, illustrated for  $f = 10$  kHz and  $m = 0.16$ . **a.** Time-dependent intensity  $I_j$  of a single beam. **b.** Quasimomentum set by the lattice acceleration. The atoms are held at  $\Gamma$  during the first part of the ramp-up and then moved to  $q_0$ . Subsequently, the Berry curvature is traversed between  $q_0$  and  $q_f$ . **c.** Time-dependent modulation amplitude (green) and frequency (red). The amplitude is increased linearly to  $m = 0.3$  and the frequency is ramped up exponentially from  $f_0 = 4.4$  kHz to  $f_f$  within  $t_r$  to load the second band. Then the modulation amplitude is decreased linearly to its final value  $m_f$ , crossing the phase transition within  $t_{q_0} - t_r$ . **d.** Calculated energy gaps  $\Delta E^\Gamma$ . The ramp-up path in parameter space is depicted by the white line, ending at a quasimomentum of  $q = q_0$ .

In the second part, the modulation amplitude is then decreased linearly from  $m = 0.3$  to its final value  $m_f$  at constant frequency  $f_f$ , while the atoms are accelerated by  $q_0$  to move away from the gap closing point at  $\Gamma$ . In this way, excitations to the first band at the transition to the Haldane regime can be avoided. However, the atoms necessarily traverse through the contracting Berry curvature around  $\Gamma$ , when the phase transition is approached. This leads to a non-vanishing transverse deflection resulting from the modulation ramp-up. To extract the signal originating from the Berry curvature between  $q_0$  and  $q_{\text{eff}}$ , the transverse deflection is measured first only for the ramp-up,  $\Gamma \rightarrow q_0$ , which is then subtracted from the result for the complete path  $\Gamma \rightarrow q_{\text{eff}}$ . This procedure needs to be performed along the  $\Gamma$ - and  $K$ -direction. The duration  $t_r$  of the first part is chosen

to be similar to the traversing time  $\Delta t$  from  $\Gamma$  to  $q_0$  for the given force, ending with a full cycle of the modulation. The ramp-up time of the second part  $t_{q_0} - t_r$  is given by the time needed to accelerate by  $q_0$  rounded up to full modulation cycles. Due to the change of the modulation period in the first part, the two times differ in general from each other.

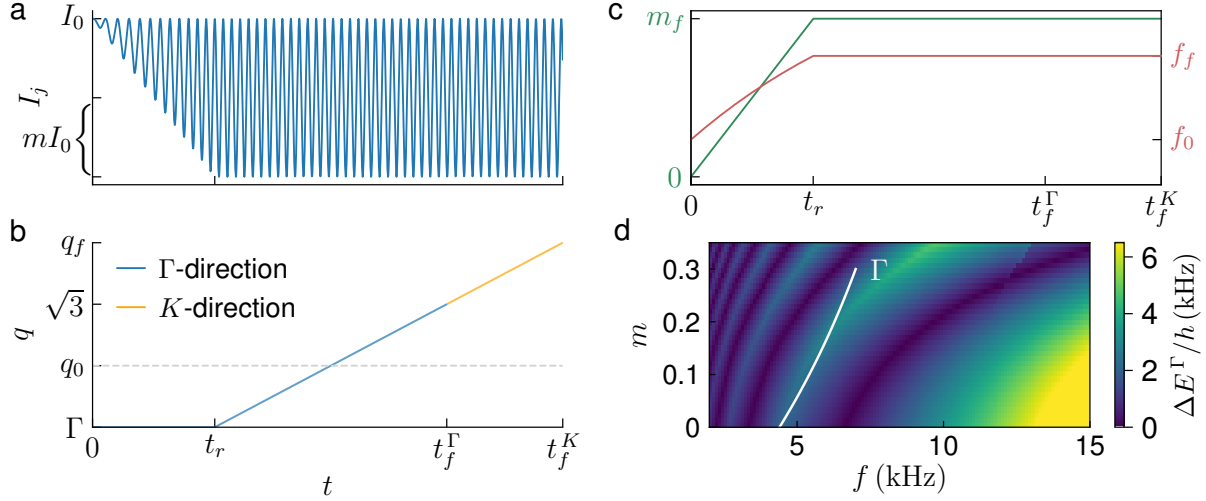


**Figure 5.19: Ramp-up sequence to load the second band in the anomalous regime.** Time-dependent parameters to probe the Berry curvature of the second band in the anomalous regime along the  $\Gamma$ - and  $K$ -direction, depicted for  $f = 7\text{ kHz}$  and  $m = 0.3$ . **a.** Time-dependent intensity  $I_j$  of a single beam. **b.** Quasimomentum set by the lattice acceleration. The atoms are held at  $\Gamma$  during the ramp-up and then moved to  $q_f$  to probe the Berry curvature. Along the  $K$ -direction, the transverse deflection for  $\Gamma \rightarrow q_0$  is subtracted from the signal for  $q_0 \rightarrow q_f = 1.5\sqrt{3}k_L$  (orange lines), along the  $\Gamma$ -direction, the path  $\Gamma \rightarrow \sqrt{3}k_L$  is traversed (blue line). **c.** Time-dependent modulation amplitude (green) and frequency (red). The amplitude is increased linearly to its final value and the frequency is ramped up exponentially to  $f_f$  within  $t_r$ . **d.** Calculated energy gaps  $\Delta E^\Gamma$ , the atoms remain at  $\Gamma$  during the ramp-up.

To probe the anomalous regime, the modulation amplitude and frequency are directly ramped to their final values while the atoms are held at  $\Gamma$ , so the ramp-up consists only of the first part. The modulation amplitude is increased linearly while the frequency again follows an exponential ramp from  $f_0 = 4.4\text{ kHz}$  to  $f_f$  with an optimized  $p$ -value. Measuring the Berry curvature around  $\Gamma$  along  $\Gamma$ - $M$ - $\Gamma$  is equivalent to  $M$ - $\Gamma$ - $M$ , and hence the cloud is subsequently accelerated by  $\sqrt{3}k_L$ . Along the  $K$ -direction, the transverse deflections for  $\Gamma \rightarrow q_{\text{eff}}$  and  $\Gamma \rightarrow q_0$  need to be subtracted, similar as in the Haldane regime. The corresponding time-traces for probing the deflection in the anomalous regime are shown in Fig. 5.19 for  $f = 7\text{ kHz}$  and  $m = 0.3$ . The ramp-up time  $t_r$  is again given by the time being closest to  $\Delta t$  and assuring that the modulation ends at full cycles.

In the third regime, the ramp-up is again divided into two parts to first load the atoms into the second band via the anomalous regime and then move across the transition to the third phase without exciting to the first band. As illustrated in Fig. 5.20, the modulation

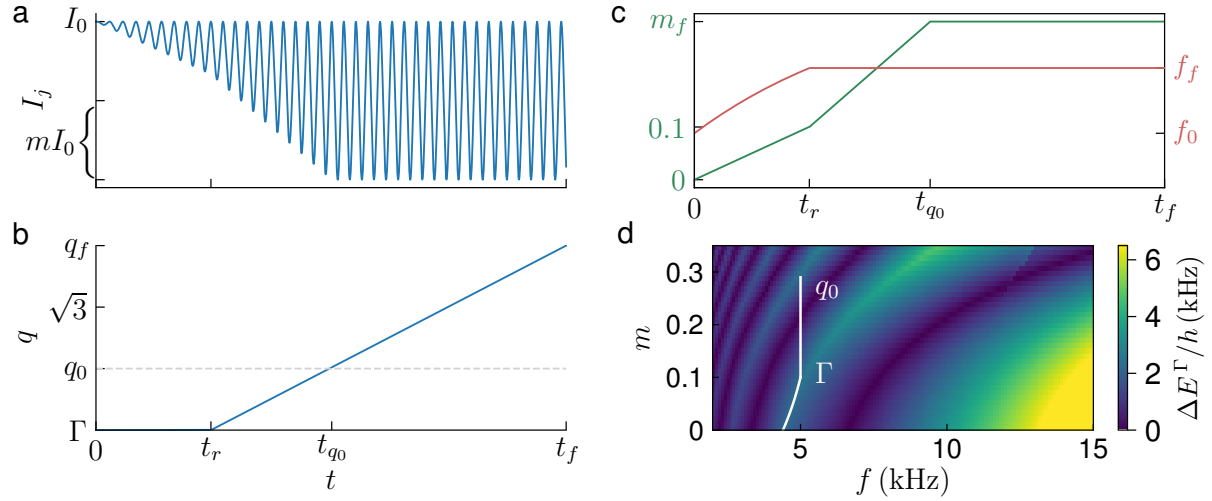


**Figure 5.20: Ramp-up sequence to load the second band in the third regime.** Time-dependent parameters to probe the Berry curvature of the second band in the third regime along the  $\Gamma$ - and  $K$ -direction, illustrated for  $f = 5$  kHz and  $m = 0.3$ . **a.** Time-dependent intensity  $I_j$  of a single beam. **b.** Quasimomentum set by the lattice acceleration. The atoms are held at  $\Gamma$  during the first part of the ramp-up and then moved to  $q_0$ . Subsequently, the Berry curvature is traversed between  $q_0$  and  $q_f$ . **c.** Time-dependent modulation amplitude (green) and frequency (red). The amplitude is increased linearly to  $m = 0.1$  and the frequency is ramped up exponentially from  $f_0 = 4.4$  kHz to  $f_f$  within  $t_r$  to load the second band. Then, the modulation amplitude is increased linearly to its final value  $m_f$  crossing the phase transition within  $t_{q_0} - t_r$ . **d.** Calculated energy gaps  $\Delta E^\Gamma$ , the white line depicts the ramp-up path in parameter space, ending at  $q = q_0$ .

amplitude is first increased linearly up to  $m = 0.1$  and the frequency is ramped up exponentially from  $f_0 = 4.4$  kHz to  $f_f$ , where the  $p$ -value is again optimized to maximize the quasienergy gap during the ramp-up. Then, in the second part, the transition to the third regime is traversed by ramping up the modulation amplitude to its final value and keeping the frequency constant at  $f_f$ .

Similar as in the Haldane regime, the atoms are accelerated by  $q_0$  in the second part to avoid the gap closing at  $\Gamma$ . Approaching the second phase transition, the Berry curvature around  $\Gamma$  spreads out, which means that both the radius and the width of the ring are increasing and the atoms can pass through some Berry curvature during this stage. The positive and negative peaks of Berry curvature at  $\Gamma$ , occurring shortly before and after the phase transition, are however not traversed, since the cloud is moved by  $q_0$ . To ensure that there is no transverse deflection during the ramp-up, the signals for  $\Gamma \rightarrow q_{\text{eff}}$  and  $\Gamma \rightarrow q_0$  are both measured and again subtracted when probing along the  $\Gamma$ - and  $K$ -direction. The ramp times  $t_r$  and  $t_{q_0} - t_r$  are chosen just as in the Haldane regime, both being close to the traversing time  $\Delta t$  and rounded to full cycles of the modulation, taking into account the changing frequency in the first part.

### 5.3.2 Probing the different topological regimes

With the ramp-up schemes described above, it is possible to load the atoms into the second band in all topological regimes to probe the Berry curvature. To test the loading schemes and to benchmark the topological regimes also in the second band, the transverse deflections are measured around the  $\Gamma$ -and  $K$ -point at several sets of modulation parameters along the path depicted in Fig. 5.1. This allows for a direct comparison with the results for the first band, presented in Fig. 5.12. The sum of the Chern numbers of the two  $s$ -bands is always zero and the Berry curvature distribution in the second band is the inverse of the distribution in the first band (in the ideal two-band tight-binding model). This is confirmed by the measured transverse deflections in the second band,  $s_{\perp}^+$ , which are shown in Fig. 5.21. The cloud is accelerated with  $Fa/h = 170$  Hz, and hence moved by  $q_{\text{eff}} \approx 1.25\sqrt{3}k_L$ , similar to the measurements in Fig. 5.12. The time needed to accelerate up to  $q_0$  during the modulation ramp-up is  $\Delta t \approx 1.96$  ms, determining the values for  $t_r$  and  $t_{q_0} - t_r$ .

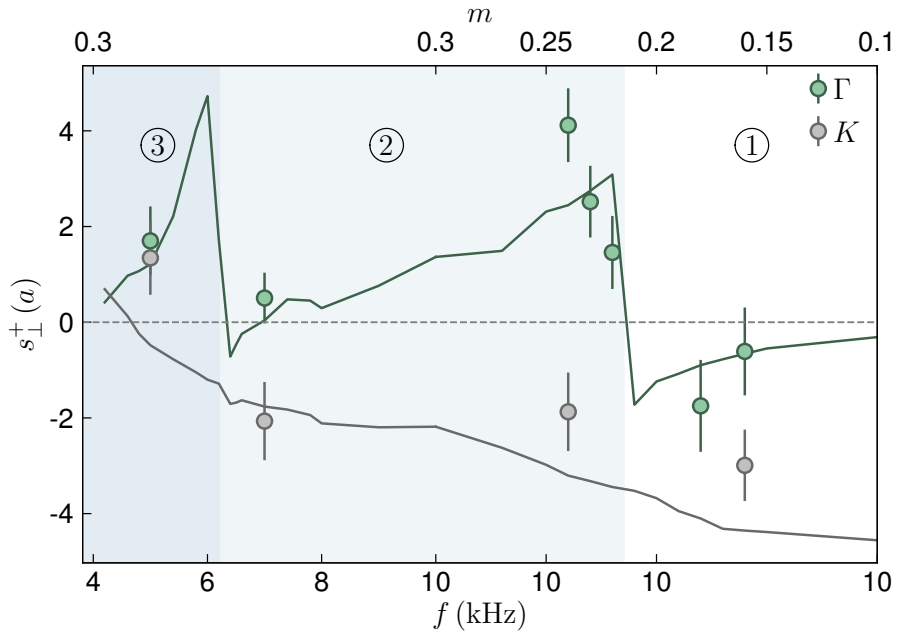


**Figure 5.21: Probing the Berry curvature of the second band.** Transverse deflections in the second band  $s_{\perp}^+$  in units of the lattice constant, measured along the  $\Gamma$ - and  $K$ -directions (green and gray data points and lines) depending on the modulation frequency and amplitude. Every data point represents the differential deflection derived from three measurement points, each being an average over 30-40 experimental realizations, the errorbars denote the SEM. The deflections are measured with  $Fa/h = 170$  Hz for  $q_0 \rightarrow q_{\text{eff}} \approx 1.25\sqrt{3}k_L$ , except for the  $\Gamma$ -direction in the anomalous regime, where  $\Gamma \rightarrow q_{\text{eff}} \approx 0.93\sqrt{3}k_L$  is probed. The solid lines depict the theoretical calculations, incorporating the measured momentum space widths. The different topological phases are indicated by the blue shaded areas and the numbers.

In the Haldane regime, the Berry curvature at  $\Gamma$  (green data points) is negative and increases in magnitude, when approaching the first phase transition. Subsequently, the deflections turn to positive values indicating the peak of positive Berry curvature arising at  $\Gamma$  and signaling again the change of the winding number:  $\Delta W^\pi = \text{sgn}(\Delta s_\perp^+(\Gamma)) = 1$ .

The second phase transition is not measured in detail, but deeper in the anomalous regime the deflection decreases in magnitude and is then distinctly positive again in the third regime. The signal at  $K$  (gray data points) remains negative throughout the Haldane and anomalous regime with decreasing magnitude, as expected from the spreading negative Berry curvature around the Dirac points, and then becomes slightly positive in the third regime. Overall, the measured transverse deflections agree well with the theoretical predictions calculated in the same way as for the first band. This confirms once more the derived change of the winding numbers across the two phase transitions.

Moreover, it shows that the loading schemes presented above are functional and the atoms are indeed loaded into the second band without many losses, as visible from the good quantitative agreement with the calculations. Hence, the connection between the lowest band of the static lattice and the first or second band of the modulated lattice in the limit  $m \rightarrow 0$  does not remain a theoretical consideration, but could be verified experimentally.

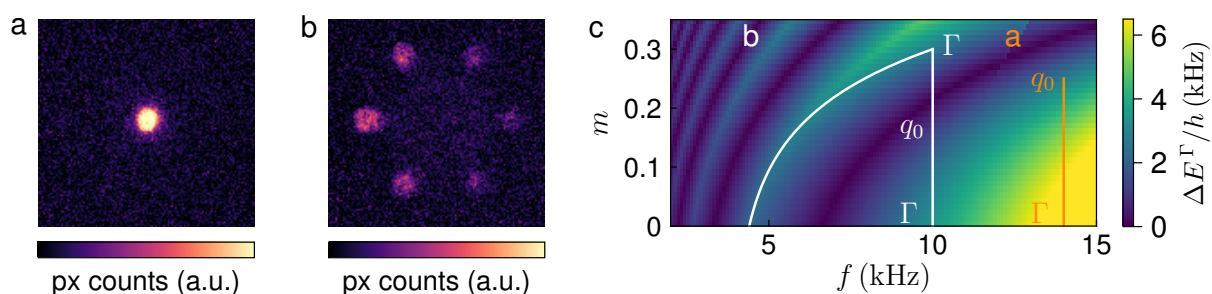


**Figure 5.22: Test of the loading schemes in the Haldane regime.** **a.** Absorption image after loading the atoms into the first band in the Haldane regime, reverting the ramp-up and subsequently performing bandmapping in the static lattice, resulting in all atoms being back in the lowest band. **b.** Absorption image when loading the atoms into the second band in the Haldane regime and then decreasing the modulation amplitude at a constant frequency while moving back to  $\Gamma$ . The population remains in the second band of the modulated lattice, which is connected to the second band of the static lattice in the Haldane regime. **c.** Calculated energy gaps  $\Delta E^\Gamma$ . The ramping paths in parameter space corresponding to the images in **a** and **b** are depicted by the orange and white lines, respectively. The CoM quasimomenta at the different stages of the ramps are noted next to the lines.

The loading schemes used for the first and second band have also been tested by performing bandmapping measurements. To verify that no excitations to the other band occur, the respective modulation ramp-up is performed as described in this and the previous section, including possible accelerations by  $q_0$ . Then, the modulation is directly

ramped down again, while also inverting the lattice acceleration, moving the atoms back to  $\Gamma$  in the static lattice. The lattice intensity is ramped down to execute bandmapping after a TOF of 3.5 ms and the populations in the first and second band are counted, resulting in most of the atoms being back in the lowest band. In Fig. 5.22a, an absorption image is shown when testing the loading into the first band in the Haldane regime, which corresponds to the orange path in Fig. 5.22c. The ramp-up times and forces presented previously are optimized by maximizing the population in the lowest band after this sequence. In addition, the loading of the second band can also be proven directly: After the second band is loaded in the Haldane regime, the modulation amplitude is ramped down linearly for constant  $f = f_f$ , while moving the atoms back to  $\Gamma$ , as illustrated by the white path in Fig. 5.22c. Hence, the modulation parameters remain in the Haldane regime, where the second band of the modulated lattice is connected to the second band of the static lattice, resulting now in all population being distributed to the outer peaks in the bandmapping images (see Fig. 5.22b).

## 5.4 Lifetimes

With the lattice intensity modulation scheme presented in this work, different topological regimes, including an anomalous Floquet setting, can be realized and have been investigated experimentally in the last sections. On the one hand, the combination of the Haldane model with larger interactions is desirable in view of exploring fractional Quantum Hall phases. On the other hand, interesting features of anomalous Floquet systems as the ring like-minimum in the lowest band or the propagation of chiral edge modes in all topological regimes are subjects of interest and will be discussed in more detail in chapter 7. To get a first idea of the experimental feasibility of these phenomena and to enable a direct comparison with the phase modulation scheme presented in chapter 6, the lifetime of the BEC is measured in the different topological regimes. The methods used to determine the lifetime and the results are described in the course of this section.

### 5.4.1 Measurement of the lifetimes

The lifetimes are measured at the  $\Gamma$ -point, since this will be the starting point for most kind of measurements. To determine the lifetimes, the modulation is ramped up at  $\Gamma$ , held for integer multiples of the driving period,  $t = NT$ ,  $N \in \mathbb{N}$ , until most of the atoms are lost, and then ramped down again. Subsequently, the intensities of all lattice beams are ramped down to perform bandmapping after a TOF of 10 ms. Here, a long TOF is used to reduce the contributions from thermal atoms expanding much faster than the BEC and to count only the condensed atoms being left in the lowest band of the static lattice. In the anomalous regime, the lifetime is measured in the second band, exhibiting a minimum at  $\Gamma$ , similar as the lowest band in the Haldane and third regime.

For modulation parameters in the Haldane regime, the amplitude is increased linearly to  $m_f$  at a constant frequency within  $t_r = 5T$ , and ramped down in the same way. In the anomalous regime, the modulation frequency is ramped exponentially from  $f_0 = 4.4$  kHz

to  $f_f$ , as described in the last section, thus loading the second band. The rampup time is  $t_r = 12T$ , being close to 2 ms for all parameters probed here. In the third regime, the lowest band is loaded as explained in Sec. 5.1.3, also using an exponential frequency ramp, starting from  $f_0 = 2.7$  kHz, with  $t_r = 7T - 8T \approx 2$  ms. The ramp-down of the modulation is always the inverse of the ramp-up. After bandmapping, the pixel sum corresponding to the population in the first band,  $\Sigma^1$  is determined, as described in Sec. 4.2.2.

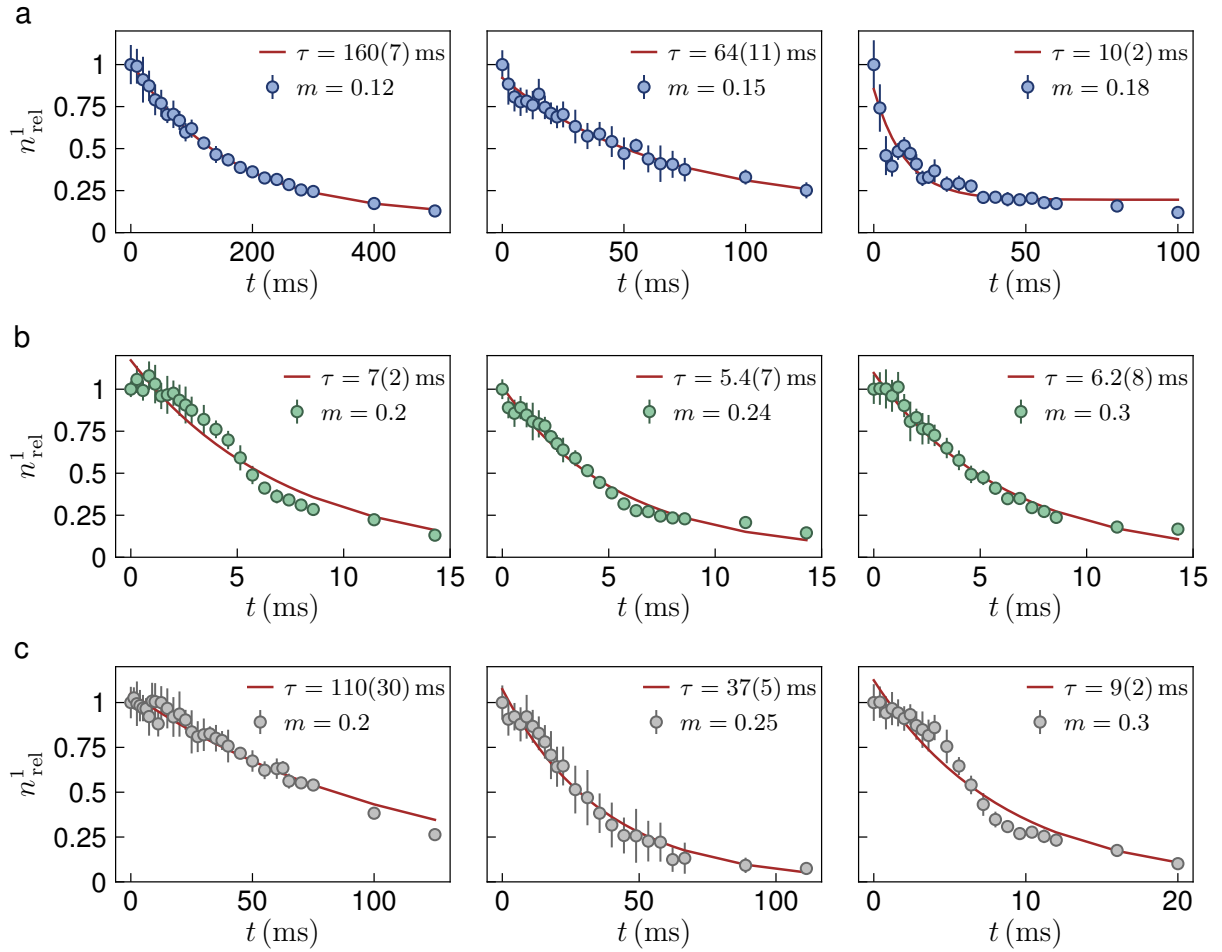


**Figure 5.23: Decay measurements of the BEC depending on the modulation parameters.** Measured relative population (data points) in the lowest band after bandmapping, normalized to the value at  $t = 0$  as a function of the hold time in the different topological regimes. The red lines depict a fit according to Eq. 5.14 to determine the lifetime  $\tau$ . **a.** Decay of the BEC loaded into the lowest band at  $\Gamma$  in the Haldane regime for  $f = 10$  kHz and  $m = (0.12, 0.15, 0.18)$  from left to right. **b.** Decay in the anomalous regime in the second band at  $\Gamma$  for  $f = 7$  kHz and  $m = (0.2, 0.24, 0.3)$  from left to right. **c.** Decay in the third regime in the lowest band at  $\Gamma$  for  $f = (4, 4.5, 5)$  kHz and  $m = (0.2, 0.25, 0.3)$  from left to right. Each data point is an average over 10 experimental realizations, the errorbars denote the standard error.

The values of the hold time are adapted to the lifetime such that most of the atoms are lost at the end of the trace, enabling a meaningful fit to determine the lifetime. For each hold time, the pixel sum for about 10 individual images is averaged and the relative sum, divided by the value for  $t = 0$ , is plotted as a function of the hold time, as shown in Fig. 5.23. To determine the lifetime, an exponential decay is assumed and the following function is fitted to the data, with  $A$ ,  $\tau$  and  $\Sigma_0$  being free parameters:

$$\Sigma_{\text{rel}}^1(t) = A e^{-\frac{t}{\tau}} + \Sigma_0. \quad (5.14)$$

Since the maximal hold times are chosen such that nearly all atoms are lost, the offset  $\Sigma_0$  is vanishing in most of the measurements.

For the static lattice and deep in the Haldane regime the measured decay is well described by Eq. 5.14. But when approaching the transition to the anomalous regime, oscillations of the population on top of the decay can be observed, as presented in Fig. 5.23a for increasing modulation amplitude and  $f = 10$  kHz. For  $m = 0.18$ , the frequency of these oscillations is around 1 kHz, roughly matching the quasienergy gap at  $\Gamma$  between the first and second band. This might be a sign of excitations to the second band during the hold time. In the anomalous regime, the shape of the decay also changes with the modulation parameters. In Fig. 5.23b, the measured decay is compared for  $f = 7$  kHz and different modulation amplitudes. At  $m = 0.2$ , it exhibits an s-shape, which turns into an exponential decay for large modulation amplitudes, departing from the phase transition. A similar behavior is observed in the third regime at  $f = 5$  kHz and  $m = 0.3$  shown in the last panel of Fig. 5.23c. But now the shape also changes to exponential for  $f = 4$  kHz and  $m = 0.2$  (left panel), which is similarly close to the phase transition. One reason for the observed s-shaped decay might be that atoms being excited at early times do not leave the trap and are still counted in the TOF images. Nevertheless, to get comparable results, the decay is fitted according to Eq. 5.14 for all modulation parameters.

### 5.4.2 Lifetimes in the different topological regimes

In the Haldane regime, the lifetime is determined at  $f = 10$  kHz for different modulation amplitudes and at  $m = 0.1$  for modulation frequencies of  $f = (10, 20)$  kHz, as presented in Fig. 5.24a. The lifetime in the static lattice is measured along with each data set and the corresponding point in Fig. 5.24a represents an average over four measurements. The lifetime decreases linearly with the modulation amplitude and increases with the modulation frequency, which corresponds to shifting the modulation parameters towards or away from the phase transition. Along with the modulation amplitude the coupling to the Floquet copies of higher bands is increased, which enhances the probability of excitations, leading to a depletion of the BEC.

At  $f = 20$  kHz and  $m = 0.1$  the lifetime is comparable to the static lattice. Due to the small modulation amplitude, the coupling to higher bands is weak and at the same time the modulation frequency is large enough that  $g^\pi > g^0$ , as the cusp with  $g^\pi = g^0$  occurs at  $f = 15.5$  kHz for  $m = 0.1$ . This yields quasienergy bands similar to the static lattice apart from the gap at  $K$ . Increasing the modulation frequency further brings the

*p*-bands into resonance: At  $f = 30$  kHz (not shown in the plot), the lifetime decreases again and takes the same value as for  $f = 10$  kHz.

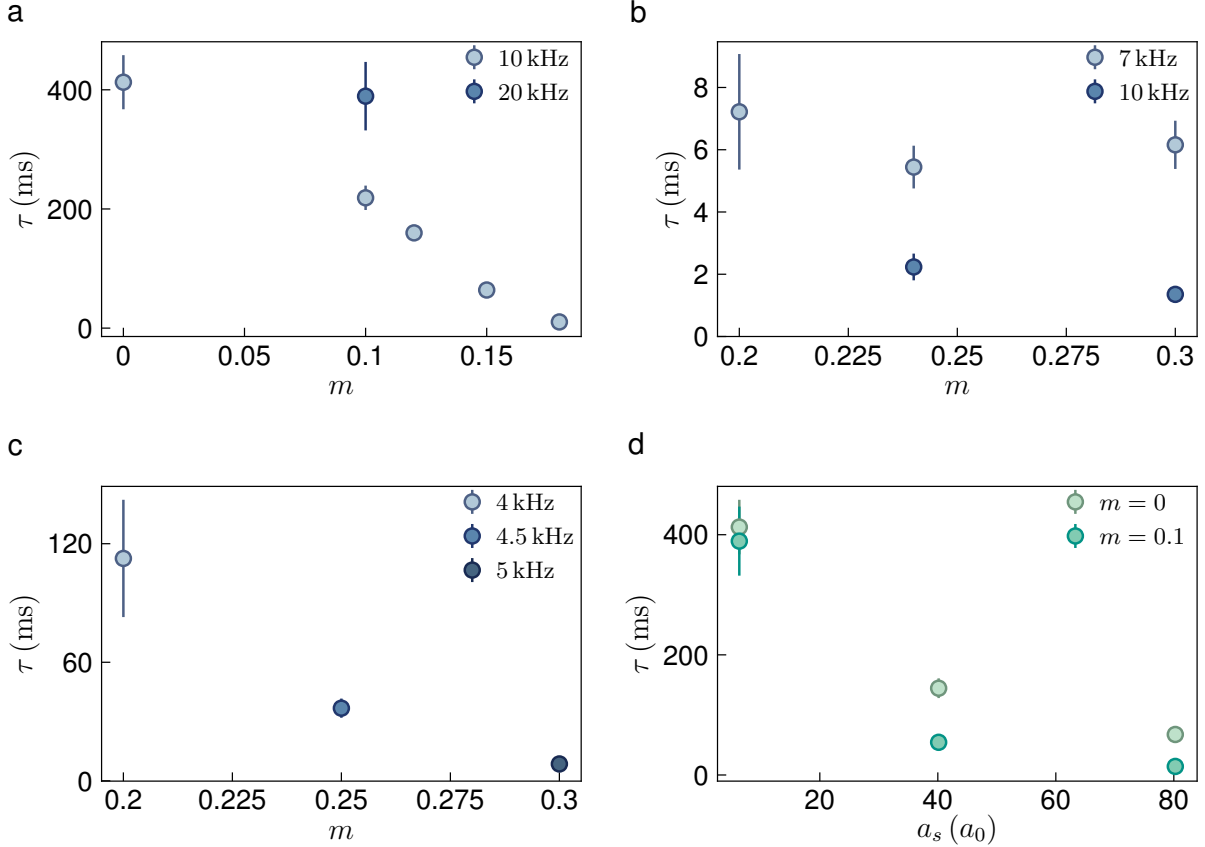


Figure 5.24: **Measured lifetimes at  $\Gamma$  in the different topological regimes.** **a.** Lifetimes for various modulation amplitudes and frequencies in the lowest band in the Haldane regime, compared to the static lattice (which is an average over 4 data sets). **b.** Anomalous regime probed in the second band, which exhibits a minimum at  $\Gamma$ . **c.** Third regime, probed in the lowest band for modulation parameters lying similarly close to the second phase transition. **d.** Lifetimes vs. scattering length measured in the lowest band in the Haldane regime for  $f = 20$  kHz and compared with the static lattice. The data points are obtained by fitting Eq. 5.14 to a decay measurement consisting of 23 points, each being an average over 10 experimental realizations, the errorbars denote the fitting errors.

In the second band and anomalous regime, the measured lifetimes at  $\Gamma$  are considerably smaller than in the Haldane regime (Fig. 5.24b). In general, the lifetimes approximately drop by a factor of two when increasing the modulation frequency, signaling more excitations to higher bands, as expected in this parameter range. The difference of the modulation parameters compared to the first phase boundary does not seem to play a major role, since  $m = 0.2$ ,  $f = 7$  kHz and  $m = 0.3$ ,  $f = 10$  kHz lie similarly close to the phase transition but the lifetimes differ by a factor of five.

This is also observed in the third regime (see Fig. 5.24c), where three sets of modulation parameters are compared, all lying similarly close to the second phase transition. The lifetime strongly depends on the absolute values of the modulation amplitude and frequency, decreasing by more than a factor of 10 from  $m = 0.2$ ,  $f = 4\text{ kHz}$  to  $m = 0.3$ ,  $f = 5\text{ kHz}$ . In total, the lifetime of the BEC at  $\Gamma$  is reduced for larger modulation amplitudes, enhancing the probability of coupling to Floquet copies of higher bands and partly also for higher modulation frequencies.

The smallest lifetimes observed in Fig. 5.24 are in the range of  $\tau \approx 2\text{ ms}$ , which is already less than the maximal durations of the deflection and Stückelberg measurement sequences: Probing the Berry curvature with  $Fa/h = 170\text{ Hz}$  up to  $q_{\text{eff}} \approx 1.25\sqrt{3}k_L$  takes about 5.88 ms. Holding the atoms at  $\Gamma$  for a time  $t = 23T$  in the Stückelberg measurements with  $f = 4.6\text{ kHz}$ , which is the smallest modulation frequency for which the quasienergy gaps are measured, takes about 5 ms. As described in Sec. 5.1.1, at these long hold times, the heating and depletion of the BEC are visible in the TOF images used for the Stückelberg interferometry, leading to the observed damping of the oscillations and limiting the maximal hold times and minimal modulation frequencies that can be probed. On the other hand, atom loss and heating have only a minor influence on the insitu images used in the deflection measurements. Here, the CoM-position is evaluated, which is not altered by a reduction of the cloud size and the BEC can still be fitted well in all insitu images used in this work.

So far, all measurements have been done in the non-interacting limit by setting the scattering length to  $a_s = 6a_0$  using the Feshbach resonance of  $^{39}\text{K}$ . As mentioned in the beginning of this section, it would be interesting to combine topological band structures with strong inter-particle interactions. Since all experiments reported here are performed in a 2D lattice of tubes with harmonic confinement along the vertical direction, the ratio of the Hubbard interaction  $U$  to the hopping will remain small, even if the Feshbach resonance is used to increase the scattering length. For  $a_s = 6a_0$ , it amounts to  $U/J \approx 0.01$  in the presence of the harmonic trapping potential with  $f_z = 200\text{ Hz}$  along the vertical direction (see Sec. 7.1.3).

Nevertheless, as a first test along these lines, the lifetimes in the Haldane regime are measured as a function of the scattering length, which is shown in Fig. 5.24d. The modulation frequency is set to  $f = 20\text{ kHz}$  and the lifetimes for  $m = 0.1$  are compared to the static lattice. The lifetime decreases non-linearly with the scattering length and the further reduction due to the lattice modulation is small compared to the effect of the interactions. In the 2D lattice system studied here, interaction-induced resonances are moreover facilitated by the harmonic confinement along the vertical axis, leading to a nearly continuous energy spectrum in this direction. These effects are investigated in chapter 9 using the example of a periodically driven 1D lattice. However, the minimal lifetime observed in the Haldane regime for  $a_s = 80a_0$  is about  $\tau \approx 15\text{ ms}$ , which is still sufficient to conduct measurements of the quasienergy gaps and the Berry curvature.

In the anomalous regime, the lifetime is probed in the second band, exhibiting a minimum at  $\Gamma$ . To measure the lifetime of the BEC in the lowest band, it would be desirable to load it into the degenerate ring-like minimum around the  $\Gamma$ -point, which

can also be the starting point to explore the interplay with interactions and to observe fermionization effects. This will be discussed in more detail in chapter 7, along with modifications of the experimental setup which enable a direct measurement of the chiral edge modes. In general, anomalous Floquet systems could be stabilized by disorder, since they allow for a many-body localized bulk, coexisting with thermalizing edge states (see Sec. 7.1 and [59]).



# Chapter 6

## Anomalous Floquet phases in a shaken honeycomb lattice

By periodic intensity modulation of the optical honeycomb lattice, different topological regimes, including an anomalous Floquet system, can be realized and have been characterized theoretically and experimentally in the previous chapters. As mentioned in Sec. 2.2, circular shaking of the entire honeycomb lattice potential has been used to generate a Haldane phase [103, 104]. This technique can also be employed to realize an anomalous Floquet system when adding a sublattice energy offset [120]. In general, a variety of topological regimes arise in the circularly shaken honeycomb lattice, these are discussed in Sec. 6.1, along with the emergence of the anomalous phase. To derive the dispersion of the chiral edge modes, a tight-binding description of the modulated lattice is introduced in Sec. 6.2, which also serves as a starting point for the analytical derivation of the effective Hamiltonian in the limit of large shaking frequencies. Measurements of the quasienergy gaps and the lifetimes of the atomic cloud in the shaken lattice are presented in Sec. 6.3. For the shaking parameters considered there, the quasienergy gaps are small compared to the regimes probed in the intensity modulated lattice. Moreover, the anomalous Floquet regime requires relatively large shaking amplitudes, where the lifetimes are expected to be strongly reduced, favoring the use of intensity modulation to realize these regimes experimentally.

### 6.1 Modulation scheme and topological phase diagram

The circular shaking of the lattice potential can be implemented by modulating the relative phases of the laser beams in a chiral manner. This results in an interference pattern moving along a circle in real space and thus breaking time-reversal symmetry. In this section, the modulation scheme is presented and the resulting phase diagram is discussed, especially in the presence of a sublattice energy offset, which additionally breaks inversion symmetry. Thereby, a formerly degenerate band touching point at  $\mathbf{q} = \Gamma$

is split in frequency and quasimomentum space, giving rise to an anomalous Floquet phase.

### 6.1.1 Circular shaking of the honeycomb lattice

The phase modulation of the honeycomb lattice is realized by changing the frequency of two laser beams periodically in time with frequency  $\omega$  and amplitude  $b$ :

$$\begin{aligned}\omega_1(t) &= \omega_L + b \sin\left(\omega t - \frac{\pi}{3}\right) \\ \omega_2 &= \omega_L \\ \omega_3(t) &= \omega_L + b \sin(\omega t),\end{aligned}\quad (6.1)$$

which corresponds to a circular motion of the interference pattern in real space. The frequency modulation gives rise to an additional, time-dependent phase in the electric fields:

$$\phi_j(t) = \int_0^t (\omega_L + b \sin(\omega t - \zeta_j)) dt' = \omega_L t - \frac{b}{\omega} (\cos(\omega t + \zeta_j) - \cos(\zeta_j)), \quad (6.2)$$

where  $\zeta_j$  denotes the phase of the frequency modulation of the  $j$ th beam. Thus, the electric field of the beam propagating along the direction  $\mathbf{k}_j$ ,  $j = \{1, 3\}$ , is given by

$$\mathbf{E}_j(\mathbf{r}, t) = \sqrt{I_j} e^{-i\mathbf{k}_j \mathbf{r} - i\omega_L t + i\frac{b}{\omega}(\cos(\omega t + \zeta_j) - \cos(\zeta_j))} (\cos(\theta_j) \mathbf{z} + \sin(\theta_j) e^{i\alpha_j} (\mathbf{z} \times \mathbf{k}_j)), \quad (6.3)$$

and the resulting interference pattern becomes time-dependent. The change of the wavevectors arising from the frequency modulation can be neglected, as  $b/c \ll \omega_L/c$  with  $b$  being in the range of several kHz. Since the complete lattice potential is moving in space, a transformation into a rotating frame, co-moving with lattice, can be performed, which leads to a time-independent potential. By defining

$$\mathbf{r} \rightarrow \mathbf{r}' + \mathbf{r}_{\text{lat}} = \mathbf{r}' + \frac{b}{\sqrt{3}k_L\omega} \begin{pmatrix} \cos(\omega t) - 1 \\ \sin(\omega t) \end{pmatrix}, \quad (6.4)$$

the intensity  $I(\mathbf{r}')$  takes the same form as in the static lattice (see Eq. 3.5):

$$I(\mathbf{r}') = \sum_{j,l=1}^3 \sqrt{I_j I_l} e^{-i\mathbf{k}_j \mathbf{r}'} (\cos(\theta_j) \cos(\theta_l) + \sin(\theta_j) \sin(\theta_l) \cos(\eta_j - \eta_l) e^{i\alpha_{jl}}). \quad (6.5)$$

The Hamiltonian in the co-moving frame can be expressed as

$$\hat{H}(\mathbf{r}', t) = \frac{(\hat{\mathbf{p}}' - \mathbf{A}(t))^2}{2m} + V(\mathbf{r}') \approx \frac{\hat{\mathbf{p}}'^2}{2m} - \frac{\hat{\mathbf{p}}' \cdot \mathbf{A}(t)}{m} + V(\mathbf{r}'), \quad (6.6)$$

where the term  $\propto \mathbf{A}(t)^2$  has been neglected, as it just describes a time-dependent offset. Hence, the modulation corresponds to an emerging gauge field  $\mathbf{A}(t)$  in the reference frame of the lattice, which is defined as

$$\mathbf{A}(t) = -m \dot{\mathbf{r}}_{\text{lat}}(t) = \frac{bm}{\sqrt{3}k_L} \begin{pmatrix} \sin(\omega t) \\ -\cos(\omega t) \end{pmatrix}. \quad (6.7)$$

To solve the Schrödinger equation for a given time  $t$ , the Hamiltonian can be expanded in plane waves, as described in Sec. 3.1.2, resulting in an eigenvalue equation for the coefficients as stated in Eq. 3.12, with the modified Hamiltonian matrix

$$H_{\mathbf{KK}'}(t) = \left( \frac{\hbar^2(\mathbf{q}' + \mathbf{K})^2}{2m} - \frac{\hbar^2}{2m} \frac{2}{\hbar} \mathbf{q}' \cdot \mathbf{A}(t) \right) \delta_{\mathbf{K},\mathbf{K}'} + V_{\mathbf{K}'-\mathbf{K}}. \quad (6.8)$$

The effective Hamiltonian describing the shaken honeycomb lattice in the co-moving frame can be calculated analogously to the case of intensity modulation, namely by numerically integrating the time-dependent Hamiltonian over one period of the driving, as defined in Eq. 3.23. The instantaneous Hamiltonian  $\hat{H}(t)$  at each time step  $t$  is derived using Eq. 6.8 for a given quasimomentum, modulation amplitude and polarization. In the following, the topological properties of the two lowest Floquet bands are considered. To allow for coupling of these bands with the  $p$ -bands during the driving period, the instantaneous Hamiltonian is projected to its six lowest eigenstates at each time step and then transferred to a common basis, similar to the procedure described in Sec. 3.2.2. To identify the two lowest Floquet bands, the overlap between the eigenstates at neighboring quasimomenta is considered, starting again with the unit vectors which correspond to the eigenstates of the static lattice in the common basis.

The influence of the higher bands on the shape of the two lowest Floquet bands depends on the modulation parameters. For the shaking amplitudes considered in the following and used in the lifetime measurements, the coupling to the  $p$ -bands is small, facilitating the determination of the two lowest bands. Moreover, in this parameter regime, the system is well described by projecting only to the two lowest bands during the modulation period or by using a two-band tight-binding model, as discussed in Sec. 6.2.

### 6.1.2 Overview of the topological phases

Using circular phase modulation of the honeycomb lattice, a variety of different topological regimes can be realized, including an anomalous Floquet system. In the following, shaking amplitudes in the range of  $\nu = b/(2\pi) \in [0, 20]$  kHz and frequencies  $f \in [2, 10]$  kHz are considered, representing a parameter regime accessible in experiments (see Sec. 6.3). The lattice depth is set to  $V_0 = 6 E_r$  and the sublattice energy offset  $\Delta$  is generated by using elliptically polarized lattice beams, as explained in Sec. 3.1.3. Its magnitude can be varied by changing the angle  $\theta = \theta_j, \forall j$  of the ellipse (see Eq. 6.5). The topological phase diagram in terms of  $f$  and  $\nu$  is presented in Fig. 6.1a for the symmetric lattice and in Fig. 6.1b for  $\theta = 0.05$  rad, which corresponds to a sublattice energy offset of  $\Delta \approx 0.051 E_r$ .

**Symmetric lattice** If  $\theta = 0$ , the shaken lattice resembles a Haldane phase ① for large frequencies and amplitudes. Quasienergy gaps have opened at the two Dirac points, giving rise to negative Berry curvature and  $\mathcal{C}^- = -1$  for the driving phases specified in Eq. 6.1, which can also be seen directly when calculating the effective Hamiltonian in the high frequency limit (Sec. 6.2.2). Reverting the modulation direction leads to a complete inversion of the Berry curvature distribution and hence of the Chern and

winding numbers. The quasienergy bands along the high-symmetry line  $\Gamma$ - $M$ - $K$ - $\Gamma$  as well as the bands and Berry curvature in the two-dimensional (2D) Brillouin zone (BZ) are shown in Fig. 6.2 in the different regimes for the symmetric lattice.

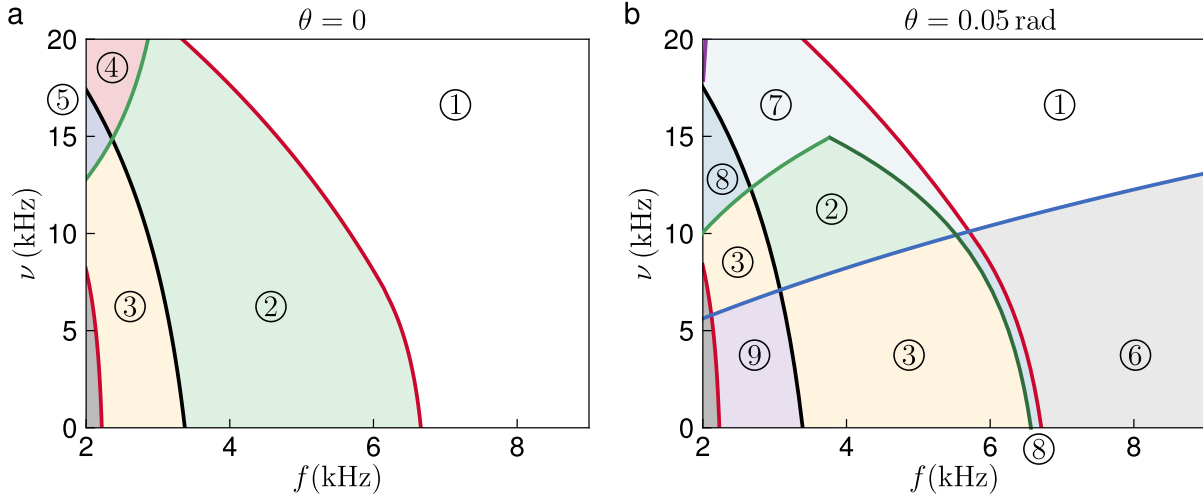


**Figure 6.1: Topological phases of the shaken honeycomb lattice for  $V_0 = 6 E_r$ .** **a.** Phases in the symmetric lattice for  $\theta = 0$  as a function of the shaking frequency  $f$  and shaking amplitude  $\nu$ . The red and black lines depict closings of the  $\pi$ - and 0-gap at  $\Gamma$ , and the green line a simultaneous closing of  $g^\pi$  at six different quasimomenta along the lines  $\Gamma$ - $K$  and  $\Gamma$ - $K'$ . For large frequencies, the system resembles a Haldane phase ① with  $\mathcal{C}^- = -1$ . The Chern numbers in the phases ②-⑤ are  $\mathcal{C}^- = (-3, -2, 3, 4)$ . **b.** Phase diagram for  $\theta = 0.05$  rad, corresponding to a sublattice energy offset of  $\Delta \approx 0.051 E_r$ . The additional blue line marks the closing of  $g^0$  at  $K$  and the purple line in the top left corner the closing of  $g^\pi$  at  $K'$ . The dark and light green lines denote simultaneous band touchings in the  $\pi$ -gap at three points along the lines  $\Gamma$ - $K'$ , forming a triangle in quasimomentum space. The corresponding radii decrease and increase with the shaking amplitude and the singularities along each line merge and annihilate for  $\nu \approx 14.9$  kHz, leading to an anomalous Floquet phase ⑦. The Chern numbers in the phases ⑥, ⑧ and ⑨ are  $\mathcal{C}^- = (0, 1, -1)$ .

Decreasing the shaking frequency results in a gap closing between the Floquet Brillouin zones (FBZs) at  $\Gamma$ , similar as in the intensity modulated lattice. However, the system does not undergo a transition to an anomalous Floquet phase but to a phase ② with  $\mathcal{C}^- = -3$ , characterized by negative Berry curvature at  $\Gamma$ , which carries a Chern number of  $-2$  and spreads in a hexagonal shape along with a nearly-degenerate minimum in the lowest band (second row of Fig. 6.2). In fact, the band touching point at  $\Gamma$  is degenerate, consisting of two subsequent transitions which have collapsed onto each other. Adding a finite sublattice energy offset lifts the degeneracy and pulls the singularities apart in the three-dimensional parameter space, which consists of  $q_x$ ,  $q_y$  and  $f$  in this case, as discussed below.

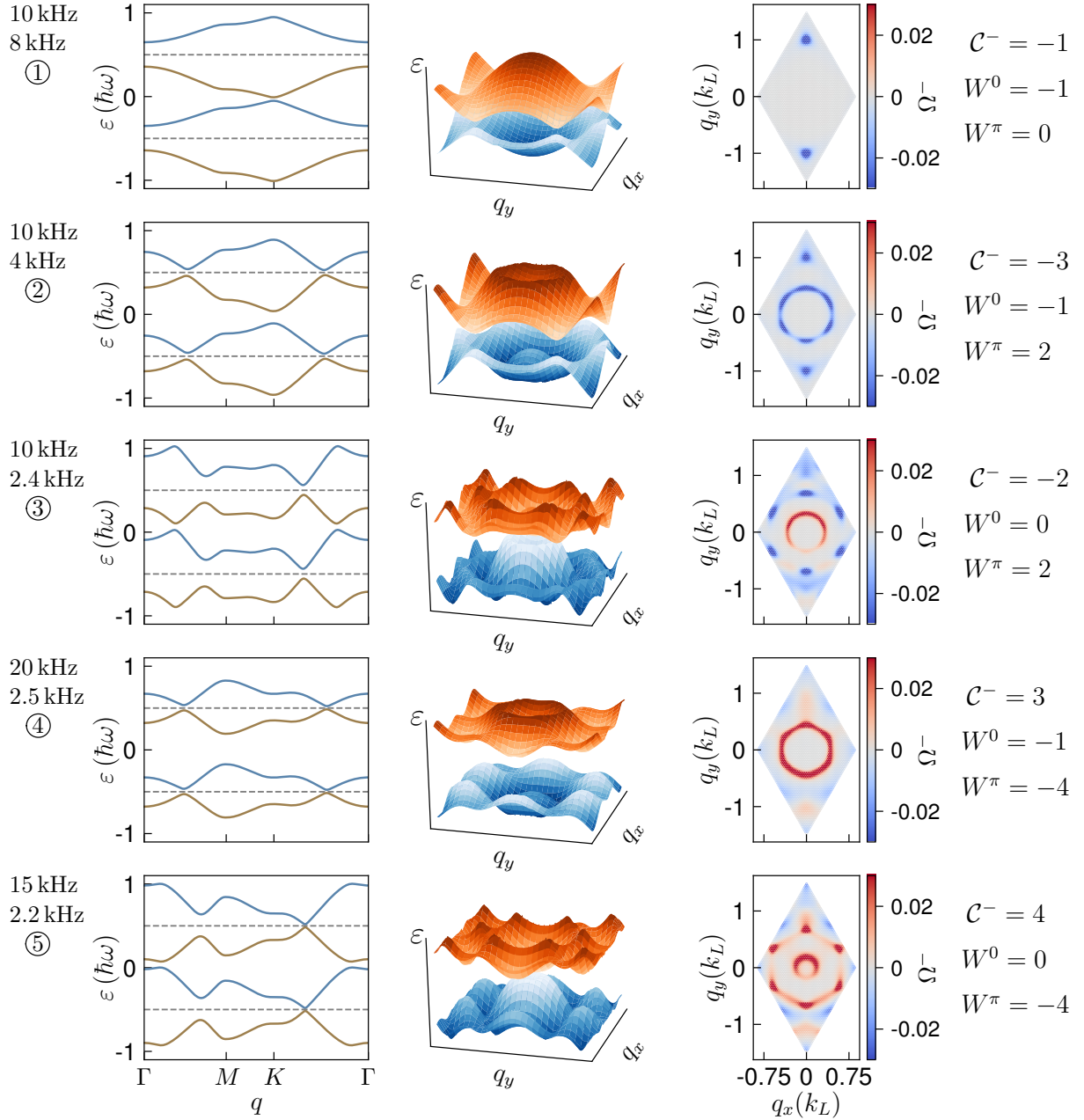


Figure 6.2: **Quasienergy bands and Berry curvature in the different topological phases for  $V_0 = 6 E_r$ .** First column: The two lowest quasienergy bands along the high-symmetry line  $\Gamma$ - $M$ - $K$ - $\Gamma$  in the extended zone scheme. Second column: Quasienergy bands as a function of the 2D quasimomentum, plotted in the reduced zone scheme. Third column: Berry curvature in the first Brillouin zone. The shaking amplitude and frequency are denoted on the left of each row, and the corresponding Chern and winding numbers on the right.

As the Berry curvature at  $\Gamma$  turns from positive values slightly before the transition to negative values,  $\text{sgn}(\Delta W^\pi) = +1$  and  $W^\pi = 2$  in phase ②. For even lower shaking frequencies, the bands touch again at  $\Gamma$ , now at quasienergy 0, which gives rise to positive Berry curvature and  $\Delta W^0 = 1$ , removing the edge state in  $g^0$ . Hence, in phase ③,  $\mathcal{C}^- = -2$ , as illustrated in the third row of Fig. 6.2. In contrast to the intensity modulated lattice, the effective bandwidth decreases with the shaking amplitude, which can be described by a renormalization of the nearest neighbor (NN) hopping in the limit of high modulation frequencies (Sec. 6.2.2), leading to a reduction of the tunneling until  $J \rightarrow 0$  for  $\nu \approx 32 \text{ kHz}$ . Without any next-nearest neighbor (NNN) hopping, this limit would correspond to flat bands which only touch for  $f \rightarrow 0$ , where all phase transitions collapse. After that, the NN hopping changes its sign and increases in magnitude again. In the system considered here, the gap closing lines at  $\Gamma$  are bent to the left for  $\nu \lesssim 32 \text{ kHz}$ , as apparent in Fig. 6.1a, and then turn to the right for  $\nu \gtrsim 32 \text{ kHz}$ , shifting the phase transitions to higher shaking frequencies again.

For larger shaking amplitudes and small frequencies, the bands touch in the  $\pi$ -gap simultaneously at six points along the high-symmetry lines  $\Gamma-K$  and  $\Gamma-K'$ . In phase ②, the six minima in the lowest band spread away from  $\Gamma$ , carrying the negative Berry curvature. Increasing the shaking amplitude first increases the gap that has opened between the two bands, but then it starts to decrease again due to the deformation of the bands and finally closes. In the parameter range considered here, the touching happens at a radius of  $q_r \in [0.72, 0.34] k_L$  and  $f \in [2, 2.84] \text{ kHz}$  for amplitudes between 13 kHz and 20 kHz, as represented by the light green line in Fig. 6.1a. Since the same quasienergy gap which has opened previously is closing again, the corresponding Berry curvature is concentrated and switches its sign at the six touching points. Thereby it changes from an effective weight of  $-1/3$  at each point (adding up to  $\mathcal{C}^- = -2$ ) to  $+2/3$ , leading to a hexagon that carries  $\mathcal{C}^- = 4$ , as illustrated in the fourth row of Fig. 6.2. Together with the negative Berry curvature at the Dirac points, this yields  $\mathcal{C}^- = 3$  and the winding number in the  $\pi$ -gap changes to  $W^\pi = -4$ , characterizing phase ④. If the shaking frequency is decreased further, the 0-gap closes at  $\Gamma$ , which leads to  $W^0 = 0$  due to the positive Berry curvature arising there, and  $\mathcal{C}^- = 4$  (phase ⑤, last row of Fig. 6.2).

**Adding a sublattice offset** If the polarization of the lattice beams is made elliptical with angle  $\theta$ , an energy offset  $\Delta$  is introduced between the A- and B-sites, which opens a trivial quasienergy gap the Dirac points. Similar as in the intensity modulated lattice, a transition from the Haldane phase to a trivial phase occurs if the gap arising from  $\Delta$  becomes larger than the topological gap. In the Haldane model, this corresponds to a sign change of the mass term (see Sec. 2.1.3) at  $K$  from  $m < 0$  to  $m > 0$  and thus from negative to positive Berry curvature, resembling the same Berry curvature distribution as in the trivial phase of the intensity modulated lattice. This transition is depicted by the blue line in Fig. 6.1b, where the trivial phase is denoted by ⑥. The quasienergy bands along both high-symmetry paths  $\Gamma-M-K-\Gamma$  and  $\Gamma-M-K'-\Gamma$  (solid and dashed lines), as well as the 2D bands and Berry curvature are shown in Fig. 6.3 for the new phases arising when  $\Delta > 0$ .

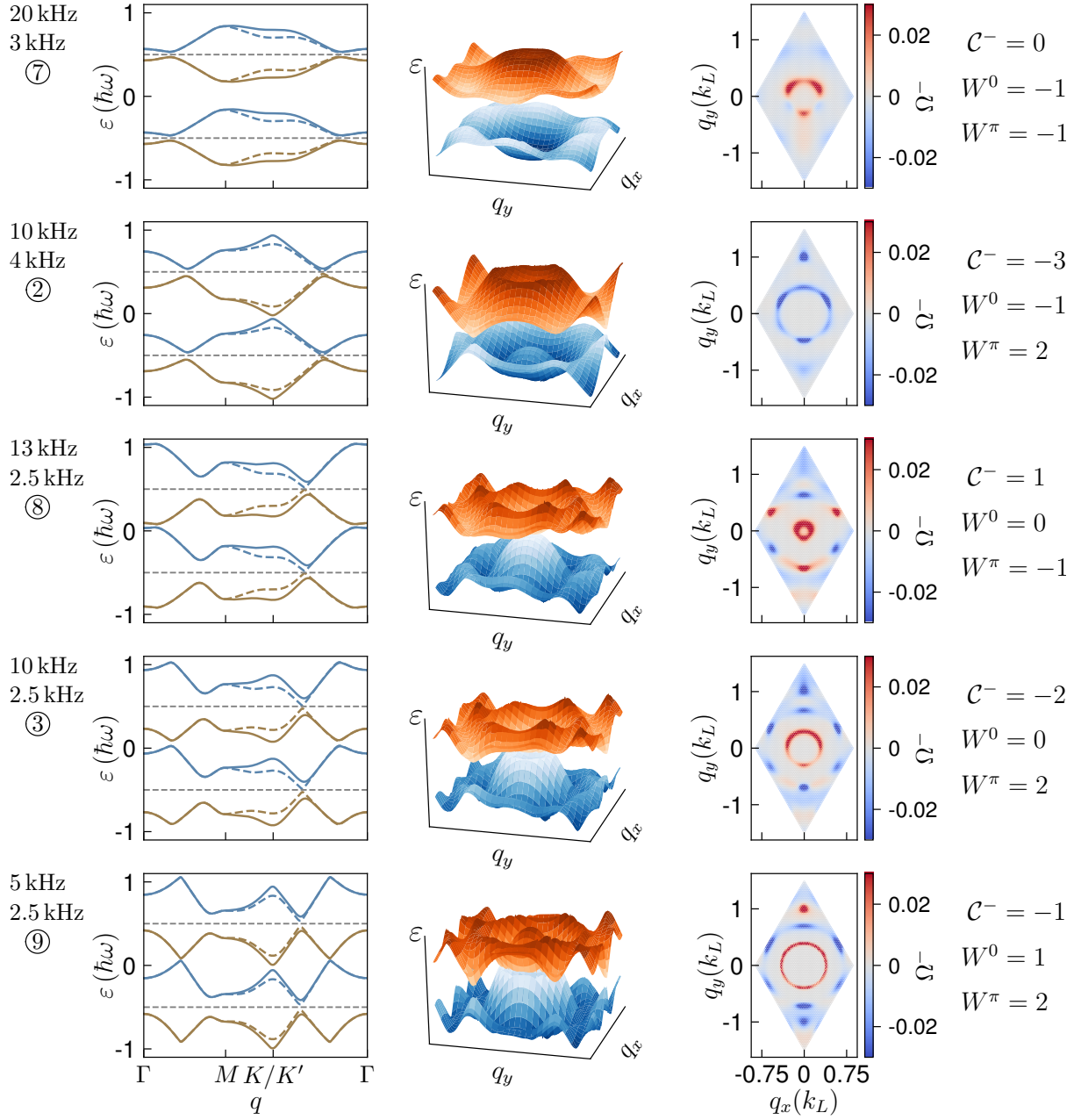


Figure 6.3: **Quasienergy bands and Berry curvature with a sublattice offset for  $\mathbf{V}_0 = 6 \mathbf{E}_r$ .** First column: The two lowest quasienergy bands along the high-symmetry lines  $\Gamma$ - $M$ - $K$ - $\Gamma$  (solid lines) and  $\Gamma$ - $M$ - $K'$ - $\Gamma$  (dashed lines) in the extended zone scheme. Second column: Quasienergy bands as a function of the 2D quasimomentum, plotted in the reduced zone scheme. Third column: Berry curvature in the first BZ. In all plots,  $\theta = 0.05$  rad, scanning the phase diagram in Fig. 6.1b. The shaking amplitude and frequency are denoted on the left of each row, and the corresponding Chern and winding numbers on the right.

The sublattice offset breaks inversion symmetry and thus the lattice is not sixfold rotationally symmetric any more, but only threefold. This lifts the degeneracy of the first band touching at  $\Gamma$ . The closing of the  $\pi$ -gap gives rise to positive Berry curvature at  $\Gamma$ , carrying a weight of 1, which spreads for smaller shaking frequencies, now along a triangle due to the broken inversion symmetry (first row in Fig. 6.3). Hence,  $\Delta W^\pi = -1$  and  $\mathcal{C}^- = 0$  for shaking amplitudes above the transition at  $K$ , resembling the transition from the Haldane to an anomalous Floquet phase ⑦ with  $W^0 = -1$  and  $W^\pi = -1$ .

If the shaking frequency is lowered and  $\nu \leq 14.9$  kHz,  $g^\pi$  starts to decrease again at the minima of the lowest band and closes simultaneously at three points, each of which is located along one of the lines  $\Gamma-K'$ , forming a triangle centered around  $\Gamma$ . The transition is depicted by the dark green line in Fig. 6.1b and illustrated in Fig. 6.4. At each of the touching points, the Berry curvature changes its sign, from an effective weight of  $+1/3$  to  $-2/3$ , thus leading to the negative structure with  $\mathcal{C}^- = -2$  and an overall Chern number of  $\mathcal{C}^- = -3$  in phase ② along with  $W^\pi = 2$ , as shown in the second row of Fig. 6.3.

The distance  $q_1 \in [0.08, 0.39] k_L$  of the touching points to the center of the BZ increases with the shaking amplitude  $\nu \in [0, 14.9]$  kHz and the transition shifts to lower frequencies. For smaller values of  $\theta$ , it moves towards the gap closing line at  $\Gamma$  and finally merges with it for  $\theta = 0$ , annihilating the anomalous Floquet phase there.

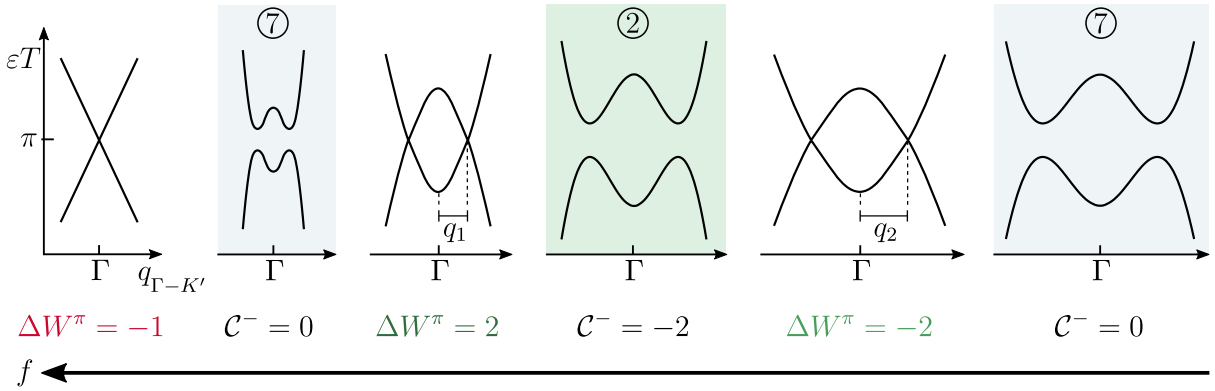


Figure 6.4: **Schematics of the phase transitions along the lines  $\Gamma-K'$ .** Sketch of the quasienergy bands for decreasing shaking frequencies  $f$  and amplitudes  $12.5$  kHz  $\lesssim \nu \leq 14.9$  kHz, illustrating the closings of  $g^\pi$  along the connection lines  $\Gamma-K'$ . Lowering  $f$ , the gap closes first at  $\Gamma$ , signaling the transition into the anomalous Floquet phase ⑦. After the band minima in the first band (drawn above the second) have spread out, the gap closes simultaneously along the three lines  $\Gamma-K'$  (only two of the closings are shown for clarity), bringing the system into phase ②. There is one touching point per connection line, each of which has a distance of  $q_1$  to the center of the BZ. At the third transition, the distance of each point has increased to  $q_2$ . For smaller shaking frequencies, the system is back in the anomalous Floquet phase. The radii  $q_1$  and  $q_2$  converge with increasing shaking amplitude and the two band touching points along each line  $\Gamma-K'$  merge for  $\nu = 14.9$  kHz.

Starting in phase ② and lowering the shaking frequency further, the  $\pi$ -gap along the lines  $\Gamma-K'$  first increases and the minima in the lowest band move to larger quasimomenta. Then the gap becomes smaller again and closes a second time (light green line), now at a larger value  $q_2 \in [0.92, 0.39] k_L$ , that decreases with the shaking amplitude  $\nu \in [10, 14.9]$  kHz and the transition shifts to higher frequencies. The Berry curvature weight changes from  $-2/3$  to  $+1/3$  at each point, bringing the system back to the anomalous Floquet phase for  $\nu \gtrsim 12.5$  kHz. The radius  $q_1$  of the first set of touching points along the line  $\Gamma-K'$  increases with the shaking amplitude, while  $q_2$  decreases. The two singularities along each line merge and annihilate at  $q_{1/2} \approx 0.39 k_L$  for  $\nu = 14.9$  kHz and  $f = 3.8$  kHz, resulting in a connected anomalous Floquet phase for amplitudes above this point. Since the same gap,  $g^\pi$ , is closing several times, the phase transitions occurring along the high-symmetry lines are qualitatively different from the band touchings at  $\Gamma$ . In the latter case, usually one of the gaps  $g^0$  or  $g^\pi$  closes and increases afterwards, and the next transition happens in the other one.

For smaller shaking frequencies, the 0-gap at  $\Gamma$  closes, creating again positive Berry curvature and changing  $\Delta W^0 = 1$ , which annihilates the edge mode there. Thus, a topological phase ⑧ with  $\mathcal{C} = 1$  and a single chiral edge mode in the  $\pi$ -gap arises (third row of Fig. 6.3), similar to the third regime in the intensity modulated lattice. Lowering the shaking amplitude, the second transition along the lines  $\Gamma-K'$  is traversed, resembling phase ③ with  $\mathcal{C}^- = -2$ . The positive contributions from the  $g^\pi$ -transition at  $\Gamma$  change their sign and weight, as described above and illustrated in the fourth row of Fig. 6.3. If the shaking amplitude is reduced further, the 0-gap at  $K$  closes and the corresponding Berry curvature is turned to positive values, leading to  $\Delta W^0 = 1$  and thus creating again an edge mode in this gap while  $W^\pi = 2$  remains. Now, the Berry curvature contributions from the two Dirac points cancel each other resulting in  $\mathcal{C}^- = -1$  together with the positive and negative triangles with total weights  $+1$  and  $-2$  from the previous transitions, characterizing phase ⑨ (last row of Fig. 6.3). Increasing the shaking frequency again for small amplitudes below the transition at  $K$ , first the 0-gap closing at  $\Gamma$  is traversed, bringing the system again into phase ③. Then,  $g^\pi$  closes along the lines  $\Gamma-K'$  at  $q_1 \in [0.08, 0.39] k_L$ , which changes the weight of each point from  $-2/3$  to  $+1/3$ , leading to a triangle carrying weight  $+1$ . Since  $W^0 = 0$ , this does not resemble an anomalous Floquet regime, but phase ⑧ with  $\mathcal{C}^- = 1$  and  $W^\pi = -1$ . The remaining edge mode in the  $\pi$ -gap is then removed at the gap closing at  $\Gamma$ , marking the transition into the trivial phase ⑥.

In summary, an anomalous Floquet regime can also be realized using circular phase modulation of an optical honeycomb lattice, if inversion symmetry is broken by a finite sublattice energy offset, lifting the degeneracy of the first band touching at  $\Gamma$ .

## 6.2 Tight-binding-description

In the previous section, the topological phase diagram and the winding numbers have been obtained from the gap closings and Berry curvature changes of the bulk bands.

The dispersion of the edge modes can be derived directly if the system is evaluated on a semi-finite geometry. To capture the details of the edge in real space, a tight-binding description of the shaken honeycomb lattice is introduced in Sec. 6.2.1. Moreover, it provides additional physical insight into the Floquet system by allowing for an analytic derivation of the effective Hamiltonian in the limit of high shaking frequencies (Sec. 6.2.2). The quasienergy bands of the semi-finite system based on the tight-binding approach are presented in Sec. 6.2.3.

### 6.2.1 Two-band tight-binding model

In the phase modulated honeycomb lattice, the tunnelings are isotropic and time-independent. The vectors  $\delta_j$  connecting the lattice sites also remain constant, basically corresponding to the symmetric, static lattice being moved on a circular trajectory in real space. The tight-binding Hamiltonian consists of a time-independent part resembling the static lattice and a time-dependent part which describes the periodic driving in terms of an on-site potential [185]:

$$\begin{aligned} \hat{H}(t) &= \hat{H}_0 + \hat{H}_1(t) \\ &= \sum_{\mathbf{r}_A} \left[ \sum_{j=1}^3 J (\hat{a}_{\mathbf{r}_A}^\dagger \hat{a}_{\mathbf{r}_A+\delta_j} + h.c.) + \frac{\Delta}{2} (\hat{a}_{\mathbf{r}_A}^\dagger \hat{a}_{\mathbf{r}_A} - \hat{a}_{\mathbf{r}_A+\delta_1}^\dagger \hat{a}_{\mathbf{r}_A+\delta_1}) \right. \\ &\quad + \sum_{j=1}^3 \tilde{J} \left( \hat{a}_{\mathbf{r}_A}^\dagger \hat{a}_{\mathbf{r}_A+\mathbf{a}_j} + \hat{a}_{\mathbf{r}_A+\delta_1}^\dagger \hat{a}_{\mathbf{r}_A+\delta_1-\mathbf{a}_j} + h.c. \right) \\ &\quad \left. - \hat{a}_{\mathbf{r}_A}^\dagger \hat{a}_{\mathbf{r}_A} (\mathbf{F}(t) \cdot \mathbf{r}_A) - \hat{a}_{\mathbf{r}_A+\delta_1}^\dagger \hat{a}_{\mathbf{r}_A+\delta_1} (\mathbf{F}(t) \cdot (\mathbf{r}_A + \delta_1)) \right]. \end{aligned} \quad (6.9)$$

The time-dependent force is defined as

$$\mathbf{F}(t) = -m\ddot{\mathbf{r}}_{\text{lat}}(t) = \frac{bm\omega}{\sqrt{3}k_L} \begin{pmatrix} \cos(\omega t) \\ \sin(\omega t) \end{pmatrix} = F \begin{pmatrix} \cos(\omega t) \\ \sin(\omega t) \end{pmatrix}. \quad (6.10)$$

Similar to the calculations in the previous section, the Hamiltonian can be transferred into a reference frame co-moving with the lattice, which moves the time-dependence into the tunneling amplitudes. The corresponding unitary transformation reads [185, 186]:

$$\hat{U}(t) = \exp \left[ \frac{i}{\hbar} \sum_{j=A,B} (\mathbf{A}(t) \cdot \mathbf{r}_j) \hat{a}_j^\dagger \hat{a}_j \right], \quad (6.11)$$

where  $\mathbf{A}(t)$  denotes the emergent vector potential introduced in Eq. 6.7 and the operator  $\hat{a}_j^\dagger$  creates a particle on the lattice site located at  $\mathbf{r}_j$ , describing either A- or B-sites. The Hamiltonian is transformed by

$$\hat{H}'(t) = \hat{U}^\dagger \hat{H}(t) \hat{U} - i\hbar \hat{U}^\dagger \partial_t \hat{U}, \quad (6.12)$$

where the second term evaluates to

$$-i\hbar\hat{U}^\dagger\partial_t\hat{U} = \sum_{j=A,B} (\partial_t \mathbf{A}(t) \cdot \mathbf{r}_j) \hat{a}_j^\dagger \hat{a}_j = \sum_{j=A,B} (\mathbf{F}(t) \cdot \mathbf{r}_j) \hat{a}_j^\dagger \hat{a}_j, \quad (6.13)$$

and thus cancels out the contribution from  $\hat{H}_1(t)$ . The hopping terms in  $\hat{H}_0$  connecting sites  $j$  and  $l$  are renormalized according to

$$J_{jl} \hat{a}_j^\dagger \hat{a}_l \rightarrow e^{-\frac{i}{\hbar} \mathbf{A}(t) \cdot (\mathbf{r}_j - \mathbf{r}_l)} J_{jl} \hat{a}_j^\dagger \hat{a}_l. \quad (6.14)$$

The vectors connecting nearest- and next-nearest neighbors can be rewritten as

$$\begin{aligned} \mathbf{r}_A - \mathbf{r}_B = \boldsymbol{\delta}_j &= a \begin{pmatrix} \cos(\varphi_j) \\ \sin(\varphi_j) \end{pmatrix}, \quad \varphi = \left( \pi, -\frac{\pi}{3}, \frac{\pi}{3} \right), \\ \mathbf{r}_A - \mathbf{r}_A = \mathbf{a}_j &= \sqrt{3}a \begin{pmatrix} \cos(\chi_j) \\ \sin(\chi_j) \end{pmatrix}, \quad \chi = \left( -\frac{5\pi}{6}, -\frac{\pi}{6}, \frac{\pi}{2} \right), \quad j = \{1, 2, 3\}, \end{aligned} \quad (6.15)$$

which yields for the phases of the prefactors in Eq. 6.14:

$$\begin{aligned} -\frac{i}{\hbar} \mathbf{A}(t) \cdot (\mathbf{r}_A - \mathbf{r}_B) &= -i \frac{Fa}{\hbar\omega} \sin(\omega t - \varphi_j) = -i\kappa \sin(\omega t - \varphi_j), \\ -\frac{i}{\hbar} \mathbf{A}(t) \cdot (\mathbf{r}_A - \mathbf{r}_A) &= -i\sqrt{3}\kappa \sin(\omega t - \chi_j), \quad j = \{1, 2, 3\}, \end{aligned} \quad (6.16)$$

where the dimensionless driving strength  $\kappa = \frac{Fa}{\hbar\omega}$  has been defined. Since the potential arising from the periodic forcing depends on the difference between the lattice sites, the transformation does not change the onsite-terms in  $\hat{H}(t)$ , describing the sublattice energy offset  $\Delta$ . Thus, the Hamiltonian in the co-moving frame is given by

$$\begin{aligned} \hat{H}'(t) = \sum_{\mathbf{r}_A} \left[ \sum_{j=1}^3 J \left( \hat{a}_{\mathbf{r}_A}^\dagger \hat{a}_{\mathbf{r}_A + \boldsymbol{\delta}_j} e^{-i\kappa \sin(\omega t - \varphi_j)} + \hat{a}_{\mathbf{r}_A + \boldsymbol{\delta}_j}^\dagger \hat{a}_{\mathbf{r}_A} e^{-i\kappa \sin(\omega t - \varphi_j + \pi)} \right) \right. \\ + \sum_{j=1}^3 \tilde{J} \left( \hat{a}_{\mathbf{r}_A}^\dagger \hat{a}_{\mathbf{r}_A + \mathbf{a}_j} e^{-i\sqrt{3}\kappa \sin(\omega t - \chi_j)} + \hat{a}_{\mathbf{r}_A + \mathbf{a}_j}^\dagger \hat{a}_{\mathbf{r}_A} e^{-i\sqrt{3}\kappa \sin(\omega t - \chi_j + \pi)} \right. \\ \left. \left. + \hat{a}_{\mathbf{r}_A + \boldsymbol{\delta}_1}^\dagger \hat{a}_{\mathbf{r}_A + \boldsymbol{\delta}_1 - \mathbf{a}_j} e^{-i\sqrt{3}\kappa \sin(\omega t - \chi_j + \pi)} + \hat{a}_{\mathbf{r}_A + \boldsymbol{\delta}_1 - \mathbf{a}_j}^\dagger \hat{a}_{\mathbf{r}_A + \boldsymbol{\delta}_1} e^{-i\sqrt{3}\kappa \sin(\omega t - \chi_j)} \right) \right] \\ \left. \frac{\Delta}{2} \left( \hat{a}_{\mathbf{r}_A}^\dagger \hat{a}_{\mathbf{r}_A} - \hat{a}_{\mathbf{r}_A + \boldsymbol{\delta}_1}^\dagger \hat{a}_{\mathbf{r}_A + \boldsymbol{\delta}_1} \right) \right]. \end{aligned} \quad (6.17)$$

As the complex conjugate terms describe hopping along the opposite direction, the connection vectors are flipped, which corresponds to changing their angles by  $\pi$ . The NNN hopping from A to A is defined along the directions  $-\mathbf{a}_1, \mathbf{a}_2, \mathbf{a}_3$  (see Fig. 2.1a), which are denoted by  $\mathbf{a}_j$  in Eq. 6.15, and along  $-\mathbf{a}_j$  from B to B. The creation and annihilation operators are Fourier transformed according to Eq. 3.34, which yields the Hamiltonian in

quasimomentum space:

$$\hat{H}'(\mathbf{q}, t) = \sum_{\mathbf{q}} \left[ \sum_{j=1}^3 J \left( e^{i\mathbf{q}\cdot\delta_j - i\kappa \sin(\omega t - \varphi_j)} \hat{a}_{\mathbf{q}}^\dagger \hat{b}_{\mathbf{q}} + e^{-i\mathbf{q}\cdot\delta_j + i\kappa \sin(\omega t - \varphi_j)} \hat{b}_{\mathbf{q}}^\dagger \hat{a}_{\mathbf{q}} \right) \right. \\ \left. + \sum_{j=1}^3 \tilde{J} 2 \cos(\mathbf{q} \cdot \mathbf{a}_j - \sqrt{3}\kappa \sin(\omega t - \chi_j)) \left( \hat{a}_{\mathbf{q}}^\dagger \hat{a}_{\mathbf{q}} + \hat{b}_{\mathbf{q}}^\dagger \hat{b}_{\mathbf{q}} \right) + \frac{\Delta}{2} \left( \hat{a}_{\mathbf{q}}^\dagger \hat{a}_{\mathbf{q}} - \hat{b}_{\mathbf{q}}^\dagger \hat{b}_{\mathbf{q}} \right) \right]. \quad (6.18)$$

By making the ansatz defined in Eq. 3.36, the Hamiltonian is then given by a  $2 \times 2$  matrix for every time  $t$  and quasimomentum  $\mathbf{q}$ . The effective Hamiltonian is calculated by numerical integration, similarly as described in the previous section for the full band calculation, employing Eq. 6.18 at every time step.

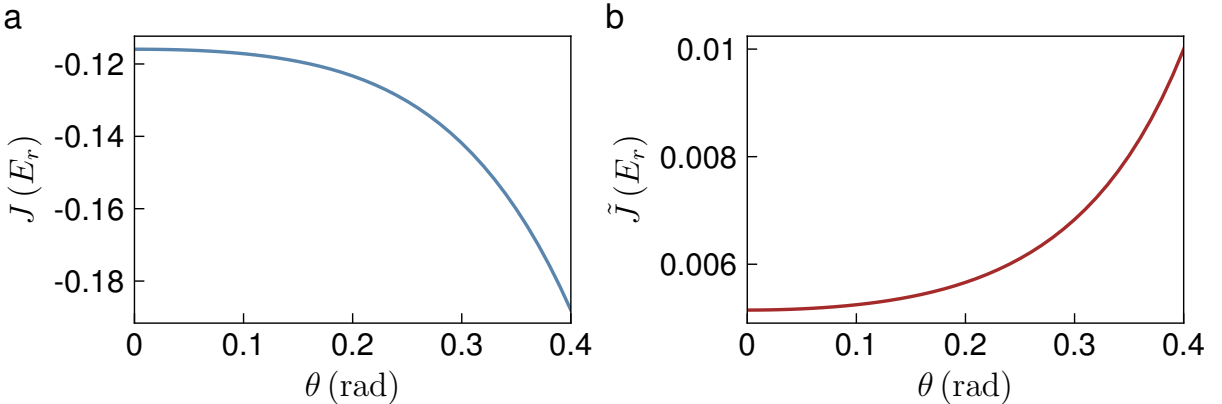


Figure 6.5: **Fitted hopping amplitudes as a function of  $\theta$  for  $V_0 = 6 E_r$ .** The parameters are obtained by fitting the tight-binding model with time-independent, isotropic hoppings to the two lowest bands of the static honeycomb lattice. **a.** The NN hopping is negative and increases in magnitude with  $\theta$ . **b.** The NNN tunneling also increases, being positive for all  $\theta$ . The dependence of both tunneling coefficients on the polarization angle can be described by polynomial functions given in Eq. 6.19.

The tight-binding parameters  $J$ ,  $\tilde{J}$  and  $\Delta$  are obtained by fitting the time-independent tight-binding model to the two lowest bands of the static honeycomb lattice for a certain value of the polarization angle  $\theta$ , evaluated on the 2D BZ. In Fig. 6.5, the resulting hopping amplitudes are shown as a function of  $\theta$  for  $V_0 = 6 E_r$ , whereas the corresponding sublattice energy offsets have been presented in Fig. 3.12b. The tunnelings themselves can be fitted by the following polynomials:

$$J(\theta) = A_J \theta^2 + B_J \theta^4 + J_0, \quad \tilde{J}(\theta) = A_{\tilde{J}} \theta^2 + B_{\tilde{J}} \theta^4 + C_{\tilde{J}} \theta^6 + \tilde{J}_0, \quad (6.19)$$

where  $J_0 = -0.1159 E_r$  and  $\tilde{J}_0 = 0.0051 E_r$  denote the hopping parameters in the sym-

metric lattice with  $\theta = 0$ . The resulting prefactors are

$$\begin{aligned} A_J &= -0.090(2) \frac{E_r}{\text{rad}^2}, & B_J &= -2.23(2) \frac{E_r}{\text{rad}^4}, \\ A_{\tilde{J}} &= 9.8(1) \cdot 10^{-3} \frac{E_r}{\text{rad}^2}, & B_{\tilde{J}} &= 0.062(2) \frac{E_r}{\text{rad}^4}, & C_{\tilde{J}} &= 0.42(1) \frac{E_r}{\text{rad}^6}. \end{aligned} \quad (6.20)$$

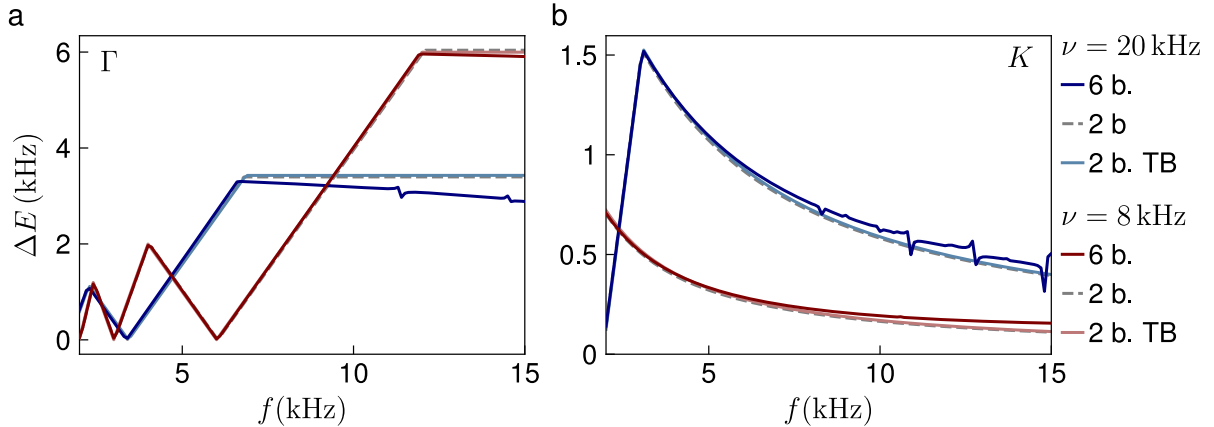


Figure 6.6: **Quasienergy gaps at  $\Gamma$  and  $K$  as a function of the shaking frequency for  $\mathbf{V}_0 = 6 \mathbf{E}_r$ .** **a.** Quasienergy gaps at  $\Gamma$  for  $\theta = 0$  and shaking amplitudes  $\nu = (20, 8)$  kHz, calculated using the full band description with projection to the first six bands (dark lines), the first two bands (gray, dashed lines) and by employing the two-band tight-binding model (light lines). The two-band descriptions deviate from the full model mainly at large  $f$  for  $\nu = 20$  kHz, the phase transition points are well resolved. **b.** Quasienergy gap at  $K$  for the same parameters and models as described in **a.** Apart from the jumps at high shaking frequencies arising from avoided crossings with higher bands, the gaps are well captured by the two-band description.

The emerging quasienergy bands resemble the full bands derived from Eq. 6.8 for small shaking frequencies and amplitudes. In Fig. 6.6 the quasienergy gaps at  $\Gamma$  and  $K$  are shown as a function of the shaking frequency for different amplitudes  $\nu$ . The gaps from the tight-binding model (light blue and red lines) are nearly identical to the results from the full calculation using only the two lowest bands (gray, dashed lines) and coincide with the six-band gaps (dark blue and red lines) at small frequencies for  $\nu = 20$  kHz and at mostly all frequencies for  $\nu = 8$  kHz. Similar to the Floquet bands of the intensity modulated lattice, jumps appear in the gap at  $K$  for large shaking parameters, which are not captured by the two-band description.

### 6.2.2 Haldane model for large shaking frequencies

In the limit of large driving frequencies, the circularly shaken honeycomb lattice directly resembles the Haldane model introduced in Sec. 2.1.3. Similar to the derivation for the

intensity modulated lattice in Sec. 3.3.4, the expansion of the effective Hamiltonian up to first order is employed:

$$\hat{H}_{\text{eff}} \approx \hat{H}_0 + \frac{1}{\hbar\omega} \sum_{n=1}^{\infty} \frac{1}{n} [\hat{H}_n, \hat{H}_{-n}] + \mathcal{O}\left(\frac{1}{(\hbar\omega)^2}\right). \quad (6.21)$$

To determine the Fourier-components of the Hamiltonian, all of the time-dependent parts in Eq. 6.18 are rewritten in their exponential form as apparent in Eq. 6.17 and the Bessel-identity defined in Eq. 3.45 is applied:

$$\begin{aligned} e^{-i\kappa \sin(\omega t - \varphi_j)} &= \sum_{n=-\infty}^{+\infty} \mathcal{J}_n(-\kappa) e^{in(\omega t - \varphi_j)} = \sum_{n=-\infty}^{+\infty} (-1)^n \mathcal{J}_n(\kappa) e^{in(\omega t - \varphi_j)} \\ e^{-i\sqrt{3}\kappa \sin(\omega t - \chi_j)} &= \sum_{n=-\infty}^{+\infty} (-1)^n \tilde{\mathcal{J}}_n(\sqrt{3}\kappa) e^{in(\omega t - \chi_j)}. \end{aligned} \quad (6.22)$$

Thus, the Hamiltonian in the lattice frame evaluates to:

$$\begin{aligned} \hat{H}'(t) &= \sum_{n=-\infty}^{+\infty} (-1)^n \sum_{\mathbf{q}} \left[ \sum_{j=1}^3 J \mathcal{J}_n(\kappa) \left( \hat{a}_{\mathbf{q}}^\dagger \hat{b}_{\mathbf{q}} e^{i\mathbf{q} \cdot \boldsymbol{\delta}_j + in(\omega t - \varphi_j)} + \hat{b}_{\mathbf{q}}^\dagger \hat{a}_{\mathbf{q}} e^{-i\mathbf{q} \cdot \boldsymbol{\delta}_j + in(\omega t - \varphi_j)} (-1)^n \right) \right. \\ &\quad + \sum_{j=1}^3 \tilde{J} \mathcal{J}_n(\sqrt{3}\kappa) \left( \hat{a}_{\mathbf{q}}^\dagger \hat{a}_{\mathbf{q}} \left( e^{i\mathbf{q} \cdot \mathbf{a}_j + in(\omega t - \chi_j)} + e^{-i\mathbf{q} \cdot \mathbf{a}_j + in(\omega t - \chi_j)} (-1)^n \right) \right. \\ &\quad \left. \left. + \hat{b}_{\mathbf{q}}^\dagger \hat{c}_{\mathbf{q}} \left( e^{-i\mathbf{q} \cdot \mathbf{a}_j + in(\omega t - \chi_j)} (-1)^n + e^{i\mathbf{q} \cdot \mathbf{a}_j + in(\omega t - \chi_j)} \right) \right) + \frac{\Delta}{2} \left( \hat{a}_{\mathbf{q}}^\dagger \hat{a}_{\mathbf{q}} - \hat{b}_{\mathbf{q}}^\dagger \hat{b}_{\mathbf{q}} \right) \right]. \end{aligned} \quad (6.23)$$

The Fourier-components  $\hat{H}_n$  can be read off as the prefactors of the terms  $\propto e^{in\omega t}$  and are expressed in terms of the Pauli matrices for each quasimomentum  $\mathbf{q}$ :

$$\begin{aligned} \hat{H}_n(\mathbf{q}) &= \hat{\sigma}_0 h_{n0}(\mathbf{q}) + \hat{\boldsymbol{\sigma}} \cdot \mathbf{h}_n(\mathbf{q}) \\ h_{n0}(\mathbf{q}) &= (-1)^n \tilde{J} \mathcal{J}_n(\sqrt{3}\kappa) \sum_{j=1}^3 e^{-in\chi_j} \left( e^{i\mathbf{q} \cdot \mathbf{a}_j} + (-1)^n e^{-i\mathbf{q} \cdot \mathbf{a}_j} \right) \\ h_{nx}(\mathbf{q}) &= J \mathcal{J}_n(\kappa) \sum_{j=1}^3 e^{-in\varphi_j} \frac{1}{2} \left( (-1)^n e^{i\mathbf{q} \cdot \boldsymbol{\delta}_j} + e^{-i\mathbf{q} \cdot \boldsymbol{\delta}_j} \right) \\ h_{ny}(\mathbf{q}) &= -i J \mathcal{J}_n(\kappa) \sum_{j=1}^3 e^{-in\varphi_j} \frac{1}{2} \left( -(-1)^n e^{i\mathbf{q} \cdot \boldsymbol{\delta}_j} + e^{-i\mathbf{q} \cdot \boldsymbol{\delta}_j} \right) \\ h_{nz}(\mathbf{q}) &= \frac{\Delta}{2} \delta_n. \end{aligned} \quad (6.24)$$

Using the commutation relations of the Pauli matrices analogously to the derivation in Sec. 3.3.4, the commutator of the  $n$ th and  $-n$ th component is given by

$$\begin{aligned} [\hat{H}_n, \hat{H}_{-n}] &= 2i(h_{nx}(\mathbf{q})h_{-ny}(\mathbf{q}) - h_{ny}(\mathbf{q})h_{-nx}(\mathbf{q}))\hat{\sigma}_z \\ &= -2(\mathcal{J}_n(\kappa))^2 J^2 2 \sum_{j=1}^3 \sin(\mathbf{q} \cdot \mathbf{a}_j) \sin(n\vartheta_j) \hat{\sigma}_z. \end{aligned} \quad (6.25)$$

Thereby, the differences of the connection vectors  $\boldsymbol{\delta}_j$  have been expressed in terms of the lattice vectors  $-\mathbf{a}_1$ ,  $\mathbf{a}_2$  and  $\mathbf{a}_3$  and the angle differences  $\vartheta_j$  are defined as

$$\boldsymbol{\vartheta} = (\varphi_3 - \varphi_1, \varphi_1 - \varphi_2, \varphi_2 - \varphi_3) = \left(-\frac{2\pi}{3}, \frac{4\pi}{3}, -\frac{2\pi}{3}\right). \quad (6.26)$$

Inserting these results into Eq. 6.21 yields the effective Hamiltonian for each quasimomentum  $\mathbf{q}$ :

$$\begin{aligned} \hat{H}_{\text{eff}}(\mathbf{q}) &= \sum_{j=1}^3 2\tilde{J} \cos(\mathbf{q} \cdot \mathbf{a}_j) \mathcal{J}_0(\sqrt{3}\kappa) \hat{\sigma}_0 \\ &\quad + \sum_{j=1}^3 J \cos(\mathbf{q} \cdot \boldsymbol{\delta}_j) \mathcal{J}_0(\kappa) \hat{\sigma}_x - \sum_{j=1}^3 J \sin(\mathbf{q} \cdot \boldsymbol{\delta}_j) \mathcal{J}_0(\kappa) \hat{\sigma}_y \\ &\quad + \left[ \frac{\Delta}{2} - \sum_{j=1}^3 \left( 2 \sin(\mathbf{q} \cdot \mathbf{a}_j) \frac{2J^2}{\hbar\omega} \sum_{n=1}^{\infty} \frac{1}{n} (\mathcal{J}_n(\kappa))^2 \sin(n\vartheta_j) \right) \right] \hat{\sigma}_z, \end{aligned} \quad (6.27)$$

which takes the form of the Haldane model in Eq. 2.21 with renormalized, real NN hoppings  $J' = J\mathcal{J}_0(\kappa)$  and complex NNN tunneling amplitudes:

$$\tilde{J}' = \tilde{J}\mathcal{J}_0(\sqrt{3}\kappa) + i \left( \frac{2J^2}{\hbar\omega} \sum_{n=1}^{\infty} \frac{1}{n} (\mathcal{J}_n(\kappa))^2 \sin\left(-n\frac{2\pi}{3}\right) \right). \quad (6.28)$$

In contrast to the effective Haldane model derived for the intensity modulated lattice with the complex NNN hoppings given by Eq. 3.50, the argument  $\kappa$  of the Bessel functions is real, which leads to an oscillating function. In Fig. 6.7a, the contributions to  $J'$  and to the real and imaginary part of  $\tilde{J}'$  are plotted as a function of  $\kappa$ , whereas Fig. 6.7b shows the corresponding parts  $\propto \mathcal{J}_0(-iB)$ ,  $\mathcal{J}_0(-i\tilde{B})$ ,  $(\mathcal{J}_n(-iB))^2$  appearing in Eq. 3.50. To account for the sign of the resulting hoppings, in both cases the complete contribution to the imaginary part of  $\tilde{J}'$  is shown, namely  $1/n(\mathcal{J}_n(\kappa))^2 \sin(-n2\pi/3)$  in Fig. 6.7a and  $(-1)^n/n(\mathcal{J}_n(iB))^2 \sin(n2\pi/3)$  in Fig. 6.7b. In general, the NN hopping amplitudes are about one order of magnitude larger than the NNN values, but for better visibility, the factors  $J$ ,  $\tilde{J}$  and  $A$ ,  $\tilde{A}$  are not taken into account in the plots.

In the shaken honeycomb lattice, the magnitude of the effective NN tunneling is decreasing with the shaking amplitude until it vanishes for  $\kappa \approx 2.39$  and then turns to negative values (black line). This resembles the observed shift of the gap closing lines at

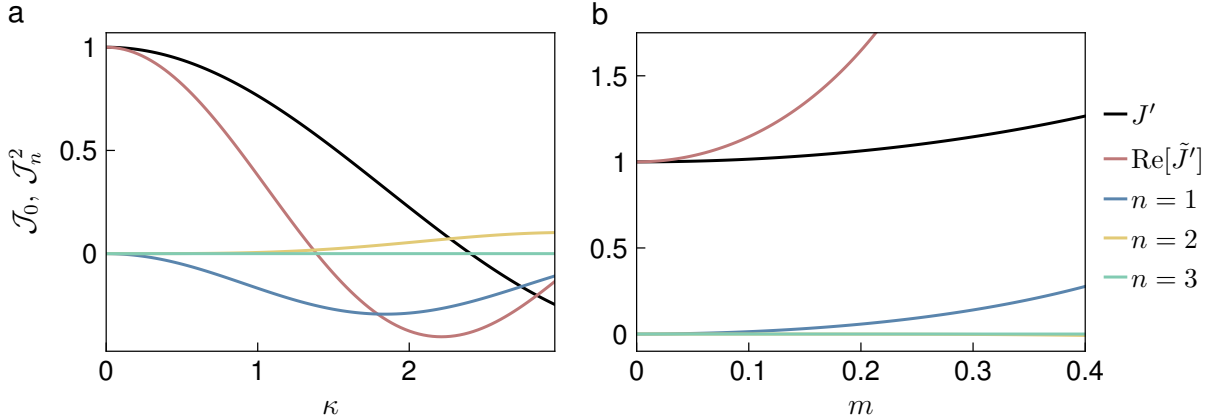


**Figure 6.7: Bessel functions contributing to the renormalized NN and NNN hoppings in the high frequency limit.** **a.** Bessel functions  $\mathcal{J}_0(\kappa)$ ,  $\mathcal{J}_0(\sqrt{3}\kappa)$  describing the NN hopping  $J'$  and the real part of the NNN hopping  $\tilde{J}'$  in Eq. 6.28, depicted by the black and red line. The main contributions to the imaginary part of  $\tilde{J}'$  are given by  $1/n (\mathcal{J}_n(\kappa))^2 \sin(-n2\pi/3)$  for  $n = 1, 2, 3$ , which are plotted as the blue, yellow and green line. For  $\kappa \lesssim 1.38$ ,  $\text{Re}[\tilde{J}'] > 0$  and  $\text{Im}[\tilde{J}'] < 0$ , which is dominated by the term  $n = 1$ . The absolute value of the NN hopping is decreasing with the shaking amplitude and turns to negative values for  $\kappa \approx 2.39$ . **b.** Corresponding Bessel functions  $\mathcal{J}_0(-iB)$ ,  $\mathcal{J}_0(-i\tilde{B})$  and  $(-1)^n/n (\mathcal{J}_n(iB))^2 \sin(n2\pi/3)$  determining the effective hoppings in the intensity modulated lattice in the high frequency limit, as defined in Eq. 3.50. The magnitude of the NN hopping is increasing with the modulation amplitude and  $\text{Re}[\tilde{J}']$ ,  $\text{Im}[\tilde{J}'] > 0$  for all  $m$ .

$\Gamma$  to smaller frequencies for larger values of  $\nu \propto \kappa$ , corresponding to a decrease in the effective bandwidth with the shaking amplitude if  $\nu \lesssim 32$  kHz. In the regime of  $\kappa \lesssim 1.38$ ,  $\text{Re}[\tilde{J}'] > 0$  and  $\text{Im}[\tilde{J}'] < 0$ , which means that the argument  $\phi$  of the complex NNN hopping is negative, yielding a Chern number of  $\mathcal{C}^- = -1$  if  $\Delta > 0$  in the phase diagram of the Haldane model (see Fig. 2.1c). In the intensity modulated lattice, the absolute value of the NN hopping, and thus the bandwidth, is monotonically growing with the modulation amplitude, as visible in Fig. 6.7b.

### 6.2.3 Edge mode dispersion

The dispersion of the edge modes is calculated in a semi-finite honeycomb lattice with an armchair-edge, being periodic along  $x$  and finite along  $y$ , as described in Sec. 3.4 and depicted in Fig. 3.20. The effective unit cell corresponds to a stripe of width  $3a$  and extends over  $N$  pairs of A- and B-sites in the  $y$ -direction. The tight-binding Hamiltonian in the armchair geometry can be derived analogously to the intensity modulated lattice.

The Hamiltonian  $\hat{H}'(\mathbf{q}, t)$  in the lattice frame, given in Eq. 6.18, takes a similar form as the Hamiltonian in Eq. 3.35 with time-independent, isotropic tunnelings  $J$  and  $\tilde{J}$ , time-independent connection vectors, and additional time-dependent factors arising from

the gauge transformation. Thus, the semi-finite system at time  $t$  in the co-moving frame is described by the Hamiltonian from Eq. 3.51, where each term corresponding to NN hopping from an A(B) to a B(A) site along the bond  $\delta_j$  acquires a factor of  $e^{\mp i\kappa \sin(\omega t - \varphi_j)}$ . For NNN tunneling along the positive (negative) directions  $\mp \mathbf{a}_1, \pm \mathbf{a}_2, \pm \mathbf{a}_3$ , the hopping amplitudes are accordingly multiplied by  $e^{\mp i\sqrt{3}\kappa \sin(\omega t - \chi_j)}$ , with  $\varphi_j$  and  $\chi_j$  being defined in Eq. 6.15 and  $\kappa = \frac{ma}{\sqrt{3}k_L h}\nu$ .

Fourier transforming along  $x$  yields the Hamiltonian in quasimomentum space and using the same ansatz as in Eq. 3.54,

$$|\psi_q\rangle = \sum_m \left( c_{mA} \hat{a}_q^\dagger(m) + c_{mB} \hat{b}_q^\dagger(m) \right) |0\rangle, \quad (6.29)$$

the Schrödinger equation is transformed into an eigenvalue equation for the coefficients  $c_{mA}$  and  $c_{mB}$ :

$$\begin{aligned} E c_{mA} &= J_1 e^{-iqa - i\kappa \sin(\omega t - \varphi_1)} c_{mB} + J_2 e^{iq\frac{a}{2} - i\kappa \sin(\omega t - \varphi_2)} c_{(m+1)B} + J_3 e^{iq\frac{a}{2} - i\kappa \sin(\omega t - \varphi_3)} c_{(m-1)B} \\ &\quad + \left( \tilde{J}_1 e^{-iq\frac{3}{2}a - i\sqrt{3}\kappa \sin(\omega t - \chi_1)} + \tilde{J}_2 e^{iq\frac{3}{2}a - i\sqrt{3}\kappa \sin(\omega t - \chi_2)} \right) c_{(m+1)A} \\ &\quad + \left( \tilde{J}_1^* e^{iq\frac{3}{2}a + i\sqrt{3}\kappa \sin(\omega t - \chi_1)} + \tilde{J}_2^* e^{-iq\frac{3}{2}a + i\sqrt{3}\kappa \sin(\omega t - \chi_2)} \right) c_{(m-1)A} \\ &\quad + \tilde{J}_3^* e^{i\sqrt{3}\kappa \sin(\omega t - \chi_3)} c_{(m+2)A} + \tilde{J}_3 e^{-i\sqrt{3}\kappa \sin(\omega t - \chi_3)} c_{(m-2)A} + \frac{\Delta}{2} c_{mA}, \\ E c_{mB} &= J_1 e^{iqa + i\kappa \sin(\omega t - \varphi_1)} c_{mA} + J_2 e^{-iq\frac{a}{2} + i\kappa \sin(\omega t - \varphi_2)} c_{(m-1)A} + J_3 e^{-iq\frac{a}{2} + i\kappa \sin(\omega t - \varphi_3)} c_{(m+1)A} \\ &\quad + \left( \tilde{J}_1 e^{iq\frac{3}{2}a + i\sqrt{3}\kappa \sin(\omega t - \chi_1)} + \tilde{J}_2 e^{-iq\frac{3}{2}a + i\sqrt{3}\kappa \sin(\omega t - \chi_2)} \right) c_{(m-1)B} \\ &\quad + \left( \tilde{J}_1^* e^{-iq\frac{3}{2}a - i\sqrt{3}\kappa \sin(\omega t - \chi_1)} + \tilde{J}_2^* e^{iq\frac{3}{2}a - i\sqrt{3}\kappa \sin(\omega t - \chi_2)} \right) c_{(m+1)B} \\ &\quad + \tilde{J}_3 e^{i\sqrt{3}\kappa \sin(\omega t - \chi_3)} c_{(m+2)B} + \tilde{J}_3^* e^{i\sqrt{3}\kappa \sin(\omega t - \chi_3)} c_{(m-2)B} - \frac{\Delta}{2} c_{mB}. \end{aligned} \quad (6.30)$$

This describes the Hamiltonian at each time  $t$  and quasimomentum  $q$  by a  $2N \times 2N$  matrix in the basis  $(c_{1A}, c_{1B}, c_{2A}, c_{2B}, \dots, c_{NA}, c_{NB})$  of the coefficients. Using the fitted tight-binding parameters of the static lattice, the effective Hamiltonian is calculated by integrating over one period of the driving, resulting in  $2N$  quasienergies at each  $q$ .

In Fig. 6.8, the quasienergy dispersion is shown for a shaking amplitude of  $\nu = 16$  kHz and  $\theta = 0.05$  rad, scanning across phase ⑧, the anomalous and the Haldane regime. For  $f = 6$  kHz, a single pair of edge modes is apparent at zero energy, arising from the opening of the gaps at the Dirac points in the Haldane phase. Decreasing the shaking frequency to  $f = 3$  kHz leads to the closing of  $g^\pi$  at  $\Gamma$ , creating an additional pair of edge modes in the  $\pi$ -gap and thus  $W^0 = -1 = W^\pi$ , constituting the anomalous Floquet phase. For  $f = 2.2$  kHz,  $g^0$  has closed at  $\Gamma$ , annihilating the edge modes in this gap and resembling phase ⑧ with  $\mathcal{C}^- = 1$ . Since the stripe considered here has an upper and a lower boundary, a pair of counter-propagating edge modes is created at each transition. The bands in Fig. 6.8 are calculated without a harmonic trapping potential, which can be included similarly as for the intensity modulated lattice.

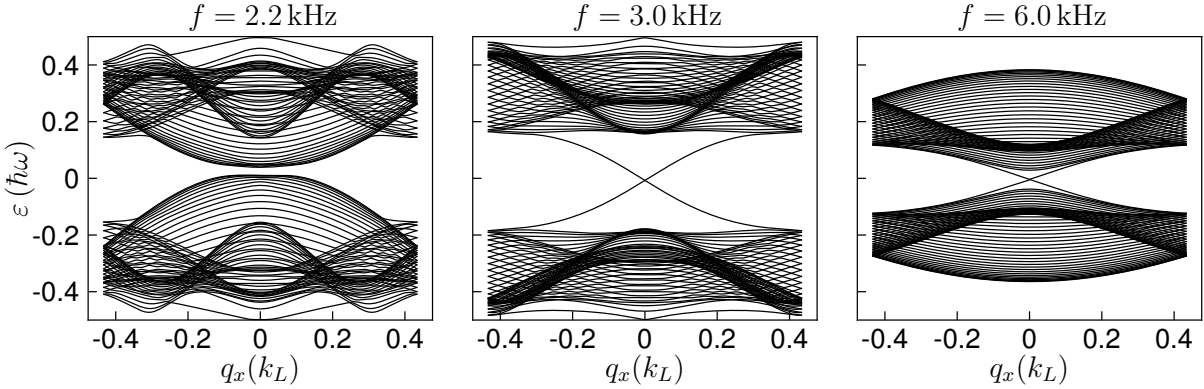


Figure 6.8: **Quasienergy bands of the shaken honeycomb lattice in the armchair geometry.** Band dispersion calculated for  $\nu = 16$  kHz,  $V_0 = 6 E_r$ ,  $N = 50$  and  $\theta = 0.05$  rad with shaking frequencies  $f = (2.2, 3, 6)$  kHz, scanning the phases ⑧, ⑦ and ① in Fig. 6.1b. The latter two describe the anomalous Floquet phase with  $W^0 = -1 = W^\pi$ , thus hosting edge modes in both gaps, and the Haldane phase with  $W^0 = -1$  and  $W^\pi = 0$ .

### 6.3 Measured energy gaps and lifetimes

In the circularly shaken honeycomb lattice, momentum-resolved measurements are complicated, as the quasimomentum itself is periodically modulated. Nevertheless, for small shaking amplitudes, the quasienergy gaps in the modulated lattice can be probed using Stückelberg interferometry, as discussed in the first part of this section. Moreover, the lifetimes in the Haldane regime are measured depending on the shaking frequency and amplitude and compared to the value in the intensity modulated lattice realizing a similar quasienergy gap at  $K$ , which is presented in the second part. All measurements are performed at a lattice depth of  $V_0 = 6 E_r$ .

#### 6.3.1 Probing the energy gaps in the shaken honeycomb lattice

The shaking of the honeycomb lattice corresponds to a time-dependent quasimomentum in the reference frame of the lattice. Thus, the CoM of the atomic cloud is effectively moving on a circular trajectory in quasimomentum space centered around the  $\Gamma$ -point. As described in chapters 4 and 5, the quasienergy gaps in the static or intensity modulated lattice can be measured using Stückelberg interferometry, which involves a fast, linear acceleration of the lattice. This usually corresponds to forces in the range of 1 – 4 kHz, being comparable to the energy scales of the lattice shaking. To probe the quasienergy gaps in the shaken lattice, the atoms are first accelerated to the corresponding point in quasimomentum space in the static lattice, using an intermediate force of  $Fa/h \approx 667$  Hz, and then the shaking is suddenly quenched on. After a certain hold time  $t$  in the effective Floquet bands, being an integer multiple of the driving frequency, the modulation is switched off suddenly and the atoms are driven back to  $\Gamma$  to perform bandmapping and count the relative population in the lowest band. Possible excitations to the second band

due to the quench correspond to an offset in the population oscillations, not changing their frequency. Assuming that the number of atoms in bands higher than the second remains small, the quasienergy gap between the two lowest bands is effectively probed along a circle in quasimomentum space, centered around the point set by the lattice acceleration. The radius of this circle is proportional to the shaking amplitude  $\nu$ :

$$q_r(\nu) = \frac{m}{\hbar} \dot{r}_{\text{lat}} = \frac{m2\pi}{\sqrt{3}k_L \hbar} \nu. \quad (6.31)$$

Thus, a single point in quasimomentum space can only be probed in the limit of small shaking amplitudes. In Fig. 6.9a, the quasienergy gap for  $\nu = 4$  kHz and  $\theta = 0$  is shown as a function of the shaking frequency, measured at a radius of  $q_r \approx 0.122 k_L$  around  $\Gamma$ . The data points are compared to the theoretical gap derived from the full six-band model at the same radius (solid line), being an average over the values along the directions  $\Gamma-M$  and  $\Gamma-K$ , which exhibit nearly identical gaps though. The calculation matches the measured data quite well, which exhibit a distinct minimum, corresponding to the first phase transition. While the actual closing occurs at  $\Gamma$ , the quasienergy gaps at points nearby are also expected to be rather small due to the low shaking amplitude. The theoretical gap nearly vanishes at  $f \approx 6.3$  kHz. Although the quasienergy gaps at  $\Gamma$  can not be probed directly using Stückelberg interferometry, the predicted phase transition can nevertheless be observed. The good quantitative agreement between the theoretical and experimental values confirms the Floquet calculations performed in the shaken honeycomb lattice. In principle, the Berry curvature in the shaken lattice could be probed with Hall deflection measurements, applying a force by lattice acceleration, similar as for the intensity modulation. In order to stay adiabatically within a single band, the force has to be small compared to the quasienergy gaps, lying at least about one order of magnitude below the forces corresponding to the shaking. However, due to the motion in quasimomentum space, the Berry curvature can not be probed locally any more, complicating the measurements directly at the phase transition points. Moreover, for the shaking amplitudes used in the gap and lifetime measurements presented here, the quasienergy gaps between the lowest bands are in general much smaller as in the parameter regimes considered for the intensity modulation. This increases the probability of excitations to the second band, demanding very small forces which lead to large displacements in real space, when being realized with lattice acceleration, and thus to an increased back-action of the harmonic trap. To realize a gap at  $K$  in the Haldane regime being comparable to the result for an intensity modulation amplitude of  $m = 0.2$ , the shaking amplitude has to be increased to at least  $\nu \sim 20$  kHz, corresponding to a large radius  $q_r \sim 0.6 k_L$ .

### 6.3.2 Lifetimes

The lifetimes are measured in the Haldane regime without applying an additional force to the atoms, so effectively for quasimomenta lying on the radius  $q_r(\nu)$  around  $\Gamma$ , corresponding to the shaking amplitude  $\nu$ . The atoms are loaded into the lowest band of the static lattice and the shaking amplitude is ramped up within  $\Delta t = 5T$ , followed by

a variable hold time in the modulated lattice, being always an integer multiple of the driving period  $T$ . Afterwards, the shaking is ramped down again in the same time and bandmapping is performed after a time-of-flight (TOF) of  $t_{\text{TOF}} = 10 \text{ ms}$ .

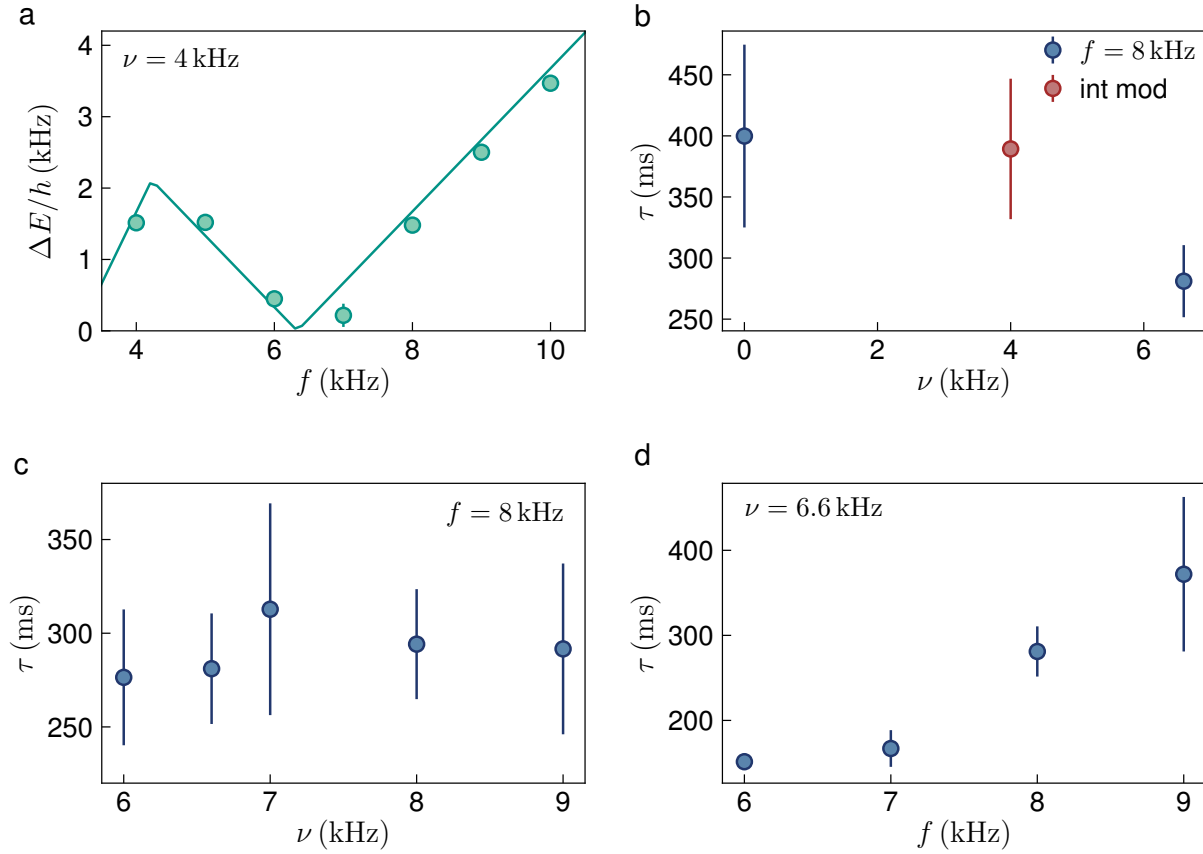


**Figure 6.9: Energy gap around  $\Gamma$  and lifetimes in the circularly shaken honeycomb lattice for  $V_0 = 6 E_r$ .** **a.** Measured quasienergy gaps as a function of the shaking frequency  $f$  for  $\nu = 4 \text{ kHz}$  along a circle in quasimomentum space with radius  $q_r \approx 0.122 k_L$  centered around  $\Gamma$ . The solid line depicts the theoretical gap derived from the six-band Floquet calculation. Every data point is the result of a fit to the Stückelberg population oscillation consisting of 23 points, each being an average over 3-4 individual images, the errorbars denote fitting errors. **b.** Lifetime in the lowest band around  $\Gamma$  for  $\nu = 6.6 \text{ kHz}$  and  $f = 8 \text{ kHz}$ , resembling the Haldane regime and leading to a quasienergy gap of  $\Delta E = 160 \text{ Hz}$  at  $K$ , along with the value for  $\nu = 0$  (blue data points). The red data point depicts the measured lifetime in the intensity modulated lattice in the Haldane regime with  $m = 0.1$  and  $f = 20 \text{ kHz}$ , corresponding to the same gap at  $K$ . **c.** Lifetimes in the Haldane regime in the lowest band around  $\Gamma$  as a function of the shaking amplitude  $\nu$  for  $f = 8 \text{ kHz}$ . **d.** Lifetimes in the Haldane regime as a function of the shaking frequency for  $\nu = 6.6 \text{ kHz}$ . The data points in **b-d** are obtained by fitting the exponential function in Eq. 6.32 to a decay measurement consisting of 23 points, each being an average over 10 realizations. The errorbars denote fitting errors.

The pixel sum corresponding to the relative population in the lowest band,  $\Sigma^1$ , is determined from each image, as described in Sec. 4.2.2. The relative population, averaged over 10 experimental realizations at each  $t$  and normalized to the mean value at  $t = 0$ , is then plotted as a function of the hold time and an exponential function is fitted to the data to extract the lifetime  $\tau$ :

$$\Sigma_{\text{rel}}^1 = A e^{-\frac{t}{\tau}} + \Sigma_0. \quad (6.32)$$

The resulting lifetimes as a function of the shaking amplitude and frequency are presented in Fig. 6.9b-d, whereas  $\theta = 0$  and  $a_s = 6 a_0$  in all measurements. For  $\nu = 6.6$  kHz and  $f = 8$  kHz, the calculated quasienergy gap at the Dirac points is  $\Delta E = 160$  Hz and the corresponding lifetime (blue data points in Fig. 6.9b) is compared to the intensity modulated lattice with  $m = 0.1$  and  $f = 20$  kHz (red data point), also resembling the Haldane regime with a similar gap. While the latter is comparable to the lifetime in the static lattice, the lifetime is reduced when realizing the same effective band structure with phase shaking, but nevertheless still large enough to probe the system experimentally. In general, the lifetimes measured in the parameter regime of  $\nu, f \in [6, 9]$  kHz are all on the order of  $\tau \sim 200 - 400$  ms and mostly depend on the difference of the shaking parameters to the first phase transition line, similar to the observations in the Haldane regime of the intensity modulated lattice (see Sec. 5.4.2). In Fig. 6.9c, the lifetime remains rather constant when increasing the shaking amplitude, which moves the system deeper into the Haldane regime, since the phase transition is shifted to smaller modulation frequencies. Keeping the shaking amplitude constant at  $\nu = 6.6$  kHz and decreasing the modulation frequency towards the phase transition at  $f \approx 6$  kHz (Fig. 6.9d) reduces lifetime by almost a factor of two.

The measured lifetimes presented in Fig. 6.9 are rather long, but they correspond to the Haldane regime with small quasienergy gaps between the two lowest bands. To prepare a system with larger gaps, facilitating the probing of a single band in the Haldane or anomalous regime, the shaking amplitude has to be increased by a factor of two or three, which is expected to reduce the lifetime considerably [74, 143].

In summary, the circularly shaken honeycomb lattice also hosts an anomalous Floquet phase when adding a sublattice offset. However, the size of the energy gaps increases slower with the shaking amplitude than in the intensity modulated lattice, demanding relatively high values of  $\nu$ , which in turn lead to reduced lifetimes. Thus, in the lattice system with  $V_0 = 6 E_r$  considered in this work, the intensity modulated lattice has major advantages over the shaken lattice both for realizing and probing anomalous Floquet systems, but also when considering the topological Haldane regime.



# Chapter 7

## Novel phenomena in anomalous Floquet systems

The experimental realization and topological characterization of an anomalous Floquet system in an optical honeycomb lattice has been shown in chapter 5. In the following, possible future directions for the experiments shall be illustrated, which utilize the special properties of the anomalous Floquet regime. As mentioned in Sec. 2.3.3, due to the zero Chern numbers, the bulk states in the anomalous regime can be completely localized by disorder, which is not possible for settings with  $\mathcal{C} \neq 0$  [42, 128]. This could be used to stabilize interacting topological systems, hosting a many-body localized (MBL) bulk, but thermalizing edge states [44, 45, 126, 127]. In view of realizing such systems experimentally, direct probing of the bulk and edge state properties is desirable. A setup for imaging of the edge modes as well as prospects of realizing and probing disorder with increasing interactions among the constituents is discussed in the first part.

Another direction could be to investigate the nearly-degenerate ring-minimum in the dispersion of the first band, that arises in the anomalous Floquet regime. Loading interacting bosons into this band minimum is expected to give rise to fermionization effects, meaning that the bosons do not condense, but behave like non-interacting fermions. In the second part, this statistical transmutation is briefly introduced along with a discussion of possible ways to detect it experimentally.

### 7.1 Probing disordered anomalous Floquet systems

In the presence of disorder, the bulk states in the anomalous Floquet regime should be localized, while the edge modes are expected to stay mobile. To probe the localization properties at the boundary, the evolution of particles occupying the edge states could be investigated insitu. Preparation of the cloud directly at the boundary of the system can facilitate the observation of the chiral motion by increasing the population in the corresponding modes, as described in Sec. 7.1.1. The realization of disorder by adding a random onsite-potential is discussed in Sec. 7.1.2, along with a method to probe the localization of the bulk states. Being able to measure the bulk and edge states, the

localization could be compared in the anomalous Floquet and the Haldane regime, presumably exhibiting different behavior in the bulk, but similar propagation along the boundary. Moreover, by increasing the disorder strength, the transition into a trivial phase [42], where also the edge states are localized, could be studied. As pointed out in [59], the anomalous Floquet Anderson insulator described above might persist in the presence of interactions. In the honeycomb lattice considered in the previous chapters, the ratio of the Hubbard interaction to the hopping is rather small. In Sec. 7.1.3, possible ways of increasing this ratio by either implementing a deeper honeycomb lattice or adding a vertical lattice are considered.

### 7.1.1 Direct imaging of the edge modes

Directly observing the time-evolution of a topological edge state is challenging because usually both, bulk and edge states are populated. In photonic setups, which employ arrays of coupled waveguides, the light can directly be launched at the boundary of the system, facilitating the observation of the chiral edge states [100, 101]. To probe the propagation along the boundary in a cold atom experiment, the atomic cloud could be released from an additional confining potential [187]. This results in a superposition of the chiral motion from the edge modes and the homogeneous spreading of particles occupying the bulk states. The speed of this spread is increased with the bulk band dispersion. Therefore, the visibility of the edge mode propagation depends on the ratio of the bulk dispersion to the group velocity associated with the edge states: If it is too small, the chiral motion will be overshadowed in the absorption images by the outspread bulk atoms. One way to ensure a good visibility of the edge modes would be to realize flat bulk bands. In the anomalous Floquet systems presented in this work, the absolute width of the band dispersion (in SI units) depends mostly on the modulation frequency. In general, it decreases with the frequency until the bands become more dispersive again shortly before the transition to the third regime. The modulation amplitude has no direct influence on the bandwidth, but the gap to the second band increases with larger amplitudes.

Another strategy is to improve the ratio of particles occupying the edge compared to the bulk states by directly preparing the cloud at the boundary of the system, using a small confining potential, as described in the supplementary material of [187] and illustrated in Fig. 7.1a. Moreover, this geometric arrangement is more suitable for the current experimental setup and will thus be implemented in the near future, as outlined below. The additional potential is realized by a tightly-focused laser beam with  $\lambda = 1064\text{ nm}$  and a focus size of  $\sim 2\mu\text{m}$ , corresponding to a strongly confining optical dipole trap. The beam propagates along the vertical direction and enters the experimental chamber from below, passing through an acousto-optical deflector (AOD), which is used to control the position of the focus in the plane of the atoms [188, 189].

After the creation of the Bose-Einstein condensate (BEC), the small trapping beam is ramped up at the center position of the cloud to capture the atoms. Subsequently, its focus is moved by the AOD in the  $x$ - $y$ -plane, positioning the cloud at the edge of the

system, after which it is loaded into the intensity modulated honeycomb lattice. The propagation of the edge state and the spread of the bulk states can be observed by taking insitu absorption images after releasing the atoms from the small trap.

In the experimental setup presented in the previous chapters, the boundary of the system in the  $x$ - $y$ -plane is determined by the harmonic trapping potential, especially by the  $z$ -dipole beam. The harmonic trap generates an extended edge region in real space, which complicates the differentiation between the bulk and edge states in energy and leads to a flattening of the edge mode dispersion, as mentioned in Sec. 3.4. Hence, the  $z$ -dipole trap will be replaced by a repulsive, hard-wall potential, which is created by imaging an obstruction target onto the atoms using blue-detuned light with  $\lambda = 532$  nm. The mask has a diameter of  $50\ \mu\text{m}$ , corresponding to a disk-shaped repulsive wall in the plane of the atoms with an inner diameter of  $\sim 30\ \mu\text{m}$  and an edge thickness of  $\sim 3\ \mu\text{m}$ . Using this technique and ramping down the  $X$ - $Y$ -trap to a minimal value, a nearly flat potential could be created, being confined by steep walls and thus constituting a suitable platform to observe the propagation of the edge modes.

### 7.1.2 Adding disorder and probing the bulk

Disorder potentials have been realized for cold atomic systems in different ways, such as passing a laser beam through a diffuser plate [190–192] or by superimposing two optical lattices with incommensurate wavelengths, which results in a quasi-random optical potential [193]. Another possibility is the use of a Digital Mirror Device (DMD) [194, 195], an array of micro-mirrors with typical sizes in the range of  $6 - 15\ \mu\text{m}$ . Each mirror is controlled individually and can be switched between two angles, reflecting the incoming light either towards the setup or into another direction corresponding to no light at the atoms' position. Due to their small size, the mirror-array acts like a grating, diffracting light into several directions. The intensity being reflected into a specific order can be maximized by optimizing the incident angle of the light and the alignment of the DMD. Due to spatial restrictions on the experimental table and the possibility of creating arbitrary potential patterns, the DMD would be suitable for creating a disorder potential in the current setup.

The disorder can be generated from a two-dimensional (2D) random distribution which is transferred to the DMD, setting the state of each mirror accordingly. Projecting the reflected laser beam onto the atoms through imaging lenses leads to a finite disorder correlation length arising from a convolution of the random distribution with the point-spread function of the imaging system [194, 195]. Superimposing the speckle pattern from the DMD with an optical lattice, the atoms experience a different light shift on each site. The strength of the disorder can be determined by the width of the histogram of all local light shifts [195]. Apart from probing the special properties of the anomalous Floquet regime mentioned in the beginning of this chapter, adding a weak disorder potential could also facilitate the observation of the chiral edge modes in general [196], by at least partly localizing the bulk states also in regimes with  $\mathcal{C} \neq 0$ .

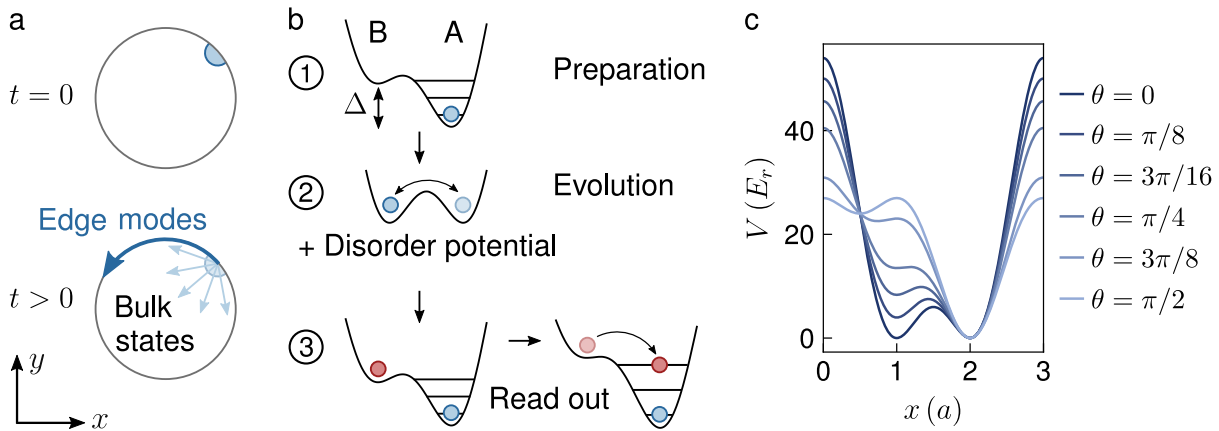


**Figure 7.1: Probing the localization of edge and bulk states.** **a.** Imaging of the edge mode propagation. The atoms (filled, blue circle) are initially prepared at the boundary of the system (gray line) to maximize the relative occupation of the edge modes, utilizing an additional, tightly focused trapping beam. Then, the small trap is switched off and atoms populating edge modes will undergo a chiral motion (dark blue arrow), while the bulk spreads out homogeneously (light blue arrows). **b.** Probing the localization of the bulk. The initial state is a CDW where only A-sites are occupied (1), realized by a large sublattice energy offset  $\Delta$ . After time-evolution in the disordered lattice potential with  $\Delta = 0$  (step 2), the population imbalance between A- and B-sites is measured (3) by increasing  $\Delta$  again and transferring atoms on B-sites to higher bands. **c.** Honeycomb lattice potential with  $V_0 = 6 E_r$  along  $x$  for different values of  $\theta$ , increasing the sublattice offset and finally converting it into a triangular lattice, needed for the last step of the sequence in **b**.

**Probing the localization of the bulk states** The localization of the bulk states could be measured by observing the time-evolution of the atomic cloud after a quench of the disorder potential, similar to the technique described in [193]. The initial state of the system is a charge-density wave (CDW), where every second lattice site is empty. In the honeycomb lattice, this could be realized by adding a large sublattice energy offset  $\Delta$ , which effectively creates a triangular array of tilted double wells, with only the A-sites being populated, as illustrated in Fig. 7.1b. Then, the potential difference between neighboring sites is suddenly reduced and subsequently the disorder potential is switched on, to allow for equilibration of the density distribution (step 2). After a certain evolution time, the populations on the A- and B-sites are frozen out by quickly ramping up the sublattice offset again and turning off the disorder.

The sublattice offset is controlled by the polarization angle  $\theta$  of the lattice beams. By increasing  $\theta$  towards  $\pi/2$ , where the potential minima form a triangular lattice (see Fig. 7.1c), and subsequently performing bandmapping, atoms occupying the B-sites after the evolution are transferred into higher energy bands of the final lattice [197–199], while the atoms occupying A-sites remain in the ground state (setp 3). In this way, the population on A- and B-sites corresponds to different bands and could be distinguished

after bandmapping and time-of-flight (TOF). The timing of the disorder and polarization ramps will have to be optimized in order to minimize excitations to higher bands arising from the quenches.

If the atoms are localized due to the disorder, they mostly remain on their initial positions and only a few B-sites will be occupied after the evolution. On the contrary, if no localization occurs, the initial density pattern will smear out and both types of sites are populated equally. This change of the distribution can be quantified by the imbalance [193]

$$I = \frac{N_A - N_B}{N_A + N_B}, \quad (7.1)$$

where  $N_{A(B)}$  denotes the number of atoms on A(B) sites. Starting with  $I$  close to 1, it will decay to zero if the system thermalizes, which is not the case if localization occurs, thus providing a quantitative measure for the localization of the bulk states.

The procedure described above involves fast ramping of the sublattice energy offset, and hence of the polarization angle  $\theta$ . In the current setup, this is not possible, as the polarization of the lattice beams is adjusted manually by waveplates placed in rotation mounts. As mentioned at the end of Sec. 4.1.5, a new setup for the honeycomb lattice is planned, including an active phase stabilization of the left- and right-circularly polarized components of each beam, which will also allow for dynamic switching of the polarization angles. Another possibility to measure the localization of the bulk states induced by the disorder would be to study the expansion of the cloud after releasing it from the small confining potential placed in the center of the system.

### 7.1.3 Interplay with interactions

Interacting, closed, periodically driven quantum systems are expected to be stabilized by disorder, leading to MBL bulk states in the high frequency limit [45, 58]. The existence of MBL in a Floquet setting with large driving frequencies has also been confirmed experimentally, using time-periodic modulation of a quasi-random one-dimensional (1D) optical lattice [200]. In contrast, the anomalous Floquet regime is manifestly not in the high-frequency limit, since  $\omega \sim J$ , but it can be mapped to an equivalent setting by time-dependent unitary transformations [59]. Numerical simulations indicate that the bulk states can be many-body localized, while the edge states thermalize [59]. In cold atom experiments, MBL has been observed in 2D for fermions in a quasi-random optical lattice [201] and for bosons subjected to a random onsite potential [194].

**Changing the interaction strength** In the 2D honeycomb lattice with  $V_0 = 6 E_r$  and  $a_s = 6 a_0$ , as used in the experiments presented in chapter 5,  $U \approx 0.01J$ , basically corresponding to a non-interacting system. Thus, to study many-body physics or to realize a Mott-insulating state in the honeycomb lattice, the ratio  $U/J$  has to be increased. The interaction strength can be enhanced by utilizing the Feshbach resonance of  $^{39}\text{K}$ , leading to a larger scattering length  $a_s$ , and by adding a lattice along the vertical direction.

As described in Sec. 4.1.5, the current setup suffers from phase noise of the honeycomb lattice beams, which has to be reduced first to be able to load the atoms into the three-dimensional (3D) lattice configuration.

If these issues can be solved in the future, the ratio  $U/J$  could indeed be increased to values much larger than 1, even close to the theoretically expected transition to the Mott-insulating regime at  $U/J \sim 18$  [202], as shown in Fig. 7.2a and b. The interacting BEC loaded into the lowest band of the optical lattice can be described by the Bose-Hubbard Hamiltonian [203]

$$\hat{H} = \sum_{\langle \mathbf{R}, \mathbf{R}' \rangle} J_{\mathbf{R}, \mathbf{R}'} \hat{a}_{\mathbf{R}}^\dagger \hat{a}_{\mathbf{R}'} + \sum_{\langle\langle \mathbf{R}, \mathbf{R}' \rangle\rangle} \tilde{J}_{\mathbf{R}, \mathbf{R}'} \hat{a}_{\mathbf{R}}^\dagger \hat{a}_{\mathbf{R}'} + \frac{1}{2} U \sum_{\mathbf{R}} \hat{a}_{\mathbf{R}}^\dagger \hat{a}_{\mathbf{R}}^\dagger \hat{a}_{\mathbf{R}} \hat{a}_{\mathbf{R}}, \quad (7.2)$$

considering nearest neighbor (NN) and next-nearest neighbor (NNN) hopping, which is denoted by the single and double angular brackets, and onsite interactions with strength  $U$ . The sum runs over all lattice sites  $\mathbf{R}$ , representing A and B. The interaction  $U$  is given by [204]

$$U = \frac{4\pi\hbar^2 a_s}{m} \int |w_1(\mathbf{r})|^4 d^3r = \frac{4\pi\hbar^2 a_s}{m} \int |w_{\text{hex}}(x, y)|^4 d^2r \int |w_Z(z)|^4 dz, \quad (7.3)$$

where  $w_1(\mathbf{r})$  denotes the Wannier function for a particle in the lowest band, which is factorized into the part describing the honeycomb lattice,  $w_{\text{hex}}(x, y)$ , and the contribution from the vertical direction,  $w_Z(z)$ . The Wannier functions of the honeycomb lattice used for the plots in Fig. 7.2 are taken from [205] and have been calculated using the method presented in [204]. Along the vertical direction, the case of a harmonic trapping potential is compared to a 1D lattice, being created as described in Sec. 4.1.5. If the system is only confined by the trap, the atoms are assumed to occupy the lowest energy level of the harmonic oscillator, where the eigenfunction corresponds to a normalized Gaussian:

$$w_Z^{\text{Trap}}(z) = \left( \frac{m\omega_z}{\pi\hbar} \right)^{1/4} e^{-\frac{m\omega_z}{2\hbar} z^2} \Rightarrow \int |w_Z^{\text{Trap}}(z)|^4 dz = \sqrt{\frac{m\omega_z}{2\pi\hbar}}, \quad (7.4)$$

with  $\omega_z = 2\pi f_z$  and  $f_z = 200$  Hz. The Wannier functions of the 1D lattice, being localized to a single unit cell, are calculated from the corresponding Bloch functions as [206]

$$w_Z(z) = \frac{a_Z}{2\pi} \int_{BZ} \psi_{q_z}^1(z) dq_z. \quad (7.5)$$

Replacing the harmonic confinement with a lattice increases the onsite interaction noticeably, allowing to enter the regime with  $U \gg J$ , as shown in Fig 7.2a, where the ratio  $U/J$  is plotted for  $a_s = 100 a_0$  as a function of the honeycomb lattice depth, being combined with either harmonic confinement along  $z$  (green dots) or with the vertical lattice at  $V_Z = 120 E_{rZ}$  and  $V_Z = 500 E_{rZ}$  (blue dots). In the latter case,  $U/J \sim 15$  can be reached in a deep honeycomb lattice with  $V_{\text{hex}} = 16 E_r$ . For the vertical lattice, the spacing of  $a_Z = 1.91 \mu\text{m}$  is used in the calculations.

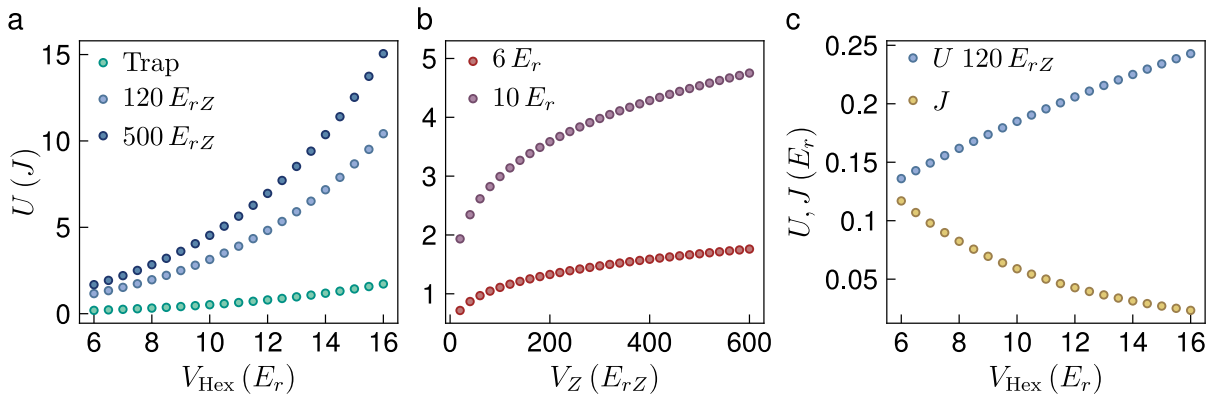


**Figure 7.2: Calculated Hubbard interaction  $U$  as a function of the lattice depth.** **a.** Interaction in units of the NN hopping  $J$  of the honeycomb lattice as a function of the honeycomb lattice depth  $V_{\text{hex}}$ . The green dots correspond to a harmonic trapping potential with  $f_z = 200$  Hz along the vertical direction, as it is the case in the experiments presented in this work. The blue dots are calculated assuming the vertical lattice with spacing  $a_Z = 1.91 \mu\text{m}$  and different depths. **b.**  $U$  as a function of the vertical lattice depth  $V_Z$ , again in units of the honeycomb tunneling amplitude  $J$ , which is now constant along each of the two curves. **c.** Interaction  $U$  in the 3D lattice (blue points) and NN hopping  $J$  of the honeycomb lattice (yellow points) as a function of the honeycomb lattice depth. While  $U$  increases with  $V_{\text{hex}}$ ,  $J$  decreases, leading to the steep rise of  $U/J$  in **a**. The scattering length is  $a_s = 100 a_0$  in all plots.

In the current setup, employing a Ti:sapphire laser to create the honeycomb lattice, the maximal depth that can be reached is about  $\sim 7 - 8 E_r$ , corresponding to  $U/J < 5$  for  $a_s = 100 a_0$ . Since  $U \propto a_s$ , the curves are simply scaled by constant factor for larger scattering lengths. In Fig 7.2b,  $U/J$  is shown as a function of the vertical lattice depth, also for  $a_s = 100 a_0$ . It exhibits a slower growth than the data in Fig 7.2a, since the interaction  $U$  is divided by the nearest neighbor hopping  $J$  of the honeycomb lattice in both cases. Changing the depth  $V_{\text{hex}}$  not only increases  $U$  but also decreases  $J$ , as illustrated in Fig 7.2c for  $a_s = 100 a_0$ , which leads to a steeper rise of  $U/J$ . Keeping the honeycomb depth constant reflects solely the growth of  $U$  with  $V_Z$ , since the points for each curve in Fig 7.2b are divided by the same number.

In general, large values of  $U/J$  could be realized when implementing a deeper honeycomb lattice in combination with the vertical lattice and a large scattering length. To raise the lattice depth  $V_{\text{hex}}$  to values above  $8 E_r$ , a much higher laser power is needed, which could be achieved by using a laser with  $\lambda = 1064 \text{ nm}$ , similar as for the optical dipole trap. In this case, a honeycomb lattice is generated for horizontal polarization, since the light is red detuned and the atoms are trapped in the intensity maxima.

## 7.2 Fermionization in the anomalous Floquet regime

In 1D lattice systems, strongly interacting Bose gases can exhibit features of non-interacting fermions, realizing what is known as the Tonks-Girardeau (TG) gas [207, 208]. In this regime, two bosons cannot occupy the same lattice site due to the strong, repulsive onsite-interactions, thus showing behavior similar to fermions. While some properties of the interacting Bose gas are similar to those of non-interacting fermions, such as the density pattern in real space, others remain different, one example being the momentum distribution. Due to the restrictions in real space, the width of the bosonic cloud in momentum space is increased, but in contrast to ideal, non-interacting fermions, several particles can still occupy the same momentum state. A TG gas has been realized experimentally with ultracold atoms in an optical lattice, confirming the theoretical predictions for the specific form of the momentum distribution [209].

Fermionization of interacting bosons has also been predicted in 2D [210, 211], whereas the detailed mechanism of the statistical transmutation is different than in 1D. In the TG gas, the dynamics are dominated by the interactions, since the interaction energy is much larger than the kinetic energy. A similar situation can be achieved if interacting bosons are loaded into a band structure with a flat dispersion, minimizing their kinetic energy. It is thereby sufficient for the energy band to be degenerate along a 1D line in quasimomentum space [211]. These dispersions are referred to as moat bands. The occurrence of statistical transmutation in a degenerate band minimum will be briefly introduced in the first part of this section, after which a possible experimental realization is discussed, utilizing the band structure in the anomalous Floquet regime.

### 7.2.1 Statistical transmutation in a degenerate band minimum

The ground state of repulsively interacting bosons in a degenerate ring-minimum is expected to be different from a BEC and can be described by non-interacting fermions placed in a magnetic field. The corresponding many-body wavefunction  $\Phi$  of  $N$  bosons can be approximated by a composite fermion state [211]

$$\Phi(\mathbf{r}_1, \dots, \mathbf{r}_N) = e^{i \sum_{j < l} \text{Arg}[\mathbf{r}_j - \mathbf{r}_l]} \Psi_F(\mathbf{r}_1, \dots, \mathbf{r}_N), \quad (7.6)$$

where  $\Psi_F(\mathbf{r}_1, \dots, \mathbf{r}_N)$  denotes the fully antisymmetric wavefunction of  $N$  non-interacting fermions, which are transformed to bosons with the Chern-Simons flux attachment, being described by the exponential prefactor. As shown in [211], the Chern-Simons factor is related to an emergent gauge field which depends on the particle density. In the mean-field approximation, this magnetic field is replaced with its mean value, thus being proportional to the average density  $n$ . The wavefunction  $\Psi_F$  then describes  $N$  non-interacting fermions subjected to a moat-like dispersion and a homogeneous magnetic field, with their energies being described by Landau-levels that depend on the density.

The realization of the composite fermion state could be verified by probing the velocity distribution of the expanding gas [211]. While condensation leads to a sharp peak at  $v = 0$  that broadens with increasing temperature, the velocity distribution of the fermionic state

follows a step function which becomes more pronounced at lower densities. The composite fermion state is expected to emerge for low densities and strong interactions [211], which are described by the dimensionless interaction strength  $g$ . For  $g = 1$ , the transition from the BEC to the fermionic state occurs at  $n \sim n_0 = q_0^2/(2\pi)$ , where  $q_0$  denotes the radius of the ring minimum in quasimomentum space [211]. If the interactions are smaller, the transition shifts to lower densities.

### 7.2.2 Probing the fermionization

The momentum distribution of a gas, being proportional to its velocity distribution, can be measured by free expansion in a TOF experiment. However, this only reveals the pure momentum distribution in the limit of  $t_{\text{TOF}} \rightarrow \infty$ , otherwise an effective convolution with the real space density distribution is probed. To overcome this problem, the technique introduced in [212] could be employed: After switching off only the lattice, the cloud expands in the harmonic trap for a time of  $T/4$ , where  $T = 2\pi/f_T$ , during which the initial momentum distribution is completely transferred to the real space density distribution, which is subsequently measured by absorption imaging. This works only for the ballistic expansion of a non- or weakly interacting gas, where the distribution is not distorted by particle collisions during the expansion. When probing a strongly interacting system, as it will be the case when realizing the statistical transmutation, the scattering length has to be ramped down prior to the expansion.

The moat dispersion can be realized when loading the atoms into the first Floquet band in the anomalous regime, where the hybridization with the second band leads to a ring-like minimum. In fact, the exact shape of the minimum is a mixture between a ring and a hexagon, as illustrated in Fig. 7.3a, where the dispersion of the first band is plotted for  $m = 0.2$  and  $f = 6 \text{ kHz}$  at the corresponding quasimomenta in the 2D Brillouin zone (BZ), which is indicated by the dashed, gray lines. The hexagon-ring is also not perfectly degenerate, but exhibits minima along the lines  $\Gamma - M$ . The flatness  $\mathcal{F}$  of the moat can be described by [211]

$$\mathcal{F} = \frac{E_{\max} - E_{\min}}{E_{\Gamma} - E_{\min}}, \quad (7.7)$$

where the maximal and minimal energy along the moat are denoted by  $E_{\max}$  and  $E_{\min}$ , and  $E_{\Gamma}$  is the energy at  $\Gamma$ . For the band minimum in the anomalous regime,  $E_{\max}$  is given by the value of the dispersion at the minimum along the line  $\Gamma - K$  and  $E_{\min}$  by the energy of the corresponding point along  $\Gamma - M$ .

Although the derivation in [211] assumes a perfectly flat moat, the authors also present a model for realizing a moat which exhibits a flatness  $\mathcal{F} \lesssim 0.1$ . This regime could indeed be reached using the anomalous Floquet band structure, as shown in Fig. 7.3b for  $m = 0.2$  and various modulation frequencies. While the flatness of the moat decreases with larger frequencies, its radius also becomes smaller, approaching the transition to the Haldane regime. Thus, the quasienergy gap to the second band at the position of the moat also decreases for  $f \gtrsim 6 \text{ kHz}$ , which is depicted in Fig. 7.3c for the band minima along the

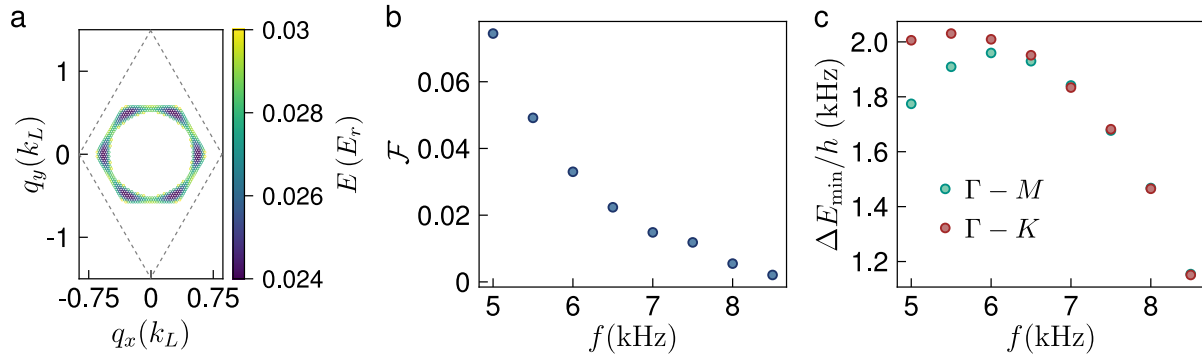


**Figure 7.3: Moat dispersion in the anomalous Floquet regime for  $m = 0.2$  and  $V_0 = 6 E_r$ .** **a.** Lowest Floquet band at the quasimomenta corresponding to the moat for  $f = 6$  kHz. The 2D BZ is indicated by the dashed, gray lines. **b.** Calculated flatness  $\mathcal{F}$  of the band minimum defined according to Eq. 7.7 as a function of the modulation frequency  $f$ . **c.** Quasienergy gap between the two lowest bands at the band minima along the lines  $\Gamma - M$  and  $\Gamma - K$  as a function of the modulation frequency, corresponding to the minimal and maximal points along the moat.

lines  $\Gamma - M$  and  $\Gamma - K$ . The decrease of the gaps for  $f \lesssim 6$  kHz signals the approach of the second phase transition. A smaller quasienergy gap could lead to excitations to the second band, and, as discussed in Sec. 5.4.2, the lifetime of the condensate is in general reduced for modulation parameters close to the phase transitions. Thus, a compromise between a small flatness and a maximal quasienergy gap has to be found, which could be achieved for  $f \sim 6 - 7$  kHz at  $m = 0.2$ .

While a relatively flat moat structure can be created in the anomalous Floquet regime, the onsite interactions would need to be increased to achieve the composite fermion regime, depending on the density of the BEC. In principle, the density could be made very small simply by decreasing the atom number of the BEC in combination with a reduction of the in-plane confinement. However, in order to probe the momentum distribution using absorption imaging, the overall density can not be too small to retain a useful signal-to-noise ratio.

The scattering amplitude for s-wave collisions in 2D in general depends logarithmically on the relative momentum of the atoms [213], in contrast to the 3D case, where it is independent of the momentum. In cold atomic gases being confined into a 2D plane by some trapping potential along the third direction, the range of the scattering potential is usually small compared to the extent of the system along this axis. Thus, the collisions can still be treated as 3D and are described by the dimensionless interaction strength [214–216]

$$g = \sqrt{8\pi} \frac{a_s}{a_{\text{ho}}}, \quad a_{\text{ho}} = \sqrt{\frac{\hbar}{m\omega_{\text{ho}}}}, \quad (7.8)$$

with the harmonic oscillator length  $a_{\text{ho}}$  describing the extent of the system along the third direction. For a harmonic trap, the corresponding frequency  $\omega_{\text{ho}}$  is directly given

by the trapping frequency. If a 1D lattice with spacing  $a_Z$  and depth  $V_Z$  is implemented along the third direction, the onsite trapping frequency is given by

$$\omega_{\text{ho}} = \sqrt{\frac{2V_Z}{m} \left(\frac{\pi}{a_Z}\right)^2}. \quad (7.9)$$

For a scattering length of  $a_s = 100 a_0$ , the dimensionless interaction strength amounts to  $g \approx 0.02$  if the system is confined by the harmonic trap with  $f_z = 200$  Hz, which is far below the value of  $g = 1$  mentioned above. Thus, the composite fermion state could only be observed for very small densities. The value of  $g$  could be raised to  $g \approx 0.2$  for  $a_s = 100 a_0$  in the presence of the vertical lattice with  $V_Z = 500 E_{rZ}$ . To determine whether the fermionization could be observed, the imaging at low densities needs to be tested, finding a lower limit for  $n$  and thus for the interaction strength that is needed.

To realize the system described above, the BEC needs to be loaded into the lowest band of the modulated lattice in the anomalous Floquet regime. Due to the gap closing at  $\Gamma$ , this involves changing the quasimomentum during the ramp-up of the modulation, to minimize excitations to the second band, as described in Sec. 5.1.3. Moreover, the atoms need to be held at the quasimomentum of the band minimum, which would lead to large displacements in real space arising from the accelerated lattice. Another option could be to directly transfer the atoms to the desired point in quasimomentum space by using Bragg beams. In this case, two laser beams with frequencies  $\omega_1 \neq \omega_2$  propagating along different directions  $\mathbf{k}_1, \mathbf{k}_2$  are imposed onto the atoms. The energy and momentum of the cloud are changed in a two-photon process by  $\hbar(\omega_1 - \omega_2)$  and  $\hbar(\mathbf{k}_1 - \mathbf{k}_2)$ , which can also be used for spectroscopy [217, 218]. In summary, after finding a way to load the condensate into the band minimum, the statistical transmutation could be measured, provided that absorption imaging is still possible at low densities and the interaction strength can me made large enough.



# Chapter 8

## Measuring symmetry protected Wilson lines

The topological properties of a single, non-degenerate energy or quasienergy band can be characterized in terms of Chern or winding numbers, which are related to the Berry curvature of the respective band. The change of the topological properties at band touching points is described by the topological charge, as outlined previously in chapters 2 and 5.

The concept of the Berry curvature, arising for adiabatic transport of a quantum state within a single Bloch band, can be generalized to the case of degenerate bands. Transport in a degenerate multiband system is captured by the matrix-valued Wilson line [81, 82], which contains off-diagonal terms that describe the mixing of bands. The eigenvalues of the Wilson line matrix are related to the  $\mathbb{Z}_2$ -invariant characterizing topological insulators [219, 220] and also play an important role in the description of symmetry protected topological phases [221, 222]. Moreover, a simplified form of the Wilson line has been used to directly access the properties of the cell-periodic Bloch-wavefunctions as a function of quasimomentum [72].

The chapter starts with a brief introduction to Wilson lines, a more detailed description can be found in [73]. Under certain circumstances, the difference of the eigenvalue phases of the Wilson line can be viewed as a topological invariant, being protected by the point-group symmetries of the lattice [223], which is discussed in Sec. 8.1.3 and 8.1.4. The measurement of the Wilson line eigenvalues in an optical honeycomb lattice is presented in the second part of the chapter, starting with the description of the experimental protocol in Secs. 8.2.1 and 8.2.2. The eigenvalue phases are derived as a function of the lattice depth for different paths in quasimomentum space [8.2.3]. In the lattice system considered here, the effect of the symmetry protection is expected to be small compared to systematic errors that arise in the measurements. The chapter concludes with the discussion of prospects how to investigate the symmetry protection of the eigenvalue phases in future experiments.

## 8.1 Wilson lines

The Wilson line describes the transport of a state in a subset of multiple, degenerate bands, which is adiabatic with respect to higher lying bands outside the corresponding subspace. In the following, this will be applied to the dispersion of the honeycomb lattice by considering the evolution of an eigenstate being transported in two-dimensional quasimomentum space by one reciprocal lattice vector  $\mathbf{G}$ . The applied force is large compared to the combined width of the two  $s$ -bands, but small with respect to the gap to the  $p$ -bands, realizing an effectively degenerate two-band system. After deriving different expressions for the Wilson line in the first part, the properties of the eigenvalue phases of the  $SU(2)$ -part of the Wilson line will be discussed. The notion of the atomic limit of a band representation is introduced, which is used to define a parameter regime where the symmetry protection of the eigenvalue phase difference of certain Wilson lines becomes relevant.

### 8.1.1 Transport in degenerate band subspaces

In Sec. 2.1.1, the adiabatic transport of a state in a single Bloch band has been considered, giving rise to a geometric phase factor, which is equal to the line integral of the Berry connection along the path being traversed in quasimomentum space. For transport along a closed path, it is gauge invariant and termed Berry phase or Zak phase [224], when the path consists of a reciprocal lattice vector  $\mathbf{G}$ , representing a closed loop due to the periodicity of the Brillouin zone (BZ). The transport in reciprocal space is realized by applying a force  $\mathbf{F}$  which changes the quasimomentum  $\mathbf{q}_0$  of the initial state to

$$\mathbf{q}(t) = \mathbf{q}_0 + \frac{\mathbf{F}t}{\hbar}. \quad (8.1)$$

The Schrödinger equation for a particle moving in a periodic, time-independent potential reads

$$i\hbar \frac{\partial}{\partial t} |\Psi(t)\rangle = (\hat{H} - \mathbf{F} \cdot \hat{\mathbf{r}}) |\Psi(t)\rangle, \quad (8.2)$$

and can be solved by writing the state as a linear combination of the Bloch states  $|\psi_{\mathbf{q}}^n(\mathbf{r})\rangle$  with time-dependent coefficients:

$$|\Psi(t)\rangle = \sum_n c^n(t) |\psi_{\mathbf{q}(t)}^n(\mathbf{r})\rangle = \sum_n c^n(t) e^{i\mathbf{q}(t) \cdot \mathbf{r}} |u_{\mathbf{q}(t)}^n(\mathbf{r})\rangle. \quad (8.3)$$

The Bloch states are eigenstates of the Hamiltonian  $\hat{H}$  with eigenvalues  $E_{\mathbf{q}}^n$ :

$$\hat{H} = \sum_{n,\mathbf{q}} E_{\mathbf{q}}^n |\psi_{\mathbf{q}}^n(\mathbf{r})\rangle \langle \psi_{\mathbf{q}}^n(\mathbf{r})|. \quad (8.4)$$

Inserting this and the ansatz from Eq. 8.3 into Eq. 8.2 yields the equations of motion for the coefficients  $c^n(t)$ :

$$\begin{aligned} i\hbar \frac{\partial}{\partial t} c^n(t) &= c^n(t) E_{\mathbf{q}(t)}^n - i \sum_{n'} c^{n'}(t) \mathbf{F} \cdot \langle u_{\mathbf{q}(t)}^n | \nabla_{\mathbf{q}} | u_{\mathbf{q}(t)}^{n'} \rangle \\ &= c^n(t) E_{\mathbf{q}(t)}^n - \sum_{n'} c^{n'}(t) \mathbf{F} \cdot \mathbf{A}^{nn'}(\mathbf{q}(t)), \end{aligned} \quad (8.5)$$

where  $\mathbf{A}^{nn'}(\mathbf{q}(t)) = i \langle u_{\mathbf{q}(t)}^n | \nabla_{\mathbf{q}} | u_{\mathbf{q}(t)}^{n'} \rangle$  is defined as the generalized Berry connection, which is often called the non-Abelian Berry connection if  $n \neq n'$ . For a two-band system, the time-evolution is described by a  $2 \times 2$  matrix

$$i\hbar \frac{\partial}{\partial t} \begin{pmatrix} c^1(t) \\ c^2(t) \end{pmatrix} = \begin{pmatrix} E_{\mathbf{q}(t)}^1 - \mathbf{F} \cdot \mathbf{A}^{11}(\mathbf{q}(t)) & -\mathbf{F} \cdot \mathbf{A}^{12}(\mathbf{q}(t)) \\ -\mathbf{F} \cdot \mathbf{A}^{21}(\mathbf{q}(t)) & E_{\mathbf{q}(t)}^2 - \mathbf{F} \cdot \mathbf{A}^{22}(\mathbf{q}(t)) \end{pmatrix} \begin{pmatrix} c^1(t) \\ c^2(t) \end{pmatrix}. \quad (8.6)$$

If the force is large compared to the energy dispersion, which means that  $\mathbf{F} \cdot \mathbf{A}^{nn'} \gg E^n$ , the equations of motion are reduced to

$$i\hbar \frac{\partial}{\partial t} \begin{pmatrix} c^1(t) \\ c^2(t) \end{pmatrix} = \begin{pmatrix} -\mathbf{F} \cdot \mathbf{A}^{11}(\mathbf{q}(t)) & -\mathbf{F} \cdot \mathbf{A}^{12}(\mathbf{q}(t)) \\ -\mathbf{F} \cdot \mathbf{A}^{21}(\mathbf{q}(t)) & -\mathbf{F} \cdot \mathbf{A}^{22}(\mathbf{q}(t)) \end{pmatrix} \begin{pmatrix} c^1(t) \\ c^2(t) \end{pmatrix} = -\mathbf{F} \cdot \hat{\mathbf{A}}_{\mathbf{q}(t)} \begin{pmatrix} c^1(t) \\ c^2(t) \end{pmatrix}. \quad (8.7)$$

The state of the system after a time  $t$  is obtained by acting with the corresponding time-evolution operator:

$$|\Psi(t)\rangle = \mathcal{T} e^{-\frac{i}{\hbar} \int_0^t \mathbf{F} \cdot \hat{\mathbf{A}}_{\mathbf{q}(t')} dt'} |\Psi(0)\rangle = \hat{W}_{\mathbf{q}_0 \rightarrow \mathbf{q}_f} |\Psi(0)\rangle, \quad (8.8)$$

with time-ordering denoted by  $\mathcal{T}$ . The operator  $\hat{W}_{\mathbf{q}_0 \rightarrow \mathbf{q}_f}$  describing the transport from quasimomentum  $\mathbf{q}_0$  to  $\mathbf{q}_f$  is called the Wilson line or Wilson-Zak loop [221]. Neglecting the energy dispersion corresponds to transport in two effectively flat and degenerate bands. Thus, the Wilson line can be viewed as the generalization of the Berry phase factor introduced in Eq. 2.7 to a subset of multiple, degenerate bands. Similar as for a single band, the Berry connection matrix  $\hat{\mathbf{A}}_{\mathbf{q}}$  and also the Wilson line are gauge dependent, whereas the eigenvalues of the Wilson line are gauge-independent for transport along a closed path, and accordingly named non-Abelian Berry phases [221]. The Berry connection matrix can be used to define the non-Abelian Berry curvature [182]

$$\mathcal{B} = \nabla_{\mathbf{q}} \times \hat{\mathbf{A}}_{\mathbf{q}} - i \hat{\mathbf{A}}_{\mathbf{q}} \times \hat{\mathbf{A}}_{\mathbf{q}}, \quad (8.9)$$

which is a gauge-dependent quantity in contrast to its single-band counterpart. While the Berry connection and curvature in the single band case have a similar structure as a vector potential and magnetic field in quasimomentum space,  $\hat{\mathbf{A}}$  and  $\mathcal{B}$  correspond to the gauge potential and gauge field in a non-Abelian  $SU(2)$  gauge theory [225].

**Wilson lines as projectors** If the bands of the degenerate subspace span the same Hilbert space at all quasimomenta, as it is the case for the  $s$ -bands of the honeycomb lattice, the integration in Eq. 8.8 becomes independent of the path in quasimomentum space [221]. The elements of the Wilson line describing the transport from  $\mathbf{q}_0$  to  $\mathbf{q}_f$  are then given by the overlap of the cell-periodic Bloch states at the initial and final quasimomentum:

$$W_{\mathbf{q}_0 \rightarrow \mathbf{q}_f}^{nm} = \langle u_{\mathbf{q}_f}^n | u_{\mathbf{q}_0}^m \rangle. \quad (8.10)$$

This effectively corresponds to the situation where the applied force is the largest energy scale of the system and  $\mathbf{F} \cdot \hat{\mathbf{r}} \gg \hat{H}$  in Eq. 8.2. In this case, the Wilson line, being equal to the time-evolution operator, simplifies to

$$\hat{W}_{\mathbf{q}_0 \rightarrow \mathbf{q}_f} = e^{\frac{i}{\hbar} \mathbf{F} \cdot \hat{\mathbf{r}} t} = e^{i(\mathbf{q}_f - \mathbf{q}_0) \cdot \hat{\mathbf{r}}}. \quad (8.11)$$

Hence, its matrix elements in the basis of the Bloch states can be expressed as

$$W_{\mathbf{q}_0 \rightarrow \mathbf{q}_f}^{nm} = \langle \psi_{\mathbf{q}_f}^n | \hat{W}_{\mathbf{q}_0 \rightarrow \mathbf{q}_f} | \psi_{\mathbf{q}_0}^m \rangle = \langle u_{\mathbf{q}_f}^n | e^{-i\mathbf{q}_f \cdot \mathbf{r}} e^{i(\mathbf{q}_f - \mathbf{q}_0) \cdot \mathbf{r}} e^{i\mathbf{q}_0 \cdot \mathbf{r}} | u_{\mathbf{q}_0}^m \rangle = \langle u_{\mathbf{q}_f}^n | u_{\mathbf{q}_0}^m \rangle. \quad (8.12)$$

The relation in Eq. 8.10 can be used for state tomography [226, 227] of the cell-periodic Bloch states, characterizing them as a function of quasimomentum [72].

**Decomposition of the Wilson line matrix** The Wilson line defined in Eq. 8.8 is a unitary  $2 \times 2$  matrix and can thus be split into a  $U(1)$ -phase and an  $SU(2)$ -part. Decomposing the Berry connection matrix as

$$\hat{\mathbf{A}} = \begin{pmatrix} \frac{A^{11} + A^{22}}{2} & 0 \\ 0 & \frac{A^{11} + A^{22}}{2} \end{pmatrix} + \begin{pmatrix} \frac{A^{11} - A^{22}}{2} & A^{12} \\ A^{21} & \frac{A^{22} - A^{11}}{2} \end{pmatrix} = \hat{\mathbf{A}}_{U(1)} + \hat{\mathbf{A}}_{SU(2)}, \quad (8.13)$$

where the dependence on the quasimomentum has been omitted for clarity, the Wilson line is given by

$$\begin{aligned} \hat{W}_{\mathbf{q}_0 \rightarrow \mathbf{q}_f} &= \mathcal{T} e^{-\frac{i}{\hbar} \int_0^t \mathbf{F} \cdot (\hat{\mathbf{A}}_{U(1)} + \hat{\mathbf{A}}_{SU(2)}) dt'} \\ &= e^{-\frac{i}{\hbar} \int_0^t \mathbf{F} \cdot \hat{\mathbf{A}}_{U(1)} dt'} \mathcal{T} e^{-\frac{i}{\hbar} \int_0^t \mathbf{F} \cdot \hat{\mathbf{A}}_{SU(2)} dt'}. \end{aligned} \quad (8.14)$$

The first part describes the sum of the geometric phases acquired in both bands and is proportional to the identity matrix, hence commuting with  $\hat{\mathbf{A}}_{SU(2)}$  and itself at all quasimomenta. The experiment reconstructs the  $SU(2)$ -part of the Wilson line [72, 73],  $W_{SU(2)} \in U(2)/U(1) = SU(2)/\mathbb{Z}_2$ , since the global  $U(1)$ -phase factor can not be measured. Here,  $\mathbb{Z}_2$  indicates the ambiguity in choosing  $\pm W_{SU(2)}$ . Writing  $W_{SU(2)}$  in the general form of an  $SU(2)$  matrix,

$$W_{SU(2)} = \begin{pmatrix} W^{11} & W^{12} \\ -(W^{12})^* & (W^{11})^* \end{pmatrix}, \quad (8.15)$$

its eigenvalues  $\lambda_{\pm}$  are given by

$$\begin{aligned}\lambda_{\pm} &= e^{\pm i\xi} = \cos(\xi) \pm i \sin(\xi) \\ &= \text{Re}[W^{11}] \pm i \sqrt{|\text{Im}[W^{11}]|^2 + |\text{Re}[W^{11}]|^2}.\end{aligned}\quad (8.16)$$

Due to the  $\mathbb{Z}_2$ -ambiguity of  $W_{SU(2)}$ , the eigenvalue phase  $\xi$  is only defined up to  $\pm\pi$ . Considering the real part of Eq. 8.16, the eigenvalue phase can be determined solely from the first entry  $W^{11}$  of the Wilson line:

$$\xi = \arccos(\text{Re}[W^{11}]) = \arccos(|W^{11}| \cos(\text{Arg}[W^{11}])). \quad (8.17)$$

By extracting the absolute value and argument of the complex number  $W^{11}$ , the eigenvalue phase is derived in the experiment, as described in Sec. 8.2.

### 8.1.2 Real space picture

In the following, transport along the  $q_x$ -direction by one reciprocal lattice vector  $\mathbf{G} = \mathbf{K}_1 + \mathbf{K}_2$  is considered, starting at  $\mathbf{q}_0 = \Gamma$  in the first BZ and ending at  $\mathbf{q}_f = \Gamma$  in the next BZ, as depicted in Fig. 8.1a. The path exhibits twofold rotational symmetry, meaning that its second half can be mapped to the first half by a rotation of  $180^\circ$ , and will be denoted by  $C_2$  accordingly.

In the absence of a sublattice energy offset, the eigenstates of the two lowest bands in the honeycomb lattice can be generally expressed as equal superpositions of wavefunctions being localized on A- and B-sites. The force applied to realize the non-adiabatic transport within the  $s$ -bands corresponds to a gradient along  $x$ , shifting the potential of neighboring lattice sites by  $Fa$  (see left panel of Fig. 8.1b). Thus, if the applied force is large compared to the energy dispersion,  $Fa \gg J$ , with  $J$  denoting the nearest neighbor (NN) hopping, the wavefunctions on A- and B-sites are effectively decoupled and can evolve independently.

During the transport, atoms being initialized on an A- or B-site acquire a phase difference of  $2\pi/3$  [73], which is illustrated in the right panel of Fig. 8.1b: Transporting a Bloch state from A to A or B to B, corresponding to a real space distance of  $3a/2$  along  $x$ , must result in a trivial phase shift of  $2\pi$ . The distance between A- and B-sites is given by  $a/2$ , corresponding to a phase shift of  $2\pi/3$  (or equivalently  $-4\pi/3$  when considering the other pair of sites spaced by  $a$ ). This can be seen directly when writing the Wilson line as the propagator in quasimomentum space [73] as given by Eq. 8.11. The system is initialized in the lowest Bloch band at  $\Gamma$  and transported by  $\mathbf{G} = (\sqrt{3}, 0) k_L$ :

$$|u_{\Gamma+\mathbf{G}}^1\rangle = e^{i\mathbf{G}\cdot\hat{\mathbf{r}}} |u_{\Gamma}^1\rangle = e^{i\mathbf{G}\cdot\hat{\mathbf{r}}} \frac{1}{\sqrt{2}} \left( \sum_{\mathbf{r}_A} |w_{\mathbf{r}_A}\rangle + \sum_{\mathbf{r}_B} |w_{\mathbf{r}_B}\rangle \right), \quad (8.18)$$

where the states localized on A- and B-sites have been expressed in terms of the Wannier functions  $|w_{\mathbf{r}_A(B)}\rangle$ , which are eigenstates of the position operator  $\hat{\mathbf{r}}$  with eigenvalues

$\mathbf{r}_{A(B)}$  [228]. Thus, they are also eigenstates of the Wilson line operator  $e^{i\mathbf{G}\cdot\hat{\mathbf{r}}}$  with eigenvalues  $e^{i\mathbf{G}\cdot\mathbf{r}_{A(B)}}$ . The locations of the B-sites can be related to the A-sites as  $\mathbf{r}_B = \mathbf{r}_A + \boldsymbol{\delta}_1$ , which directly reveals the phase difference of  $2\pi/3$  when transporting by  $\mathbf{G}$ :

$$\begin{aligned} |u_{\Gamma+\mathbf{G}}^1\rangle &= \frac{1}{\sqrt{2}} \left( \sum_{\mathbf{r}_A} e^{i\mathbf{G}\cdot\mathbf{r}_A} |w_{\mathbf{r}_A}\rangle + e^{i\mathbf{G}\cdot(\mathbf{r}_A+\boldsymbol{\delta}_1)} |w_{\mathbf{r}_A+\boldsymbol{\delta}_1}\rangle \right) \\ &= \frac{1}{\sqrt{2}} \left( \sum_{\mathbf{r}_A} |w_{\mathbf{r}_A}\rangle + e^{i\frac{2\pi}{3}} |w_{\mathbf{r}_A+\boldsymbol{\delta}_1}\rangle \right) = \frac{1}{\sqrt{2}} \left( |u_{\Gamma}^A\rangle + e^{i\frac{2\pi}{3}} |u_{\Gamma}^B\rangle \right), \end{aligned} \quad (8.19)$$

where  $\mathbf{G} \cdot \mathbf{r}_A = 2\pi$ , since  $\mathbf{r}_A$  can be written as a sum over the lattice vectors  $\mathbf{a}_1$  and  $\mathbf{a}_2$ . This means that the system only returns to its original state after transporting by  $3\mathbf{G}$ , which has also been measured experimentally by observing the population of the lowest band after non-adiabatic transport along  $q_x$  for various path lengths [72, 73]. The phase difference between wavefunctions localized on A- and B-sites, that is acquired during the transport by  $\mathbf{G}$ , directly corresponds to the difference of the eigenvalue phases of the Wilson line  $e^{i\mathbf{G}\cdot\hat{\mathbf{r}}}$ , as outlined above. This relation will be investigated in more detail in the next section, as well as possible deviations from the value of  $2\pi/3$ .

### 8.1.3 Symmetry protection of the eigenvalue phase difference

In the situation discussed above, the two lowest bands of the honeycomb lattice can be expressed by superpositions of two  $s$ -orbitals being localized on A- and B-sites. In general, this kind of mapping is called a band representation. The *atomic limit* of such a band representation describes the situation that a finite number of bands can be represented by a superposition of a finite number of Wannier functions per unit cell [223]. In this sense, the first six bands of the symmetric honeycomb lattice at  $V_0 = 6 E_r$  are not in the atomic limit, since they can not be completely described by a set of six tight-binding orbitals, as discussed in Sec. 3.3.2. On the other hand, the two lowest bands are in the atomic limit for  $V_0 = 6 E_r$ , being fully captured by the two  $s$ -orbitals with negligible  $sp$ -coupling.

In the atomic limit, there exists a one-to-one correspondence between the eigenvalue phase differences of the Wilson line and the phase difference between the wavefunctions localized on A- and B-sites acquired during the transport [223, 229]. Thus, the difference of the eigenvalue phases just depends on the angle of the force relative to the vector  $\boldsymbol{\delta}_1$  connecting A- and B-sites, as illustrated in the previous section. As a consequence of this, the phase difference is similar for all paths that are homotopically equivalent, which means that they can be continuously deformed into each other. The path  $C_3$ , which connects the centers of the first and second BZ via the  $K'$ -point (see Fig. 8.1c), and accordingly exhibits threefold rotational symmetry, is homotopically equivalent to  $C_2$  and thus  $\Delta\xi(C_3) = 2\pi/3$ .

Away from the atomic limit, the eigenvalue phase differences will be modified in general, but for certain paths they remain quantized as long as the point-group symmetry of the path is preserved [223, 229]. This is the case for the  $C_3$  path, where  $\Delta\xi$  is protected by threefold rotational symmetry. In contrast, the phase difference for the  $C_2$  path is

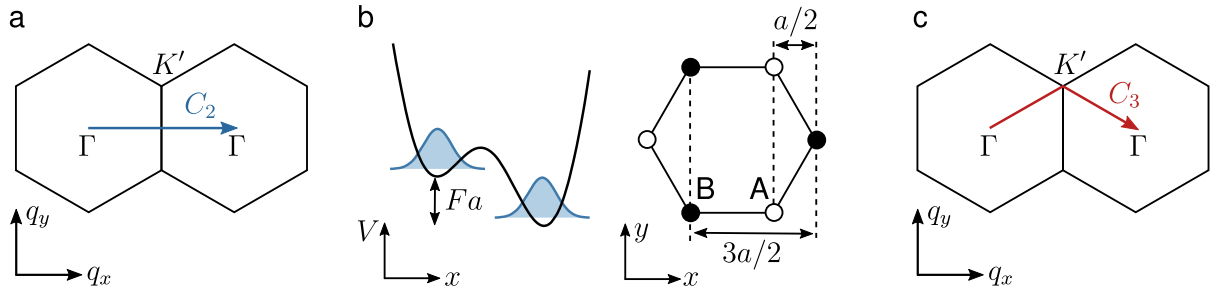


Figure 8.1: **Transport paths in reciprocal space and real space embedding of the Wilson line eigenvalues.** a. Path  $C_2$  in quasimomentum space for transport by  $\mathbf{G} = \mathbf{K}_1 + \mathbf{K}_2$  from  $\Gamma$  to  $\Gamma$ . b. The applied force corresponds to a gradient  $Fa$  of the lattice potential. If  $Fa \gg J$ , the wavefunctions (filled, blue lines) localized on A- and B-sites can evolve independently and acquire a phase difference of  $2\pi/3$  when transporting along  $C_2$ , since the distance between A and B equals  $1/3$  of the total distance from A to A. [72, 73]. c. Path  $C_3$  being homotopically equivalent to  $C_2$ , but threefold rotationally symmetric. Away from the atomic limit, the eigenvalue phase difference of the corresponding Wilson line is protected by threefold rotational symmetry.

expected to change when leaving the atomic limit, independent of whether inversion symmetry is broken or not. The atomic limit is characterized by vanishing non-Abelian Berry curvature, which accordingly acquires a finite value away from it.

Symmetry protected phase differences of the Wilson line eigenvalues can also occur in topological bands with non-zero Chern numbers. Although no description in terms of Wannier functions exists there [230, 231], the geometrical phases arising from transport in reciprocal space can always be formulated [223].

As mentioned in the beginning, Wilson lines can be employed to obtain the  $\mathbb{Z}_2$ -invariant characterizing topological insulators. These systems can be viewed as two copies of a Chern insulator having opposite Chern numbers  $\mathcal{C}_{\uparrow, \downarrow}$  for particles with opposite spin, preserving time-reversal symmetry. This results in no net chiral edge current, as the particles with spin up and down move in opposite directions. Since the Chern numbers for the different spin components have the same magnitude, their difference is given by a  $\mathbb{Z}_2$ -number  $\mathcal{C}_\uparrow - \mathcal{C}_\downarrow = \pm 1$ , which is a topological invariant characterizing the system. The Chern number can be expressed in terms of polarizations [220], that essentially describe the transverse motion of a particle when its quasimomentum is changed. Similar to the Wannier functions above, they are related to the eigenvalue phases of the Wilson line which allows for determination of the  $\mathbb{Z}_2$ -invariant from  $\Delta\xi$  [219, 220].

In order to observe the symmetry protection of the eigenvalue phase difference, a band-subspace has to be found which is not described by an atomic limit, corresponding to a non-zero value of the non-Abelian Berry curvature. The strong gradient dynamics mentioned above can be realized experimentally for the  $s$ -bands of the honeycomb lattice, since they are separated by a gap from the  $p$ -bands, allowing to choose the magnitude of the force such that it lies in the gap between the  $s$ - and  $p$ -bands. Going away from the atomic

limit there means that the two lowest bands need to be described as superpositions of *s*- and *p*-orbitals, amounting to a finite *sp*-coupling. As mentioned above and in Sec. 3.3, the *sp*-coupling vanishes in the static, symmetric honeycomb lattice for  $V_0 = 6 E_r$ . The *sp*-hybridization could be enhanced by lowering the lattice depth, since this reduces the energy gap between the *s*- and *p*-bands, as described in the next section.

### 8.1.4 Correction terms

The limit of completely flat, degenerate bands can not be reached in the experiment, since the force can not be arbitrarily large due to the presence of higher bands. There are two kinds of corrections to the Wilson line matrix defined in Eq. 8.8 that can arise in a realistic setting: If the force is not large enough, the dispersion of the two lowest bands can not be neglected any more and the time integration in Eq. 8.8 needs to be carried out over the full matrix given in Eq. 8.6, which contains the band energies on the diagonal. In general, this leads to deviations of the eigenvalue phase difference from  $2\pi/3$  which scale with  $(\Delta E_{\max}^{21}/Fa)^2$  [229], where  $\Delta E_{\max}^{21}$  denotes the maximal energy gap between the two lowest bands, being equal to their combined width.

If the force is too large, excitations to higher bands will occur, leading to corrections of the order  $Fa/\Delta E_{\min}^{32}$  [229], with  $\Delta E_{\min}^{32}$  being the minimal gap to the higher bands. To include these in the dynamics, a six-band model needs to be considered. In a tight-binding description, the excitations from the *s*- to the *p*-bands would scale with the *sp*-hybridization. This illustrates the difficulties which appear in the experiment: Increasing the *sp*-hybridization to observe the effect of the symmetry protection, e.g. by reducing the lattice depth, leads to an enhanced probability of excitations to higher bands. Moreover, as discussed in Sec. 8.2.3, the *s*-band dispersion is also increased in a shallow lattice, complicating the realization of the strong gradient regime and the distinction between the effects from the symmetry protection and the correction terms.

To isolate the effect of the *sp*-hybridization in the calculations, leading to the finite non-Abelian Berry curvature and hence to the symmetry protection, a  $2 \times 2$ -Wilson line not containing the energy dispersion can be used, thereby also excluding excitations to the *p*-bands. The eigenstates of the two lowest bands, that enter the derivation of the Berry connection matrix, are however obtained from either a full band calculation which incorporates all couplings, or from a tight-binding model with more than two bands, containing non-zero *sp*-hoppings [229].

Using the full band calculation, care must be taken when carrying out the derivatives of the band eigenstates, since the Berry connections are gauge-dependent (in contrast to the gauge-independent single-band Berry curvature which has been calculated e.g. in Sec. 3.1.2). To derive the Berry connections, a suitable gauge choice has to be made which ensures that the cell-periodic Bloch functions are numerically differentiable everywhere in the BZ [72, 73, 232]. In a two-band tight-binding model, this is not necessary, since the eigenstates and Berry connections can be calculated analytically.

## 8.2 Measurement of the eigenvalue phases

The eigenvalues of the Wilson line can be measured experimentally, enabling the derivation of their phases, and thus of the phase difference and its potential symmetry protection. As mentioned at the end of Sec. 8.1.1, the experiment reconstructs the  $SU(2)$ -part of the Wilson line, which has eigenvalues  $e^{\pm i\xi}$ . Hence, the phase difference is given by  $\Delta\xi = 2\xi$  and its quantization to a value of  $2\pi/3$  corresponds to  $\xi$  being quantized to  $\pi/3$ , which will be considered in the following for simplicity.

The eigenvalue phase of the Wilson line is measured along the  $C_2$  and  $C_3$  paths introduced above for different lattice depths between  $V_0 = 7 E_r$  and  $V_0 = 3 E_r$ , simulating the presence or absence of the atomic limit. The data in the symmetric lattice are compared to the values in an imbalanced lattice, where threefold rotational symmetry is broken, in order to detect the predicted symmetry protection of the eigenvalue phase along  $C_3$ . As mentioned in the last section, deviations of the eigenvalue phase from  $\pi/3$  will also occur due to excitations to higher bands and the non-negligible energy dispersion. To probe the influence of these corrections independently of each other, the measurements are carried out for two different force settings where either  $Fa/\Delta E_{\max}^{21}$  or  $Fa/\Delta E_{\min}^{32}$  is kept constant while varying the lattice depth.

From the theoretical considerations in Sec. 8.1.3 it would be expected that the eigenvalue phase of the  $C_3$  path should only deviate from  $\pi/3$  away from the atomic limit if threefold rotational symmetry is broken, thus in the shallow, imbalanced lattice, while  $\xi$  along  $C_2$  should always change when lowering the lattice depth, regardless of the lattice symmetry.

### 8.2.1 Experimental sequence to obtain the eigenvalue phase

According to Eq. 8.17, the eigenvalue phase of the  $SU(2)$  Wilson line is completely determined by the complex number  $W^{11}$ . In the experiment, the absolute value and argument of this number are obtained by band population measurements, as described in [72, 73]. The Bose-Einstein condensate of  ${}^{39}\text{K}$  at  $a_s = 6 a_0$  is loaded into the lowest band of the honeycomb lattice at  $\mathbf{q}_0 = \Gamma$ . The force is applied by lattice acceleration, being directed either along the  $q_x$ -direction corresponding to the  $C_2$  path or towards  $K'$  to realize transport along the  $C_3$  path. For the latter, the direction of the force is then switched when reaching  $K'$  (see Fig. 8.1c) to continue the acceleration towards  $\Gamma$  in the second BZ. The fast switching of the force direction did not lead to heating or excitations, probably also due to the relatively large angle of the path. The band population measurements are carried out by performing bandmapping at the end of the path and counting the population in the lowest band at  $\mathbf{q}_f = \Gamma$ . This corresponds to a projection to the eigenstate  $|u_\Gamma^1\rangle$ .

**Population measurements:**  $|\mathbf{W}^{11}|$  Writing the entries of the Wilson line as projection operators as introduced in Eq. 8.10, the absolute value of the matrix entry  $W^{11}$  can directly be accessed by measuring the population in the lowest band after transporting

from  $\Gamma$  by one reciprocal lattice vector  $\mathbf{G}$ , either along  $C_2$  or  $C_3$ :

$$|W_{\Gamma \rightarrow \Gamma + \mathbf{G}}^{11}|^2 = |\langle u_{\Gamma + \mathbf{G}}^1 | u_{\Gamma}^1 \rangle|^2 = n^1(\Gamma + \mathbf{G}), \quad |W_{\Gamma \rightarrow \Gamma + \mathbf{G}}^{11}| = \sqrt{n^1(\Gamma + \mathbf{G})}. \quad (8.20)$$

The relative population  $n^1$  in the lowest band is derived from absorption images, which are taken after performing bandmapping at  $\Gamma$  in the second BZ and a time-of-flight (TOF) of  $t_{\text{TOF}} = 3.5$  ms, by counting the pixel sum in the central peak corresponding to the lowest band. The background is subtracted by choosing appropriate regions-of-interest as described in Sec. 4.2.2 and the relative population is given as the pixel sum in the central peak divided by the total sum. From these images it can not be inferred whether the atoms not being in the lowest band are populating the second or higher bands. Nevertheless, it can be deduced that there is vanishing population in bands higher than the 6th in the measurements presented here.

Since the imaging intensity is larger in the center of the images, the population in the central peak is slightly underestimated compared to the outer peaks. This effect is reduced by performing the mentioned subtraction of the local background pixels close to each peak and by choosing a short TOF, resulting in a more equal intensity at the location of the different peaks.

**Oscillation measurements:  $\text{Arg}[\mathbf{W}^{11}]$**  The argument of  $W^{11}$  is obtained from interferometric measurements [72, 73] similar to Stückelberg oscillations [4.2.2], which is illustrated in Fig. 8.2a for the  $C_3$  path. The atoms are loaded into the lowest band at  $\Gamma$  and then accelerated along  $q_x$  to the next  $\Gamma$ -point in the second BZ, creating a coherent superposition of populations in the first and second band (step 1). In this part, an intermediate force is used which depends on the lattice depth and varies between  $Fa = 0.68$  kHz and  $6.80$  kHz for  $V_0 \in [3, 7] E_r$ . The atoms are held at  $\Gamma$  for a variable time  $t$  (step 2), leading to the time-dependent superposition state

$$|\psi_{(2)}(t)\rangle = a_1 |u_{\Gamma}^1\rangle + a_2 e^{i(\omega t + \phi_0)} |u_{\Gamma}^2\rangle, \quad (8.21)$$

with  $\omega = (E^2(\Gamma) - E^1(\Gamma))/\hbar$ . This constitutes the initial state for the application of the Wilson line, transporting from  $\Gamma$  in the second BZ to  $\Gamma$  in the third BZ either along  $C_2$  or  $C_3$  (step 3). After the transport, the population in the lowest band is measured as a function of the initial hold time, again by performing bandmapping and TOF-imaging. The population measurement after transport by  $\hat{W}_{\Gamma \rightarrow \Gamma + \mathbf{G}}$  corresponds to projecting the initial state in Eq. 8.21 to the projector state

$$|u_{\Gamma + \mathbf{G}}^1\rangle = \langle u_{\Gamma}^1 | u_{\Gamma + \mathbf{G}}^1 \rangle |u_{\Gamma}^1\rangle + \langle u_{\Gamma}^2 | u_{\Gamma + \mathbf{G}}^1 \rangle |u_{\Gamma}^2\rangle = (W_{\Gamma \rightarrow \Gamma + \mathbf{G}}^{11})^* |u_{\Gamma}^1\rangle + (W_{\Gamma \rightarrow \Gamma + \mathbf{G}}^{12})^* |u_{\Gamma}^2\rangle, \quad (8.22)$$

where the second part directly follows from Eq. 8.10. Hence, the population in the lowest band oscillates a function of the hold time  $t$  according to

$$\begin{aligned} n_{C+}^1(t) &= |\langle u_{\Gamma + \mathbf{G}}^1 | \psi_{(2)}(t) \rangle|^2 = |a_1 W^{11} + a_2 e^{i(\omega t + \phi_0)} W^{12}|^2 \\ &= |a_1 W^{11}|^2 + |a_2 W^{12}|^2 + 2|a_1 a_2 W^{11} W^{12}| \cos(\omega t + \phi_0 + \text{Arg}[W^{12}] - \text{Arg}[W^{11}]) \\ &= |a_1 W^{11}|^2 + |a_2 W^{12}|^2 + 2|a_1 a_2 W^{11} W^{12}| \cos(\omega t - \phi_{C+}). \end{aligned} \quad (8.23)$$

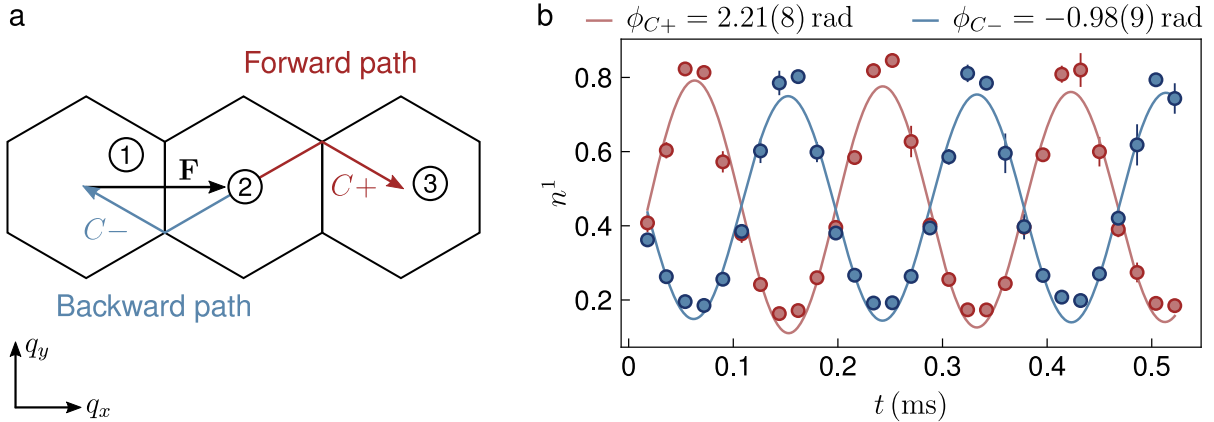


Figure 8.2: **Schematic representation of the experiment to measure  $\text{Arg}[W^{11}]$  and experimental data.** **a.** The atoms are first accelerated to  $\Gamma$  in the second BZ (1) and held there for a variable time (2) to create a time-dependent superposition state between the first and second band. Subsequently, the Wilson line path is traversed either along the forward ( $C+$ , red arrow) or along the backward direction ( $C-$ , blue arrow). Bandmapping at the end of the path (3) results in an oscillation of the relative population in the lowest band with a frequency given by the energy gap at  $\Gamma$ , which is fitted to obtain its phase. The argument of  $W^{11}$  is derived from the difference of the oscillation phases between  $C+$  and  $C-$ . **b.** Measured relative population  $n^1$  in the lowest band (data points) as a function of the hold time  $t$  at (2) along the forward and backward direction for the  $C_3$  path with  $V_0 = 7 E_r$  and  $Fa = 3\Delta E_{\Gamma}^{21} \approx 16.7$  kHz. The solid lines depict the fit according to Eq. 8.24. Each data point is obtained by averaging  $n^1$  over three individual images, the errorbars denote the standard deviation.

By fitting a damped cosine-function to the measured, time-dependent populations,

$$n^1(t) = Ae^{-\frac{t}{\tau}} \cos(\omega t - \phi) + n_0, \quad (8.24)$$

the phase  $\phi_{C+} = \text{Arg}[W^{11}] - \text{Arg}[W^{12}] - \phi_0$  of the oscillation is extracted. In principle, the phase of the population oscillation would be a gauge-dependent quantity [73], that becomes gauge-independent when comparing it at different quasimomenta. This corresponds to choosing a reference point in the BZ, relative to which all other phases are defined. In Eq. 8.23, this reference momentum is the  $\Gamma$ -point and the fitted oscillation phase corresponds to the difference between the Wilson line phase and the offset phase  $\phi_0$ . The latter arises from the initial transport which generates the superposition state.

To obtain  $\text{Arg}[W^{11}]$ , the measurement is repeated, but after creating and holding the superposition state in the second BZ, the subsequent path is traversed in the opposite direction (blue arrow in Fig. 8.2a). The Wilson line matrix corresponding to the reversed path is given by

$$\hat{W}_{\Gamma \rightarrow \Gamma - \mathbf{G}} = \hat{W}_{\Gamma \rightarrow \Gamma + \mathbf{G}}^\dagger = \begin{pmatrix} (W^{11})^* & -W^{12} \\ -(W^{12})^* & W^{11} \end{pmatrix}, \quad (8.25)$$

which is known as the back-tracking condition [73,233]. Since the first part of the sequence remains unchanged, the same offset phase  $\phi_0$  is acquired as when transporting along the forward direction. The oscillation phase for the backward path  $C_-$  can be accordingly expressed as

$$\begin{aligned}\phi_{C_-} &= \text{Arg}[W_{\Gamma \rightarrow \Gamma - \mathbf{G}}^{11}] - \text{Arg}[W_{\Gamma \rightarrow \Gamma - \mathbf{G}}^{12}] - \phi_0 \\ &= \text{Arg}[(W_{\Gamma \rightarrow \Gamma + \mathbf{G}}^{11})^*] - \text{Arg}[-W_{\Gamma \rightarrow \Gamma + \mathbf{G}}^{12}] - \phi_0 \\ &= -\text{Arg}[W_{\Gamma \rightarrow \Gamma + \mathbf{G}}^{11}] - (\text{Arg}[W_{\Gamma \rightarrow \Gamma + \mathbf{G}}^{12}] + \pi) - \phi_0.\end{aligned}\quad (8.26)$$

Subtracting the oscillation phases for the forward and backward path yields  $\text{Arg}[W^{11}]$ :

$$\text{Arg}[W_{\Gamma \rightarrow \Gamma + \mathbf{G}}^{11}] = \frac{1}{2}(\phi_{C+} - \phi_{C-} - \pi). \quad (8.27)$$

Thus, for each parameter setting and path, the population oscillation is measured along the forward and backward direction and the fitted oscillation phases are inserted into Eq. 8.27. In Fig. 8.2b, the measured oscillations along both directions are shown together with the corresponding fit for the  $C_3$  path in the symmetric lattice with  $V_0 = 7 E_r$  and  $Fa = 3\Delta E_\Gamma^{21} \approx 16.7$  kHz. The relative populations at the end of the path are counted similarly as described above. In the oscillation measurements,  $t_{\text{TOF}} = 5$  ms is used, since the systematic reduction of  $n^1$  due to the imaging intensity just shifts the values for all times by a constant offset, not changing the frequency or phase of the oscillation.

### 8.2.2 Strong gradient regime

The ideal strong gradient regime, where the Wilson line is given by Eq. 8.8, would be reached if the applied force is very large compared to the combined width of the two  $s$ -bands, but still much smaller than the gap to the  $p$ -bands. This situation can be realized approximately if the lattice is sufficiently deep, providing a large gap between  $s$ - and  $p$ -bands with negligible dispersion for the  $s$ -bands. To test whether the dynamics correspond to the strong gradient regime, the population in the lowest band is measured as a function of the force after transporting along  $C_2$  [72,73], which is plotted in Fig. 8.3a for  $V_0 = 7 E_r$ . Starting with all atoms in the lowest band, the relative population is lowered for larger forces until it nearly saturates around  $n^1 \sim 0.25$ , but still slightly decreases. In the ideal case of transport in two flat, degenerate bands, the population would be  $n^1 = 0.25$  (as indicated by the dashed line), resulting from a two-band tight-binding model [72,73]. The deviations from this value at very large forces arise from excitations to higher bands. This is confirmed by a full band calculation (solid line), including the first six bands in the time-integration in Eq. 8.8 as well as the band dispersion, that mostly coincides with the measured values. In the calculation, the gauge of the eigenstates has been chosen such that the cell-periodic Bloch functions are differentiable along  $q_x$ , as described in [72,73]. To simulate the transport along the  $C_3$  path, a different gauge has to be used, enabling also the differentiation along  $q_y$ .

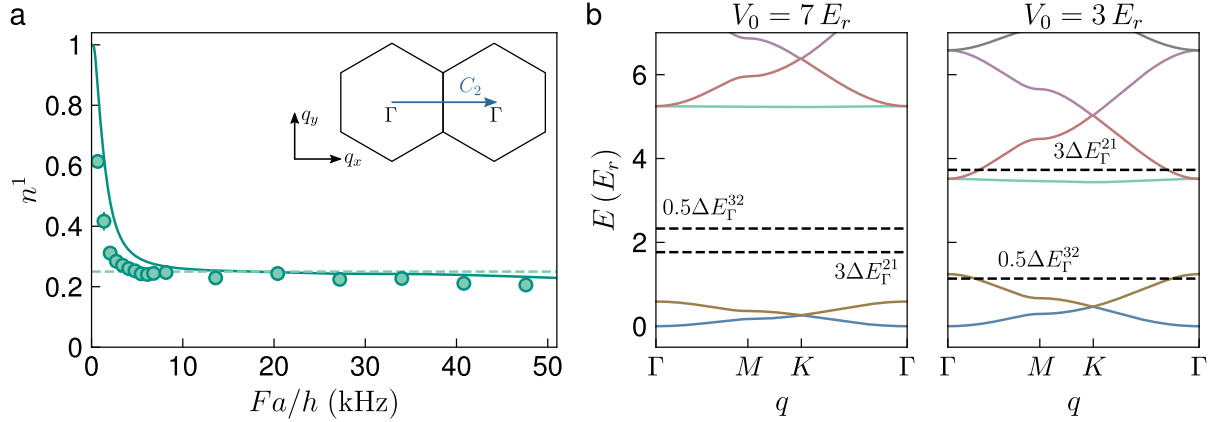


**Figure 8.3: Test of the strong gradient regime and band dispersions for different lattice depths.** **a.** Relative population in the lowest band as a function of the applied force when transporting along  $C_2$  for  $V_0 = 7 E_r$ . In the ideal case of two flat, degenerate bands the population would be  $n^1 = 0.25$ , as indicated by the dashed line. The solid line depicts a full band calculation including the first six bands in the dynamics and capturing the slight decrease of  $n^1$  below 0.25 at large forces. Each data point is an average over three individual images, the errorbars denote the standard error. **b.** Energy bands in the symmetric lattice along the high-symmetry line  $\Gamma$ - $M$ - $K$ - $\Gamma$  for  $V_0 = 7 E_r$  and  $V_0 = 3 E_r$ . The dashed, black lines mark the energies corresponding to the forces  $Fa$  in the different settings probed in the experiments. While the strong gradient regime can be reached for  $V_0 = 7 E_r$  in both cases, at  $V_0 = 3 E_r$ , excitations to the  $p$ -bands will occur for  $Fa = 3\Delta E_{\Gamma}^{21}$ , while  $Fa = 0.5\Delta E_{\Gamma}^{32}$  lies within the energy range of the  $s$ -bands, complicating the realization of strong gradient dynamics.

The saturation of the population with increasing force indicates that the underlying dynamics are different from Landau-Zener dynamics, describing the tunneling of atoms between bands at points in quasimomentum space where the bands are close [234]. For forces in the range of  $Fa/h \in [10, 40]$  kHz, the transport in a lattice with  $V_0 = 7 E_r$  well approximates the strong gradient regime.

### 8.2.3 Investigating the symmetry protection

The eigenvalue phases  $\xi$  of the Wilson lines along the  $C_2$  and  $C_3$  path are determined by combining the population and oscillation measurements described in Sec. 8.2.1 to obtain  $W^{11}$ , and applying Eq. 8.17. As mentioned above, a lattice depth of  $V_0 = 6 E_r$  still corresponds to the atomic limit of the two  $s$ -bands. To observe the symmetry protection of the  $C_3$  eigenvalue phase, the lattice depth is reduced, in order to increase the  $sp$ -coupling and move away from the atomic limit. The breaking of threefold rotational symmetry is achieved by increasing the relative intensity of one lattice beam by a factor of 1.44 compared to the other two. The depth  $V_0$  in the imbalanced lattice is defined as  $V_0 = V_{2,3}$  and accordingly  $V_1 = 1.44V_0$ . In the deep lattice, the eigenvalue phases for both

paths are always expected to be quantized to  $\pi/3$ , regardless of the lattice symmetry. The value of the phase should persist for the  $C_3$  path in the symmetric lattice also at lower depths, but deviate when breaking threefold rotation.

To estimate the size of the  $sp$ -hybridization in the different lattice settings, the eight-band tight-binding model introduced in Sec. 3.3.2 is fitted to the first eight bands obtained from the full band calculation for each lattice depth in the symmetric and imbalanced lattice. As pointed out in Sec. 3.3.2, the  $f$ -bands are not captured completely, but the  $p$ -bands can be described reasonably well, even for the smallest depth of  $V_0 = 3 E_r$ . The resulting  $sp$ -NN tunneling amplitudes decrease with the lattice depth, similar as the other hopping parameters. For  $V_0 = 7 E_r$ ,  $J^{sp}/J^s \approx 0.03$ , which increases for lower lattice depths to  $J^{sp}/J^s \approx 0.32$  at  $V_0 = 3 E_r$ . In the imbalanced lattice, the hoppings along  $\delta_1$  are enhanced compared to the other two directions. The absolute values of  $J_1^{sp}$  and  $J_{2,3}^{sp}$  do not change with the lattice depth any more, but  $J^s$  still decreases, leading to an increase of the relative  $sp$ -coupling from  $J_1^{sp}/J_1^s \approx 0.35$ ,  $J_{2,3}^{sp}/J_{2,3}^s \approx 0.25$  for  $3 E_r$  to  $J_1^{sp}/J_1^s \approx 0.42$  and  $J_{2,3}^{sp}/J_{2,3}^s \approx 0.99$  at  $7 E_r$ . The calculated deviation of  $\xi$  from  $\pi/3$  as a function of the relative  $sp$ -coupling can be found in [229]. It remains rather small - even for a very large band hybridization of  $J^{sp}/J^s = 10$ , the eigenvalue phase is expected to be reduced by only 1%. Thus, for the values of the  $sp$ -coupling presented above, the expected change of the eigenvalue phase due to the symmetry breaking is even smaller than that. The corrections arising from the presence of higher bands and the finite  $s$ -band dispersion are much larger, as shown below.

To probe the influence of the  $s$ -band dispersion and the coupling to  $p$ -bands, two different settings of forces are used to measure the eigenvalue phases. In the first set of experiments, the force per lattice site is set to  $Fa = 3\Delta E_{\max}^{21} = 3\Delta E_{\Gamma}^{21}$  for all lattice depths, keeping the effect of the  $s$ -band dispersion constant. Since the combined  $s$ -bandwidth decreases with the lattice depth, the force is reduced, and adapted accordingly in the imbalanced lattice, which exhibits modified energy dispersions. The measured eigenvalue phases along both paths are shown in Fig. 8.4a. In this setting, the coupling to higher bands varies with the lattice depth. At high lattice depths  $V_0 \geq 6 E_r$ , the measured eigenvalue phase in the symmetric lattice is close to the expected value of  $\pi/3$ .

Away from the atomic limit, the eigenvalue phase of the  $C_2$  path is not expected to be quantized any more, but for the  $C_3$  path this should be the case. Lowering the lattice depth leads to similar deviations along both paths, which thus most probably arise from excitations to higher bands due to the decreasing gap between the  $s$ - and  $p$ -bands. The energy bands of the symmetric lattice for  $V_0 = 7 E_r$  and  $V_0 = 3 E_r$  are shown in Fig. 8.3b along the high-symmetry line  $\Gamma$ - $M$ - $K$ - $\Gamma$ . The values of  $Fa$  in units of  $E_r$  are indicated by the dashed, black lines for both force settings. From this plot it becomes clear that there must be excitations to the  $p$ -bands for  $V_0 = 3 E_r$ , as the line corresponding to  $Fa = 3\Delta E_{\Gamma}^{21}$  lies within the 3rd and 4th band. In the imbalanced lattice, the eigenvalue phases are increased to  $\xi \sim 1.3 \pi/3$  even for high lattice depths. Considering the different parts that amount to the determination of  $\xi$ , the largest effect can be seen in the measured populations  $|W^{11}|^2$ , which lie slightly below 0.25 in the deep, symmetric lattice, but are reduced to  $|W^{11}|^2 \sim 0.05$  in the imbalanced lattice due to the strongly modified band

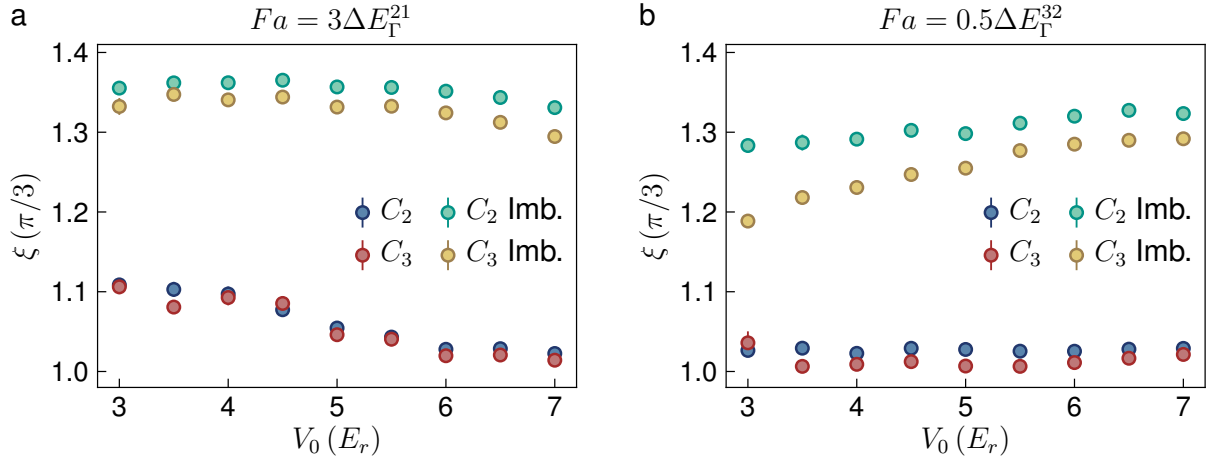


**Figure 8.4: Eigenvalue phases of the Wilson lines along  $C_2$  and  $C_3$  as a function of the lattice depth.** The eigenvalue phase  $\xi$  is measured for increasing lattice depths, simulating the absence or presence of the atomic limit. The values are compared for the  $C_2$  and  $C_3$  path in the symmetric and imbalanced lattice with  $V_1/V_{2,3} = 1.44$  and  $V_0 = V_{2,3}$ . **a.** By setting  $Fa = 3\Delta E_{\Gamma}^{21}$ , the influence of the finite  $s$ -band dispersion is held constant at all lattice depths, effectively probing the effect of excitations to higher bands, which increase for small  $V_0$ . The phases in the imbalanced lattice strongly deviate from  $\pi/3$  due to the modified band dispersion. **b.** Eigenvalue phases for  $Fa = 0.5\Delta E_{\Gamma}^{32}$ , corresponding to a similar excitation probability for all lattice depths to investigate the influence of the  $s$ -band dispersion. The data points in **a** and **b** are determined from  $|W^{11}|$  and  $\text{Arg}[W^{11}]$  which are obtained by averaging the results from 3 or 5 individual images, respectively. The errorbars are derived from error propagation of the corresponding standard deviations.

dispersion, leading to larger values of  $\xi$ . The influence of the band dispersion is constant for the different lattice depths, resulting in similar phases, which are slightly changed from the different coupling to higher bands.

In the second setting,  $Fa = 0.5\Delta E_{\min}^{32} = 0.5\Delta E_{\Gamma}^{32}$ , which corresponds to a similar probability of band excitations for all lattice depths while probing the influence of the  $s$ -band dispersion. Since the gap to the  $p$ -bands increases with the lattice depth, the force now becomes larger with  $V_0$  and is modified accordingly in the imbalanced case. In Fig. 8.4b, the measured eigenvalue phases are presented. In the symmetric lattice,  $\xi$  remains close to  $\pi/3$  for both paths, although  $Fa = 0.5\Delta E_{\Gamma}^{32}$  corresponds to an energy lying already within the upper  $s$ -band for  $V_0 = 3 E_r$  (see Fig. 8.3b). The values along  $C_2$  deviate slightly more than for  $C_3$ , especially at low lattice depths, except for the  $C_3$  data point at  $3 E_r$ . This could be an indication for the general change of  $\xi_{C_2}$  away from the atomic limit. Comparing the results for the symmetric lattice with Fig. 8.4a shows that the excitations to  $p$ -bands seem to play a larger role than the finite  $s$ -band dispersion, when lowering the lattice depth. The eigenvalue phases in the imbalanced lattice are again increased due to the modified dispersion and vary with the lattice depth.

The larger influence of the band dispersion at low lattice depths interestingly leads to smaller eigenvalue phases, which could however also arise from changes in  $\text{Arg}[W^{11}]$  due to excitations.

In general, the deviations of the eigenvalue phase from  $\pi/3$  due to the finite  $s$ -band dispersion and excitations to higher bands are much larger than a possible change of  $\xi_{C_3}$  when breaking threefold rotational symmetry. Especially in the imbalanced lattice, realizing the symmetry broken case, the value of  $\xi$  strongly increases due to the modified band dispersion, complicating a meaningful comparison to the symmetric lattice. Thus, in the experimental setting presented here, the symmetry protection of the Wilson line eigenvalue phase could not be investigated. Increasing the  $sp$ -hybridization by lowering the lattice depth leads to an enhanced influence of the  $s$ -band dispersion and excitations.

Higher  $sp$ -coupling can also be obtained in the imbalanced lattice, and since  $J^{sp}$  remains mostly constant, the ratio  $J^{sp}/J^s$  is increased in a deeper lattice, which facilitates the realization of strong gradient dynamics. While this approach is not suitable for probing the protection of  $\xi_{C_3}$  by threefold rotational symmetry, since it is already broken, the eigenvalue phases could be studied for the  $C_2$  and  $C_3$  paths being oriented along different directions, which exhibit different values of  $J^{sp}/J^s$ . Another possibility to increase the  $sp$ -hybridization could be the use of an additional Raman laser [229, 235].

As mentioned in Sec. 8.1.3, the symmetry protection of the Wilson line eigenvalue phase can also occur in bands with a non-zero Chern number. Creating an effective Haldane model by periodic intensity modulation, incorporating increased  $sp$ -coupling within the driving period, could also result in an enhanced band hybridization between the Floquet  $s$ - and  $p$ -bands. This would need to be checked by first identifying the 3rd to 6th Floquet band similar as the two lowest bands (see Sec. 3.2.2) and then fitting at least a six-band tight-binding model to the effective band structure. The measurement schemes for  $|W^{11}|$  and  $\text{Arg}[W^{11}]$  presented here could be applied in principle also to the Floquet bands, if the modulation frequency is large enough to ensure that the time-interval during which the force is applied amounts to at least one period of the driving.

# Chapter 9

## Parametric instabilities in a shaken 1D optical lattice

Topological band structures can be created by time-periodic modulation of two-dimensional (2D) optical lattice potentials, as presented in the previous chapters. In view of combining periodically driven systems with interactions, which is expected to result in an infinite temperature state in the thermodynamic limit [45, 236], a better understanding of the heating effects in interacting systems is desirable. A periodically driven one-dimensional (1D) optical lattice, although not resulting in topological Floquet bands itself, can serve as a more simple starting point to gain insight into the physical processes that dominate the interplay between interactions and lattice modulation.

In this chapter, a weakly interacting Bose-Einstein condensate (BEC) in a phase modulated 1D lattice is studied at short timescales, where the behavior is expected to be dominated by coherent excitations which can be described in terms of parametric instabilities. The physical processes leading to these excitations are investigated in the first section. Moreover, the influence of the harmonic trapping potential is discussed, which eventually prevents the existence of a stable parameter regime. The occurrence of parametric instabilities can be measured by observing the dynamics of the excited atoms in momentum space, as presented in the second section. A more detailed description of the experiments and parametric instabilities in shaken 1D optical lattices can be found in [75, 76].

### 9.1 Heating effects in 1D shaken lattices

Due to the periodic quasienergies, a periodically driven system can exchange energy quanta  $\hbar\omega$  with the drive, leading to heating effects as mentioned above. In the absence of interactions, particles can be excited to higher bands when the driving frequency matches the corresponding energy gap of the static lattice [237], constituting the major loss channel in this case. These resonances can usually be avoided by carefully choosing the shaking frequency. In contrast, the presence of interactions leads to scattering processes, which are always resonant in low dimensional lattice systems, as the lattice degrees of freedom

are coupled to the transverse directions.

Moreover, if the shaking frequency is larger than the energy gap to the next higher band, a variety of different processes can arise [74], in which scattering of two particles is combined with excitations. For shaking frequencies being smaller than the gap, mainly two-particle scattering within the lowest band occurs. These incoherent processes dominate the behavior of the system at long timescales and are well captured by a Floquet Fermi's golden rule (FFGR) [74, 238–240]. In contrast, the dynamics of a periodically driven 1D lattice at short timescales can be described by coherent processes, as discussed below.

### 9.1.1 Parametric instabilities

The energy of weakly interacting bosons in a periodically driven 1D lattice is given by the effective Bogoliubov-dispersion [241]:

$$E_{\text{eff}}(q) = \sqrt{4|J_{\text{eff}}| \sin^2\left(\frac{a}{2}q\right) \left(4|J_{\text{eff}}| \sin^2\left(\frac{a}{2}q\right) + 2g\right)}, \quad (9.1)$$

where the hopping  $J$  in the static lattice is renormalized by the drive to  $J_{\text{eff}} = J\mathcal{J}_0(\alpha)$ , similar as in the shaken honeycomb lattice, and  $\alpha$  ( $\equiv \kappa$ , see Eq. 6.16) denotes the dimensionless driving strength being proportional to the shaking amplitude. The interactions are described by  $g = nU$  with the Hubbard interaction parameter  $U$  and the particle density  $n$  [76], thus being different from the dimensionless interactions strength defined in Eq. 7.8. If the energy of the drive, quantized in multiples of  $\hbar\omega$ , matches the energy  $2E_{\text{eff}}$  of a collective excitation, parametric instabilities occur. Two atoms being initially at  $q = 0$  are excited to  $E_{\text{eff}}(q_{\text{res}})$  corresponding to a change of their quasimomentum by  $\pm q_{\text{res}}$ , conserving the total momentum, which is illustrated in Fig. 9.1a. These instabilities can only arise for even multiples of  $\hbar\omega$  [241], and thus the resonance condition is to lowest order given by  $2\hbar\omega = 2E_{\text{eff}}(q_{\text{res}})$ .

In a true 1D system without a harmonic trap, the occurrence of instabilities could be prevented for  $\hbar\omega > \hbar\omega_{\text{sat}} \approx W_{\text{eff}}$ , where  $W_{\text{eff}} = E_{\text{eff}}(\pi/a)$  denotes the effective Bogoliubov bandwidth. In this case, the energy cannot be transformed into an excitation and the system would be stable, provided that  $\hbar\omega$  is still smaller than the energy gap to the next higher band. However, in many optical lattice experiments, the system is three-dimensional (3D) and consists of a low-dimensional lattice combined with a harmonic trapping potential along all directions, which couples the lattice with the perpendicular degrees of freedom. In this case, the resonance condition needs to be defined with respect to the 3D quasimomentum:

$$\hbar\omega = E_{\text{eff}}(\mathbf{q}_{\text{res}}) \quad \mathbf{q}_{\text{res}} = (q_{\text{res}}^x, \mathbf{q}_{\text{res}}^\perp), \quad (9.2)$$

describing a 1D lattice of 'pancakes' directed along the  $x$ -axis, as used in the experiments described below. Thus, in the coupled 3D system, for  $\hbar\omega > \hbar\omega_{\text{sat}}$  the excess energy can always be dumped into the transverse directions and there is no stable parameter regime any more.

### 9.1.2 Most unstable mode

The parametric resonance has a finite width, resulting in several collective excitations with different quasimomenta  $\mathbf{q}$  lying around  $\mathbf{q}_{\text{res}}$  defined in Eq. 9.2. Each of these modes grows exponentially in time with a certain rate  $\Gamma_{\mathbf{q}}$ . The overall behavior of the system is dominated by the mode exhibiting the largest growth rate  $\Gamma_{\text{mum}} = \max_{\mathbf{q}} \Gamma_{\mathbf{q}}$ , which is accordingly called the most unstable mode (mum) and associated with the quasimomentum  $\mathbf{q}_{\text{mum}}$ . Using the time-dependent Bogoliubov–de Gennes (BdG) equations of motion, approximate analytical expressions can be derived for the momentum and growth rate of the most unstable mode [241, 242], showing a clear separation between the lattice and transverse degrees of freedom: If  $\hbar\omega < \hbar\omega_{\text{sat}}$  (regime I), the energy of the drive is mainly transformed into excitations along the lattice direction and  $\mathbf{q}_{\text{mum}}$  is directly defined by the Bogoliubov dispersion:

$$q_{\text{mum}}^x(\omega, \alpha) = \frac{2}{a} \arcsin \left( \sqrt{\left( \sqrt{g^2 + (\hbar\omega)^2} - g \right) \frac{1}{4|J_{\text{eff}}|(\alpha)}} \right),$$

$$|\mathbf{q}_{\text{mum}}^\perp| = 0, \quad \omega < \omega_{\text{sat}}. \quad (9.3)$$

In the second regime  $\hbar\omega > \hbar\omega_{\text{sat}}$ , the quasimomentum of the excitations along the lattice direction saturates at  $\pi/a$  and the remaining energy is distributed into the perpendicular directions, leading to a growth of the transverse quasimomentum according to

$$q_{\text{mum}}^x = \frac{\pi}{a},$$

$$\frac{\hbar^2(\mathbf{q}_{\text{mum}}^\perp(\omega, \alpha))^2}{2m} = \sqrt{g^2 + (\hbar\omega)^2} - g - 4|J_{\text{eff}}|(\alpha), \quad \omega > \omega_{\text{sat}}, \quad (9.4)$$

as depicted in Fig. 9.1b. The momentum of the most unstable mode is determined experimentally as a function of the shaking frequency  $\omega$  for two different values of  $\alpha$ , which can directly be compared with Eq. 9.3, as described in the next section.

The presence of the harmonic trap along the transverse directions leads to the coupling between the lattice and the perpendicular degrees of freedom, enabling the transfer of energy from the periodic drive into a growth of  $\mathbf{q}_{\text{mum}}^\perp$ . In the experiments, the potential of the  $X$ - $Y$ -trap is also present along the lattice direction  $x$ . Using numerical simulations, it has been shown [76] that even in a true 1D system, a trapping potential along the lattice direction prevents the existence of a stable parameter regime. The spectrum in the combined potential hosts states with continuous energies above the Bogoliubov dispersion of the lowest band, which can be resonantly excited by the drive, thus leading to instabilities. To reduce the amount of excitations, a 3D lattice configuration would be desirable, limiting the number of available states along the transverse directions. Another possibility could be the engineering of box-potentials [243, 244] to replace the weak harmonic confinement.

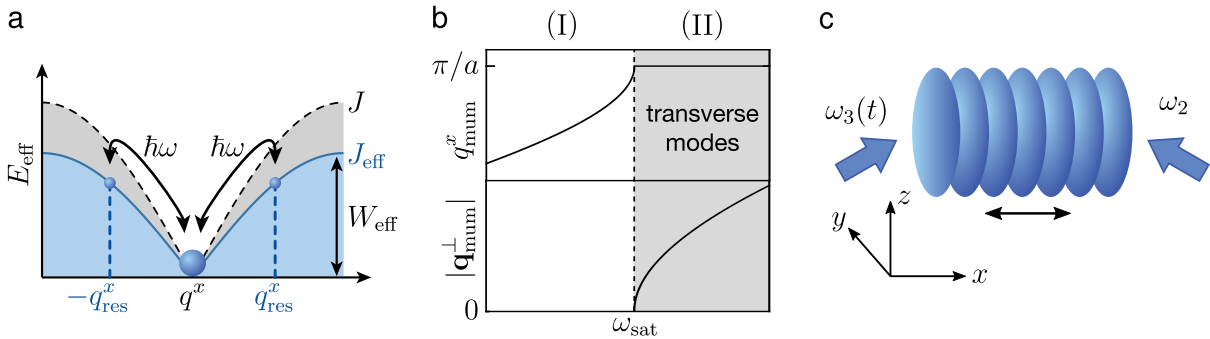


**Figure 9.1: Sketch of parametric excitations and creation of the 1D lattice.**

**a.** Parametric instabilities occur in a periodically driven 1D lattice when two atoms are excited to quasimomenta  $\pm q_{\text{res}}^x$  by absorbing  $2\hbar\omega$  from the drive. The bandwidth  $W_{\text{eff}}$  of the dispersion is reduced compared to the static lattice, since the hopping  $J$  is renormalized to  $J_{\text{eff}} = J\mathcal{J}_0(\alpha)$ .

**b.** Momentum of the most unstable mode along the lattice direction  $x$  and along the perpendicular directions as a function of the driving frequency. If  $\omega < \omega_{\text{sat}}$ , excitations in the lattice direction occur, whereas the energy is completely dumped into the transverse modes for  $\omega > \omega_{\text{sat}}$ .

**c.** Creation of the 1D lattice by interference of two laser beams. The frequency of one beam is changed periodically in time, resulting in the potential moving back and forth.

## 9.2 Measurement of parametric instabilities

The occurrence of parametric instabilities is detected by recording the momentum distribution of the BEC after holding it in the modulated 1D lattice and subsequently performing bandmapping. Since the atoms which are excited by the drive do not leave the harmonic trap, they appear in the absorption images, having a different quasimomentum than the main peak representing the BEC. The maximum of these satellite peaks corresponds to the most unstable mode and  $\mathbf{q}_{\text{num}}$  can be directly determined from the time-of-flight (TOF) images for different shaking parameters and compared to the theoretical predictions.

### 9.2.1 Modulated lattice potential

The 1D optical lattice potential is created by switching off one laser beam in the honeycomb setup described in Sec. 3.1, resulting in the interference of two beams at angles of  $120^\circ$ . Using the beams  $\mathbf{E}_2$  and  $\mathbf{E}_3$  propagating along  $\mathbf{k}_2$  and  $\mathbf{k}_3$  (see Fig. 3.1), the resulting 1D lattice is directed along  $x$ :

$$V_{1\text{D}}(x) = V_0 \cos^2 \left( \frac{\sqrt{3}}{2} k_L x \right). \quad (9.5)$$

The wavelength of the light is  $\lambda_L = 736.8 \text{ nm}$ , which corresponds to a lattice spacing of  $a = \lambda_L/\sqrt{3} = 425 \text{ nm}$ . Due to the modified geometry, higher lattice depths can

be reached in the 1D potential, when using the same laser power as in the honeycomb lattice. The experiments presented in this chapter are performed at a lattice depth of  $V_0 = 11 E_r$ , again using a BEC of  $^{39}\text{K}$ . The harmonic trap is present in all measurements, being set to similar values as in the experiments described previously, resulting in a 1D lattice of disks elongated along the perpendicular directions (see Fig. 9.1c). The measured trapping frequencies in the combined potential are  $f_T = 26(2)$  Hz in the  $x$ - $y$ -plane and  $f_z = 204(3)$  Hz along the vertical direction [75].

The 1D lattice is characterized by turning the lattice on for a variable time and recording the diffraction peaks. When switching on the lattice suddenly, the ground state  $|q_0\rangle$  of the BEC in the harmonic trap is projected onto the Bloch states  $|\psi_{q_0}^n\rangle$  with the same quasimomentum. Due to parity conservation, only states with the same parity as the ground state appear in the superposition. If the lattice is shallow, only the lowest and third band are populated and the state after the projection is given by

$$|\psi(t)\rangle = \langle\psi_{q_0}^1|q_0\rangle e^{-\frac{i}{\hbar}E_1(q_0)t} |\psi_{q_0}^1\rangle + \langle\psi_{q_0}^3|q_0\rangle e^{-\frac{i}{\hbar}E_3(q_0)t} |\psi_{q_0}^3\rangle. \quad (9.6)$$

After holding the atoms in the lattice for a certain time, the lattice and the trap are switched off suddenly and the state is projected back to the free space dispersion, resulting in different momenta of 0 or  $\pm 2\pi/a$ , depending on the band the atoms have populated before. These components appear as peaks located at the center of the first and second Brillouin zone (BZ) when taking absorption images after TOF. If the hold time is varied, the population oscillates between the two bands and hence between the peaks, with a frequency corresponding to the band gap at  $q_0 = 0$ :

$$f_{\Delta E}(q_0) = (E_3(q_0) - E_1(q_0))/\hbar. \quad (9.7)$$

Counting the relative population in the lowest band and fitting a cosine function to the oscillation allows for the extraction of the energy gap, which can be compared to band structure calculations to obtain the lattice depth.

The shaking of the lattice is realized by changing the frequency of one laser beam periodically in time with frequency  $\omega$  and amplitude  $b$ :

$$\begin{aligned} \omega_2 &= \omega_L \\ \omega_3(t) &= \omega_L + b \sin(\omega t), \quad \alpha = \frac{ma^2b}{\hbar}. \end{aligned} \quad (9.8)$$

Since the driving amplitudes  $\nu = b/(2\pi)$  are usually in the range of several kHz, the time-dependence of the wavevectors can be neglected. The resulting interference pattern is moving back and forth in real space. To study parametric instabilities, the shaking frequency lies in the range of  $f = \omega/(2\pi) \in [0.5, 1]$  kHz, being much smaller than the energy gap to the second band of  $\Delta E/\hbar = 41.6(5)$  kHz.

### 9.2.2 Determination of the most unstable mode

The momentum of the most unstable mode along the lattice and transverse directions is determined as a function of the shaking frequency for different shaking amplitudes. The

coherent processes underlying the parametric instabilities described above can only be observed at short time scales, before they are overlain by incoherent scattering processes. This defines a short time regime  $t \lesssim t_s$ , in which the coherent processes dominate the behavior. In the following, the determination of  $t_s$  and the extraction of  $\mathbf{q}_{\text{mum}}$  from TOF images in this time range is described.

**Analysis of the absorption images** The momentum and growth rate of the most unstable mode are measured by holding the atoms in the modulated lattice for a variable time being an integer multiple of the driving period,  $t = NT, N \in \mathbb{N}$ , and observing the excitation peaks in momentum space. The atoms are loaded into the lowest band of the 1D lattice with the scattering length set to  $a_s = 20 a_0$ , resembling the weakly interacting regime which is expected to be described by Bogoliubov theory. Since the coherent dynamics related to parametric instabilities occur at short times, the shaking is quenched on, in order to probe the system in this regime. After the hold time, the shaking amplitude is also switched off suddenly and the lattice is ramped down within  $\sim 100 \mu\text{s}$  to perform bandmapping. It has been verified experimentally, that the quench does not change the resulting momentum distribution [76]. The cloud expands for  $t_{\text{TOF}} = 6 \text{ ms}$  and subsequently the momentum distribution is recorded by taking absorption images in the  $x$ - $y$ -plane. These consist of a large peak in the center of the first BZ resembling the BEC and a pair of small satellite peaks at larger quasimomenta located within the first BZ, which correspond to atoms being excited by the drive. The axes of the images can be transformed into quasimomentum by measuring the diffraction peaks when switching off the lattice suddenly, which are known to have a relative distance of  $2\pi/a$ .

The most unstable mode corresponds to the maximum of the excitation peaks. These are quantified by first subtracting an image at  $t = 0$ , containing only the BEC, from each image at  $t > 0$ , which results in a 2D difference image showing only the excitation peaks, as depicted in Fig. 9.2. To account for shot-to-shot fluctuations of the peak positions on the camera, all images are shifted such that the BEC is located at  $(0, 0)$  before subtracting them. The position of the excitation peaks along the lattice direction is determined by integrating the image along the perpendicular axis to obtain a 1D profile, which is fitted by two Lorentzian functions separately for  $q_x > 0$  and  $q_x < 0$  (black lines in Fig. 9.2). The center region of the image is excluded, which contains negative pixels arising due to the depletion of the BEC. The amplitude  $A^x$  and center position  $q_{\text{max}}^x$  of both peaks are extracted from the fit. For each hold time  $t > 0$ , the fitted amplitudes and positions from 10 individual images are averaged, with 5 images being taken with a driving phase of  $\phi = 0$  and 5 with  $\phi = \pi$  to minimize systematic deviations.

Along the transverse direction, the excitations result in a broadening of the peaks, due to the extent of the BEC in momentum space and the width of the parametric resonance. Thus,  $q_{\text{mum}}^y$  can not be measured directly, but its growth is indicated by the increasing transverse width of the satellite peaks in time. To determine the transverse peak width, the difference images are integrated along the lattice direction, now within two separate regions-of-interest containing only the excitation peaks. The resulting 1D profiles are again fitted with a Lorentzian and the full width at half maximum (FWHM)  $\Delta q^y$  is

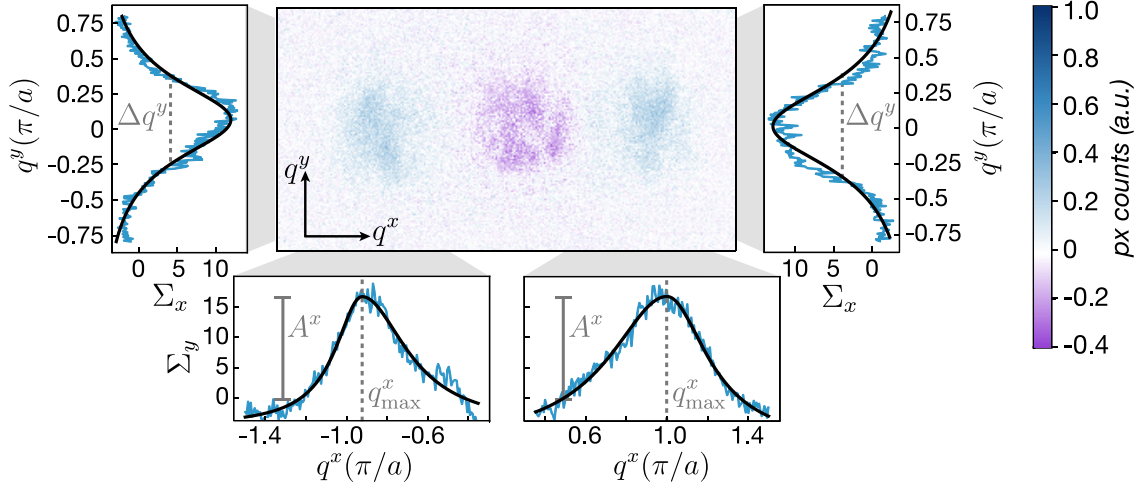


**Figure 9.2: Difference image with integrated profiles.** Absorption image at  $t = 14T$  for  $\alpha = 1.78$  and  $f = 0.72$  kHz from which the image at  $t = 0$  has been subtracted, resulting in negative pixel values in the center due to the depletion of the BEC. The satellite peaks correspond to atoms being excited by the drive. Their position  $q_x^{\max}$  and amplitude  $A^x$  along the lattice direction  $q_x$  are extracted by fitting asymmetric Lorentzian functions to the pixel sum  $\Sigma_y$  integrated along  $y$ , accounting for the thermal background which increases the peak height towards the center. Along the perpendicular direction, the FWHM  $\Delta q^y$  of the peak is extracted from a symmetric Lorentzian fit to the integrated profiles  $\Sigma_x$ . The blue curves depict the profiles and the black lines the fitted functions.

extracted for each peak and averaged over the 10 images for every hold time  $t > 0$ . A more detailed description of the data analysis can be found in the supplementary material of [76].

**Extraction of the momentum and growth rates** In Fig. 9.3a, the logarithm of the amplitude  $A^x$  of the left and right excitation peak is plotted as a function of the hold time for  $\alpha = 1.78$  and  $f = 0.72$  kHz. At short times  $t \lesssim t_s$ , the amplitude grows exponentially, as expected from the analytical description based on the BdG equations. At long times, the growth slows down, resulting in a nearly constant curve for  $\ln(A^x)$  due to interactions between the excited atoms and the condensate, that are described by incoherent processes. Thus, the purely coherent excitations only occur in a small time window. The end  $t_s$  of this short time regime is defined by the onset of the backscattering and determined by fitting a 'kink' function to  $\ln(A^x)$ , consisting of a linear and a constant part (solid lines in Fig. 9.3a). The time  $t_s$  is derived as the mean over the fit results from the left and right peak. The momentum of the most unstable mode is obtained by averaging the positions  $q_{\max}^x(t)$  for the left and right peak over all times  $t \leq t_s$ , with  $t_s$  being determined for each set of shaking parameters separately. Within the short time regime, the peak maximum position stays mainly constant but then starts to decrease for long times (see Fig. 9.3b), which also signals the onset of incoherent scattering, changing

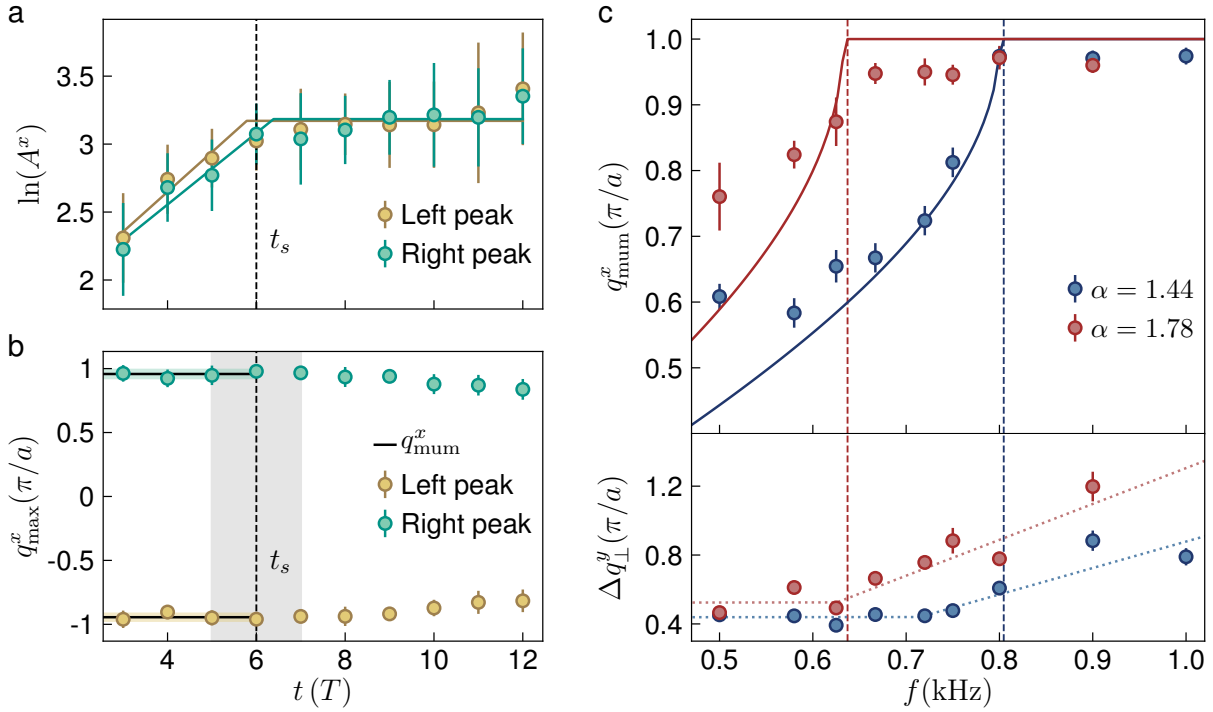


**Figure 9.3: Peak parameters, momentum of the most unstable mode and transverse width.** **a.** Logarithm of the fitted peak amplitudes  $A^x$  as a function of the hold time for  $\alpha = 1.78$  and  $f = 0.72$  kHz. The solid lines depict the fitted kink functions to determine the end  $t_s$  of the short time regime. **b.** Momentum  $q_{\max}^x$  of the peak maximum as a function of the hold time for the same shaking parameters. The points for  $t \leq t_s$  are averaged to obtain  $q_{\text{mum}}^x$  (black solid line), being the mean over the results for the left and right peak. The yellow and green shaded bars illustrate its standard error of the weighted mean. The grey shaded area depicts the time range over which the transverse widths are averaged, yielding  $\Delta q_{\perp}^y$ . Each data point in **a** and **b** corresponds to the average over 10 individual images, the errorbars denote the standard deviation. **c.** Momentum of the most unstable mode and transverse width as a function of the shaking frequency for  $\alpha = 1.44$  and  $\alpha = 1.78$ , the errorbars denote the standard error of the mean. The dark blue and red solid lines depict Eq. 9.3 for  $g = 11.5$   $J$  and the vertical dashed lines mark the corresponding saturation frequency. The dotted lines serve as a guide to the eye.

the quasimomentum of the excited atoms. The transverse peak width is evaluated at the end of the short time regime, where the amount of excitations is expected to be maximal, by averaging  $\Delta q^y$  over  $t \in [t_s - T, t_s + T]$  which defines  $\Delta q_{\perp}^y$ , representing the transverse momentum component of the most unstable mode.

The momentum of the most unstable mode  $q_{\text{mum}}^x$  and the transverse width  $\Delta q_{\perp}^y$  are measured as a function of the shaking frequency, spanning the range below and above  $\omega_{\text{sat}}$  to verify the behavior predicted in Eq. 9.3. The resulting values are plotted in Fig. 9.3c for shaking amplitudes of  $\nu = 13$  kHz (blue data points) and  $\nu = 16$  kHz (red data points),

corresponding to  $\alpha = 1.44$  and  $\alpha = 1.78$ . For increasing modulation frequencies,  $q_{\text{mum}}^x$  grows until it saturates at  $q \approx \pi/a$ , approximately following the theoretical prediction from Eq. 9.3 for  $g = 11.5 J$  (solid lines) [76]. As expected, the saturation frequency shifts to smaller values when increasing  $\alpha$ , since the effective bandwidth decreases with the shaking amplitude due to the renormalization of the tunneling.

The slight deviation of the final quasimomentum from  $\pi/a$  arises due to the finite TOF used in the experiments, as described in [76]. For small frequencies, the deviation between the experimental and theoretical values increases, especially for  $\alpha = 1.78$ . Since the incoherent scattering processes are enhanced for smaller shaking frequencies and larger amplitudes [74], the time window  $t \lesssim t_s$ , in which the coherent excitations can be observed, becomes shorter, complicating the observation of the most unstable mode, as it might not yet fully dominate over the other modes. Moreover, due to the finite width of the BEC in momentum space, the satellite peaks can only be reliably detected if they are centered at  $q_{\text{max}}^x \gtrsim 0.4\pi/a$ , which sets a lower bound for the shaking frequencies that can be probed. The transverse width  $\Delta q_\perp^y$  remains constant for frequencies below the saturation frequency and then increases for  $\omega > \omega_{\text{sat}}$ , signaling the transfer of energy into the perpendicular directions.

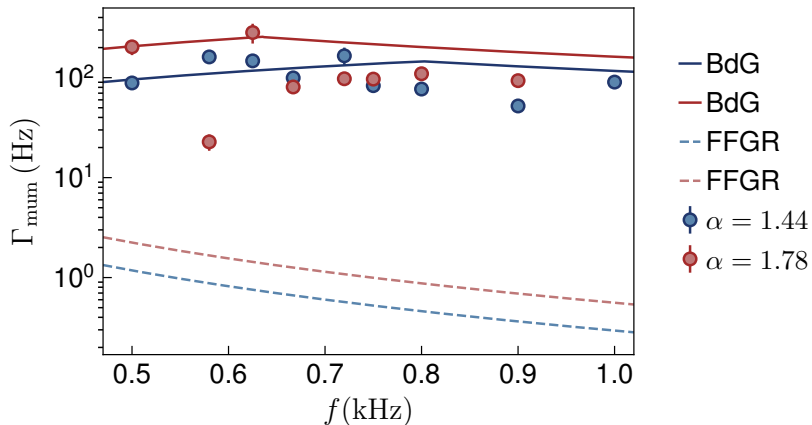


Figure 9.4: **Measured instability rates.** Growth rates  $\Gamma_{\text{mum}}$  of the most unstable mode for  $\alpha = 1.44$  and  $\alpha = 1.78$  as a function of the shaking frequency (data points), obtained from linear fits to the logarithmic peak amplitudes for  $t \leq t_s$ , errorbars denote the standard deviation. The solid lines depict the theoretical rates calculated with BdG theory for  $g = 11.5 J$ , approximately coinciding with the experimental data. The rates derived using an FFGR approach for the same modulation parameters (dashed lines), describing incoherent scattering processes which dominate on long time scales, are about two orders of magnitude smaller.

According to BdG theory, the peak amplitudes along the lattice direction are expected to grow exponentially in time:

$$A^x \propto e^{2\Gamma t}. \quad (9.9)$$

The instability rates  $\Gamma$  can be extracted from the slopes  $\mu$  of the kink functions fitted to  $\ln(A^x)$  for  $t \leq t_s$  as  $\Gamma = \mu/2$  and are averaged over the left and right peak. The resulting mean values corresponding to  $\Gamma_{\text{mum}}$  are plotted in Fig. 9.4 as a function of the shaking frequency for  $\alpha = 1.44$  and  $\alpha = 1.78$  (blue and red data points). Lying in the range of  $\sim 200$  Hz, the measured rates approximately coincide with the theoretical predictions from the BdG equations [241], which are depicted by the solid lines. In contrast, the rates derived from FFGR theory (dashed lines) are about two orders of magnitude smaller, validating the role played by coherent excitations at short modulation times. The growth rates have also been studied in a linearly shaken 2D square lattice [245], revealing the effects of parametric instabilities in a higher dimensional lattice.

In summary, the growth and saturation of  $q_{\text{mum}}^x$ , along with the dependence of the saturation frequency on the shaking amplitude, confirms the assumption that the observed peaks in momentum space indeed arise due to coherent excitations which can be described by parametric instabilities. The increase of the transverse peak width indicates the transfer of energy into the perpendicular directions for  $\omega > \omega_{\text{sat}}$ , which are coupled to the lattice shaking via the harmonic trap. Thus, the presence of the trap prevents the existence of a stable parameter regime, even in 1D systems, as described above. To overcome these limitations and reduce the heating in periodically driven, weakly interacting systems, the transverse degrees of freedom could be frozen by engineering 3D lattice potentials.

# Chapter 10

## Conclusions and Outlook

In this thesis, the experimental realization and characterization of different Floquet topological systems in an optical honeycomb lattice have been demonstrated. The periodic modulation of the tunneling amplitudes along the different bond directions, achieved by continuous variation of the laser intensities, gives rise to multiple topological regimes, including an anomalous Floquet phase. The winding numbers describing the different regimes have been determined by measurements of the quasienergy gaps and Berry curvature, as described in chapters 2 and 5.

Using ultracold, bosonic atoms, which only occupy a narrow range of quasimomenta, these quantities could be probed locally in reciprocal space. The small extent of the atomic cloud in quasimomentum space, stemming from finite temperatures and interactions, does not affect the measurements of the winding numbers, as these are derived from sign changes of the Berry curvature. Applying the respective forces via lattice acceleration allows for precise control over the magnitude and direction of the force, but leads to large displacements in real space along the longitudinal direction. However, as shown in chapter 4, the effect of these displacements on the transverse deflections, which are used to measure the sign of the Berry curvature, is negligible. Simultaneously ramping the laser frequencies and intensities has enabled to probe the topological properties of the first and second Floquet band in each of the regimes, utilizing the hybridization of the two lowest bands due to the lattice modulation.

Anomalous Floquet systems can also be generated by circular phase shaking of the honeycomb lattice potential, as pointed out in chapter 6. In this case, inversion symmetry needs to be broken to observe the anomalous Floquet regime, lifting a degenerate band touching point. Applying the measurement techniques introduced in chapter 4 and used in chapter 5 to the shaken lattice is however more complicated, since the quasimomentum is already periodically modified, hindering localized measurements in reciprocal space. This highlights one major advantage of the intensity modulation, namely that the periodic driving itself and the measurement of the system's properties rely on two independent degrees of freedom. Moreover, Floquet band structures with larger quasienergy gaps can be realized as compared to circular phase shaking, since the lifetimes of the Bose-Einstein condensate (BEC) remain sufficiently long even for relatively high modulation

amplitudes. This facilitates the measurement of the Berry curvature of a single band, as excitations to higher bands can be avoided.

The effective Floquet Hamiltonian of the intensity modulated lattice has been calculated numerically, employing the first six bands of the instantaneous Hamiltonian during the time-evolution, as discussed in chapter 3. The resulting quasienergy gaps and transverse deflections are in very good quantitative agreement with the experimental data (chapter 5). Hence, this model provides an accurate description of the periodically driven system in the entire parameter regime considered in this work. It has been used to derive the topological phase diagram also in the presence of a sublattice offset, which gives rise to an additional regime with a Chern number of 2. The properties of the phase shaked lattice have been calculated similarly, predicting the anomalous Floquet regime when breaking inversion symmetry and revealing a variety of other topological phases with higher Chern numbers up to 4.

In order to describe the modulated lattice in a finite or semi-finite geometry, a tight-binding model has been introduced. The coupling to higher bands, which comprises an essential part of the full six-band calculation, can be partially implemented by fitting the hopping amplitudes using an eight-band tight-binding model, while representing the Hamiltonian by a  $2 \times 2$  matrix. A satisfying description of the intensity modulated honeycomb lattice employing two tight-binding bands has been found in each of the topological regimes (see chapter 3). Based on these models, the dispersion of the chiral edge modes has been derived in a semi-finite geometry. In the future, this could be extended to a completely finite system to provide a quantitative comparison of the edge states' group velocity with the bulk dispersion in a setting which resembles the experiment as close as possible.

The geometric properties of degenerate multiband systems, captured by Wilson lines, have been outlined in chapter 8. While the eigenvalue phases of the Wilson lines have been derived experimentally, their predicted symmetry protection could not be measured directly. The changes of the eigenvalue phases arising from the presence of higher bands and the finite band dispersion have emerged as being much larger than the theoretically expected effects of symmetry breaking. In future experiments, the Wilson line eigenvalues could be probed in the topological bandstructure of the intensity modulated lattice, which might help to reveal the symmetry protection. Moreover, Bloch state tomography of the Floquet bands could be performed, as suggested in [72]. Another option could be the investigation of the static, imbalanced lattice, where the properties of the Wilson line depend on the specific direction of the path.

Periodically driven, closed, interacting quantum systems are expected to heat up to infinite temperature in the thermodynamic limit [44, 45]. To gain insight into the processes which trigger the onset of heating, a periodically shaken one-dimensional (1D) optical lattice has been investigated in chapter 9, based on the results reported in [75, 76]. As expected from the approximate analytic theory, the dynamics of the system at short times are indeed dominated by coherent excitations which can be described in terms of parametric instabilities. The crucial role played by the harmonic trapping potential perpendicular to the lattice as well as parallel to it has been revealed. While the former

leads to a coupling of the lattice shaking to the continuous, transverse degrees of freedom, the latter results in additional states along the lattice direction, preventing the existence of a stable parameter regime even in a true 1D setting. To reduce the amount of these coherent excitations, especially in the two-dimensional honeycomb lattice, the vertical lattice introduced in chapter 4 could be added, restricting the number of available states in the transverse direction.

In the anomalous Floquet regime, the bulk states can be completely localized in the presence of disorder, due to the vanishing Chern numbers of all quasienergy bands, while the edge modes remain mobile [42]. This promises a potential solution to the heating problem by realizing a many-body localized bulk coexisting with thermalizing edge states [59]. To investigate these intriguing properties of anomalous Floquet systems, an independent probe of the chiral edge modes and the bulk states is needed. In chapter 7, modifications to the current setup are described to enable the direct imaging of the edge modes, which will also be facilitated by replacing the harmonic trap in the  $x$ - $y$ -plane with a hard-wall potential. The propagation of the edge modes could be compared in the different topological regimes, including the setting with Chern number 2. The disorder could be realized by projecting a random optical potential pattern onto the atoms with a digital mirror device. Provided that a dynamic switching of the polarizations of the laser beams can be implemented, the localization of the bulk states can then be quantified by the population imbalance between A and B sites. In this regard, the differences between the anomalous Floquet and Haldane regime are of particular interest, as the latter should not allow for a complete localization, even for large disorder strengths, owing to the non-zero Chern numbers.

Another interesting phenomenon that can occur in the anomalous Floquet regime is the fermionization of interacting bosons being loaded into the nearly degenerate ring-like minimum of the first Floquet band. To be able to observe this phenomenon, a scheme has to be derived to load the BEC into this minimum. Moreover, the currently small ratio of the Hubbard interaction  $U$  to the nearest neighbor hopping  $J$  has to be increased to enter the strongly-correlated regime. As discussed in chapter 7, this can be achieved by adding the vertical lattice and by implementing a deeper honeycomb lattice. The former relies on building the planned active phase stabilization of the honeycomb lattice to enable a loading of the BEC into the three-dimensional lattice configuration. This setup will also provide the desired full control over the lattice beam polarizations mentioned before. To obtain a deeper honeycomb lattice, probably a different laser has to be used, as the currently available Ti:sapphire lasers do not provide sufficiently high power.

Further future experiments could also investigate topological band structures with a degenerate Fermi gas, the creation of which is in principle technically possible with the current setup.



# Appendix A

## Shape of the calculated Berry curvature distribution

As described in Sec. 3.2.2, the quasienergy bands obtained from the six-band calculation are symmetric, but the Berry curvature distribution exhibits a slight asymmetry arising from the projection of the Hamiltonian to its six lowest eigenstates. The shape of the distribution can be modified when adding an offset  $\Delta\phi$  to the modulation phase of all lattice beams, as illustrated in Fig. A.1a.

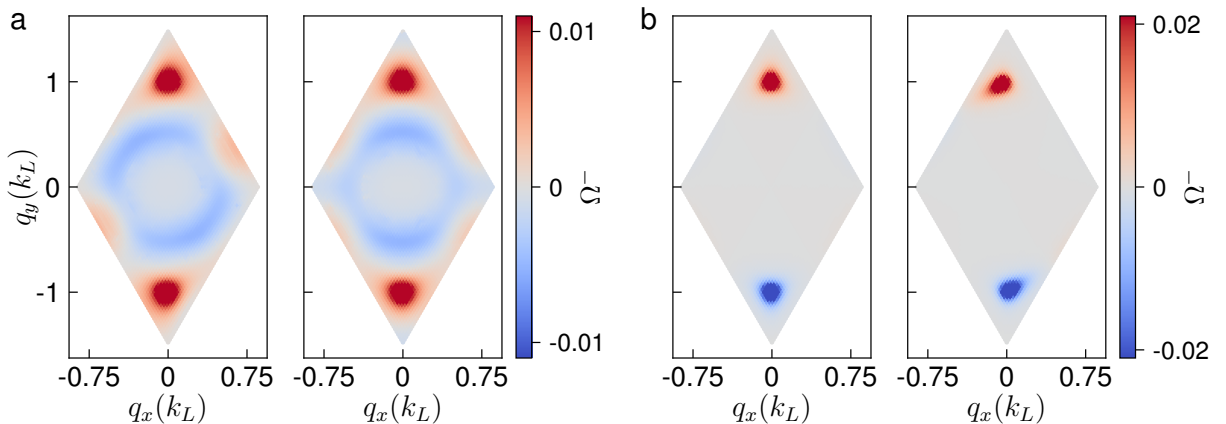


**Figure A.1: Berry curvature in the modulated and static lattice for  $V_0 = 6 E_r$ .**  
**a.** Berry curvature of the lowest band in the first Brillouin zone (BZ) for  $m = 0.2$  and  $f = 6 \text{ kHz}$  with an initial phase offset  $\Delta\phi = 0$  (left panel) and  $\Delta\phi = \pi/3$  (right panel). The asymmetry of the distribution arising from the projection of the Hamiltonian is rotated with the initial phase. **b.** Berry curvature of the lowest band in the symmetric, static lattice with  $\theta = 0.05 \text{ rad}$ , calculated from the full eigenstates (left panel) and when truncating the eigenstates to the six lowest bands (right panel). The truncation leads to a similar asymmetry as in the modulated lattice with  $\Delta\phi = 0$ .

The left panel shows the Berry curvature distribution in the anomalous phase for  $\Delta\phi = 0$ , as used in the calculations of the transverse deflections. In the right panel, the Berry curvature is plotted for  $\Delta\phi = \pi/3$ , which effectively turns the pattern by  $\sim 30^\circ$ . In the static lattice, the Berry curvature distribution is fully symmetric as visible in the left panel of Fig. A.1b, displaying the distribution for a sublattice offset with  $\theta = 0.05$  rad. In this case, the full eigenstates of the lowest band are used in the calculation, each having a length of  $(2l_{\max} + 1)^2 = 225$ . If the eigenstates are however truncated to their first six entries, the Berry curvature becomes also asymmetric (right panel) with a similar shape as in the modulated lattice for  $\Delta\phi = 0$ . This suggests that the asymmetry observed in the Berry curvature of the effective Floquet Hamiltonian originates from the projection of the Hamiltonian to its six lowest eigenstates at every time step in the calculation.

In the experiment, the Berry curvature is of course expected to be fully symmetric and the properties of the Floquet Hamiltonian should in general be independent of the initial driving phase, since the modulation is ramped up adiabatically. To estimate the influence of the asymmetry in the numerically calculated Berry curvature, the initial phase offset is varied and the resulting theoretical transverse deflections are compared to the measured values for  $m = 0.2$  at different modulation frequencies across the Haldane and anomalous regime, as shown in Fig. A.2.

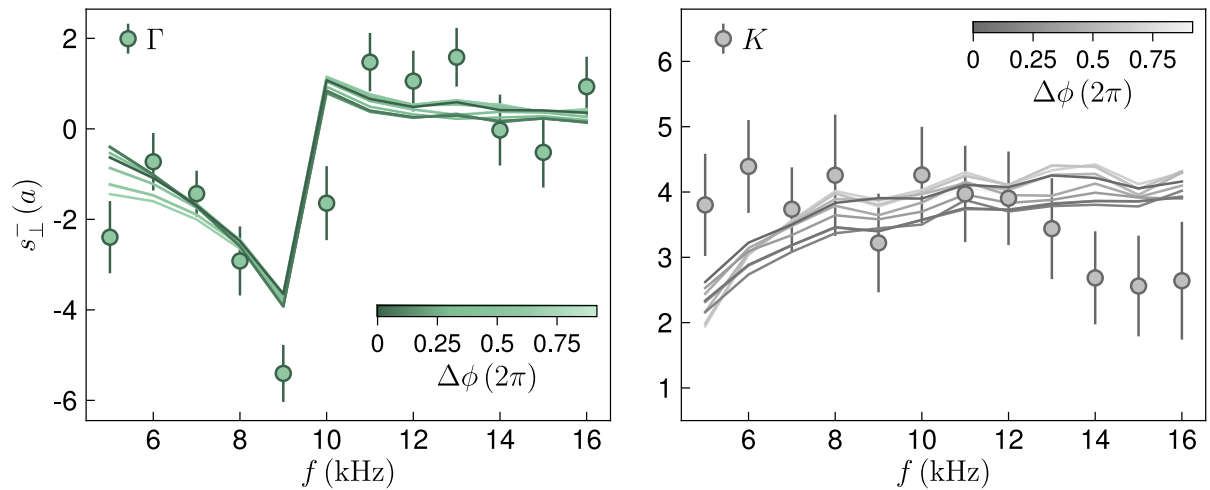


**Figure A.2: Transverse deflections depending on the initial driving phase.** Transverse deflections in the lowest band as a function of the modulation frequency for  $m = 0.2$  and  $V_0 = 6 E_r$ , the measured data are the same as in the bottom line of Fig. 5.17a and b. Every data point is derived from three measurement points each being an average over 30-40 experimental realizations, the errorbars denote the SEM. The solid lines represent the corresponding theoretical values, whereas the color shading indicates the offset of the initial driving phase  $\Delta\phi$  used in the calculation. The left and right panel show the deflections for probing along the  $\Gamma$ - and  $K$ -direction, respectively.

---

Along the  $\Gamma$ -direction (left panel), the theoretical curves are similar for most modulation frequencies and only start to deviate at  $f = 5$  kHz, whereas the relative difference is larger along the  $K$ -direction (right panel) for all modulation frequencies. In general however, the change of the transverse deflection due to the asymmetry is small compared to the deviation from the measured values and the measurement errors. Hence, replacing the Berry curvature for  $\Delta\phi = 0$  by a mean distribution averaged over all initial phases would not lead to a significant change in the deflection curves compared to the experimental values, which justifies the use of  $\Delta\phi = 0$  in all calculations.



## Appendix B

# Details on the eight-band tight-binding model

The eight-band tight-binding model introduced in Sec. 3.3.2 consists of  $s$ -,  $p$ - and  $f$ -orbitals, which exhibit different spatial symmetries [139], as illustrated in Fig. B.1a. The hopping of  $p$ -orbitals is described in terms of oriented orbitals being linear combinations of  $p_x$  and  $p_y$ , which are directed either parallel or perpendicular to the corresponding bond [138]. The following tunneling terms are considered in the tight-binding description of the imbalanced honeycomb lattice:

$$\begin{aligned} \text{NN : } & s - s, \quad s - p, \quad p^{\parallel} - p^{\parallel}, \quad p^{\perp} - p^{\perp}, \quad p - f, \quad f - f, \\ \text{NNN : } & s - s, \quad p^{\parallel} - p^{\parallel}. \end{aligned}$$

Including also a possible sublattice offset  $\Delta$  between the A- and B-sites, the tight-binding Hamiltonian reads:

$$\begin{aligned} \hat{H}(t) = \sum_{\mathbf{r}_A} \left[ \sum_{j=1}^3 \left[ J_j^{ss}(t) (\hat{s}_{\mathbf{r}_A}^\dagger \hat{s}_{\mathbf{r}_A + \delta_j(t)} + c.c.) + \tilde{J}_j^{ss}(t) \left( \hat{s}_{\mathbf{r}_A}^\dagger \hat{s}_{\mathbf{r}_A + \mathbf{a}_j} + \hat{s}_{\mathbf{r}_A + \delta_1}^\dagger \hat{s}_{\mathbf{r}_A + \delta_1 - \mathbf{a}_j} + c.c. \right) \right. \right. \\ + J_j^{sp}(t) \left( \hat{s}_{\mathbf{r}_A}^\dagger \hat{p}_{j \mathbf{r}_A + \delta_j(t)}(t) + c.c. \right) + J_j^{sp}(t) \left( \hat{p}_{j \mathbf{r}_A}^\dagger(t) \hat{s}_{\mathbf{r}_A + \delta_j(t)} + c.c. \right) \\ + J_j^{p\parallel}(t) \left( \hat{p}_{j \mathbf{r}_A}^\dagger(t) \hat{p}_{j \mathbf{r}_A + \delta_j(t)}(t) + c.c. \right) + J_j^{p\perp}(t) \left( \hat{r}_{j \mathbf{r}_A}^\dagger(t) \hat{r}_{j \mathbf{r}_A + \delta_j(t)}(t) + c.c. \right) \\ + \tilde{J}_j^{p\parallel}(t) \left( \hat{t}_{j \mathbf{r}_A}^\dagger \hat{t}_{j \mathbf{r}_A + \mathbf{a}_j} + \hat{t}_{j \mathbf{r}_A + \delta_1}^\dagger \hat{t}_{j \mathbf{r}_A + \delta_1 - \mathbf{a}_j} + c.c. \right) \\ + J_j^{pf}(t) \left( \hat{p}_{j \mathbf{r}_A}^\dagger(t) \hat{f}_{\mathbf{r}_A + \delta_j(t)} + c.c. \right) + J_j^{pf}(t) \left( \hat{f}_{\mathbf{r}_A}^\dagger \hat{p}_{j \mathbf{r}_A + \delta_j(t)}(t) + c.c. \right) \\ + J_j^{ff}(t) \left( \hat{f}_{\mathbf{r}_A}^\dagger \hat{f}_{\mathbf{r}_A + \delta_j(t)} + c.c. \right) \Big] + \frac{\Delta}{2} \left( \hat{s}_{\mathbf{r}_A}^\dagger \hat{s}_{\mathbf{r}_A} + \hat{p}_{x \mathbf{r}_A}^\dagger \hat{p}_{x \mathbf{r}_A} + \hat{p}_{y \mathbf{r}_A}^\dagger \hat{p}_{y \mathbf{r}_A} + \hat{f}_{\mathbf{r}_A}^\dagger \hat{f}_{\mathbf{r}_A} \right. \\ \left. \left. - \hat{s}_{\mathbf{r}_A + \delta_1}^\dagger \hat{s}_{\mathbf{r}_A + \delta_1} - \hat{p}_{x \mathbf{r}_A + \delta_1}^\dagger \hat{p}_{x \mathbf{r}_A + \delta_1} - \hat{p}_{y \mathbf{r}_A + \delta_1}^\dagger \hat{p}_{y \mathbf{r}_A + \delta_1} - \hat{f}_{\mathbf{r}_A + \delta_1}^\dagger \hat{f}_{\mathbf{r}_A + \delta_1} \right) \right]. \end{aligned} \quad (\text{B.1})$$

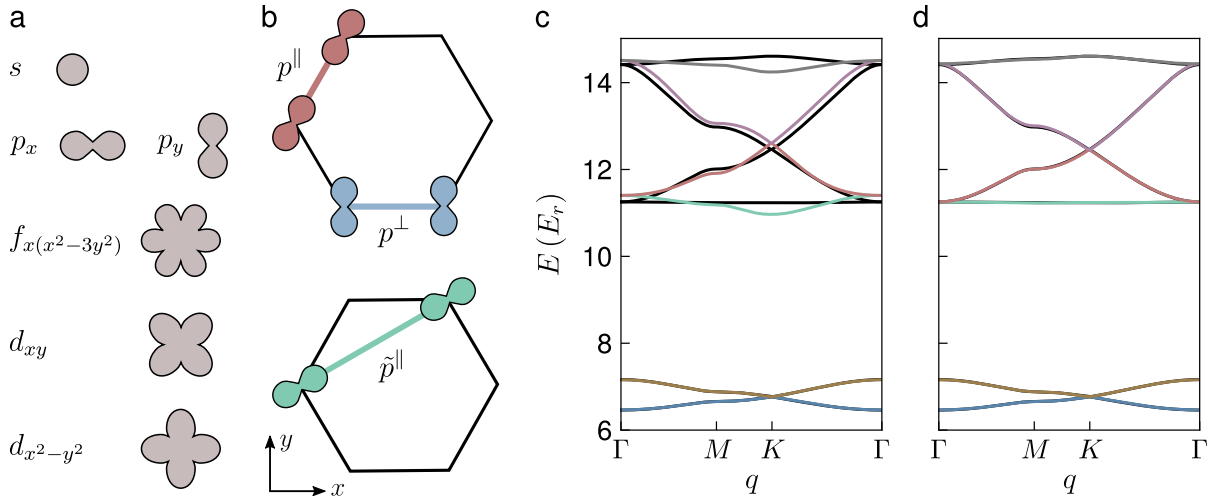


**Figure B.1: Orbitals used in the tight-binding models and bands in the symmetric lattice.** **a.** Sketch of the different orbitals which describe the first 12 bands of the honeycomb lattice in a tight-binding model. **b.**  $p$ -orbitals oriented parallel or perpendicular to the nearest neighbor (NN) and next-nearest neighbor (NNN) bonds, defined according to Eq. B.2. **c.** Tight-binding bands (colorful lines) fitted to the full calculation (black lines) for  $V_0 = 6 E_r$  using a model which only includes  $s$ - and  $p$ -orbitals. The  $p$ -bands can not be fully described without coupling to higher bands. **d.** Fitted tight-binding bands using the eight-band model described in the text. Due to the large  $p$ - $f$ -coupling, the  $f$ -bands (not shown) need to be taken into account to correctly describe the  $p$ -bands.

The creation and annihilation operators are directly denoted by the orbitals to simplify the notation. The direction-dependent  $p$ -orbitals are defined similarly as in Eq. 3.41 and 3.42:

$$\begin{aligned} \hat{p}_{j\mathbf{r}_A}^\dagger(t) &= \hat{\delta}_j^x(t) \hat{p}_{x\mathbf{r}_A}^\dagger + \hat{\delta}_j^y(t) \hat{p}_{y\mathbf{r}_A}^\dagger, & \hat{\delta}_j(t) &= \frac{\boldsymbol{\delta}_j(t)}{|\boldsymbol{\delta}_j(t)|} \\ \hat{r}_{j\mathbf{r}_A}^\dagger(t) &= \hat{\gamma}_j^x(t) \hat{p}_{x\mathbf{r}_A}^\dagger + \hat{\gamma}_j^y(t) \hat{p}_{y\mathbf{r}_A}^\dagger, & \hat{\gamma}_j(t) \cdot \hat{\delta}_j(t) &= 0, \quad j = \{1, 2, 3\}, \\ \hat{t}_{j\mathbf{r}_{A(B)}}^\dagger &= \pm \hat{a}_j^x \hat{p}_{x\mathbf{r}_{A(B)}}^\dagger \pm \hat{a}_j^y \hat{p}_{y\mathbf{r}_{A(B)}}^\dagger, & \hat{a}_j &= \frac{\mathbf{a}_j}{|\mathbf{a}_j|}, \quad \mathbf{a}_j = \{-\mathbf{a}_1, \mathbf{a}_2, \mathbf{a}_3\}. \end{aligned} \quad (\text{B.2})$$

The creation and annihilation operators can be Fourier transformed analogously to the two-band case, yielding the Hamiltonian in quasimomentum space. By making the general ansatz

$$\begin{aligned} |\psi(\mathbf{q}, t)\rangle &= c_A^s(\mathbf{q}, t) |\phi_A^s(\mathbf{q})\rangle + c_B^s(\mathbf{q}, t) |\phi_B^s(\mathbf{q})\rangle + c_A^{p_x}(\mathbf{q}, t) |\phi_A^{p_x}(\mathbf{q})\rangle + c_B^{p_x}(\mathbf{q}, t) |\phi_B^{p_x}(\mathbf{q})\rangle \\ &\quad + c_A^{p_y}(\mathbf{q}, t) |\phi_A^{p_y}(\mathbf{q})\rangle + c_B^{p_y}(\mathbf{q}, t) |\phi_B^{p_y}(\mathbf{q})\rangle + c_A^f(\mathbf{q}, t) |\phi_A^f(\mathbf{q})\rangle + c_B^f(\mathbf{q}, t) |\phi_B^f(\mathbf{q})\rangle, \end{aligned} \quad (\text{B.3})$$

the Hamiltonian for a certain quasimomentum  $\mathbf{q}$  and time  $t$  can be written as an  $8 \times 8$  matrix in the basis  $(|\phi_A^s\rangle, |\phi_B^s\rangle, |\phi_A^{px}\rangle, |\phi_A^{py}\rangle, |\phi_B^{px}\rangle, |\phi_B^{py}\rangle, |\phi_A^f\rangle, |\phi_B^f\rangle)$  of the localized orbitals:

$$H_{\mathbf{q}}^t = \begin{pmatrix} \tilde{M}^{ss} + \frac{\Delta}{2} & M^{ss} & 0 & 0 & M_x^{sp} & M_y^{sp} & 0 & 0 \\ M^{ss*} & \tilde{M}^{ss} - \frac{\Delta}{2} & -M_x^{sp*} & -M_y^{sp*} & 0 & 0 & 0 & 0 \\ 0 & -M_x^{sp} & \tilde{M}_{xx}^{p\parallel} + \frac{\Delta}{2} & \tilde{M}_{xy}^{p\parallel} & M_{xx}^{pp} & M_{xy}^{pp} & 0 & M_x^{pf} \\ 0 & -M_y^{sp} & \tilde{M}_{xy}^{p\parallel} & \tilde{M}_{yy}^{p\parallel} - \frac{\Delta}{2} & M_{xy}^{pp} & M_{yy}^{pp} & 0 & M_y^{pf} \\ M_x^{sp*} & 0 & M_{xx}^{pp*} & M_{xy}^{pp*} & \tilde{M}_{xx}^{p\parallel} + \frac{\Delta}{2} & \tilde{M}_{xy}^{p\parallel} & -M_x^{pf*} & 0 \\ M_y^{sp*} & 0 & M_{xy}^{pp*} & M_{yy}^{pp*} & \tilde{M}_{xy}^{p\parallel} & \tilde{M}_{yy}^{p\parallel} - \frac{\Delta}{2} & -M_y^{pf*} & 0 \\ 0 & 0 & 0 & 0 & -M_x^{pf} & -M_y^{pf} & \frac{\Delta}{2} & M^{ff} \\ 0 & 0 & M_x^{pf*} & M_y^{pf*} & 0 & 0 & M^{ff} & -\frac{\Delta}{2} \end{pmatrix}, \quad (\text{B.4})$$

where each entry is given by a sum over the corresponding hopping terms:

$$\begin{aligned} M^{ss} &= \sum_{j=1}^3 J_j^{ss}(t) e^{i\mathbf{q}\cdot\delta_j(t)} & \tilde{M}^{ss} &= \sum_{j=1}^3 \tilde{J}_j^{ss}(t) 2 \cos(\mathbf{q} \cdot \mathbf{a}_j) \\ M_x^{sp} &= \sum_{j=1}^3 J_j^{sp}(t) \hat{\delta}_j^x(t) e^{i\mathbf{q}\cdot\delta_j(t)} & M_y^{sp} &= \sum_{j=1}^3 J_j^{sp}(t) \hat{\delta}_j^y(t) e^{i\mathbf{q}\cdot\delta_j(t)} \\ M_{xx}^{pp} &= \sum_{j=1}^3 J_j^{p\parallel}(t) (\hat{\delta}_j^x(t))^2 e^{i\mathbf{q}\cdot\delta_j(t)} + J_j^{p\perp}(t) (\hat{\gamma}_j^x(t))^2 e^{i\mathbf{q}\cdot\delta_j(t)} \\ M_{xy}^{pp} &= \sum_{j=1}^3 J_j^{p\parallel}(t) \hat{\delta}_j^x(t) \hat{\delta}_j^y(t) e^{i\mathbf{q}\cdot\delta_j(t)} + J_j^{p\perp}(t) \hat{\gamma}_j^x(t) \hat{\gamma}_j^y(t) e^{i\mathbf{q}\cdot\delta_j(t)} \\ M_{yy}^{pp} &= \sum_{j=1}^3 J_j^{p\parallel}(t) (\hat{\delta}_j^y(t))^2 e^{i\mathbf{q}\cdot\delta_j(t)} + J_j^{p\perp}(t) (\hat{\gamma}_j^y(t))^2 e^{i\mathbf{q}\cdot\delta_j(t)} \\ \tilde{M}_{xx}^{p\parallel} &= \sum_{j=1}^3 \tilde{J}_j^{p\parallel}(t) (\hat{a}_j^x)^2 2 \cos(\mathbf{q} \cdot \mathbf{a}_j) & \tilde{M}_{xy}^{p\parallel} &= \sum_{j=1}^3 \tilde{J}_j^{p\parallel}(t) \hat{a}_j^x \hat{a}_j^y 2 \cos(\mathbf{q} \cdot \mathbf{a}_j) \\ \tilde{M}_{yy}^{p\parallel} &= \sum_{j=1}^3 \tilde{J}_j^{p\parallel}(t) (\hat{a}_j^y)^2 2 \cos(\mathbf{q} \cdot \mathbf{a}_j) & M^{ff} &= \sum_{j=1}^3 J_j^{ff}(t) e^{i\mathbf{q}\cdot\delta_j(t)}. \end{aligned} \quad (\text{B.5})$$

To account for the higher energy of the  $p$ - and  $f$ -bands with respect to the  $s$ -bands, a diagonal term  $H_E$  needs to be added to the Hamiltonian, containing constant energy

offsets which are also fitted along with the hopping parameters:

$$H_E = \begin{pmatrix} 0 & & \dots & & 0 \\ & 0 & & & \\ & & E_{sp} & & \\ & \vdots & & E_{sp} & \vdots \\ & \vdots & & E_{sp} & \vdots \\ & & & E_{sp} & E_{pf} \\ 0 & & \dots & & E_{pf} \end{pmatrix}. \quad (\text{B.6})$$

## Appendix C

### Edge modes in the zigzag-geometry

A semi-finite honeycomb lattice can also be described in a zigzag-geometry which is periodic along the  $y$ -direction and consists of  $N$  pairs of sites in  $x$ . The effective unit cell corresponds to a stripe of height  $\sqrt{3}a$ , as depicted in Fig. C.1. The zigzag-geometry has the advantage that the  $\Gamma$ - and  $K$ -points are in principle differentiable, when being projected to the  $q_y$ -axis. At the edge of the zigzag-stripe, the original honeycomb-unit cell is effectively cut, yielding single lattice sites. This leads to the emergence of flat edge modes with zero energy at  $q_y = \pi/(\sqrt{3}a)$  which further extend into the BZ with increasing width of the stripe, up to  $q_y = 2\pi/(3\sqrt{3}a)$  in the limit of  $N \rightarrow \infty$  [140]. In general, the identification of topological edge modes arising from the lattice modulation might be complicated due to the presence of the intrinsic edge states. However, as illustrated below, the latter usually exhibit a flat dispersion, corresponding to localized states, in contrast to the edge modes induced by the lattice modulation.

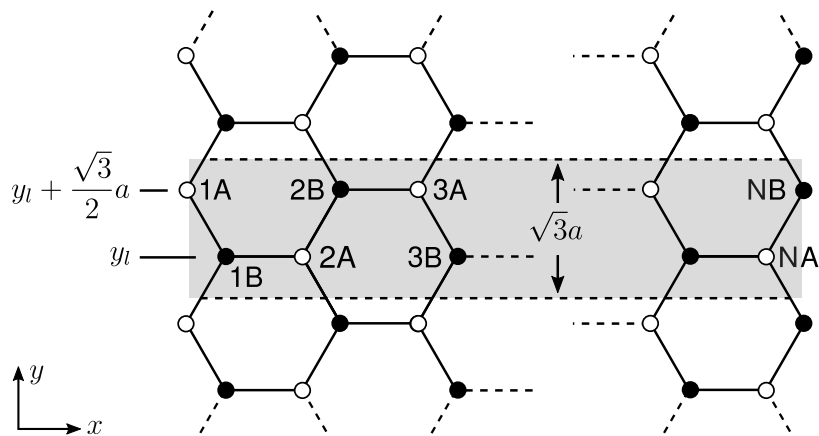


Figure C.1: **Sketch of the zigzag-geometry.** The system is periodic in the  $y$ -direction and finite along  $x$ , consisting of  $N$  pairs of A- and B-sites. The effective unit cell (gray shaded area) is a horizontal stripe with height  $\sqrt{3}a$ . The presence of single lattice sites at the edges results in the appearance of intrinsic, localized edge states in the energy spectrum.

The tight-binding Hamiltonian in the zigzag-geometry is obtained similarly to the case of the armchair edge described in Sec. 3.4, including direction- and time-dependent hoppings:

$$\begin{aligned}
\hat{H}(t) = & \sum_l \left[ J_1(t) \sum_m \left( \hat{a}_l^\dagger(m) \hat{b}_l(m-1) + c.c. \right) + \frac{\Delta}{2} \left( \hat{a}_l^\dagger(m) \hat{a}_l(m) - \hat{b}_l^\dagger(m) \hat{b}_l(m) \right) \right. \\
& + \sum_{m \text{ odd}} \left( J_2(t) \hat{a}_l^\dagger(m) \hat{b}_l(m) + J_3(t) \hat{a}_l^\dagger(m) \hat{b}_{l+1}(m) + c.c. \right) \\
& + \sum_{m \text{ even}} \left( J_2(t) \hat{a}_l^\dagger(m) \hat{b}_{l-1}(m) + J_3(t) \hat{a}_l^\dagger(m) \hat{b}_l(m) + c.c. \right) \\
& + \sum_{m \text{ odd}} \left( \tilde{J}_1(t) \hat{a}_l^\dagger(m) \hat{a}_l(m-1) + \tilde{J}_1(t) \hat{b}_l^\dagger(m) \hat{b}_l(m+1) + c.c. \right. \\
& \quad \left. + \tilde{J}_2(t) \hat{a}_l^\dagger(m) \hat{a}_l(m+1) + \tilde{J}_2(t) \hat{b}_l^\dagger(m) \hat{b}_l(m-1) + c.c. \right) \\
& + \sum_{m \text{ even}} \left( \tilde{J}_1(t) \hat{a}_l^\dagger(m) \hat{a}_{l-1}(m-1) + \tilde{J}_1(t) \hat{b}_l^\dagger(m) \hat{b}_{l+1}(m+1) + c.c. \right. \\
& \quad \left. + \tilde{J}_2(t) \hat{a}_l^\dagger(m) \hat{a}_{l-1}(m+1) + \tilde{J}_2(t) \hat{b}_l^\dagger(m) \hat{b}_{l+1}(m-1) + c.c. \right) \\
& \left. + \sum_m \left( \tilde{J}_3(t) \hat{a}_l^\dagger(m) \hat{a}_{l+1}(m) + \tilde{J}_3(t) \hat{b}_l^\dagger(m) \hat{b}_{l-1}(m) + c.c. \right) \right]. \tag{C.1}
\end{aligned}$$

Now, the 1D Fourier transform is performed along the  $y$ -direction

$$\hat{a}_l^\dagger(m) = \sum_q e^{-iqy_{l,mA}} \hat{a}_q^\dagger(m) \quad \hat{b}_l^\dagger(m) = \sum_q e^{-iqy_{l,mB}} \hat{b}_q^\dagger(m), \tag{C.2}$$

whereas the locations of the A-sites are again assumed to be fixed and the  $y$ -coordinates of the B-sites are obtained from the normalized, time-dependent connection vectors in the case of NN tunneling:

$$\begin{aligned}
m \text{ odd:} \quad & y_{l,mA} = y_l + \frac{\sqrt{3}}{2}a & y_{l,(m-1)B}(t) = y_{l,mA} + \hat{\delta}_1^y(t) \\
& y_{l,mB}(t) = y_{l,mA} + \hat{\delta}_2^y(t) & y_{l+1,mB}(t) = y_{l,mA} + \hat{\delta}_3^y(t) \\
\\
m \text{ even:} \quad & y_{l,mA} = y_l & y_{l,(m-1)B}(t) = y_{l,mA} + \hat{\delta}_1^y(t) \\
& y_{l-1,mB}(t) = y_{l,mA} + \hat{\delta}_2^y(t) & y_{l,mB}(t) = y_{l,mA} + \hat{\delta}_3^y(t). \tag{C.3}
\end{aligned}$$

For NNN hopping, the connection vectors are time-independent and the corresponding coordinates of  $-\mathbf{a}_1$ ,  $\mathbf{a}_2$  and  $\mathbf{a}_3$  can be directly used, leading to a fixed difference appearing in the exponential factors.

By making the same ansatz for the wavefunction as in the case of the armchair edge

$$|\psi_q\rangle = \sum_m \left( c_{mA} \hat{a}_q^\dagger(m) + c_{mB} \hat{b}_q^\dagger(m) \right) |0\rangle, \quad (\text{C.4})$$

using the commutations relations defined in Eq. 3.55 and relabeling  $m \rightarrow \pm m$  accordingly, the eigenvalue equation for the coefficients evaluates to

$$\begin{aligned} E c_{mA} &= J_1(t) e^{iq\hat{\delta}_1^y(t)} c_{(m-1)B} + J_2(t) e^{iq\hat{\delta}_2^y(t)} c_{mB} + J_3(t) e^{iq\hat{\delta}_3^y(t)} c_{mB} \\ &\quad + \left( \tilde{J}_1(t) e^{-iq\frac{\sqrt{3}}{2}a} + \tilde{J}_2^*(t) e^{iq\frac{\sqrt{3}}{2}a} \right) c_{(m-1)A} + \left( \tilde{J}_1^*(t) e^{iq\frac{\sqrt{3}}{2}a} + \tilde{J}_2(t) e^{-iq\frac{\sqrt{3}}{2}a} \right) c_{(m+1)A} \\ &\quad + \left( \tilde{J}_3(t) e^{iq\sqrt{3}a} + \tilde{J}_3^*(t) e^{-iq\sqrt{3}a} + \frac{\Delta}{2} \right) c_{mA} \\ E c_{mB} &= J_1(t) e^{-iq\hat{\delta}_1^y(t)} c_{(m+1)A} + J_2(t) e^{-iq\hat{\delta}_2^y(t)} c_{mA} + J_3(t) e^{-iq\hat{\delta}_3^y(t)} c_{mA} \\ &\quad + \left( \tilde{J}_1^*(t) e^{-iq\frac{\sqrt{3}}{2}a} + \tilde{J}_2(t) e^{iq\frac{\sqrt{3}}{2}a} \right) c_{(m-1)B} + \left( \tilde{J}_1(t) e^{iq\frac{\sqrt{3}}{2}a} + \tilde{J}_2^*(t) e^{-iq\frac{\sqrt{3}}{2}a} \right) c_{(m+1)B} \\ &\quad + \left( \tilde{J}_3(t) e^{-iq\sqrt{3}a} + \tilde{J}_3^*(t) e^{iq\sqrt{3}a} - \frac{\Delta}{2} \right) c_{mB}. \end{aligned} \quad (\text{C.5})$$

The energies are derived by finding the eigenvalues of the  $2N \times 2N$  Hamiltonian-matrix for every quasimomentum  $q_y \in [-\frac{\pi}{\sqrt{3}a}, \frac{\pi}{\sqrt{3}a}]$ . In the modulated lattice, either the fitted time-dependent hoppings are used to calculate an effective Hamiltonian by integration over the driving period in the anomalous and third regime, or the parameters obtained from the Haldane-model are employed directly in this regime.

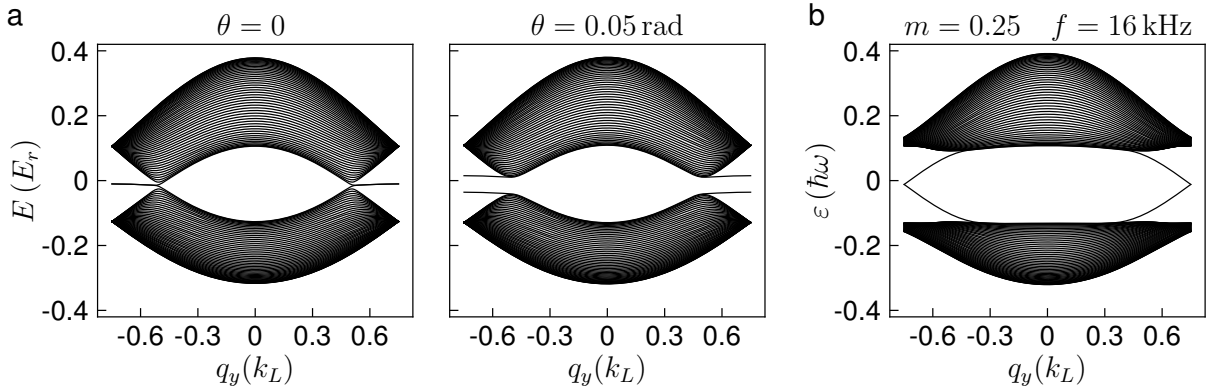


**Figure C.2: Energy bands in the zigzag-geometry for  $V_0 = 6 E_r$ .** **a.** Energy bands of the static honeycomb lattice for  $\theta = 0$  and  $\theta = 0.05 \text{ rad}$ , exhibiting localized, intrinsic edge modes around  $E = 0$ . **b.** Quasienergy bands in the Haldane regime for  $m = 0.25$  and  $f = 16 \text{ kHz}$ . The topological edge modes are dispersive and cross the gap between the bands. In all calculations, the system size is  $N = 50$ .

The harmonic trap could be included similarly as for the armchair edge, now being described by a 1D potential along  $x$ , depending on the distance of the sites to the center

of the stripe. In Fig. C.2a, the energy bands of the static honeycomb lattice in the zigzag-geometry are shown for  $\theta = 0$  (left panel) and  $\theta = 0.05$  rad (right panel). In the symmetric lattice, the bands touch at the Dirac points and the intrinsic edge state at  $E \approx 0$  extends from there to the outer edge of the BZ. Adding a sublattice offset opens a gap between the two bands. This also results in a splitting of the edge states which remain flat in energy. In contrast, the topological edge modes in the Haldane regime, presented in Fig. C.2b, are dispersive and cross the gap between the bands at zero quasienergy.

## Appendix D

# Changing between ramp-up schemes in the anomalous regime

To probe the Berry curvature of the lowest band in the different topological regimes, the ramp-up of the modulation is combined with a change of the quasimomentum to avoid the gap closings at the  $\Gamma$ -point, as described in Sec. 5.1.3. In the anomalous regime, the modulation frequency is thereby held constant or ramped up exponentially, depending on the modulation parameters. The limiting values  $f_{\text{lim}}$  at which the ramp-up of the frequency is changed to the exponential scheme are set by considering the quasienergy gaps along the ramp-up path as well as the distance between the cloud's edge and the location of the spreading Berry curvature in quasimomentum space. In the following, the scheme involving a linear ramp of the modulation amplitude at a constant frequency will be denoted as 'linear', while 'exponential' describes the scheme employing a linear amplitude ramp and an exponential change of the frequency, as given by Eq. 5.9. The quasienergy gaps are calculated for the corresponding modulation parameters during the linear or exponential ramp at  $q \in [0, q_0]$  along the  $\Gamma$ - and  $K$ -direction, as well as at the borders of the cloud in reciprocal space, traversing the same paths shifted by the width  $\sigma$  in quasimomentum space.

The minimum of the gap over the different quasimomenta of the cloud,  $\Delta E_{\text{min}}$ , is plotted in Fig. D.1 for every point during the ramp-up, when moving along the  $\Gamma$ - or the  $K$ -direction. The different colors depict the minimal quasienergy gap for certain modulation parameters that are probed within this work with modulation frequencies close to  $f_{\text{lim}}$ . At  $f = 7\text{ kHz}$  and  $m = 0.2$ , the gaps are compared for the linear and the exponential ramp: When linearly increasing the modulation amplitude at  $f = 7\text{ kHz}$ , the minimal quasienergy gaps along the  $\Gamma$ - and  $K$ -direction (solid, blue lines) become much smaller than 500 Hz (light gray line), which is set as the lower limit, being about a factor of two larger than the average value of  $Fa/h$  used in the deflection measurements. Changing the ramp to exponential (dashed, blue lines), considerably increases the minimal gap in both directions, illustrating the choice of  $f_{\text{lim}} = 7\text{ kHz}$  here: For  $f = 8\text{ kHz}$ , which is the next larger modulation frequency probed for  $m = 0.2$ , both gaps are well above the limit of 500 Hz for the linear ramp (solid, green line). The linear and exponential ramp

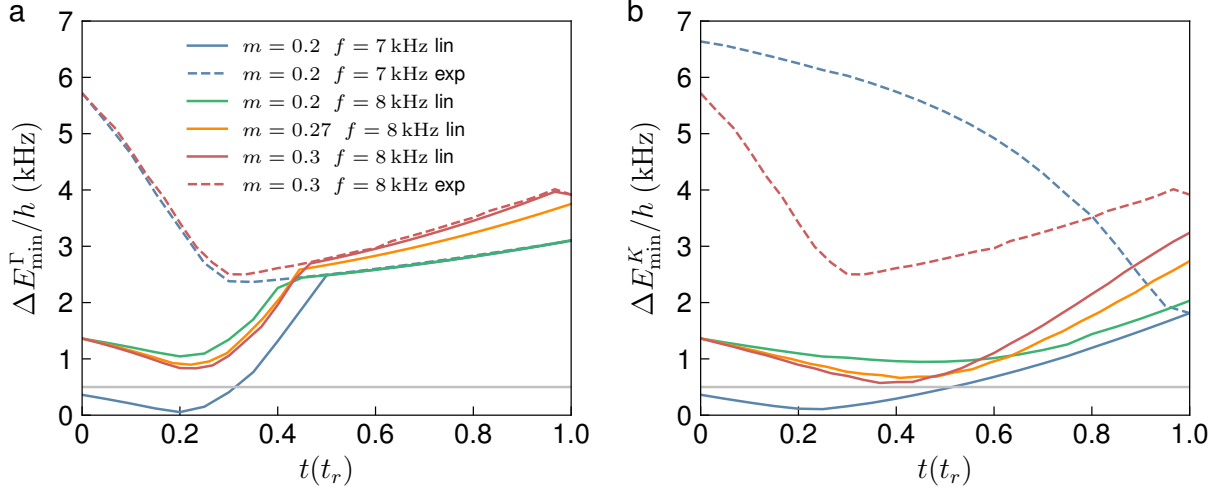


**Figure D.1: Minimal quasienergy gap during the ramp-up along the  $\Gamma$ - and  $K$ -directions for various modulation parameters and different ramping schemes.**  
**a.** Calculated minimal quasienergy gap over the extent of the cloud in reciprocal space vs. time when moving the center along the path  $\Gamma$ - $M$  during the modulation ramp-up. The different colors and line shapes represent different final modulation parameters and ramp-up schemes: Either increasing the modulation amplitude linearly at constant modulation frequency (lin) or while changing the frequency exponentially (exp). The mean width  $\bar{\sigma} = 0.153 k_L$  of the BEC averaged over all measured widths is used in the calculations.  
**b.** Minimal quasienergy gap during the ramp-up when probing along the  $K$ -direction for the same modulation parameters as in the left panel.

are also compared for  $f = 8\text{ kHz}$  and  $m = 0.3$  (red lines). The minimal gaps are larger than 500 Hz for both path directions also for the linear ramp, similar to  $f = 8\text{ kHz}$  and  $m = 0.27$  (solid, orange lines), where a linear ramp-up is used. The choice of  $f_{\text{lim}} = 8\text{ kHz}$  for  $m = 0.3$  results from considerations of the Berry curvature that the cloud potentially probes during the ramp-up.

In the anomalous regime, the negative Berry curvature arising at  $\Gamma$  spreads out in reciprocal space after the first phase transition. The Berry curvature ring is located at the nearly degenerate minimum of the lowest band which occurs due to the crossing and hybridization of the two lowest bands. Hence, the minimum of the ring along the radial direction resides at the point  $q_{\text{cross}}$  where the bands would intersect for  $m \rightarrow 0$ . The value of this crossing point is calculated as a function of time for the same modulation parameters and ramping schemes as the minimal gaps and is compared to the width of the moving BEC in Fig. D.2, exhibiting similar values for probing the  $\Gamma$ - and  $K$ -direction. The center of the BEC moves linearly from  $q = 0$  to  $q_0 = 0.5\sqrt{3}$  (dark gray line) and its extent in reciprocal space is illustrated by the gray shaded area. In order to avoid transverse deflections during the ramp-up, the minimal distance between the center of the spreading Berry curvature and the edge of the cloud is set to  $0.1 k_L$  (solid, light gray line), corresponding to the average width of the Berry curvature along the ring.

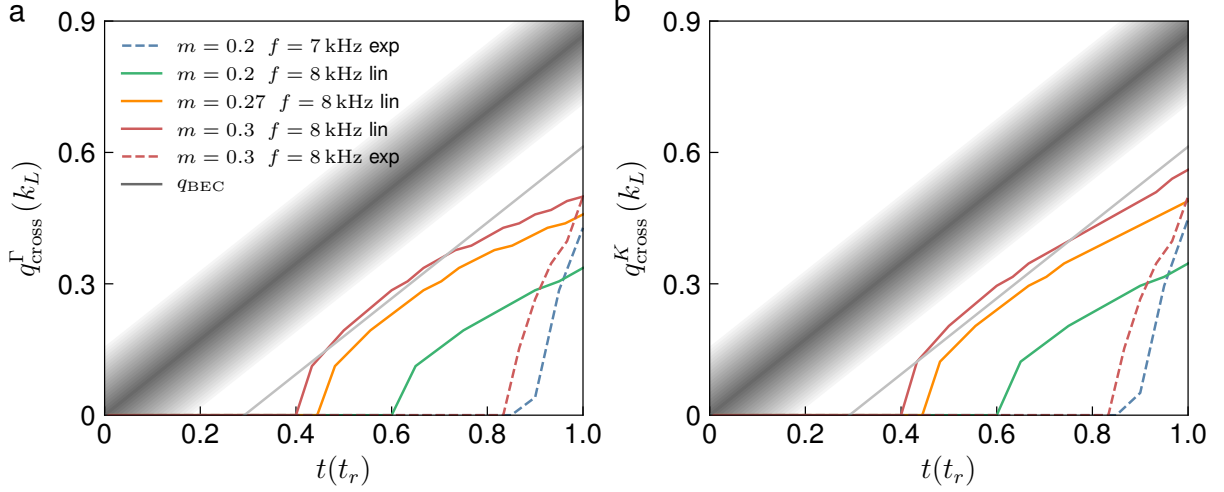


**Figure D.2: Calculated band crossing points as a function of time.** Band crossing points during the modulation ramp-up for various modulation parameters and ramp-up schemes. **a.** Crossing points  $q_{\text{cross}}^{\Gamma}$  along the  $\Gamma$ - $M$ -axis, the dark gray line depicts the quasimomentum of the cloud's center during the ramp-up, while the Gaussian width of  $\bar{\sigma} = 0.153 k_L$  is illustrated by the gray shaded stripes. The light gray line marks the minimal distance of  $0.1 k_L$  from the band crossing points to the edge of the cloud to ensure that no Berry curvature is traversed. The different colors and line shapes represent different final modulation parameters and ramp-up schemes: Either increasing the modulation amplitude linearly at constant modulation frequency (lin) or while changing the frequency exponentially (exp). **b.** Calculated crossing points along the  $\Gamma$ - $K$ -axis for the same parameters as in **a.**

For the linear ramp-up at  $f = 8 \text{ kHz}$  and  $m = 0.3$  (solid, red line), the crossing point surpasses this limit and hence the exponential ramp-up is applied for these modulation parameters (dashed, red line). For the next smaller modulation amplitude that is probed at  $f = 8 \text{ kHz}$ ,  $m = 0.27$ , the distance is sufficiently larger than  $0.1 k_L$  (solid, orange line) when using the linear ramp-up, justifying  $f_{\text{lim}} = 7 \text{ kHz}$  for  $m < 0.3$ . At  $m = 0.2$ , the exponential and linear ramps for  $f = 7 \text{ kHz}$  and  $f = 8 \text{ kHz}$  (dashed, blue and solid, green lines) also ensure that no significant amount of Berry curvature is probed during the modulation ramp-up.



# Bibliography

- [1] L. L. D. and E. M. Lifshitz, *Statistical Physics - Course of Theoretical Physics vol. 5*. Pergamon Press, 1958.
- [2] K. v. Klitzing, G. Dorda, and M. Pepper, “New Method for High-Accuracy Determination of the Fine-Structure Constant Based on Quantized Hall Resistance,” *Physical Review Letters*, vol. 45, no. 6, pp. 494–497, 1980.
- [3] D. J. Thouless, M. Kohmoto, M. P. Nightingale, and M. den Nijs, “Quantized Hall Conductance in a Two-Dimensional Periodic Potential,” *Physical Review Letters*, vol. 49, no. 6, pp. 405–408, 1982.
- [4] X.-G. Wen, “Topological orders and edge excitations in fractional quantum hall states,” *Advances in Physics*, vol. 44, pp. 405–473, 1995.
- [5] M. Z. Hasan and C. L. Kane, “Colloquium: Topological insulators,” *Reviews of Modern Physics*, vol. 82, no. 4, pp. 3045–3067, 2010.
- [6] X.-G. Wen, “Topological Order: From Long-Range Entangled Quantum Matter to a Unified Origin of Light and Electrons,” *ISRN Condensed Matter Physics*, vol. 2013, pp. 1–20, 2013.
- [7] B. Jeckelmann and B. Jeanneret, “The quantum Hall effect as an electrical resistance standard,” *Reports on Progress in physics*, vol. 64, p. 54, 2001.
- [8] P. J. Mohr, B. N. Taylor, and D. B. Newell, “CODATA recommended values of the fundamental physical constants: 2010,” *Reviews of Modern Physics*, vol. 84, no. 4, pp. 1527–1605, 2012.
- [9] M. Nakahara, *Geometry, Topology and Physics*. CRC Press, 2003.
- [10] A. Altland and M. R. Zirnbauer, “Nonstandard symmetry classes in mesoscopic normal-superconducting hybrid structures,” *Physical Review B*, vol. 55, no. 2, pp. 1142–1161, 1997.
- [11] P. Heinzner, A. Huckleberry, and M. Zirnbauer, “Symmetry Classes of Disordered Fermions,” *Communications in Mathematical Physics*, vol. 257, no. 3, pp. 725–771, 2005.

- [12] F. Harper, R. Roy, M. S. Rudner, and S. Sondhi, “Topology and Broken Symmetry in Floquet Systems,” *Annual Review of Condensed Matter Physics*, vol. 11, no. 1, pp. 345–368, 2020.
- [13] C. L. Kane and E. J. Mele, “Z 2 Topological Order and the Quantum Spin Hall Effect,” *Physical Review Letters*, vol. 95, no. 14, p. 146802, 2005.
- [14] C. L. Kane and E. J. Mele, “Quantum Spin Hall Effect in Graphene,” *Physical Review Letters*, vol. 95, no. 22, p. 226801, 2005.
- [15] J. E. Moore and L. Balents, “Topological invariants of time-reversal-invariant band structures,” *Physical Review B*, vol. 75, no. 12, p. 121306, 2007.
- [16] R. Roy, “Z 2 classification of quantum spin Hall systems: An approach using time-reversal invariance,” *Physical Review B*, vol. 79, no. 19, p. 195321, 2009.
- [17] L. Fu and C. L. Kane, “Probing Neutral Majorana Fermion Edge Modes with Charge Transport,” *Physical Review Letters*, vol. 102, no. 21, p. 216403, 2009.
- [18] L. Fu and C. L. Kane, “Topological insulators with inversion symmetry,” *Physical Review B*, vol. 76, no. 4, p. 045302, 2007.
- [19] P. Ghaemi and F. Wilczek, “Near-Zero Modes in Superconducting Graphene,” *arXiv:0709.2626 [cond-mat]*, 2011. arXiv: 0709.2626.
- [20] M. Konig, S. Wiedmann, C. Brune, A. Roth, H. Buhmann, L. W. Molenkamp, X.-L. Qi, and S.-C. Zhang, “Quantum Spin Hall Insulator State in HgTe Quantum Wells,” *Science*, vol. 318, no. 5851, pp. 766–770, 2007.
- [21] D. Hsieh, D. Qian, L. Wray, Y. Xia, Y. S. Hor, R. J. Cava, and M. Z. Hasan, “A topological Dirac insulator in a quantum spin Hall phase,” *Nature*, vol. 452, no. 7190, pp. 970–974, 2008.
- [22] Y. Xia, D. Qian, D. Hsieh, L. Wray, A. Pal, H. Lin, A. Bansil, D. Grauer, Y. S. Hor, R. J. Cava, and M. Z. Hasan, “Observation of a large-gap topological-insulator class with a single Dirac cone on the surface,” *Nature Physics*, vol. 5, no. 6, pp. 398–402, 2009.
- [23] H. Zhang, C.-X. Liu, X.-L. Qi, X. Dai, Z. Fang, and S.-C. Zhang, “Topological insulators in Bi<sub>2</sub>Se<sub>3</sub>, Bi<sub>2</sub>Te<sub>3</sub> and Sb<sub>2</sub>Te<sub>3</sub> with a single Dirac cone on the surface,” *Nature Physics*, vol. 5, no. 6, pp. 438–442, 2009.
- [24] B. I. Halperin, “Statistics of Quasiparticles and the Hierarchy of Fractional Quantized Hall States,” *Physical Review Letters*, vol. 52, no. 18, pp. 1583–1586, 1984.
- [25] D. Arovas, J. R. Schrieffer, and F. Wilczek, “Fractional Statistics and the Quantum Hall Effect,” *Physical Review Letters*, vol. 53, no. 7, pp. 722–723, 1984.

- [26] X. G. Wen, “Non-Abelian statistics in the fractional quantum Hall states,” *Physical Review Letters*, vol. 66, no. 6, pp. 802–805, 1991.
- [27] G. Moore and N. Read, “Nonabelions in the fractional quantum hall effect,” *Nuclear Physics B*, vol. 360, no. 2-3, pp. 362–396, 1991.
- [28] A. Kitaev, “Fault-tolerant quantum computation by anyons,” *Annals of Physics*, vol. 303, no. 1, pp. 2–30, 2003.
- [29] B. I. Halperin, “Quantized Hall conductance, current-carrying edge states, and the existence of extended states in a two-dimensional disordered potential,” *Physical Review B*, vol. 25, no. 4, pp. 2185–2190, 1982.
- [30] A. H. MacDonald, “Edge states in the fractional-quantum-Hall-effect regime,” *Physical Review Letters*, vol. 64, no. 2, pp. 220–223, 1990.
- [31] X. G. Wen, “Gapless boundary excitations in the quantum Hall states and in the chiral spin states,” *Physical Review B*, vol. 43, no. 13, pp. 11025–11036, 1991.
- [32] F. Zangeneh-Nejad and R. Fleury, “Topological analog signal processing,” *Nature Communications*, vol. 10, no. 1, p. 2058, 2019.
- [33] R. Roy, “Topological superfluids with time reversal symmetry,” *arXiv:0803.2868 [cond-mat]*, 2008. arXiv: 0803.2868.
- [34] A. P. Schnyder, S. Ryu, A. Furusaki, and A. W. W. Ludwig, “Classification of topological insulators and superconductors in three spatial dimensions,” *Physical Review B*, vol. 78, no. 19, p. 195125, 2008.
- [35] X.-L. Qi, T. L. Hughes, S. Raghu, and S.-C. Zhang, “Time-Reversal-Invariant Topological Superconductors and Superfluids in Two and Three Dimensions,” *Physical Review Letters*, vol. 102, no. 18, p. 187001, 2009.
- [36] X.-L. Qi and S.-C. Zhang, “Topological insulators and superconductors,” *Reviews of Modern Physics*, vol. 83, no. 4, pp. 1057–1110, 2011.
- [37] G. E. Volovik, “Fermion zero modes on vortices in chiral superconductors,” *Journal of Experimental and Theoretical Physics Letters*, vol. 70, no. 9, pp. 609–614, 1999.
- [38] N. Read and D. Green, “Paired states of fermions in two dimensions with breaking of parity and time-reversal symmetries and the fractional quantum Hall effect,” *Physical Review B*, vol. 61, no. 15, pp. 10267–10297, 2000.
- [39] D. A. Ivanov, “Non-Abelian Statistics of Half-Quantum Vortices in p -Wave Superconductors,” *Physical Review Letters*, vol. 86, no. 2, pp. 268–271, 2001.
- [40] T. Oka and S. Kitamura, “Floquet Engineering of Quantum Materials,” *Annual Review of Condensed Matter Physics*, vol. 10, no. 1, pp. 387–408, 2019.

- [41] M. S. Rudner, N. H. Lindner, E. Berg, and M. Levin, “Anomalous Edge States and the Bulk-Edge Correspondence for Periodically Driven Two-Dimensional Systems,” *Physical Review X*, vol. 3, no. 3, p. 031005, 2013.
- [42] P. Titum, E. Berg, M. S. Rudner, G. Refael, and N. H. Lindner, “Anomalous Floquet-Anderson Insulator as a Nonadiabatic Quantized Charge Pump,” *Physical Review X*, vol. 6, no. 2, p. 021013, 2016.
- [43] M. Rudner and N. Lindner, “Band structure engineering and non-equilibrium dynamics in Floquet topological insulators,” *Nature reviews physics*, vol. 2, p. 229–244, 2020.
- [44] A. Lazarides, A. Das, and R. Moessner, “Equilibrium states of generic quantum systems subject to periodic driving,” *Physical Review E*, vol. 90, no. 1, p. 012110, 2014.
- [45] L. D’Alessio and M. Rigol, “Long-time Behavior of Isolated Periodically Driven Interacting Lattice Systems,” *Physical Review X*, vol. 4, no. 4, p. 041048, 2014.
- [46] M. Bukov, S. Gopalakrishnan, M. Knap, and E. Demler, “Prethermal Floquet Steady States and Instabilities in the Periodically Driven, Weakly Interacting Bose-Hubbard Model,” *Physical Review Letters*, vol. 115, no. 20, p. 205301, 2015.
- [47] E. Canovi, M. Kollar, and M. Eckstein, “Stroboscopic prethermalization in weakly interacting periodically driven systems,” *Physical Review E*, vol. 93, no. 1, p. 012130, 2016.
- [48] T. Mori, T. Kuwahara, and K. Saito, “Rigorous Bound on Energy Absorption and Generic Relaxation in Periodically Driven Quantum Systems,” *Physical Review Letters*, vol. 116, no. 12, p. 120401, 2016.
- [49] D. A. Abanin, W. De Roeck, W. W. Ho, and F. Huveneers, “Effective Hamiltonians, prethermalization, and slow energy absorption in periodically driven many-body systems,” *Physical Review B*, vol. 95, no. 1, p. 014112, 2017.
- [50] D. Abanin, W. De Roeck, W. W. Ho, and F. Huveneers, “A Rigorous Theory of Many-Body Prethermalization for Periodically Driven and Closed Quantum Systems,” *Communications in Mathematical Physics*, vol. 354, no. 3, pp. 809–827, 2017.
- [51] A. Haldar, R. Moessner, and A. Das, “Onset of Floquet thermalization,” *Physical Review B*, vol. 97, no. 24, p. 245122, 2018.
- [52] K. Mallayya, M. Rigol, and W. De Roeck, “Prethermalization and Thermalization in Isolated Quantum Systems,” *Physical Review X*, vol. 9, no. 2, p. 021027, 2019.

- [53] K. Mallayya and M. Rigol, “Heating Rates in Periodically Driven Strongly Interacting Quantum Many-Body Systems,” *Physical Review Letters*, vol. 123, no. 24, p. 240603, 2019.
- [54] A. Rubio-Abadal, M. Ippoliti, S. Hollerith, D. Wei, J. Rui, S. Sondhi, V. Khemani, C. Gross, and I. Bloch, “Floquet Prethermalization in a Bose-Hubbard System,” *Physical Review X*, vol. 10, no. 2, p. 021044, 2020.
- [55] P. Ponte, Z. Papić, F. Huveneers, and D. A. Abanin, “Many-Body Localization in Periodically Driven Systems,” *Physical Review Letters*, vol. 114, no. 14, p. 140401, 2015.
- [56] A. Lazarides, A. Das, and R. Moessner, “Fate of Many-Body Localization Under Periodic Driving,” *Physical Review Letters*, vol. 115, no. 3, p. 030402, 2015.
- [57] D. A. Abanin, W. De Roeck, and F. Huveneers, “Exponentially Slow Heating in Periodically Driven Many-Body Systems,” *Physical Review Letters*, vol. 115, no. 25, p. 256803, 2015.
- [58] D. A. Abanin, W. De Roeck, and F. Huveneers, “Theory of many-body localization in periodically driven systems,” *Annals of Physics*, vol. 372, pp. 1–11, 2016.
- [59] F. Nathan, D. Abanin, E. Berg, N. H. Lindner, and M. S. Rudner, “Anomalous Floquet insulators,” *Physical Review B*, vol. 99, no. 19, p. 195133, 2019.
- [60] I. Bloch, J. Dalibard, and S. Nascimbène, “Quantum simulations with ultracold quantum gases,” *Nature Physics*, vol. 8, no. 4, pp. 267–276, 2012.
- [61] C. Gross and I. Bloch, “Quantum simulations with ultracold atoms in optical lattices,” *Science*, vol. 357, no. 6355, pp. 995–1001, 2017.
- [62] M. B. Dahan, E. Peik, J. Reichel, Y. Castin, and C. Salomon, “Bloch Oscillations of Atoms in an Optical Potential,” *Physical Review Letters*, vol. 76, no. 24, p. 4, 1996.
- [63] B. P. Anderson, “Macroscopic Quantum Interference from Atomic Tunnel Arrays,” *Science*, vol. 282, no. 5394, pp. 1686–1689, 1998.
- [64] Z. A. Geiger, K. M. Fujiwara, K. Singh, R. Senaratne, S. V. Rajagopal, M. Lipatov, T. Shimasaki, R. Driben, V. V. Konotop, T. Meier, and D. M. Weld, “Observation and Uses of Position-Space Bloch Oscillations in an Ultracold Gas,” *Physical Review Letters*, vol. 120, no. 21, p. 213201, 2018.
- [65] M. Greiner, O. Mandel, T. Rom, A. Altmeyer, A. Widera, T. Hänsch, and I. Bloch, “Quantum phase transition from a superfluid to a Mott insulator in an ultracold gas of atoms,” *Physica B: Condensed Matter*, vol. 329-333, pp. 11–12, 2003.

- [66] I. Bloch, J. Dalibard, and W. Zwerger, “Many-body physics with ultracold gases,” *Reviews of Modern Physics*, vol. 80, no. 3, pp. 885–964, 2008.
- [67] N. Goldman and J. Dalibard, “Periodically Driven Quantum Systems: Effective Hamiltonians and Engineered Gauge Fields,” *Physical Review X*, vol. 4, no. 3, p. 031027, 2014.
- [68] M. Bükov, L. D’Alessio, and A. Polkovnikov, “Universal high-frequency behavior of periodically driven systems: from dynamical stabilization to Floquet engineering,” *Advances in Physics*, vol. 64, no. 2, pp. 139–226, 2015.
- [69] M. Holthaus, “Floquet engineering with quasienergy bands of periodically driven optical lattices,” *Journal of Physics B: Atomic, Molecular and Optical Physics*, vol. 49, no. 1, p. 013001, 2016.
- [70] A. Eckardt, “Colloquium: Atomic quantum gases in periodically driven optical lattices,” *Reviews of Modern Physics*, vol. 89, no. 1, p. 011004, 2017.
- [71] K. Wintersperger, C. Braun, F. N. Ünal, A. Eckardt, M. D. Liberto, N. Goldman, I. Bloch, and M. Aidelsburger, “Realization of an anomalous Floquet topological system with ultracold atoms,” *Nature Physics*, 2020.
- [72] T. Li, L. Duca, M. Reitter, F. Grusdt, E. Demler, M. Endres, M. Schleier-Smith, I. Bloch, and U. Schneider, “Bloch state tomography using Wilson lines,” *Science*, vol. 352, no. 6289, pp. 1094–1097, 2016. arXiv: 1509.02185.
- [73] T. Li, *Probing Bloch band geometry with ultracold atoms in optical lattices*. PhD thesis, Ludwig-Maximilians-Universität München, 2016.
- [74] M. Reitter, J. Näger, K. Wintersperger, C. Sträter, I. Bloch, A. Eckardt, and U. Schneider, “Interaction Dependent Heating and Atom Loss in a Periodically Driven Optical Lattice,” *Physical Review Letters*, vol. 119, no. 20, p. 200402, 2017.
- [75] J. Näger, *Parametric Instabilities of Interacting Bosons in Driven Optical Lattices*. PhD thesis, Ludwig-Maximilians-Universität München, 2019.
- [76] K. Wintersperger, M. Bükov, J. Näger, S. Lellouch, E. Demler, U. Schneider, I. Bloch, N. Goldman, and M. Aidelsburger, “Parametric Instabilities of Interacting Bosons in Periodically Driven 1D Optical Lattices,” *Physical Review X*, vol. 10, no. 1, p. 011030, 2020.
- [77] N. W. Ashcroft and N. D. Mermin, *Solid State Physics*. Saunders College Publications, 1976.
- [78] A. Messiah, *Quantum mechanics Vol. 2*. Noth-Holland Publishing company, 1962.
- [79] M. Berry, “Quantal phase factors accompanying adiabatic changes,” *Proceedings of the Royal Society A*, vol. 392, pp. 45–57, 1984.

- [80] Y. Aharonov and D. Bohm, "Significance of Electromagnetic Potentials in the Quantum Theory," *Physical Review*, vol. 115, no. 3, pp. 485–491, 1959.
- [81] F. Wilczek and A. Zee, "Appearance of Gauge Structure in Simple Dynamical Systems," *Physical Review Letters*, vol. 52, no. 24, pp. 2111–2114, 1984.
- [82] Y. M. Makeenko, "Brief introduction to Wilson loops and large N," *Physics of Atomic Nuclei*, vol. 73, no. 5, pp. 878–894, 2010.
- [83] L. Schweitzer, B. Kramer, and A. MacKinnonS, "Magnetic field and electron states in two-dimensional disordered systems," *Journal of Physics C: Solid State Physics*, vol. 17, pp. 4111–4125, 1984.
- [84] Y. Hatsugai, "Chern number and edge states in the integer quantum Hall effect," *Physical Review Letters*, vol. 71, no. 22, pp. 3697–3700, 1993.
- [85] X.-L. Qi, Y.-S. Wu, and S.-C. Zhang, "General theorem relating the bulk topological number to edge states in two-dimensional insulators," *Physical Review B*, vol. 74, no. 4, p. 045125, 2006.
- [86] Y. Hatsugai, "Edge states in the integer quantum Hall effect and the Riemann surface of the Bloch function," *Physical Review B*, vol. 48, no. 16, pp. 11851–11862, 1993.
- [87] F. D. M. Haldane, "Model for a Quantum Hall Effect without Landau Levels: Condensed-Matter Realization of the "Parity Anomaly"," *Physical Review Letters*, vol. 61, no. 18, pp. 2015–2018, 1988.
- [88] F. Gerbier and J. Dalibard, "Gauge fields for ultracold atoms in optical superlattices," *New Journal of Physics*, vol. 12, no. 3, p. 033007, 2010.
- [89] D. Jaksch and P. Zoller, "Creation of effective magnetic fields in optical lattices: the Hofstadter butterfly for cold neutral atoms," *New Journal of Physics*, vol. 5, pp. 56–56, 2003.
- [90] M. Aidelsburger, M. Atala, S. Nascimbène, S. Trotzky, Y.-A. Chen, and I. Bloch, "Experimental Realization of Strong Effective Magnetic Fields in an Optical Lattice," *Physical Review Letters*, vol. 107, no. 25, p. 255301, 2011.
- [91] Y.-J. Lin, R. Compton, A. Perry, W. Phillips, J. Porto, and I. Spielman, "Bose-Einstein Condensate in a Uniform Light-Induced Vector Potential," *Physical Review Letters*, vol. 102, no. 13, p. 130401, 2009.
- [92] Y.-J. Lin, R. L. Compton, K. Jiménez-García, J. V. Porto, and I. B. Spielman, "Synthetic magnetic fields for ultracold neutral atoms," *Nature*, vol. 462, no. 7273, pp. 628–632, 2009.

- [93] A. Celi, P. Massignan, J. Ruseckas, N. Goldman, I. Spielman, G. Juzeliūnas, and M. Lewenstein, “Synthetic Gauge Fields in Synthetic Dimensions,” *Physical Review Letters*, vol. 112, no. 4, p. 043001, 2014.
- [94] M. Aidelsburger, M. Atala, M. Lohse, J. T. Barreiro, B. Paredes, and I. Bloch, “Realization of the Hofstadter Hamiltonian with Ultracold Atoms in Optical Lattices,” *Physical Review Letters*, vol. 111, no. 18, p. 185301, 2013.
- [95] H. Miyake, G. A. Siviloglou, C. J. Kennedy, W. C. Burton, and W. Ketterle, “Realizing the Harper Hamiltonian with Laser-Assisted Tunneling in Optical Lattices,” *Physical Review Letters*, vol. 111, no. 18, p. 185302, 2013.
- [96] T. Oka and H. Aoki, “Photovoltaic Hall effect in graphene,” *Physical Review B*, vol. 79, no. 8, p. 081406, 2009.
- [97] Z. Gu, H. A. Fertig, D. P. Arovas, and A. Auerbach, “Floquet Spectrum and Transport through an Irradiated Graphene Ribbon,” *Physical Review Letters*, vol. 107, no. 21, p. 216601, 2011.
- [98] G. Usaj, P. M. Perez-Piskunow, L. E. F. Foa Torres, and C. A. Balseiro, “Irradiated graphene as a tunable Floquet topological insulator,” *Physical Review B*, vol. 90, no. 11, p. 115423, 2014.
- [99] M. C. Rechtsman, J. M. Zeuner, Y. Plotnik, Y. Lumer, D. Podolsky, F. Dreisow, S. Nolte, M. Segev, and A. Szameit, “Photonic Floquet topological insulators,” *Nature*, vol. 496, no. 7444, pp. 196–200, 2013.
- [100] S. Mukherjee, A. Spracklen, M. Valiente, E. Andersson, P. Öhberg, N. Goldman, and R. R. Thomson, “Experimental observation of anomalous topological edge modes in a slowly driven photonic lattice,” *Nature Communications*, vol. 8, no. 1, p. 13918, 2017.
- [101] L. J. Maczewsky, J. M. Zeuner, S. Nolte, and A. Szameit, “Observation of photonic anomalous Floquet topological insulators,” *Nature Communications*, vol. 8, no. 1, p. 13756, 2017.
- [102] M. Aidelsburger, M. Lohse, C. Schweizer, M. Atala, J. Barreiro, S. Nascimbène, N. Cooper, I. Bloch, and N. Goldman, “Measuring the Chern number of Hofstadter bands with ultracold bosonic atoms,” *Nature Physics*, vol. 11, no. 2, pp. 162–166, 2015.
- [103] G. Jotzu, M. Messer, R. Desbuquois, M. Lebrat, T. Uehlinger, D. Greif, and T. Esslinger, “Experimental realization of the topological Haldane model with ultracold fermions,” *Nature*, vol. 515, no. 7526, pp. 237–240, 2014.
- [104] L. Asteria, D. T. Tran, T. Ozawa, M. Tarnowski, B. S. Rem, N. Fläschner, K. Sengstock, N. Goldman, and C. Weitenberg, “Measuring quantized circular dichroism in ultracold topological matter,” *Nature Physics*, vol. 15, no. 5, pp. 449–454, 2019.

- [105] M. Tarnowski, F. N. Ünal, N. Fläschner, B. S. Rem, A. Eckardt, K. Sengstock, and C. Weitenberg, “Measuring topology from dynamics by obtaining the Chern number from a linking number,” *Nature Communications*, vol. 10, no. 1, p. 1728, 2019.
- [106] J. Struck, C. Olschlager, R. Le Targat, P. Soltan-Panahi, A. Eckardt, M. Lewenstein, P. Windpassinger, and K. Sengstock, “Quantum Simulation of Frustrated Classical Magnetism in Triangular Optical Lattices,” *Science*, vol. 333, no. 6045, pp. 996–999, 2011.
- [107] A. Zenesini, H. Lignier, D. Ciampini, O. Morsch, and E. Arimondo, “Coherent Control of Dressed Matter Waves,” *Physical Review Letters*, vol. 102, no. 10, p. 100403, 2009.
- [108] J. H. Shirley, “Solution of the Schrödinger Equation with a Hamiltonian Periodic in Time,” *Physical Review*, vol. 138, no. 4B, pp. B979–B987, 1965.
- [109] T. Fromherz, “Floquet states and intersubband absorption in strongly driven double quantum wells,” *Physical Review B*, vol. 56, no. 8, pp. 4772–4777, 1997.
- [110] M. Grifoni and P. Hänggi, “Driven quantum tunneling,” *Physics Reports*, vol. 304, no. 5–6, pp. 229–354, 1998.
- [111] W. R. Salzman, “Quantum mechanics of systems periodic in time,” *Physical Review A*, vol. 10, no. 2, pp. 461–465, 1974.
- [112] S. Rahav, I. Gilary, and S. Fishman, “Effective Hamiltonians for periodically driven systems,” *Physical Review A*, vol. 68, no. 1, p. 013820, 2003.
- [113] W. Magnus, “On the exponential solution of differential equations for a linear operator,” *Communications on Pure and Applied Mathematics*, vol. 7, no. 4, pp. 649–673, 1954.
- [114] M. M. Maricq, “Application of average Hamiltonian theory to the NMR of solids,” *Physical Review B*, vol. 25, no. 11, pp. 6622–6632, 1982.
- [115] W. Hu, J. C. Pillay, K. Wu, M. Pasek, P. P. Shum, and Y. Chong, “Measurement of a Topological Edge Invariant in a Microwave Network,” *Physical Review X*, vol. 5, no. 1, p. 011012, 2015.
- [116] F. Gao, Z. Gao, X. Shi, Z. Yang, X. Lin, H. Xu, J. D. Joannopoulos, M. Soljačić, H. Chen, L. Lu, Y. Chong, and B. Zhang, “Probing topological protection using a designer surface plasmon structure,” *Nature Communications*, vol. 7, no. 1, p. 11619, 2016.

- [117] A. D'Errico, F. Cardano, M. Maffei, A. Dauphin, R. Barboza, C. Esposito, B. Piccirillo, M. Lewenstein, P. Massignan, and L. Marrucci, "Two-dimensional topological quantum walks in the momentum space of structured light," *Optica*, vol. 7, no. 2, p. 108, 2020.
- [118] T. Kitagawa, E. Berg, M. Rudner, and E. Demler, "Topological characterization of periodically driven quantum systems," *Physical Review B*, vol. 82, no. 23, p. 235114, 2010.
- [119] F. Nathan and M. S. Rudner, "Topological singularities and the general classification of Floquet–Bloch systems," *New Journal of Physics*, vol. 17, no. 12, p. 125014, 2015.
- [120] F. N. Ünal, B. Seradjeh, and A. Eckardt, "How to Directly Measure Floquet Topological Invariants in Optical Lattices," *Physical Review Letters*, vol. 122, no. 25, p. 253601, 2019.
- [121] J. Bellissard, "Change of the Chern number at band crossings," *arXiv:cond-mat/9504030*, 1995. arXiv: cond-mat/9504030.
- [122] B. Simon, "Holonomy, the Quantum Adiabatic Theorem, and Berry's Phase," *Physical Review Letters*, vol. 51, no. 24, pp. 2167–2170, 1983.
- [123] P. Leboeuf, J. Kurchan, M. Feingold, and D. P. Arovas, "Phase-space localization: Topological aspects of quantum chaos," *Physical Review Letters*, vol. 65, no. 25, pp. 3076–3079, 1990.
- [124] A. Barelli and R. Fleckinger, "Semiclassical analysis of Harper-like models," *Physical Review B*, vol. 46, no. 18, pp. 11559–11569, 1992.
- [125] A. Kubasiak, P. Massignan, and M. Lewenstein, "Topological superfluids on a lattice with non-Abelian gauge fields," *EPL (Europhysics Letters)*, vol. 92, no. 4, p. 46004, 2010.
- [126] P. Ponte, A. Chandran, Z. Papić, and D. A. Abanin, "Periodically driven ergodic and many-body localized quantum systems," *Annals of Physics*, vol. 353, pp. 196–204, 2015.
- [127] V. Khemani, A. Lazarides, R. Moessner, and S. Sondhi, "Phase Structure of Driven Quantum Systems," *Physical Review Letters*, vol. 116, no. 25, p. 250401, 2016.
- [128] A. Tanaka and M. Miyamoto, "Quasienergy Anholonomy and its Application to Adiabatic Quantum State Manipulation," *Physical Review Letters*, vol. 98, no. 16, p. 160407, 2007.
- [129] R. Grimm, M. Weidmüller, and Y. B. Ovchinnikov, "Optical Dipole Traps for Neutral Atoms," *Advances in Atomic Molecular and Optical Physics*, vol. 42, p. 95170, 2000.

- [130] N. R. Cooper and J. Dalibard, “Optical flux lattices for two-photon dressed states,” *EPL (Europhysics Letters)*, vol. 95, no. 6, p. 66004, 2011.
- [131] N. R. Cooper, “Optical Flux Lattices for Ultracold Atomic Gases,” *Physical Review Letters*, vol. 106, no. 17, p. 175301, 2011.
- [132] T. Fukui, Y. Hatsugai, and H. Suzuki, “Chern Numbers in Discretized Brillouin Zone: Efficient Method of Computing (Spin) Hall Conductances,” *Journal of the Physical Society of Japan*, vol. 74, no. 6, pp. 1674–1677, 2005.
- [133] B. Bernevig and T. Hughes, *Topological Insulators and Topological Superconductors*. Princeton University Press, 2013.
- [134] Y. Hasegawa, R. Konno, H. Nakano, and M. Kohmoto, “Zero modes of tight-binding electrons on the honeycomb lattice,” *Physical Review B*, vol. 74, no. 3, p. 033413, 2006.
- [135] J. L. Mañes, F. Guinea, and M. A. H. Vozmediano, “Existence and topological stability of Fermi points in multilayered graphene,” *Physical Review B*, vol. 75, no. 15, p. 155424, 2007.
- [136] L. Tarruell, D. Greif, T. Uehlinger, G. Jotzu, and T. Esslinger, “Creating, moving and merging Dirac points with a Fermi gas in a tunable honeycomb lattice,” *Nature*, vol. 483, no. 7389, pp. 302–305, 2012.
- [137] L. Duca, T. Li, M. Reitter, I. Bloch, M. Schleier-Smith, and U. Schneider, “An Aharonov-Bohm interferometer for determining Bloch band topology,” *Science*, vol. 347, no. 6219, pp. 288–292, 2015.
- [138] C. Wu and S. Das Sarma, “ $p_x, p_y$ -orbital counterpart of graphene: Cold atoms in the honeycomb optical lattice,” *Physical Review B*, vol. 77, no. 23, p. 235107, 2008.
- [139] L.-H. Wu and X. Hu, “Topological Properties of Electrons in Honeycomb Lattice with Detuned Hopping Energy,” *Scientific Reports*, vol. 6, no. 1, p. 24347, 2016.
- [140] K. Wakabayashi, K.-i. Sasaki, T. Nakanishi, and T. Enoki, “Electronic states of graphene nanoribbons and analytical solutions,” *Science and Technology of Advanced Materials*, vol. 11, no. 5, p. 054504, 2010.
- [141] M. Buchhold, D. Cocks, and W. Hofstetter, “Effects of Smooth Boundaries on Topological Edge Modes in Optical Lattices,” *Physical Review A*, vol. 85, no. 6, p. 063614, 2012. arXiv: 1204.0016.
- [142] L. Duca, *Probing topological properties of Bloch bands with ultracold atoms in a honeycomb optical lattice*. PhD thesis, Ludwig-Maximilians-Universität München, 2015.

- [143] M. Reitter, *Scattering processes in interacting Floquet systems*. PhD thesis, Ludwig-Maximilians-Universität München, 2017.
- [144] D. A. Steck, “Rubidium 87 D Line Data.” <https://steck.us/alkalidata/>, 2015.
- [145] T. G. Tiecke, “Properties of Potassium.” <https://tobiastiecke.nl/archive/PotassiumProperties.pdf>, 2019.
- [146] J. Schoser, A. Batär, R. Löw, V. Schweikhard, A. Grabowski, Y. B. Ovchinnikov, and T. Pfau, “Intense source of cold Rb atoms from a pure two-dimensional magneto-optical trap,” *Physical Review A*, vol. 66, no. 2, p. 023410, 2002.
- [147] K. Dieckmann, R. J. C. Spreeuw, M. Weidemüller, and J. T. M. Walraven, “Two-dimensional magneto-optical trap as a source of slow atoms,” *Physical Review A*, vol. 58, no. 5, pp. 3891–3895, 1998.
- [148] J. Catani, P. Maioli, L. De Sarlo, F. Minardi, and M. Inguscio, “Intense slow beams of bosonic potassium isotopes,” *Physical Review A*, vol. 73, no. 3, p. 033415, 2006.
- [149] H. J. Metcalf and P. van der Straten, *Laser Cooling and Trapping*. Springer-Verlag New York, Inc., 1999.
- [150] V. Gokhroo, G. Rajalakshmi, R. K. Easwaran, and C. S. Unnikrishnan, “Sub-Doppler deep-cooled bosonic and fermionic isotopes of potassium in a compact 2D + –3D MOT set-up,” *Journal of Physics B: Atomic, Molecular and Optical Physics*, vol. 44, no. 11, p. 115307, 2011.
- [151] W. Petrich, M. H. Anderson, J. R. Ensher, and E. A. Cornell, “Behavior of atoms in a compressed magneto-optical trap,” *Journal of the Optical Society of America B*, vol. 11, no. 8, p. 1332, 1994.
- [152] M. Landini, S. Roy, L. Carcagní, D. Trypogeorgos, M. Fattori, M. Inguscio, and G. Modugno, “Sub-Doppler laser cooling of potassium atoms,” *Physical Review A*, vol. 84, no. 4, p. 043432, 2011.
- [153] M. Greiner, I. Bloch, T. W. Hänsch, and T. Esslinger, “Magnetic transport of trapped cold atoms over a large distance,” *Physical Review A*, vol. 63, no. 3, p. 031401, 2001.
- [154] D. M. Brink and C. V. Sukumar, “Majorana spin-flip transitions in a magnetic trap,” *Physical Review A*, vol. 74, no. 3, p. 035401, 2006.
- [155] D. S. Naik and C. Raman, “Optically plugged quadrupole trap for Bose-Einstein condensates,” *Physical Review A*, vol. 71, no. 3, p. 033617, 2005.
- [156] A. L. Migdall, J. V. Prodan, W. D. Phillips, T. H. Bergeman, and H. J. Metcalf, “First Observation of Magnetically Trapped Neutral Atoms,” *Physical Review Letters*, vol. 54, no. 24, pp. 2596–2599, 1985.

- [157] L. De Sarlo, P. Maioli, G. Barontini, J. Catani, F. Minardi, and M. Inguscio, “Collisional properties of sympathetically cooled K 39,” *Physical Review A*, vol. 75, no. 2, p. 022715, 2007.
- [158] A. Simoni, M. Zaccanti, C. D’Errico, M. Fattori, G. Roati, M. Inguscio, and G. Modugno, “Near-threshold model for ultracold KRb dimers from interisotope Feshbach spectroscopy,” *Physical Review A*, vol. 77, no. 5, p. 052705, 2008.
- [159] F. Ferlaino, C. D’Errico, G. Roati, M. Zaccanti, M. Inguscio, G. Modugno, and A. Simoni, “Feshbach spectroscopy of a K-Rb atomic mixture,” *Physical Review A*, vol. 73, no. 4, p. 040702, 2006.
- [160] C. D’Errico, M. Zaccanti, M. Fattori, G. Roati, M. Inguscio, G. Modugno, and A. Simoni, “Feshbach resonances in ultracold  $^{39}\text{K}$ ,” *New Journal of Physics*, vol. 9, no. 7, pp. 223–223, 2007.
- [161] C. Chin, R. Grimm, P. Julienne, and E. Tiesinga, “Feshbach resonances in ultracold gases,” *Reviews of Modern Physics*, vol. 82, no. 2, pp. 1225–1286, 2010.
- [162] E. Timmermans, “Feshbach resonances in atomic Bose-Einstein condensates,” *Physics Reports*, vol. 315, no. 1-3, pp. 199–230, 1999.
- [163] T. Köhler, K. Góral, and P. S. Julienne, “Production of cold molecules via magnetically tunable Feshbach resonances,” *Reviews of Modern Physics*, vol. 78, no. 4, pp. 1311–1361, 2006.
- [164] H. Feshbach, “Unified Theory of Nuclear Reactions,” *Annals of Physics*, vol. 5, no. 4, p. 34, 1958.
- [165] A. J. Moerdijk, B. J. Verhaar, and A. Axelsson, “Resonances in ultracold collisions of Li 6 , Li 7 , and Na 23 ,” *Physical Review A*, vol. 51, no. 6, pp. 4852–4861, 1995.
- [166] W. Ketterle, D. S. Durfee, and S. D. M. Kurn, “Making, probing and understanding bose-einstein condensates,” in *Bose-einstein condensation in atomic gases*, proceedings of the international school of physics Enrico Fermi, 1999.
- [167] H. Haken and H. Wolf, *The physics of atoms and quanta: Introduction to experiments and theory*. Springer-Verlag, 1994.
- [168] G. Reinaudi, T. Lahaye, Z. Wang, and D. Guéry-Odelin, “Strong saturation absorption imaging of dense clouds of ultracold atoms,” *Optics Letters*, vol. 32, no. 21, p. 3143, 2007.
- [169] F. Gerbier, A. Widera, S. Fölling, O. Mandel, T. Gericke, and I. Bloch, “Interference pattern and visibility of a Mott insulator,” *Physical Review A*, vol. 72, no. 5, p. 053606, 2005.

- [170] M. Greiner, I. Bloch, O. Mandel, T. W. Hänsch, and T. Esslinger, “Exploring Phase Coherence in a 2D Lattice of Bose-Einstein Condensates,” *Physical Review Letters*, vol. 87, no. 16, p. 160405, 2001.
- [171] S. Stringari, “Collective Excitations of a Trapped Bose-Condensed Gas,” *Physical Review Letters*, vol. 77, no. 12, pp. 2360–2363, 1996.
- [172] J. L. Ville, T. Bienaimé, R. Saint-Jalm, L. Corman, M. Aidelsburger, L. Chomaz, K. Kleinlein, D. Perconte, S. Nascimbène, J. Dalibard, and J. Beugnon, “Loading and compression of a single two-dimensional Bose gas in an optical accordion,” *Physical Review A*, vol. 95, no. 1, p. 013632, 2017.
- [173] T. C. Li, H. Kelkar, D. Medellin, and M. G. Raizen, “Real-time control of the periodicity of a standing wave: an optical accordion,” *Optics Express*, vol. 16, no. 8, p. 5465, 2008.
- [174] R. Jáuregui, N. Poli, G. Roati, and G. Modugno, “Anharmonic parametric excitation in optical lattices,” *Physical Review A*, vol. 64, no. 3, p. 033403, 2001.
- [175] T. A. Savard, K. M. O’Hara, and J. E. Thomas, “Laser-noise-induced heating in far-off resonance optical traps,” *Physical Review A*, vol. 56, no. 2, pp. R1095–R1098, 1997.
- [176] C. Robens, J. Zopes, W. Alt, S. Brakhane, D. Meschede, and A. Alberti, “Low-Entropy States of Neutral Atoms in Polarization-Synthesized Optical Lattices,” *Physical Review Letters*, vol. 118, no. 6, p. 065302, 2017.
- [177] C. Robens, S. Brakhane, W. Alt, D. Meschede, J. Zopes, and A. Alberti, “Fast, High-Precision Optical Polarization Synthesizer for Ultracold-Atom Experiments,” *Physical Review Applied*, vol. 9, no. 3, p. 034016, 2018.
- [178] A. Zenesini, D. Ciampini, O. Morsch, and E. Arimondo, “Observation of Stückelberg oscillations in accelerated optical lattices,” *Physical Review A*, vol. 82, no. 6, p. 065601, 2010.
- [179] S. Kling, T. Salger, C. Grossert, and M. Weitz, “Atomic Bloch-Zener Oscillations and Stückelberg Interferometry in Optical Lattices,” *Physical Review Letters*, vol. 105, no. 21, p. 215301, 2010.
- [180] A. Dauphin and N. Goldman, “Extracting the Chern Number from the Dynamics of a Fermi Gas: Implementing a Quantum Hall Bar for Cold Atoms,” *Physical Review Letters*, vol. 111, no. 13, p. 135302, 2013.
- [181] H. M. Price and N. R. Cooper, “Mapping the Berry curvature from semiclassical dynamics in optical lattices,” *Physical Review A*, vol. 85, no. 3, p. 033620, 2012.
- [182] D. Xiao, M.-C. Chang, and Q. Niu, “Berry Phase Effects on Electronic Properties,” *Reviews of Modern Physics*, vol. 82, no. 3, pp. 1959–2007, 2010. arXiv: 0907.2021.

- [183] T. Kitagawa, M. A. Broome, A. Fedrizzi, M. S. Rudner, E. Berg, I. Kassal, A. Aspuru-Guzik, E. Demler, and A. G. White, “Observation of topologically protected bound states in photonic quantum walks,” *Nature Communications*, vol. 3, no. 1, p. 882, 2012.
- [184] A. Bouhon, A. M. Black-Schaffer, and R.-J. Slager, “Wilson loop approach to fragile topology of split elementary band representations and topological crystalline insulators with time-reversal symmetry,” *Physical Review B*, vol. 100, no. 19, p. 195135, 2019.
- [185] A. Eckardt and E. Anisimovas, “High-frequency approximation for periodically driven quantum systems from a Floquet-space perspective,” *New Journal of Physics*, vol. 17, no. 9, p. 093039, 2015. arXiv: 1502.06477.
- [186] M. Modugno and G. Pettini, “Correspondence between a shaken honeycomb lattice and the Haldane model,” *Physical Review A*, vol. 96, no. 5, p. 053603, 2017. arXiv: 1708.00242.
- [187] N. Goldman, J. Dalibard, A. Dauphin, F. Gerbier, M. Lewenstein, P. Zoller, and I. B. Spielman, “Direct imaging of topological edge states in cold-atom systems,” *Proceedings of the National Academy of Sciences*, vol. 110, no. 17, pp. 6736–6741, 2013.
- [188] M. Endres, H. Bernien, A. Keesling, H. Levine, E. R. Anschuetz, A. Krajenbrink, C. Senko, V. Vuletic, M. Greiner, and M. D. Lukin, “Atom-by-atom assembly of defect-free one-dimensional cold atom arrays,” *Science*, vol. 354, no. 6315, pp. 1024–1027, 2016.
- [189] D. Barredo, S. de Léséleuc, V. Lienhard, T. Lahaye, and A. Browaeys, “An atom-by-atom assembler of defect-free arbitrary two-dimensional atomic arrays,” *Science*, vol. 354, no. 6315, pp. 1021–1023, 2016.
- [190] J. Billy, V. Josse, Z. Zuo, A. Bernard, B. Hambrecht, P. Lugan, D. Clément, L. Sanchez-Palencia, P. Bouyer, and A. Aspect, “Direct observation of Anderson localization of matter waves in a controlled disorder,” *Nature*, vol. 453, no. 7197, pp. 891–894, 2008.
- [191] S. S. Kondov, W. R. McGehee, J. J. Zirbel, and B. DeMarco, “Three-Dimensional Anderson Localization of Ultracold Matter,” *Science*, vol. 334, no. 6052, pp. 66–68, 2011.
- [192] F. Jendrzejewski, A. Bernard, K. Müller, P. Cheinet, V. Josse, M. Piraud, L. Pezzé, L. Sanchez-Palencia, A. Aspect, and P. Bouyer, “Three-dimensional localization of ultracold atoms in an optical disordered potential,” *Nature Physics*, vol. 8, no. 5, pp. 398–403, 2012.

- [193] M. Schreiber, S. S. Hodgman, P. Bordia, H. P. Luschen, M. H. Fischer, R. Vosk, E. Altman, U. Schneider, and I. Bloch, “Observation of many-body localization of interacting fermions in a quasirandom optical lattice,” *Science*, vol. 349, no. 6250, pp. 842–845, 2015.
- [194] J.-y. Choi, S. Hild, J. Zeiher, P. Schauss, A. Rubio-Abadal, T. Yefsah, V. Khemani, D. A. Huse, I. Bloch, and C. Gross, “Exploring the many-body localization transition in two dimensions,” *Science*, vol. 352, no. 6293, pp. 1547–1552, 2016.
- [195] A. Rubio-Abadal, J.-y. Choi, J. Zeiher, S. Hollerith, J. Rui, I. Bloch, and C. Gross, “Many-Body Delocalization in the Presence of a Quantum Bath,” *Physical Review X*, vol. 9, no. 4, p. 041014, 2019.
- [196] N. Goldman, G. Jotzu, M. Messer, F. Görg, R. Desbuquois, and T. Esslinger, “Creating topological interfaces and detecting chiral edge modes in a two-dimensional optical lattice,” *Physical Review A*, vol. 94, no. 4, p. 043611, 2016.
- [197] J. Sebby-Strabley, B. Brown, M. Anderlini, P. Lee, W. Phillips, J. Porto, and P. Johnson, “Preparing and Probing Atomic Number States with an Atom Interferometer,” *Physical Review Letters*, vol. 98, no. 20, p. 200405, 2007.
- [198] S. Fölling, S. Trotzky, P. Cheinet, M. Feld, R. Saers, A. Widera, T. Müller, and I. Bloch, “Direct observation of second-order atom tunnelling,” *Nature*, vol. 448, no. 7157, pp. 1029–1032, 2007.
- [199] S. Trotzky, Y.-A. Chen, A. Flesch, I. P. McCulloch, U. Schollwöck, J. Eisert, and I. Bloch, “Probing the relaxation towards equilibrium in an isolated strongly correlated one-dimensional Bose gas,” *Nature Physics*, vol. 8, no. 4, pp. 325–330, 2012.
- [200] P. Bordia, H. Lüschen, U. Schneider, M. Knap, and I. Bloch, “Periodically driving a many-body localized quantum system,” *Nature Physics*, vol. 13, no. 5, pp. 460–464, 2017.
- [201] P. Bordia, H. Lüschen, S. Scherg, S. Gopalakrishnan, M. Knap, U. Schneider, and I. Bloch, “Probing Slow Relaxation and Many-Body Localization in Two-Dimensional Quasiperiodic Systems,” *Physical Review X*, vol. 7, no. 4, p. 041047, 2017.
- [202] W. Zwerger, “Mott-Hubbard transition of cold atoms in optical lattices,” *arXiv:cond-mat/0211314*, 2003.
- [203] J. Hubbard, “Electron correlations in narrow energy bands,” *Proceedings of the Royal Society A*, vol. 276, pp. 238–257, 1963.
- [204] R. Walters, G. Cotugno, T. H. Johnson, S. R. Clark, and D. Jaksch, “*ab initio* derivation of hubbard models for cold atoms in optical lattices,” *Physical Review A*, vol. 87, no. 4, p. 043613, 2013.

- [205] Private communication with Stuart Flannigan.
- [206] N. Marzari, A. A. Mostofi, J. R. Yates, I. Souza, and D. Vanderbilt, “Maximally localized Wannier functions: Theory and applications,” *Reviews of Modern Physics*, vol. 84, no. 4, pp. 1419–1475, 2012.
- [207] L. Tonks, “The Complete Equation of State of One, Two and Three-Dimensional Gases of Hard Elastic Spheres,” *Physical Review*, vol. 50, no. 10, pp. 955–963, 1936.
- [208] E. H. Lieb and W. Liniger, “Exact Analysis of an Interacting Bose Gas. I. The General Solution and the Ground State,” *Physical Review*, vol. 130, no. 4, pp. 1605–1616, 1963.
- [209] B. Paredes, A. Widera, V. Murg, O. Mandel, S. Fölling, I. Cirac, G. V. Shlyapnikov, T. W. Hänsch, and I. Bloch, “Tonks–Girardeau gas of ultracold atoms in an optical lattice,” *Nature*, vol. 429, no. 6989, pp. 277–281, 2004.
- [210] T. A. Sedrakyan, A. Kamenev, and L. I. Glazman, “Composite fermion state of spin-orbit-coupled bosons,” *Physical Review A*, vol. 86, no. 6, p. 063639, 2012.
- [211] T. A. Sedrakyan, V. M. Galitski, and A. Kamenev, “Statistical Transmutation in Floquet Driven Optical Lattices,” *Physical Review Letters*, vol. 115, no. 19, p. 195301, 2015.
- [212] P. A. Murthy, D. Kedar, T. Lompe, M. Neidig, M. G. Ries, A. N. Wenz, G. Zürn, and S. Jochim, “Matter-wave Fourier optics with a strongly interacting two-dimensional Fermi gas,” *Physical Review A*, vol. 90, no. 4, p. 043611, 2014.
- [213] D. S. Petrov and G. V. Shlyapnikov, “Interatomic collisions in a tightly confined Bose gas,” *Physical Review A*, vol. 64, no. 1, p. 012706, 2001.
- [214] S. Tung, G. Lamporesi, D. Lobser, L. Xia, and E. A. Cornell, “Observation of the Presuperfluid Regime in a Two-Dimensional Bose Gas,” *Physical Review Letters*, vol. 105, no. 23, p. 230408, 2010.
- [215] T. Yefsah, R. Desbuquois, L. Chomaz, K. J. Günter, and J. Dalibard, “Exploring the Thermodynamics of a Two-Dimensional Bose Gas,” *Physical Review Letters*, vol. 107, no. 13, p. 130401, 2011.
- [216] L. Corman, *The Two-Dimensional Bose Gas in Box Potentials*. PhD thesis, PSL Research University, Paris, 2016.
- [217] J. Stenger, S. Inouye, A. P. Chikkatur, D. M. Stamper-Kurn, D. E. Pritchard, and W. Ketterle, “Bragg Spectroscopy of a Bose-Einstein Condensate,” *Physical Review Letters*, vol. 82, no. 23, pp. 4569–4573, 1999.

- [218] P. T. Ernst, S. Götze, J. S. Krauser, K. Pyka, D.-S. Lühmann, D. Pfannkuche, and K. Sengstock, “Probing superfluids in optical lattices by momentum-resolved Bragg spectroscopy,” *Nature Physics*, vol. 6, no. 1, pp. 56–61, 2010.
- [219] R. Yu, X. L. Qi, A. Bernevig, Z. Fang, and X. Dai, “Equivalent expression of Z 2 topological invariant for band insulators using the non-Abelian Berry connection,” *Physical Review B*, vol. 84, no. 7, p. 075119, 2011.
- [220] F. Grusdt, D. Abanin, and E. Demler, “Measuring Z 2 topological invariants in optical lattices using interferometry,” *Physical Review A*, vol. 89, no. 4, p. 043621, 2014.
- [221] A. Alexandradinata, X. Dai, and B. A. Bernevig, “Wilson-loop characterization of inversion-symmetric topological insulators,” *Physical Review B*, vol. 89, no. 15, p. 155114, 2014.
- [222] A. Alexandradinata and B. A. Bernevig, “Berry-phase description of topological crystalline insulators,” *Physical Review B*, vol. 93, no. 20, p. 205104, 2016.
- [223] J. Höller and A. Alexandradinata, “Topological Bloch oscillations,” *Physical Review B*, vol. 98, no. 2, p. 024310, 2018.
- [224] J. Zak, “Berry’s phase for energy bands in solids,” *Physical Review Letters*, vol. 62, no. 23, pp. 2747–2750, 1989.
- [225] F. Wilczek, “Two applications of axion electrodynamics,” *Physical Review Letters*, vol. 58, no. 18, pp. 1799–1802, 1987.
- [226] P. Hauke, M. Lewenstein, and A. Eckardt, “Tomography of Band Insulators from Quench Dynamics,” *Physical Review Letters*, vol. 113, no. 4, p. 045303, 2014.
- [227] N. Flaschner, B. S. Rem, M. Tarnowski, D. Vogel, D.-S. Luhmann, K. Sengstock, and C. Weitenberg, “Experimental reconstruction of the Berry curvature in a Floquet Bloch band,” *Science*, vol. 352, no. 6289, pp. 1091–1094, 2016.
- [228] S. Kivelson, “Wannier functions in one-dimensional disordered systems: Application to fractionally charged solitons,” *Physical Review B*, vol. 26, no. 8, pp. 4269–4277, 1982.
- [229] J. Hoeller, *Topological Quantization of Berry Phases in Quantum and Classical Systems*. PhD thesis, Yale University, New Haven, Connecticut, 2020.
- [230] C. Brouder, G. Panati, M. Calandra, C. Mourougane, and N. Marzari, “Exponential Localization of Wannier Functions in Insulators,” *Physical Review Letters*, vol. 98, no. 4, p. 046402, 2007.
- [231] G. Panati, “Triviality of Bloch and Bloch–Dirac Bundles,” *Annales Henri Poincaré*, vol. 8, no. 5, pp. 995–1011, 2007.

- [232] W. Kohn, “Analytic Properties of Bloch Waves and Wannier Functions,” *Physical Review*, vol. 115, no. 4, pp. 809–821, 1959.
- [233] Y. Makeenko, *Methods of Contemporary Gauge Theory*. Cambridge University Press, 2005.
- [234] S. N. Shevchenko, S. Ashhab, and F. Nori, “Landau-Zener-Stückelberg interferometry,” *Physics reports*, vol. 492, no. 1, pp. 1–30, 2010.
- [235] H. Chen, X.-J. Liu, and X. Xie, “Chern Kondo Insulator in an Optical Lattice,” *Physical Review Letters*, vol. 116, no. 4, p. 046401, 2016.
- [236] A. Lazarides, A. Das, and R. Moessner, “Periodic Thermodynamics of Isolated Quantum Systems,” *Physical Review Letters*, vol. 112, no. 15, p. 150401, 2014.
- [237] M. Weinberg, C. Ölschläger, C. Sträter, S. Prell, A. Eckardt, K. Sengstock, and J. Simonet, “Multiphoton interband excitations of quantum gases in driven optical lattices,” *Physical Review A*, vol. 92, no. 4, p. 043621, 2015.
- [238] T. Kitagawa, T. Oka, A. Brataas, L. Fu, and E. Demler, “Transport properties of nonequilibrium systems under the application of light: Photoinduced quantum Hall insulators without Landau levels,” *Physical Review B*, vol. 84, no. 23, p. 235108, 2011.
- [239] S. Choudhury and E. J. Mueller, “Transverse collisional instabilities of a Bose-Einstein condensate in a driven one-dimensional lattice,” *Physical Review A*, vol. 91, no. 2, p. 023624, 2015.
- [240] T. Bilitewski and N. R. Cooper, “Scattering theory for Floquet-Bloch states,” *Physical Review A*, vol. 91, no. 3, p. 033601, 2015.
- [241] S. Lellouch, M. Bukov, E. Demler, and N. Goldman, “Parametric Instability Rates in Periodically Driven Band Systems,” *Physical Review X*, vol. 7, no. 2, p. 021015, 2017.
- [242] C. E. Creffield, “Instability and control of a periodically driven Bose-Einstein condensate,” *Physical Review A*, vol. 79, no. 6, p. 063612, 2009.
- [243] L. Corman, L. Chomaz, T. Bienaimé, R. Desbuquois, C. Weitenberg, S. Nascimbène, J. Dalibard, and J. Beugnon, “Quench-Induced Supercurrents in an Annular Bose Gas,” *Physical Review Letters*, vol. 113, no. 13, p. 135302, 2014.
- [244] N. Navon, A. L. Gaunt, R. P. Smith, and Z. Hadzibabic, “Critical dynamics of spontaneous symmetry breaking in a homogeneous Bose gas,” *Science*, vol. 347, no. 6218, pp. 167–170, 2015.

- [245] T. Boulier, J. Maslek, M. Bukov, C. Bracamontes, E. Magnan, S. Lellouch, E. Demler, N. Goldman, and J. Porto, “Parametric Heating in a 2D Periodically Driven Bosonic System: Beyond the Weakly Interacting Regime,” *Physical Review X*, vol. 9, no. 1, p. 011047, 2019.

## Acknowledgments

I would like to say thank you to all the great people who have made this work possible in one or the other way.

First of all I want to thank Immanuel Bloch for giving me the opportunity to do my PhD in his group. He has created an excellent environment to conduct research, allowed me to visit many conferences and workshops and to get in contact with numerous proficient collaborators. I benefited a lot from the scientific discussions in which he shared his knowledge and ideas with us. I also want to thank Ulrich Schneider for offering me to work in his team and for the support and help he provided in the beginning of my PhD. For the largest part of my PhD I had the pleasure to work with and to be supervised by Monika Aidelsburger. Although successfully leading four research labs, she always had the time to answer my questions, for which I am very grateful. She took our team forward with many important ideas and the work we have done in the last years would not have been possible without her.

A big thanks goes to the Fermi 2 team. Most of my time in the lab I spent with Christoph Braun, who is a very talented physicist with a sharp mind. I really enjoyed working together and I learned a lot from you. Thank you for the great and funny times! I also want to thank my former colleagues Martin Reitter, Jakob Näger and Tracy Li, who taught me how to run the lab and most importantly how to fix it, especially Martin for the drinks, the discussions and for always answering my questions. Recently our team was joined by Raphaël Saint-Jalm and Alexander Hesse, who already contribute a lot. I am sure the lab is in capable hands and you will produce many exciting results in the future.

Furthermore, I want to thank all the former and current members of the Bloch group, I very much appreciated the open atmosphere and the mutual support. At LMU, special thanks also goes to Sebastian Scherg, Thomas Kohlert, Hendrik von Raven, Till Klostermann, Christian Schweizer, Michael Lohse, Cesar Cabrera, Julian Wienand, Henrik Lüschen, Oscar Bettermann and Giulio Pasqualetti for the relaxing lunch breaks, beers and fruitful discussions. And not to forget the team from the Bürgerliche Dämmerung, motivating me to go running even when the weather was bad. Even though Garching sometimes seemed to be far away, also our MPQ colleagues have been helpful and supportive at all times. In particular I want to thank Antonio Rubio Abadal, Jayadev Vijayan, Simon Hollerith, Timon Hilker, Roman Bause, Marcel Duda and Nikolaus Lorenz.

Thanks to Ildiko Kecskei, Kristina Schuldt and Doreen Seidl I enjoyed numerous nice group retreats and Christmas parties. Many thanks goes to Ildiko for finding flexible and unbureaucratic solutions to any kind of problem, being kind and creating a pleasant atmosphere. I also want to thank Bodo Hecker for his valuable technical support and always being in a good mood.

I would like to thank our theory collaborators André Eckardt, Nur Ünal, Nathan Goldman, Marin Bukov, Judith Höller, Andrew Daley and Stuart Flannigan for being patient when the experiment did not work or the measurements took longer than expected, as well as for answering my questions and also explaining basic things to me.

Moreover, I would like to express my gratitude to Sonya Gzyl for arranging lots of interesting events and to all members of the IMPRS-QST program, especially from the first cohort, for the inspiring times and discussions we had.

Thank you also to the whole MCQST office team for organizing great conferences and workshops, that have provided opportunities for scientific and personal development. Special thanks goes to Barbara Tautz for her competent management of the mentoring and the leadership program, but also for having an open ear to personal problems and creating a warm atmosphere where everyone feels welcome. Another thanks to the members of the mentoring program for our nice discussion rounds which I really enjoyed and which showed me that I am not alone with many of the troubles I encountered.

I am very grateful to Monika Aidelsburger, Chrsitoph Braun, Alexander Hesse, Raphaël Saint-Jalm and Lukas Knips for their proof-reading, which improved this thesis a lot. Also, thanks to Frank Pollmann for being the second referee of my thesis as well as to Jan Lipfert and Alexander Högele for being part of my thesis defense committee.

I would like to thank my family and friends, who have supported me in everything I was doing and accepted me as I am. And finally I want to thank Lukas for always being there for me, living through all the highs and lows. Thank you for your support, your advice and your love.